Spring 5-15-2016

Goggle Augmented Imaging and Navigation System for Fluorescence-Guided Surgery

Suman Bikash Mondal
Washington University in St. Louis

Recommended Citation

Mondal, Suman Bikash, "Goggle Augmented Imaging and Navigation System for Fluorescence-Guided Surgery" (2016). *McKelvey School of Engineering Theses & Dissertations*. 173.
https://openscholarship.wustl.edu/eng_etds/173

WASHINGTON UNIVERSITY IN ST. LOUIS

School of Engineering & Applied Science
Department of Biomedical Engineering

Dissertation Examination Committee:
Samuel Achilefu, Chair
Mark Anastasio
Joseph Culver
Viktor Gruev
Julie Margenthaler
Lihong Wang

Goggle Augmented Imaging and Navigation System for Fluorescence-Guided Surgery

by
Suman Bikash Mondal

A dissertation presented to the
Graduate School of Arts & Sciences
of Washington University in
partial fulfillment of the
requirements for the degree
of Doctor of Philosophy

May 2016
St. Louis, Missouri

Table of Contents

List of Figures

List of Tables

Acknowledgments

I would like to thank Dr. Samuel Achilefu, my research advisor. Dr. Achilefu is a wonderful mentor and teacher. I have learnt a lot about science, research and life in general over the years from him. I would like to thank him for providing me the opportunity, support, guidance and encouragement to pursue this research. I would like to thank the members of the Optical Radiology Laboratory, who helped me at every step. I would specially like to thank Dr. Walter J Akers, Dr. Rui Tang, Dr. Joseph Culver, Dr. Adam Bauer, Gail P. Sudlow, Kexiang Liang, Dr. Nalinikanth Kotagiri for their invaluable support, mentorship and scientific inputs.

I would like to specially thank our collaborators Dr. Viktor Gruev and Dr. Rongguang Liang for their support, collaborative research and guidance which was critical for this research. I worked very closely with Dr. Gruev's graduate student Dr. Shengkui Gao who worked tirelessly to help us develop the imaging sensor circuit electronics and image processing solutions for this research. I enjoyed working with Dr. Gao as a team and as a friend. I also worked closely with Dr. Liang's postdoctoral fellow, Dr. Nan Zhu, whose efforts were critical in developing the display and optical systems for the research. I learned a lot from Dr. Zhu and I am grateful to have worked with him. This work would not have been possible without them.

I would like to acknowledge my funding sources. I was supported by the Imaging Sciences Pathway awarded by Washington Univerity. This research was funded by National Cancer Institute grant R01CA171651-01A1.

Personally, I would like to thank my parents, for ensuring I got the best education and become the person I am today. They instilled in me the values that have guided me throughout my life and made me who I am. There love and support has always been a beacon of hope for me in even the most difficult of times. I would like to thank my sister for her encouragement throughout this

process. Talking to her even from far away always lifted my spirits. Finally, I would like to thank my wife for enduring love, understanding and support. Staying apart was not easy, but she was always there with me in spirit. She lifted me up during difficult times and was the first to celebrate even the most mundane of achievements. This would not have been possible without her by my side.

Suman Bikash Mondal

Washington University in St. Louis

May 2016

Dedicated to

Asim Mondal, my father and philosopher;

Kajal Mondal, my mother, and guiding star;

Soumashree Mondal, my sister and inspiration;

Monalisa Munsi, my wife and the love of my life.

ABSTRACT OF THE DISSERTATION

Goggle Augmented Imaging and Navigation System for Fluorescence-Guided Surgery

by

Suman Bikash Mondal

Doctor of Philosophy in Biomedical Engineering

Washington University in St. Louis, 2016

Professor Samuel Achilefu, Chair

Surgery remains the only curative option for most solid tumors. The standard-of-care usually involves tumor resection and sentinel lymph node biopsy for cancer staging. Surgeons rely on their vision and touch to distinguish healthy from cancer tissue during surgery, often leading to incomplete tumor resection that necessitates repeat surgery. Sentinel lymph node biopsy by conventional radioactive tracking exposes patients and caregivers to ionizing radiation, while blue dye tracking stains the tissue highlighting only superficial lymph nodes. Improper identification of sentinel lymph nodes may misdiagnose the stage of the cancer. Therefore there is a clinical need for accurate intraoperative tumor and sentinel lymph node visualization. Conventional imaging modalities such as x-ray computed tomography, positron emission tomography, magnetic resonance imaging, and ultrasound are excellent for preoperative cancer diagnosis and surgical planning. However, they are not suitable for intraoperative use, due to bulky complicated hardware, high cost, non-real-time imaging, severe restrictions to the surgical workflow and lack of sufficient resolution for tumor boundary assessment. This has propelled interest in fluorescence-guided surgery, due to availability of simple hardware that can achieve real-time, high resolution and sensitive imaging. Near-infrared fluorescence imaging is of particular interest due to low background absorbance by photoactive biomolecules, enabling thick tissue assessment. As a result several near-infrared fluorescence-guided surgery systems have been developed. However, they are limited by bulky hardware, disruptive information display and non-matched field of view to the user.

To address these limitations we have developed a compact, light-weight and wearable goggle augmented imaging and navigation system (GAINS). It detects the near-infrared fluorescence from a tumor accumulated contrast agent, along with the normal color view and displays accurately aligned, color-fluorescence images via a head-mounted display worn by the surgeon, in real-time. GAINS is a platform technology and capable of very sensitive fluorescence detection. Image display options include both video see-through and optical see-through head-mounted displays for high-contrast image guidance as well as direct visual access to the surgical bed. Image capture options from large field of view camera as well high magnification handheld microscope, ensures macroscopic as well as microscopic assessment of the tumor bed. Aided by tumor targeted near-infrared contrast agents, GAINS guided complete tumor resection in subcutaneous, metastatic and spontaneous mouse models of cancer with high sensitivity and specificity, in real-time. Using a clinically-approved near-infrared contrast agent, GAINS provided real-time image guidance for accurate visualization of lymph nodes in a porcine model and sentinel lymph nodes in human breast cancer and melanoma patients with high sensitivity. This work has addressed issues that have limited clinical adoption of fluorescence-guided surgery and paved the way for research into developing this approach towards standard-of-care practice that can potentially improve surgical outcomes in cancer.

Chapter 1: Real-time fluorescence-guided surgery

This chapter is based on a published article (1): Suman B. Mondal, Shengkui Gao, Nan Zhu, Rongguang Liang, Viktor Gruev, Samuel Achilefu, Chapter Five - Real-Time Fluorescence Image-Guided Oncologic Surgery, In: Martin G. Pomper and Paul B. Fisher, Editor(s), Advances in Cancer Research, Academic Press, 2014, Volume 124, Pages 171-211, ISSN 0065-230X, ISBN 9780124116382. I wrote the manuscript in collaboration with the co-authors, compiled the information, made illustrations and edited the manuscript.

1.1 Abstract

Medical imaging plays a critical role in cancer diagnosis and planning. Many of these patients rely on surgical intervention for curative outcomes. This requires a careful identification of the primary and microscopic tumors, and the complete removal of cancer. Although there have been efforts to adapt traditional imaging modalities for intraoperative image guidance, they suffer from several constraints such as large hardware footprint, high operation cost, and disruption of the surgical workflow. Because of the ease of image acquisition, relatively low cost devices and intuitive operation, optical imaging methods have received tremendous interests for use in real-time image-guided surgery. To improve imaging depth under low interference by tissue autofluorescence, many of these applications utilize light in the near-infra red (NIR) wavelengths, which is invisible to human eyes. With the availability of a wide selection of tumor-avid contrast agents, advancements in imaging sensors, electronic and optical designs, surgeons are able to combine different attributes of NIR optical imaging techniques to improve treatment outcomes. The emergence of diverse commercial and experimental image guidance systems, which are in various stages of clinical translation, attests to the potential high impact of intraoperative optical imaging methods to improve speed of oncologic surgery with high accuracy and minimal margin positivity.

1.2 Introduction

Imaging plays a central role in advancing biomedical and clinical research by providing critical information about molecular and functional processes of normal and diseased states of the body. Today, medical imaging methods have become indispensable in oncologic diagnosis, treatment planning, and monitoring treatment response. In oncology, the need for accurate visualization of tumors during surgery to ensure successful removal of all of the cancerous tissue in the first attempt while preserving healthy tissue has spurred the application of image guidance in the operating room. To be successful, the imaging methods are expected to detect tumors in the surgical suite in real-time with high sensitivity and specificity. Importantly, displaying the information in an accessible, easy to comprehend fashion to the surgeon will facilitate adoption of the method in clinics.

Although real-time image guidance is highly desirable in the operating room, it imposes technological hurdles, notably a minimum of 24 frames per second data acquisition and image display. As a result, the imaging time must be short (in the millisecond range) and any image processing must be very fast to allow display of images without latency to the surgeon. An approach to improve tumor-to-background ratio, which is needed for rapid assessment of suspicious lesions, is to incorporate molecular imaging agents in the imaging procedure. Molecular probes suitable for this application have been an area of enhanced research in the last two decades. This review discusses the need for real-time image guidance in oncologic surgery, current methods available for image guidance, along with their limitations and their advantages. Because fluorescence methods hold the most promise for clinical translation, emphasis on fluorescent molecular probes, imaging system design considerations, and current fluorescent image guidance systems highlights the promise and challenges of translating optical methods to humans within the context of oncologic image-guided resection of cancer.

1.2.1 Need for real time image-guided surgery

Cancer remains a major public health problem in the US and poses a huge economic burden (2). One in 4 deaths in the USA is caused by cancer (3). Although chemotherapy radiotherapy continue to play major roles in cancer treatment, surgery remains the primary curative option for most solid cancers (4). An important goal of oncologic surgery is to remove all cancerous tissue while preserving as much of the healthy tissue as possible. In this process, it is critical to avoid iatrogenic damage to vital organs and anatomic structures. With this overarching goal, delineation of tumors and their infiltration into healthy surrounding tissue will facilitate surgical resection with low margin positivity. Although the primary tumor mass are readily detectable, the boundary of the tumor and microscopic tumors are difficult to identify with unaided eyes.

Currently, preoperative imaging modalities such as magnetic resonance imaging (MRI), computed tomography (CT), and positron emission tomography (PET) provide exquisite structural or functional images that highlight the location of cancerous tissues. These modalities have facilitated early tumor detection, improved diagnostic accuracy, and helped in better staging and preoperative planning (5). Unfortunately, these systems are not currently amenable to use in the operating room because of their large hardware footprint, slow image reconstruction, lack of microscopic imaging capability, use of ionizing radiation, prohibitive cost, and specialized operator requirement (6, 7). Currently, surgeons rely only on their sight and touch to distinguish tumors from surrounding tissue. Human eyes cannot see deeper than the tissue surface, while human touch may not be able to distinguish small tumor nodes from the surrounding healthy tissue. It is even more difficult to distinguish diffuse tumors from healthy tissue merely by visual inspection and palpation. This may lead to incomplete tumor removal or resection of healthy tissue. Inaccurate delineation of the extent of the tumor tissue can endanger vital structures such as the nerves, leading to iatrogenic damage. Without image guidance, the accurate identification of tumors can be subjective and relies heavily on the surgeon’s experience. This creates significant variability in surgical outcomes.

Ex vivo histologic validation of excised tissue is used to determine if the resected tissue harbors tumors on the margins (Fig. 1). In some organs, a significant volume of healthy tissue is removed to minimize the chances of positive margins. However, this luxury is not available for certain organs such as the brain, where debulking of tumors is tailored to avoid disruption of brain functions. In breast cancer patients undergoing breast conserving surgery (BCS), between 20-70% have positive margins, typically indicating the presence of cancerous cells at or near the surgical margins (8-10). Invasive ductal carcinoma (IDC), the most common form of invasive breast cancer, has worse outcome for BCS, due to its poorly-defined tumor boundaries, rendering mastectomy a more reliable procedure (11). The issue of positive margins is prevalent in cancers at other locations as well. For example the standard 0.5 cm margin recommended for melanoma in-situ leads to 14%-50% of patients with positive margins that need subsequent re-excision (12-14). Therefore the gold standard remains histopathology, a procedure that renders its verdict after the patient has left the operating room (6). These cases generally necessitate repeat surgery, which is not only expensive, but has limited success because of the difficulty in seeing microscopic tumors or diffuse cells. Additionally, scar tissue formation also perturbs the surgical planes, making it more difficult for the surgeon to identify the remnant tumor tissue. Some studies suggested that surgery is a major perturbing factor for metastasis development in lab animals and in breast cancer (15) and that the neovasculature spawned after surgery may actually promote metastatic tumor growth (16). These studies underline the added importance of complete tumor removal in the first surgery. Thus, adoption of real-time image-guided surgery may help in reducing recall rates for oncologic surgery and prevent residual tumors from proliferating because of the perturbations from surgery.

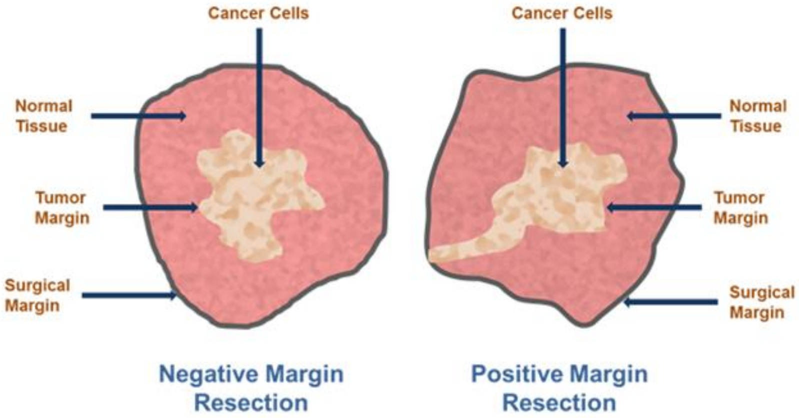

Figure 1: Surgical margins of resection in breast cancer.

These studies illustrate the tremendous interest in developing intraoperative image guidance systems that can help surgeons to visualize tumors in real-time and improve the accuracy of tumor resection without disrupting the normal surgical workflow. Some general requirements for such a system are summarized in Table 1.

Table 1: Desirable characteristics for real-time image guidance surgery.

Characteristic	Description
Intraoperative	Hardware conducive to be used in the operating room, during surgery
Real-time	≥ 24p frames per second image acquisition and display to surgeon without latency
High specificity	Contrast agent that very specifically accumulates in the tumor being imaged. Low false negatives
High sensitivity	High detection sensitivity of imaging system Detection of low fluorescence signal and small tumors
High resolution	Detection of small tumors and interrogation of the tumor boundary
Wearable	Ergonomic, hands-free unrestrictive movement
Non-interfering	Information display in a form that does not distract surgeon from the surgical bed
User friendly	Requires minimal training and no specialized operators

1.2.2 Current methods available for image-guided surgery

Some traditional imaging methods are currently used for surgical navigation. These include fluoroscopy and intraoperative ultrasonography (IUS). However, X-ray-based techniques such as fluoroscopy suffer from many challenges, including the exposure of patients to ionizing radiation, need for high concentration of contrast agents to compensate for the poor detection sensitivity, inability to detect microscopic lesions, and difficulty in miniaturizing X-Ray equipment. IUS can be used for tumor detection based primarily on tissue morphology, leading to significant false positive and negative rates (17-20). Moreover, IUS is a contact based method, which is less useful for identifying tumor boundaries or microscopic tumors during open surgeries, hampering detection of superficial and small tumors (21). Advanced instruments that mimic global positioning systems have been developed, where preoperative CT or MR image can be projected onto the appropriate anatomical structures. These systems suffer from limitations of the pre-operative imaging method, unsatisfactory registration due to tissue deformation and motion, and the inability to interrogate surgical margins for the presence of tumors. Intraoperative versions of MRI and CT systems have been developed, which are useful for preoperative staging and intraoperative guidance during tumor resection, especially in neurosurgery (6). Recent studies have shown that intraoperative MRI has is more effective than conventional neuro-navigation-guided surgery in increasing the extent of glioblastoma multiforme resection, enhancing quality of life, and prolonging survival after surgery (22). However, these systems have a large hardware footprint, require a complex infrastructure, specialized surgical suites and currently configured for neurosurgical applications only (23). Using MRI or CT in the operating room severely restricts the reach of the surgeon due to the small area in the scanner bore and the required compatibility of surgical instruments with the system’s magnetic field. Additionally, the preoperative view provided by these imaging modalities does not correspond to the field of view of the surgeon, which could disrupt normal surgical workflow. These limitations created a niche for intraoperative optical imaging systems for use in the operating room.

1.2.3 Optical methods amenable to image-guided surgery

Optical imaging techniques extract diagnostic information from light-tissue interactions. This imaging platform enjoys a combination of interesting features that uniquely makes it amenable to surgical applications. These include the ease of detection, high spatial and temporal resolution, and availability of a wide variety of contrast agents with unique signaling mechanisms. For these reasons, various optical techniques have been developed, which are at different stages of development or clinical translation.

Spectroscopic imaging, for example, uses spectral analysis methods to identify unique optical signatures that are characteristic of a target tissue. This approach has been used extensively to improve early detection of gastrointestinal malignancies (24), for intraoperative assessment of breast cancer margins (25) and detection of other forms of cancer (26). The vibrational spectra of biological specimens has been used to identify the biochemical constituents of tissue, but the relatively low sensitivity and limited spatial and temporal resolutions of this technique limits its application for *in vivo* use. Much stronger vibrational signals can be obtained with coherent anti-Stokes Raman scattering (CARS), a nonlinear Raman technique (27). CARS microscopy is useful for mapping lipid compartments, protein clusters and water distribution. Utilization of these spectral imaging methods for real-time image-guided surgery has not fully materialized, but they can readily play a role in characterizing focal suspicious lesions in situ. This could accelerate medical decision in the operating room.

Optical coherence tomography (OCT) is another optical technique that is used to provide surgical guidance. OCT is a nondestructive, high-resolution optical approach that uses low-coherence light and interferometry techniques to generate cross-sectional depth resolved two-dimensional (2D) and three dimensional (3D) images (28). The technique is similar in principle to ultrasound imaging, but, rather than measuring back reflected sound echoes from the tissue, it measures the amount of backscattered light (29). Intraoperative OCT can provide both qualitative and quantitative three-dimensional information. A recent study utilized OCT in many surgical specialties, especially in ophthalmology imaging (30-37) and coronary imaging (38-40). Intraoperative evaluation of breast tumor margins using OCT has also been reported (41). Several commercially OCT systems are available, including portable handheld OCT scanners for intraoperative applications (30, 33, 35, 37, 42). The handheld OCT scanner can be positioned in close proximity to a patient. The scanning head can be operated from any angle, facilitating the scanning of patients in the supine position. Difficulties with handheld OCT scanners principally involve stability and sterility, which necessitates the wrapping of the OCT probe and attached cord in sterile drapes before use in the operative field. Resolution and reproducibility are limited by operator stability. Newer OCT systems hold more promise for intraoperative applications. Examples include the Bioptigen OCT instrument (Bioptigen, Inc., Research Triangle Park, NC), iVue (Optovue, Inc., Fremont, CA) and Spectralis (Heidelberg Engineering). Wide applications of OCT in the operating room are envisaged in future.

Photoacoustic imaging is an emerging hybrid imaging technology that uses short laser pulses to irradiate chromophores in tissue, inducing localized thermo-elastic expansion that is detectable by wide-band ultrasonic transducers. Photoacoustic tomography offers improved depth resolution in the 3–20 mm range (43). Taking advantage of the high absorption coefficient of blood, photoacoustic imaging can display exquisite images of vascular network around tumors without the need for exogenous contrast agents. Ironically, fluorescent dyes with high absorption coefficient but low fluorescent quantum efficiency (which are not optimal for fluorescence imaging) are excellent contrast agents for photoacoustic imaging. A handheld photoacoustic probe system was recently developed for image-guided needle biopsy of sentinel lymph nodes for use in the operating room (44). With current efforts to miniaturize the technology, it is hoped that this imaging method could become an enabling platform for diverse surgical procedures.

1.3 Fluorescence Imaging Systems for Intraoperative Procedures

Fluorescence guided surgical resection of tumors

Although methods such as light scattering, absorption spectroscopy, Raman spectroscopy, bioluminescence imaging, and optical coherence tomography continue to make major advances, fluorescence techniques have dominated the field of intraoperative image-guided surgery recently. Accordingly, the remaining sections of this review focus on current and future status of fluorescence-based methods for real-time image guidance in the operating room.

1.3.1 Fluorescence sensor parameters

In this section, we consider the detection sensitivity of an imaging system for fluorescent signals. There are many factors that influence the performance of the fluorescence detection. These include the sensors' quantum efficiency in the emission wavelengths of the fluorescent dye, signal-to-noise ratio of the imaging sensor, transmission and optical density of both excitation and emission filters, and optical and electrical crosstalk between photodiodes, which is typically modeled via an overall modulation transfer function of the entire system. All of these effects contribute to the contrast ratio and the signal-to-noise ratio of the fluorescence signal. Each one of these factors is examined in details below.

Quantum efficiency of a photodiode

Quantum efficiency (QE) of a photodiode describes the amount of electron-hole pairs that are generated for a given number of incident photons per wavelength. QE is mathematically modeled via equation (*1*).

$$QE(\lambda) = \frac{N_{sig(\lambda)}}{N_{ph(\lambda)}} \quad (1)$$

In equation (*1*), N_{sig} is the signal charge in one pixel, and N_{ph} is the number of incident photon in one pixel. For example, if there are 100 incident photons at 780 nm and 30 electron-hole pairs are generated by the photo detectors, the quantum efficiency of the photo-detector is 30%. Higher quantum efficiency is preferred over lower one in order to detect the smallest amount of emitted photons by the detector. Most imaging sensors are tailored for maximum quantum efficiency in the green wavelengths (~550 nm), where the human visual system is highly sensitive. The quantum efficiency in the NIR is determined by the depth of the p-n (positively doped silicon and negative doped silicon) photo sensitive junction, as well as the doping concentration of the p-n junctions. In silicon photo-detectors, 99% of the incident NIR photons will penetrate and will get absorbed up to 20 microns. Most imaging sensors are fabricated on anepitaxial silicon, where the maximum depth of the photodiode is around 3 to 5 microns. Hence, most of the NIR photons will not get absorbed by the photodiode. This is the chief reason for the poor NIR sensitivity in complementary metal–oxide–semiconductor (CMOS) photo-detectors. Older CMOS process, such as 0.5 micron feature technology, tends to have deeper p-n junction, but they suffer from lower silicon doping. Hence, the overall benefit of deeper junctions is lost and the quantum efficiency in the NIR region remains around 30%. Nevertheless, semiconductor systems can drastically increase quantum efficiency in the NIR, but the size of the market prevents manufacturers from investing in the necessary resources to develop these sensors.

Signal-to-noise ratio (SNR)of an imaging sensor

The SNR is a metric that quantifies the smallest signal that can be detected by the imaging system in the presence of noise. The SNR of an imaging sensor can be computed by the equation (*2*):

$$SNR = 20log\frac{S}{N}\,[\mathrm{dB}] \qquad (2)$$

In equation (*2*), *S* is the number of electron-hole pairs generated for a given incident photon flux and *N* is noise in the detected signal.

To understand the SNR performance of a sensor, all noise sources in a sensor should be analyzed. There are two dominant noise sources in an imager. The first noise contributor is the read-out noise of the sensor or the thermal and 1/f noise of the read-out electronics in a sensor. This comprises source follower amplifier and switch transistors in the pixel, current source biasing transistor at the periphery of the imaging array, sample and hold circuit necessary for correlated double sampling operation, and an analog-to-digital converter (ADC). Once the photo-voltage, which is in an analog format, is digitized or quantized, there are no additional thermal noise contributors to the photo-signal. The thermal noise of the reset transistor, also known as reset noise, can be cancelled via a technique known as correlated double sampling (CDS). This technique subtracts the photodiode voltage from a known reference voltage using special charge transfer transistors, a technique borrowed from the charge-coupled device (CCD) imaging arena, and cancelling the thermal noise of the reset transistor. The CDS operation also effectively cancels 1/f noise because subtraction of the two voltages mentioned above is performed at high speed (~10 MHz to ~100 MHz), while the 1/f noise fluctuations have maximum bandwidth of 100 kHz. The biasing circuitry (typically a current mirror or cascoded current mirror), the sample and hold circuitry and the ADC circuitry introduce minimal thermal noise to the photo-signal. Since these circuits are placed outside the imaging array, where silicon real-estate is relatively cheap compared to the pixel's real-estate, which has prime value due to the small pixel pitch requirements, circuit designers utilize the silicon space to design low noise read-out circuits. Today's state-of-the-art imaging sensors have read-out noise close to few electrons, a remarkable feat allowing for extraordinary image quality in low light settings.

The second noise contributor in the imaging system is the photodiode shot noise. The shot noise arises from the uncertainty that an electron-hole pair, which is generated by the absorption of a photon, will pass though the depletion region of the p-n junction. This uncertainty is modeled as a Poisson distribution, which gives the typical approximation estimate of the shot noise power as N e^{-2}, where N is the total number of generated electron-hole pairs. From the two dominant noise sources, i.e. read-out noise of the electronic circuitry and photodiode's shot noise, the SNR of the imaging sensor can be computed via the equation (*3*):

$$SNR = 20log\left(\frac{S-B}{\sqrt{n_{read}^{2}+n_{photon\,shot}^{2}}}\right)[\mathrm{dB}] \qquad (3)$$

It is important to differentiate which one of the two noise sources is dominant and how to optimize the SNR performance for a given illumination conditions (or a photon flux). For low light conditions, the read-out noise is the dominant noise source in the system (Fig. 2). In this region of operation, the SNR of the imaging sensor can be approximated by equation (*4*):

$$SNR \approx 20log\left(\frac{S-B}{n_{read}}\right)[\text{dB}] \tag{4}$$

Under bright light conditions, the performance of the imaging sensor is limited by the shot noise of the photodiode (Fig. 2). For example, if the read-out noise is 10 e^-, and there are 10,000 electron-hole pairs generated by the photodiode, the shot noise will be 100 e^-. Since the read-out noise and shot noise powers are added, the total noise in the system is $\sqrt{(10^2+100^2)}$ =100.5 e^-. Hence, the contribution of the read-out noise is 0.5% from the total noise figure in the system and therefore is negligible. The SNR performance of the imaging sensor in this region of operation can be approximated via equation (*5*):

$$SNR = 20log\left(\frac{S-B}{n_{photon-shot}}\right) = 20log\left(\frac{S-B}{\sqrt{S}}\right) \xrightarrow{B \ll S} \approx 20log\left(\sqrt{S}\right)[\text{dB}] \tag{5}$$

To maximize the SNR performance, the imaging sensor should be used close to the saturation level of the sensor or close to the full well-depth capacity of the pixel. For a given light intensity, the integration time (also known as exposure time) of the sensor can be adjusted such that the total number of integrated electrons does not exceed the total pixel well-depth capacity. Also the integration time should not exceed 33 msec to ensure 33 frames per second read out speed. This will guarantee that the sensor is limited by the shot noise and will give the maximum SNR performance of the sensor. In this configuration, the sensor will be able to discern signal from noise with the highest confidence.

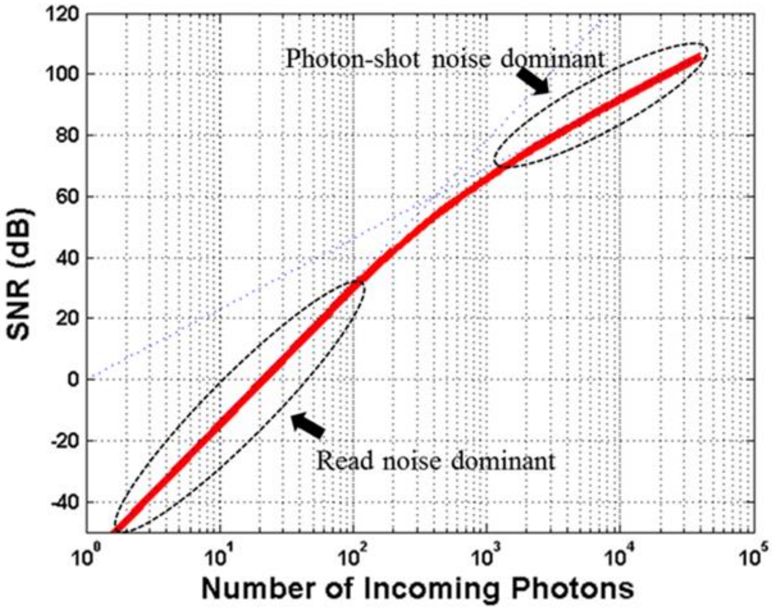

Figure 2: Model of signal to noise ratio of an imaging sensor with read-out noise of 10e^- and maximum well depth capacity of 100 ke^-.

Electrical and optical crosstalk

Electrical and optical crosstalk is another important aspect of the imager performance. The electrical cross talk refers to portion of the electron-hole pairs that are generated by incident photons from one photodiode but registered by neighboring pixels. In other words, the photo-voltage from a given photodiode contains contributions from photons absorbed by this photodiode as well as a portion from photons absorbed from neighboring photodiodes. Today's state-of-the-art imaging sensors try to mitigate this effect via various vertical trenches between photodiodes, but the crosstalk is not completely eradicated. The optical crosstalk is due to the lenses, filters, antireflective coatings and other optical elements used in the imaging system. The effect causes light to reflect and refract multiple times within the imaging system, such that light that should be absorbed by one photo-detector will be absorbed by neighboring photo-detectors causing optical crosstalk.

The electrical and optical crosstalk has two fold negative effects on the performance of the imaging sensor. First, the photodiode signal is diminished because part of the dynamic range is "wasted" on the neighboring photons. Computational models can mitigate this effect at the expense of reduced SNR. The second effect is related to the decrease of resolution or decrease in the modulation transfer function (MTF) of the system. MTF is a measure of the electrical response of the imaging system when a sinusoidal pattern with varying spatial frequency is presented. The amplitude ratio of the sinusoidal function for a given spatial frequency defines the MTF parameter for that particular spatial frequency. Ideally this number should be 1, but due to low pass filtering from the lenses and optics integrated with the sensor, the MTF tends to decrease with increase of the spatial frequency.

The MTF of the entire imaging system is composed of the MTF of the imaging lens, MTF of the optical filters and MTF of the sensor (Fig. 3). The MTF of the lens is determined by the various lenses included in the lens system, as well as the material used to construct the lenses. The MTF of the optical filter is typically a weak function of spatial frequency and the MTF of the sensor is determined by the pixel pitch and the electrical crosstalk between pixels. The overall MTF function is a product of all three MTF functions as shown by equation (*6*):

$$MTF_{System}(\lambda) = MTF_{Lens}(\lambda) \cdot MTF_{Filter}(\lambda) \cdot MTF_{Imager}(\lambda) \qquad (6)$$

The mixing of information between a neighborhood of pixels has the same effect as a low pass filtering of the image, which tends to blur the image. Once the image is low pass filtered, high resolution components are removed and details of the image are compromised. These blurring effects are a function of wavelengths due to the dependency of the photon absorption depth as a function of wavelength. Hence, red photons tend to blur images more than blue photons.

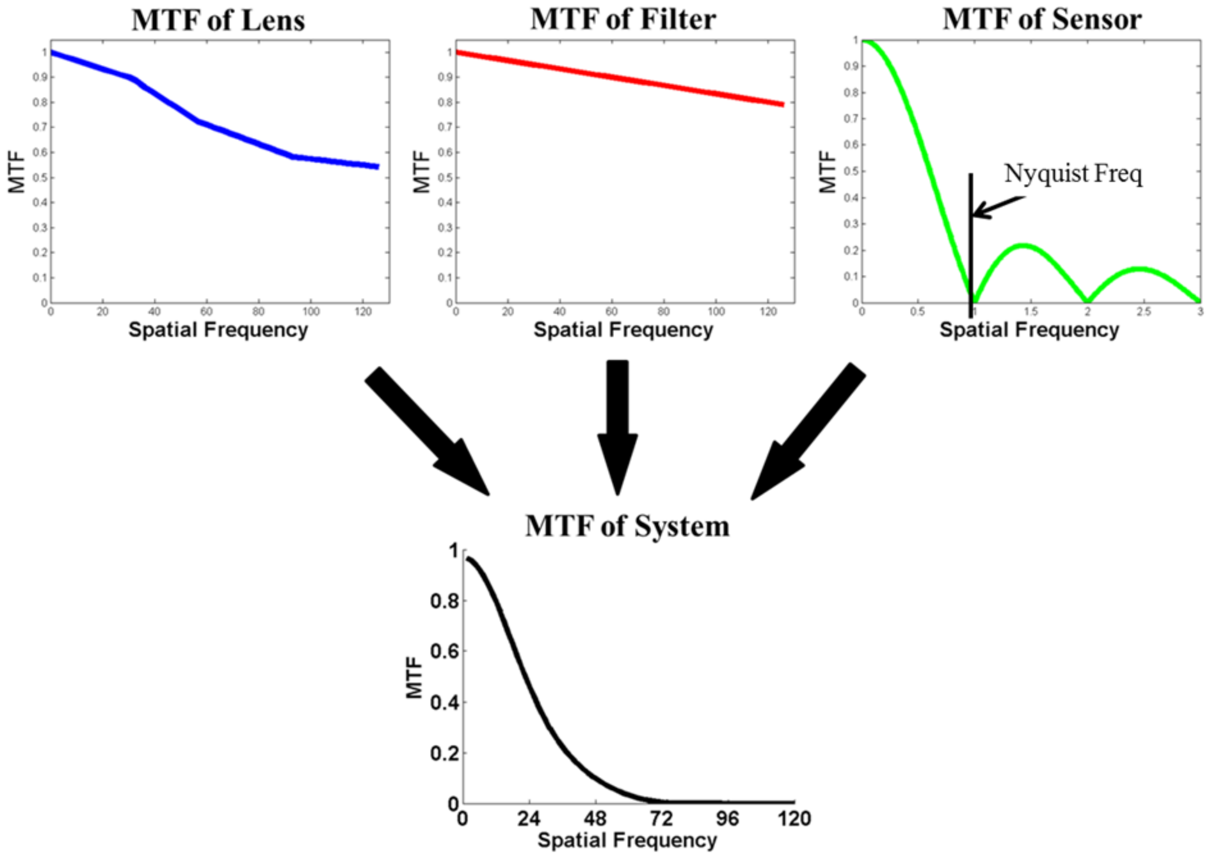

Figure 3: MTF of fluorescent imaging system and components.

Transmission and optical density of excitation and emission filters

Transmission and optical density of the filters used for both the excitation light source and the emitted light are equality important in the overall imaging sensor design. The transmission wavelength of the excitation light source is tailored to coincide with the maximum absorption coefficient of the dye used to tag the desired molecules. For example, the maximum absorption coefficient of ICG is at about 780 nm. Hence, the emission filter for the light source should allow transmission of 780 nm with high efficiency and block higher wavelengths with high optical density factor. A typical filter in this case will have transmission efficiency of ~90% at 780 nm and optical density of 6 at 800 nm. The emission filter is then placed on the imager side to block the emission light and pass higher wavelengths.

Overall SNR and contrast ratio of fluorescence signal

In most of the fluorescence imaging experiments, background signal could generate large amounts of photons at the same wavelength as the fluorescent light. Therefore, the background interference has to be considered in the SNR computation, and SNR computation using equation (*7*):

$$SNR = 20log\left(\frac{S-B}{N}\right) \text{ [dB]} \qquad (7)$$

The contrast ratio is the ratio of the fluorescent light intensity to the total incoming light intensity received by the imaging sensor, as shown in equation (*8*):

$$Contrast\ Ratio = \frac{I_{Fluorescent\ Light}}{I_{Total\ Light}} = \frac{I_{Total\ Light} - I_{Leakage\ Light}}{I_{Total\ Light}} \qquad (8)$$

The ideal contrast ratio should be 1. However, most organic NIR fluorescent dyes have a narrow band gap between the excitation light and emitting light (narrow Stokes shift), with significant spectral overlap between excitation and emission spectra (Fig. 4). This feature results in significant excitation light leakage, which is reflected by the object in the same emergent angle as the fluorescent light. Therefore, the contribution of the interfering light should be subtracted from the captured light to enhance the detection sensitivity and accuracy. To obtain high contrast ratio and precision, high optical density filters are placed on both imager side and the light source side. The longpass filter on the sensor side eliminates the visible spectrum interference. The bandpass filter on the light source side is used to ensure only the light of appropriate wavelength excites the target tissue.

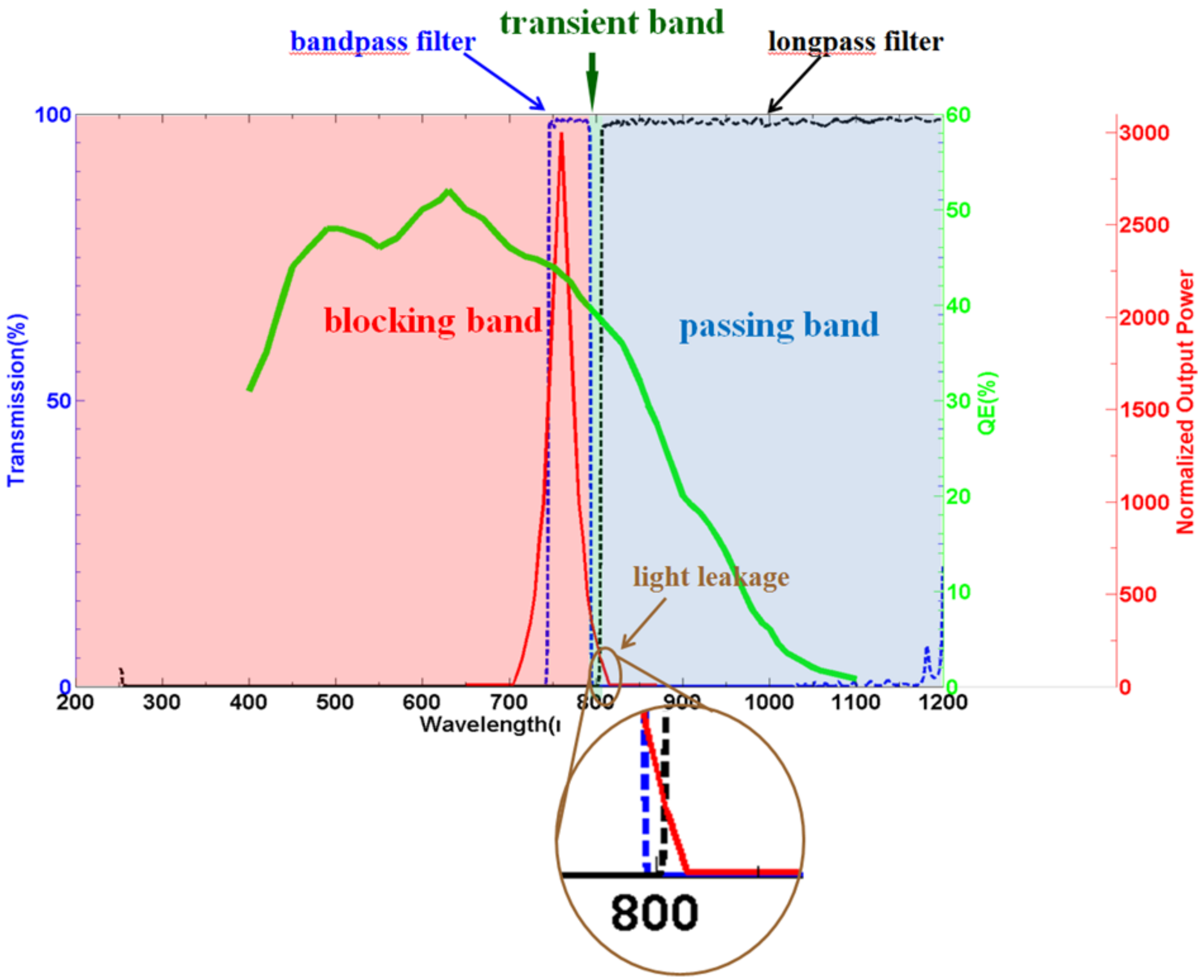

Figure 4: Example of a fluorescent imaging system setup. Dotted lines show the transmission of the corresponding filters. The blue dotted line is the bandpass filter used to trim the excitation light, the black dotted line is the longpass filter to keep the emitting light. Green solid line shows QE of the imager, and red solid line is the spectral response of the LED output light. The brown circle marks the light leakage from the excitation light.

1.3.2 Optical design parameters

The design parameters for a fluorescence imaging system include the power and homogeneity of the excitation light, the field of view (FOV) and numerical aperture (NA) of the detection system that collects the emission light, the sensitivity and noise characteristics of the detector, and the transmission and blocking capabilities of the fluorescence filters.

At low concentration of molecular probes in tissue, fluorescence signals are usually weak and require long exposure time for data acquisition. Therefore, the design of an optical system for fluorescence analysis must consider the entire optical path. Low fluorescence signal requires a highly efficient optical system to improve light-capturing abilities for a higher throughput, to provide a higher dynamic range that accommodates the vast differences in fluorophore concentrations across the sample, and to reduce crosstalk between sample spots through improved optical resolution.

Lens and filter strategy

The basic requirements for good fluorescence detection systems include high-resolution and high-fluorescence signal collection and transmission. Generally, high resolution and high light-collection efficiency are related through the NA. The larger the NA is, the higher the resolution and light-collection efficiency. In cases where the fluorescence signal is more critical than the resolution, the imaging lens is often designed with a large NA, but a lower aberration correction (fewer optical elements). As a general guideline, the optical elements in the detection and excitation paths should be as few as possible to increase light transmission and minimize the autofluorescence of the optical components.

An infinite-conjugate imaging system is preferred, but not required, when the excitation and emission share the same objective lens, so that the dichroic mirror and other components can be inserted or removed between the objective lens and the tube lens without introducing aberrations and image shift. Generally, a telecentric imaging system is desirable, especially for off-axis point scanning, so that the collection efficiency of fluorescence signal is uniform across the entire FOV.

The transmission of both the excitation and emission light should be as high as possible. Antireflection (AR) coatings are essential for achieving high transmission. Depending on the excitation and emission wavelengths, as well as the locations of the optical elements, various types of coatings can be applied. For optical elements used in both the excitation and emission paths, either a W-shaped AR coating with two minimal reflection bands or a broadband AR coating is required. For elements used only in the excitation path, a V-shaped AR coating is enough to minimize the reflection of the excitation light. Similarly, a V-shaped AR coating with minimal reflection at the emission wavelength can be sufficient for the elements in the detection path.

Most of optical glasses and plastics have good transmission performance in NIR spectrum up to 1500 nm or even longer. Therefore, a traditional lens designed for visible spectrum can be used in the spectrum for fluorescence image-guided surgery. The optical surfaces in a visible lens are normally optimized for visible spectrum (400-700 nm). For use in fluorescence image-guided surgery, optics with surface coating optimized for NIR is needed to have maximum transmission in the working spectrum.

To optimize the detection of a fluorescence signal, excitation filters are selected to maximize blocking in the transmission passband of the emission filter in the illumination path and to maximize blocking in the corresponding transmission passband of the excitation filter in the detection path. In general, it is preferable to block out-of-band light with an excitation filter instead of an emission filter so that the sample will be exposed to less radiation. In addition, fewer components and less-complicated optical systems re required in the detection path.

The optimal position of the excitation filter is where the range of the ray angle is small and away from the light source to reduce the angular effect of the optical coatings and autofluorescence of the components in the illumination path. The emission filter should be placed in front of other optical components in the detection path to reduce autofluorescence from those components. However, in many applications, it is not practical to place the emission filter as the first element. For a very compact device where there is not enough space for the emission filter in front of the objective lens, the next optical location is where the range of the ray angle is small.

Illumination design

In fluorescence imaging, it is desirable to closely match the excitation wavelength of the light source with the maximum excitation wavelength of the fluorophore to achieve a high-contrast image. Wavelength is also the major factor in determining the imaging depth because the penetration depth of light in tissue strongly depends on the wavelength. Light-source intensity is another factor in fluorescence imaging; it determines how much excitation light can reach the sample. For fluorophores with low quantum yields, high power light sources are needed to sufficiently excite enough molecules for fluorescence capture by detectors such as a photomultiplier tube (PMT), avalanche photodiodes (APDs), a CCD, or a CMOS sensor. The human eye is less sensitive than most electronic detection systems, and thus, applications involving visual observation require higher levels of illumination intensity.

Noncoherent and coherent light sources are used in fluorescence imaging. Noncoherent light sources are usually broadband and are typically used in fluorescence spectrometers and large area imaging systems. The spectral output of noncoherent light sources can be tuned to a narrow band of excitation light or a predefined spectrum by using gratings, filters, and spatial light modulators, such as liquid crystal devices or digital micromirror devices. Mercury and xenon arc lamps are the most common noncoherent light sources used in fluorescence imaging. Historically, mercury high-pressure arc lamps (commonly referred to as HBO lamps) were the most prevalent light source for fluorescence imaging. The light intensity of a mercury lamp is not evenly distributed from ultraviolet (UV) to NIR region, with peaks of intensity at 313, 334, 365, 406, 435, 546, and 578 nm. Between these peaks, the excitation energy of the light source is very low. If these lines coincide with or are close to the peak of the fluorophore's excitation spectrum, a mercury lamp is the optimal light source. HBO lamps are suitable for applications that need blue or UV light to excite fluorescence. They typically have a short life span (~300 hours), necessitating relatively frequent bulb changes.

In contrast, xenon arc (XBO) lamps have a relatively flat emission across the visible spectrum. The uniform emission levels and lower fluctuations make XBO lamps better suited for applications in ratio imaging and other quantitative applications. XBO lamps also have stable emission intensity over time, contributing to the long life span of these lamps (400–2000 hours).

The xenon-mercury arc lamp has the best characteristics of both xenon and high-pressure mercury lamps. The spectral distribution of a mercury-xenon lamp includes a continuous spectrum from the UV to the infrared and the strong mercury line spectrum. This combination is an ideal source for some applications because it provides extremely high excitation energy over large spectral bandwidth.

Metal halide (HXP) white-light sources have an emission spectrum similar to that of mercury lamps. HXP lamps have an emission output featuring pressure-broadened versions of the prominent mercury arc spectral lines in addition to higher radiation levels in the continuous regions between lines. Therefore, HXP lamps usually produce much brighter images of fluorophores, which have absorption bands in the spectral regions between the mercury lines. Commercial HXP lamps have extended arc-lamp lifespans (up to 2000 hours).

To eliminate traditional alignment problems and provide uniform illumination across the entire FOV, a liquid light guide or fiber light guide is often used to couple the light out from the arc lamp. The light guide acts as a scrambler to homogenize the arc output and create an even field of illumination. The light guide also has the advantage of reducing heat transfer from the light source to the sample.

One advantage of arc lamps is that one light source can be used to excite several fluorophores independently or to excite several fluorophores simultaneously. They can also be used as a light source for white-light illumination. One disadvantage of using arc lamps is that one or more filters are required to select the spectrum for optimal fluorescence excitation. There are several other issues related to arc lamps. The bulbs may explode because of high working temperatures and pressures, although the possibility of explosion is low. For all gas-discharge lamps, reaching optimal working conditions usually takes time, and restarting them after they are turned off requires a certain period of time. The light intensity may fluctuate and drop throughout the lifetime of the lamp.

For simple fluorescence imaging systems, the excitation light is delivered directly to the sample from a light source without any additional optics. For most fluorescence imaging systems, illumination optics is needed for efficient and uniform delivery of the excitation light to the sample. Because of the relatively weak fluorescence signal, the efficiency of the light delivery system becomes critical to optimize fluorescence imaging systems. Thus, uniform illumination is required because the fluorescence signal at each point is proportional to the illumination light at that location. Beam-shaping elements (such as a lenslet array, light pipe, or aspheric elements) are usually used to provide spatially uniform excitation light to the samples. For some applications, an array of light sources, typically LEDs, provide sufficient excitation light with reasonable uniformity.

It is also important to protect the sample, especially in live-cell imaging applications, from overexposure and heat from the light source during illumination. This can be achieved by attenuating the light intensity and by limiting the duration of the illumination to exactly the exposure time of the sensor.

1.4 Current Intraoperative Optical Image Guidance Systems

Several complete intraoperative NIR fluorescence imaging systems are now available for pre-clinical and clinical studies (45, 46). Although differing in their technical specifications, all of these systems provide the surgeon with an image of the NIR fluorescence signal that would otherwise be invisible to the human eye (Table 2). Some of these systems have been approved by the U.S. Food and Drug Administration (FDA) for use in humans. For example, the Novadaq SPY system is an intraoperative imaging system that uses indocyanine green (ICG) fluorescence for a variety of surgical procedures, including for guidance in coronary artery bypass grafting, plastic and reconstructive surgeries, and organ transplant (47, 48). Another system, the photodynamic eye (PDE) developed by Hamamatsu is a handheld imaging system that can detect ICG fluorescence. The majority of clinical studies published to date use this imaging system to identify sentinel lymph nodes (SLNs) in breast cancer patients (49) and to perform image-guided surgical resection of hepatocellular carcinoma (HCC) (50). Other commercially available handheld imaging systems are Fluobeam (Fluoptics, France) and Artemis (Quest Medical

Imaging BV, Netherlands). They are capable of perfusion imaging, and display the acquired information in a remote monitor.

Because of the clear advantage of these fluorescence image-guided systems for intraoperative procedures, a variety of newer experimental systems have emerged in various laboratories and evaluated in humans. These include the fluorescence assisted resection and exploration (FLARE) system and head mounted display devices.

The FLARE system is an intraoperative real-time imaging system developed by the Frangioni team. This system has been successfully used for SLN mapping in breast cancer patients (51). A smaller and more portable version has also been developed and validated for SLN mapping in human breast cancer patients (52). Other successful applications of this system include the SLN imaging in cervical (52) and vulvar (53) cancer patients. Although the FLARE system can detect NIR fluorescence with high sensitivity in real-time, it is not portable and has a large hardware footprint.

Another experimental fluorescence image-guided system in early stages of clinical studies is a goggle assisted imaging and navigation system for intraoperative image guidance (54). Initial prototypes have been validated in extensive small animal studies (55) and also shown to work well in HCC detection in human patients (56). Further improvements were made in the system to improve wearability and video rate image display. The current system is capable of detecting both color and fluorescence signals from the surgical bed using a very small camera. Using fast processing, real-time superimposed images are displayed on the head mounted display worn by a surgeon. This allows image guidance without any disruption of the normal surgical workflow (Fig. 5). High detection sensitivity, ease of usage, ergonomic design and wearablity make it an attractive candidate for wide clinical adoption. At Washington University in St. Louis, the system is undergoing pilot human studies with breast cancer and melanoma patients. Using ICG as the contrast agent for SLN mapping the goggles system compared favorably against traditional radioactive and blue dye methods (57).

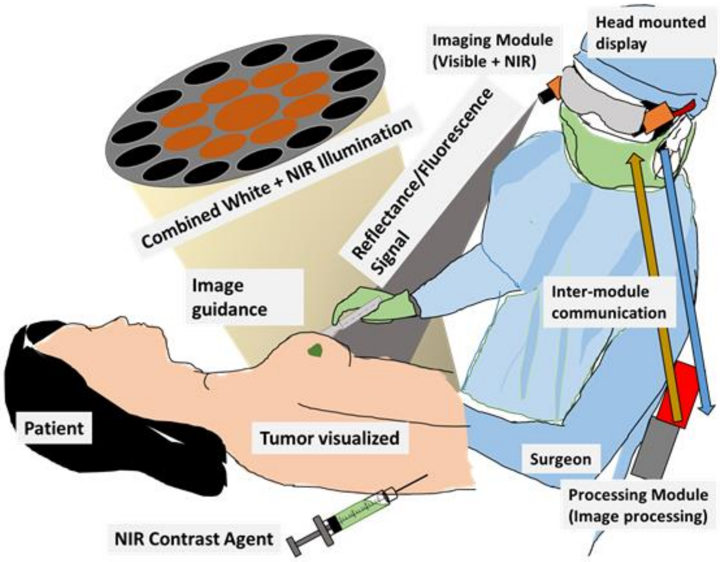

Figure 5: Goggle system overview. We have developed a NIR contrast agent that is selectively retained in tumors. After injection of this agent our system excites the contrast agent. The NIR fluorescence and color reflectance images are captured and processed to generate a superimposed image where fluorescence is highlighted in a false color on the normal view. This superimposed image is seen in the head mounted display in real time, by the surgeon, which allows him to visualize the tumor boundary, thus providing image guidance for cancer surgery.

Other experimental systems under development for clinical applications are making significant progress. For example, the HyperEYE system was successfully used for intraoperative graft assessment using ICG fluorescence (58). A frequency domain photon migration (FDPM) system was developed for integration into commercial small animal imaging scanners for fluorescence tomography (59). It has now been used for non-invasive dynamic lymphatic mapping in humans (60). Finally, a multispectral fluorescence imaging system, SurgOptix, was developed (61) and used to assess SLN detection in cervical (62) and ovarian (63) cancer patients.

Table 2: Fluorescence image guidance systems.

System	Real-time	NIR-color overlay	Display	Status	References
Mounted					
SPY		No	Remote Monitor	Commercially available. FDA approved	(47, 64)
FLARE	Yes	Yes	Remote Monitor	Clinical Studies	(51)
SurgOptix	Yes	Yes	Remote Monitor	Clinical Studies	(61-63)
ArteMIS	Yes	No	Remote Display	Commercially available	(65)
HyperEye		Yes	Remote Display	Experimental	(58)
FDPM		No	Remote Display	Experimental	(59, 60)
Handheld					
Fluobeam		Yes	Remote display	Commercially available	(66)
PDE		No	Remote display	Commercially available. FDA approved	(49)
Wearable					
Goggle System		Yes	Head mounted display	Clinical studies.	(54, 67)

1.5 Fluorescent Agents Used in Image-Guided Surgery

Fluorescence imaging techniques are able to report molecular events with exceptionally high detection sensitivity because of the low background signal prior to excitation of the target tissue with light of the appropriate wavelength. The high detection sensitivity clearly favors the application of fluorescence in image-guided surgery. Fluorescence signal can be mediated by endogenous or exogenous fluorophores. The differential expression of endogenous fluorophores (autofluorescence) or selective accumulation of extrinsic fluorescent molecular probes in the diseased versus normal tissue provides the source of contrast for fluorescence imaging (Table 3).

1.3.1 Endogenous fluorophores

Tissues and cells express some biomolecules that can serve as a source for autofluorescence imaging. These biomolecules are typically upregulated or downregulated in diseased versus healthy tissues. In autofluorescence imaging, the tissue may be excited by UV, visible, or NIR light with sufficient irradiance to induce specific fluorescence for diagnostic purposes (68, 69). In particular, autofluorescence-based spectroscopic imaging has been used for clinical differentiation of cancerous, inflamed and normal tissue in cervical cancer patients (70), and for the diagnosis of bladder cancer (71). Simple handheld devices has been shown to identify oral cancer (43) and decrease oral cancer recurrence rate in human patients (72, 73). To visualize these lesions, intravital and other microscopic techniques are widely used in autofluorescence imaging (74), as demonstrated by their use to distinguish malignancies from benign and healthy tissues (75).

A major advantage of autofluorescence imaging and spectroscopy in the context of intraoperative image-guided surgery is that exogenous fluorophore are not needed. With minimal regulatory hurdles compared to the use of exogenous fluorescence dyes or nanomaterials, the approach is readily translatable to clinics. If the goal is to detect microscopic lesions or clearly define tumor boundaries in real time, low tumor-to-background autofluorescence signal may be inadequate. In addition, the shallow penetration of light in the UV and visible spectrum (~400-600 nm) allows the sampling of only superficial tissue. Recent application of intravital multiphoton microscopy promises to improve the imaging depth and spatial resolution, but requires sufficiently large field of view and real-time image display to be practically useful to guide surgical resection of tumors.

1.3.2 Exogenous fluorescent agents

To overcome some of the above challenges of autofluorescence imaging, exogenous imaging agents are widely used to enhance signal specificity, interrogate molecular events, and improve tumor-to-background contrast in intraoperative fluorescence guided surgery. Exogenous fluoresce is generally provided by synthetic dyes or nanoparticles. The use of exogenous dyes for fluorescence imaging has been in existence as early as 1955, when fluorescent porphyrin was administered and used to detect tumors (76). Although many fluorescent agents in clinical use are not designed to target specific tissue, efforts to improve detection specificity and sensitivity have led to the development of tumor-targeted or activatable molecular imaging probes. Earlier studies focused on visible fluorophores because of the availability and experience in handling those dyes, as well as the potential to visualize the emitted light with the unaided eye. However, new emphasis on low background signal and improvement in imaging depth has stimulated interest in the development of NIR fluorophores and dedicated camera systems for image-guided oncologic surgery. Human tissue has low optical absorption and scattering in the NIR window (600 to 1000 nm) that can allow the NIR light to penetrate several centimeters or even further in tissue (51, 77). The narrow NIR window between 750 and 900 nm is particularly useful to minimize tissue autofluorescence (78, 79). Recent studies suggest that the 1300 nm spectral range further improves imaging depth (80) and has generated interest in the second optical window of 1000 nm - 1350 nm which can afford much higher depths of penetration (81). An additional benefit of working in the NIR spectrum is that human eyes are insensitive to this light, thereby minimizing interference with the surgical field, especially under conditions where high intensity continuous or pulsed light source is used (82). The most widely used fluorescent agents for fluorescence image-guided surgery in human patients are summarized below.

Fluorescein

Fluorescein was one of the early dyes used to highlight tumors against surrounding normal tissue (83). The first clinical report of fluorescence imaging in the operating room dates back to 1948, when Moore *et al*. (84) used fluorescein to localize brain tumors during neurosurgery. Specific visualization of colorectal carcinomas *in vivo* in patients was accomplished by labeling carcinoembryonic antigen-targeted antibody with fluorescein. This bioconjugate selectively binds to the antigen overexpressed on colon cancer cells. The study was vital in demonstrating the clinical potential of this approach during surgery (85). Although antibodies are highly specific for their target antigens, the slow clearance from circulation contributes to high background fluorescence for several days. As a result, small ligands for cell surface receptors overexpressed by tumors are viable alternatives to large biomolecules because their fluorescein derivatives can achieve rapid extravasation, tumor uptake, and excretion of the unbound molecular probe from circulation. An example of this approach is the use of folate-fluorescein conjugate to visualize ovarian cancer intraoperatively and to guide cancer debulking in the operating room (63). Although these landmark studies successfully demonstrate the feasibility of using fluorescein for fluorescence guided surgery, fluorescein suffers from the limitation of most visible dyes. These include high autofluorescence that could confound image analysis, and shallow penetration of light that only interrogates superficial lesions.

Methylene Blue

Methylene blue is a small molecular weight dye that is widely used in many intraoperative procedures. The ease of visualizing the dark blue color of methylene blue with unaided eyes during surgery facilitated its use for sentinel node mapping. However, high concentration of this dye is needed to visualize the blue color (absorption mode). Recent studies have shown that methylene blue fluorescence at about 700 nm can provide a mechanism to detect the distribution of this dye with highly sensitive sensor systems (7, 46). This high detection sensitivity of the fluorescence signal facilitates the use of low doses of this dye for image-guided surgery, thereby minimizing the side effects of the dye in some patients. This fluorescence approach has found wide application in identifying the ureters during surgery (86), detecting extrahepatic bile ducts, (86) and assessment of cardiac perfusion (87). The dye has also been applied to the detection of neuroendocrine tumors, such as insulinoma (88). Although some studies have demonstrated that methylene blue can accumulate in some tumors, this uptake can be sporadic and depends of the tumor type. In addition, relatively high concentration must be used to overcome autofluorescence. Because of the need to detect small tumors during surgery, methylene blue may not be suitable for image-guided surgical margin assessment in real-time. The dye also suffers from limitation of other visible dyes because of the excitation in the 600 nm range.

5-Aminolevulinic acid

5-Aminolevulinic acid (5-ALA) is a small molecule involved in the early phase of porphyrin biosynthesis, which is responsible for heme production in mammals. Through this pathway, 5-ALA serves as the major substrate for protoporphyrin IX (PpIX) synthesis, a naturally fluorescent molecule that is overexpressed in cancerous tissue, especially malignant gliomas and meningiomas. 5-ALA has been used clinically for tumor detection (fluorescence imaging) and treatment (photodynamic therapy). The compound, which is typically administered in topical or oral form, induces the biosynthesis and accumulation of PpIX in epithelial and neoplastic tissues (89, 90). PpIX has two major emission peaks, with its second emission peak centered at 700 nm, which is at the fringes NIR fluorescence. A growing area of application is in managing brain cancer. For example, the PpIX precursor has been used for quantitative fluorescence imaging and debulking of gliomas (91) and for image-guided resection of glioblastoma, where it was shown to improve tumor free survival in patients (90). Previous studies reported the use of 5-ALA as a biomarker for distinguishing normal brain tissue from low and high grade gliomas via quantitative fluorescence imaging of PpIX (92). 5-ALA has also been used to identify urothelial cancer using fluorescence guided cystoscopy(93). A persistent concern with 5-ALA approach is the poor sensitivity and a negative predictive value, especially for surgical guidance of glioma resection (94).

Indocyanine Green

ICG is the workhorse imaging agent for NIR fluorescence image-guided surgery in human subjects because it is currently FDA approved for use in humans (95). ICG can be excited at 780 nm and the fluorescence is captured around 810 - 830 nm (96). In blood, ICG interacts with lipids and plasma proteins which enhance its NIR fluorescence and increase its hydrodynamic diameter (96). This allows ICG to remain in circulation for a longer duration and accumulate in tumor via the enhanced permeability and retention effect, before being cleared through the liver (7). Intravenous ICG injection is currently used for NIR angiography of blood vessels (87, 97, 98), identification of the extrahepatic bile ducts (86), and identification of liver metastases (99). Subcutaneous ICG injection has been used for sentinel lymph node (SLN) mapping in breast cancer (51), gastric cancer (100, 101), gastrointestinal cancer (102), skin cancer (103) and squamous cell carcinoma (104). The major limitation of this imaging agent is the lack of specificity for tumors. New NIR molecular probes targeted to tumors have shown impressive results in preclinical studies. Unfortunately, these molecular probes have not been approved for use in humans by the US FDA.

Table 3: Fluorescence contrast agents used for real-time image-guided surgery. EPR, enhanced permeability and retention. [a]Peak fluorescence emission wavelength.

Agent	λ_{em}[a] (nm)	Tumor targeting	Applications	References
ICG	820	EPR effect	SLNM in breast, skin, cervical cancer Tumor imaging in HCC Reconstructive surgery	(51, 53, 77, 105, 106)
Fluorescein	520	EPR effect	Image guided resection of glioblastoma	(107)
Methylene Blue	680	EPR effect	SLNM Insulinoma	(108, 109)
5-ALA	635	Porphyrin IX expression	Glioma resection Glioma grade biomarker	(90, 92)

1.6 Clinical Applications of Fluorescence Image-Guided Surgery

Fluorescence-guided surgery is widely used today in oncologic and other intraoperative procedures (7, 110). Most of the clinical studies have focused on NIR fluorescence. Because the human eye is not sensitive for light in the NIR region, dedicated camera systems are required to detect the fluorescence signals emission from these molecules. Fluorescence imaging instruments are relatively inexpensive, simple and can be very compact to adapt many kinds of surgeries. However, optical image guidance has certain limitations and scope. For example, tumors that have a high incidence of positive margins would mostly benefit from this procedure. The choice of contrast agent and its application route is determined by the patient tolerance to the contrast agent and the anatomical position of the area of interest. The major areas of oncologic applications are summarized below.

1.3.1 Sentinel Lymph Node Mapping

The SLN is the first drainage site of disseminating cancer cells from the primary tumor. Thus, the SLN positivity or negativity is used to stage the metastatic potential of some solid tumors (111). Negative SLN suggests that the tumor is confined to the primary tissue, and could be readily treated by surgical resection. In contrast, positive SLN suggests the potential of cancer metastasis, which triggers a high level of diagnostic assessment and therapeutic regimens. SLN staging is frequently used in the staging of breast cancer and melanoma, and the procedure is under investigation for use in colorectal, gastric, esophageal, head and neck, thyroid, and non-small cell lung cancers (112). During SLN biopsy, the tissue is first identified and removed for histologic verification of the lymph node status. Currently, SLN mapping is performed by tracking a radiotracer, a visible blue dye, or a combination of both radiotracer and dye (113, 114).

Blue dyes such as methylene blue are injected in the vicinity of the primary tumor and allowed to drain to the sentinel lymph node. Because of the high concentration of the injected dose, the stained tissue is readily visible with the naked eye. Since the human eye can only visualize superficial tissue, this technique is complemented by administering tracer levels of radionuclides. Using a gamma counter, the radioactivity is track to identify the general location of the SLN, which can then be confirmed by visualizing the blue dye. In addition to the poor detection sensitivity of the blue dyes, the procedure exposes health professionals to frequent ionizing radiation and the gamma probe suffers from poor spatial resolution (115). In contrast, NIR fluorescence imaging with dyes such as ICG enables detection of the SLN with high sensitivity at low doses of a fluorescent dye. ICG passively accumulates in SLNs, but the small size of the molecule facilitates its further migration to adjacent nodes. To address this issue, SLN selective tracer was designed to bind mannose-binding protein receptor found in reticuloendothelial cells of lymph nodes (116). This agent has satisfactory performance both as a radiolabeled and fluorescent imaging agents for SLN detection (117) It was recently approved by the FDA for SLN mapping based on results from a phase 2 clinical trials in breast cancer and melanoma patients (118).

Although the NIR fluorescence imaging approach improves imaging depth, good resolution images are still confined to 5-15 mm deep from the tissue surface. To address this limitation, a combination of NIR fluorescence and radioactive tracers are currently used for SLN mapping in head and neck melanoma (91, 119), prostate cancer (120) and squamous cell carcinoma of the oral cavity(115). Future studies will determine potential of using NIR fluorescence imaging without the need for administering radioactive materials (121).

1.3.2 Tumor Imaging

A major application of real-time fluorescence –guided surgery is to visualize tumors in the operating bed in real-time. ICG was first used clinically to visualize colorectal hepatic metastases and HCC (122). Different spatial distribution of ICG in liver tumors has been reported, ranging from a rim of fluorescence around hepatic metastases to localize fluorescence within HCC (50, 123-125). A recent report suggests that ICG-mediated NIR fluorescence image-guided surgery could identify small HCC nodules in the liver, which was not detected by preoperative CT (126). Similar findings were reported in the detection of hepatic metastases of pancreatic cancer (127) or colorectal metastases (7) in the liver that were not visible by preoperative CT, MR, intraoperative US, visual inspection, or palpation. These studies illustrate the potential of using fluorescence image guidance to survey the operating bed and ensure the removal of small tumor lesions that could readily be missed during surgery. Beyond focused tumors, ICG videography was successfully used for image-guided resection of spinal cord hemangioblastoma (128), CNS tumors(129) and dynamic imaging during hemangioblastoma surgery (130).

Other than ICG, methylene blue has served as important cancer imaging agent because of its intrinsic affinity to cancer cells. This important feature has been known several decades ago, including the selective staining of parathyroid glands after high dose intravenous injection of the dye (131) or detection of insulinomas after intra-arterial injection (131, 132). Recent studies have now demonstrated successfully the use of methylene blue fluorescence to identify insulinomas in preclinical models (88) and as well as visualizing rare solitary fibrous tumors of the pancreas in a patient (133), though it remains to be clinically approved for insulinoma imaging. The application of 5-ALA in image-guided surgery was discussed above. With the ongoing development of new fluorescent systems for surgical applications, it is important to identify areas of high clinical impact in order to support the introduction of another imaging tool into the already hectic surgical environment.

Protecting vital organs is critical during oncologic imaging because surgery can cause unintended iatrogenic damage to vital structures such as the nerves or sensitive surrounding tissue. For example, nerve damage during rectal cancer surgery may cause urinary and fecal incontinence (134), while nerve damage during bladder and prostate cancer surgery may result in sexual dysfunctions (135). Damage to ureters or bile duct may lead to renal dysfunction and biliary peritonitis (136, 137). ICG, which is removed from circulation by the liver, is used for intraoperative NIR fluorescence cholangiography (138, 139). The clinical significance of preserving vital organs has stimulated the development of simple dyes that selectively accumulate in specific tissue, as well as high throughput fluorescence imaging devices for real-time delineation of these tissues during surgery.

1.7 Future Directions

With recent advances in molecular medicine, high resolution and wide FOV systems could inform clinical research about molecular processes pertinent to the disease in real-time (5). By coupling imaging with optional therapy, it is anticipated that the procedure will also guide treatment planning and monitor treatment response. These efforts could improve patient outcomes, reduce hospital revisits, and enhance the quality of life. Some specific areas for improvement are summarized below.

From molecular imaging perspective, cancer-targeted fluorescent molecular will improve the specificity and sensitivity of fluorescence-guided surgery. The molecular agents could be designed for instant activation of fluorescence after topical application during surgery to improve the tumor-to-background fluorescence. New activatable molecular probes were recently reported to have this desirable property (140). An alternative approach is to design fluorescent molecular probes that can be trapped in cancer cells for several days, allowing the surgeons flexibility to conduct surgery at any time during that period (54, 141).

From device development perspective, the rapid development of CMOS process and modern digital imaging technology has improved the performance of recent CMOS imaging sensor used in fluorescence imaging system. High performance sensors can provide more accurate and stronger fluorescence signal as image output. Using the latest 130 nm - 180 nm analog fabrication process, commercial CMOS imaging sensor are optimized to obtain high SNR and much higher image resolution than previous systems. Furthermore, vertically stacked 3-D technology offers high resolution of pixel array, and nearly 100% fill factor by stacking photodiode structure, row/column readout circuit, and storage logic onto different layers. Although the fabrication process of 3-D chip still needs a lot of optimization, it provides an alternative way for CMOS sensor to achieve high resolution and better sensitivity (142). Finally, imaging sensor research on detection of special light property has increased recently. For example, recent development of division of focal plane polarization imaging sensor enables real-time, high resolution polarization detection, which could be embedded in future fluorescence imaging system for additional polarization information detection (143).

System-on-chip (SOC) CMOS imaging sensor can offer flexibility in fluorescence imaging system design. By moving ADC readout circuitry and image pre-processing unit on chip, the imaging sensor system becomes much more compact and power efficient (144). Further reduction in the size and weight of the sensor system is achieved because less peripheral circuits and components are needed for SOC sensor system. This configuration will benefit the compact fluorescence imaging system design.

1.7 Concluding Remarks

Real-time image-guided surgery is gaining interest because of its potential to improve patient outcome following oncologic surgery. Not only can this approach guide intraoperative surgical margin assessment, the approach is uniquely positioned to detect microscopic tumors or residual lesions that are readily missed during surgery. Numerous types of optical imaging devices are available today to guide surgery. With the ever increasing miniaturization capability, simpler, smaller, and more efficient optical imaging systems will become available for clinical use in high and low resource clinical centers. Current bottleneck preventing full realization of the potential benefits of NIR fluorescence guided surgery is the lack ok FDA approved tumor-selective molecular imaging agents. This missing link is expected to be rectified soon because of dedicated efforts by many investigators and some federal funding agencies such as the National Institutes of Health to support early phase clinical trials with novel imaging agents. Beyond identifying tumors, coupling therapeutic options to either the device or molecular probe arm of the technology could further enhance its potential clinical impact. 5-ALA is currently capable of achieving this goal by providing both imaging and therapeutic capabilities. Alternative theranostic platforms can be developed to harness the modular design of contrast agents and light-triggered drug release.

1.7 References

1. Mondal SB, Gao S, Zhu N, Liang R, Gruev V, Achilefu S. Real-time fluorescence image-guided oncologic surgery. Advances in cancer research. 2014;124:171-211. Epub 2014/10/08. doi: 10.1016/B978-0-12-411638-2.00005-7. PubMed PMID: 25287689; PubMed Central PMCID: PMC4245053.

2. Yabroff KR, Lund J, Kepka D, Mariotto A. Economic burden of cancer in the United States: estimates, projections, and future research. Cancer epidemiology, biomarkers & prevention : a publication of the American Association for Cancer Research, cosponsored by the American Society of Preventive Oncology. 2011;20(10):2006-14. Epub 2011/10/08. doi: 10.1158/1055-9965.EPI-11-0650. PubMed PMID: 21980008; PubMed Central PMCID: PMC3191884.

3. Siegel R, Ma J, Zou Z, Jemal A. Cancer statistics, 2014. CA: a cancer journal for clinicians. 2014;64(1):9-29. Epub 2014/01/09. doi: 10.3322/caac.21208. PubMed PMID: 24399786.

4. Ries LAG, Melbert D, Krapcho M, Stinchcomb DG, Howlader N, Horner MJ, et al. SEER cancer statistics review, 1975-2005. Bethesda, MD: U.S. National Institutes of Health, National Cancer Institute, 2008.

5. Weissleder R, Pittet MJ. Imaging in the era of molecular oncology. Nature. 2008;452(7187):580-9. Epub 2008/04/04. doi: 10.1038/nature06917. PubMed PMID: 18385732; PubMed Central PMCID: PMC2708079.

6. Jolesz FA. Intraoperative imaging and image-guided therapy: SpringerLink; 2014. 1 online resource (xvii, 893 pages) p.

7. Vahrmeijer AL, Hutteman M, van der Vorst JR, van de Velde CJH, Frangioni JV. Image-guided cancer surgery using near-infrared fluorescence. Nat Rev Clin Oncol. 2013;10(9):507-18. doi: DOI 10.1038/nrclinonc.2013.123. PubMed PMID: ISI:000323698900005.

8. Jacobs L. Positive margins: The challenge continues for breast surgeons. Annals of Surgical Oncology. 2008;15(5):1271-2. PubMed PMID: ISI:000254623100002.

9. Collins L, Schnitt S, Achacoso N, Haque R, Nekhlyudov L, Fletcher S, et al. Outcome of Women with Ductal Carcinoma In Situ (DCIS) Treated with Breast-Conserving Surgery Alone: A Case-Control Study of 225 Patients from the Cancer Research Network. Modern Pathology. 2009;22:34A-5A. PubMed PMID: ISI:000262371500144.

10. Vicini FA, Kestin LL, Goldstein NS, Chen PY, Pettinga J, Frazier RC, et al. Impact of young age on outcome in patients with ductal carcinoma-in-situ treated with breast-conserving therapy. Journal of Clinical Oncology. 2000;18(2):296-306. PubMed PMID: ISI:000084836100009.

11. Skripenova S, Layfield LJ. Initial margin status for invasive ductal carcinoma of the breast and subsequent identification of carcinoma in reexcision specimens. Archives of

pathology & laboratory medicine. 2010;134(1):109-14. Epub 2010/01/16. doi: 10.1043/2008-0676-OAR1.1. PubMed PMID: 20073613.

12. Agarwal-Antal N, Bowen GM, Gerwels JW. Histologic evaluation of lentigo maligna with permanent sections: implications regarding current guidelines. Journal of the American Academy of Dermatology. 2002;47(5):743-8. Epub 2002/10/26. PubMed PMID: 12399768.

13. Kunishige JH, Brodland DG, Zitelli JA. Surgical margins for melanoma in situ. Journal of the American Academy of Dermatology. 2012;66(3):438-44. Epub 2011/12/27. doi: 10.1016/j.jaad.2011.06.019. PubMed PMID: 22196979.

14. Moller MG, Pappas-Politis E, Zager JS, Santiago LA, Yu D, Prakash A, et al. Surgical management of melanoma-in-situ using a staged marginal and central excision technique. Annals of Surgical Oncology. 2009;16(6):1526-36. Epub 2008/12/04. doi: 10.1245/s10434-008-0239-x. PubMed PMID: 19050971.

15. Demicheli R, Valagussa P, Bonadonna G. Does surgery modify growth kinetics of breast cancer micrometastases? Brit J Cancer. 2001;85(4):490-2. doi: DOI 10.1054/bjoc.2001.1969. PubMed PMID: ISI:000170626900003.

16. Retsky M, Bonadonna G, Demicheli R, Folkman J, Hrushesky W, Valagussa P. Hypothesis: Induced angiogenesis after surgery in premenopausal node-positive breast cancer patients is a major underlying reason why adjuvant chemotherapy works particularly well for those patients. Breast Cancer Res. 2004;6(4):372-4. doi: Doi 10.1186/Bcr804. PubMed PMID: ISI:000222828200021.

17. Arii S, Tanaka S, Mitsunori Y, Nakamura N, Kudo A, Noguchi N, et al. Surgical strategies for hepatocellular carcinoma with special reference to anatomical hepatic resection and

intraoperative contrast-enhanced ultrasonography. Oncology. 2010;78 Suppl 1:125-30. Epub 2010/07/17. doi: 10.1159/000315240. PubMed PMID: 20616594.

18. van Vledder MG, Torbenson MS, Pawlik TM, Boctor EM, Hamper UM, Olino K, et al. The effect of steatosis on echogenicity of colorectal liver metastases on intraoperative ultrasonography. Archives of Surgery. 2010;145(7):661-7. Epub 2010/07/21. doi: 10.1001/archsurg.2010.124. PubMed PMID: 20644129.

19. Ukimura O, Okihara K, Kamoi K, Naya Y, Ochiai A, Miki T. Intraoperative ultrasonography in an era of minimally invasive urology. International journal of urology : official journal of the Japanese Urological Association. 2008;15(8):673-80. Epub 2008/06/20. doi: 10.1111/j.1442-2042.2008.02090.x. PubMed PMID: 18564203.

20. Kane RA. Intraoperative ultrasonography: history, current state of the art, and future directions. Journal of ultrasound in medicine : official journal of the American Institute of Ultrasound in Medicine. 2004;23(11):1407-20. Epub 2004/10/23. PubMed PMID: 15498905.

21. Sahani DV, Kalva SP, Tanabe KK, Hayat SM, O'Neill MJ, Halpern EF, et al. Intraoperative US in patients undergoing surgery for liver neoplasms: comparison with MR imaging. Radiology. 2004;232(3):810-4. Epub 2004/07/27. doi: 10.1148/radiol.2323030896. PubMed PMID: 15273336.

22. Kubben PL, ter Meulen KJ, Schijns OE, ter Laak-Poort MP, van Overbeeke JJ, van Santbrink H. Intraoperative MRI-guided resection of glioblastoma multiforme: a systematic review. The lancet oncology. 2011;12(11):1062-70. Epub 2011/08/27. doi: 10.1016/S1470-2045(11)70130-9. PubMed PMID: 21868286.

23. Mislow JM, Golby AJ, Black PM. Origins of intraoperative MRI. Neurosurgery clinics of North America. 2009;20(2):137-46. Epub 2009/06/27. doi: 10.1016/j.nec.2009.04.002. PubMed PMID: 19555875; PubMed Central PMCID: PMC2902263.

24. Liu Y, Brand RE, Turzhitsky V, Kim YL, Roy HK, Hasabou N, et al. Optical markers in duodenal mucosa predict the presence of pancreatic cancer. Clinical cancer research : an official journal of the American Association for Cancer Research. 2007;13(15 Pt 1):4392-9. Epub 2007/08/03. doi: 10.1158/1078-0432.CCR-06-1648. PubMed PMID: 17671121.

25. Wilke LG, Brown JQ, Bydlon TM, Kennedy SA, Richards LM, Junker MK, et al. Rapid noninvasive optical imaging of tissue composition in breast tumor margins. American journal of surgery. 2009;198(4):566-74. Epub 2009/10/06. doi: 10.1016/j.amjsurg.2009.06.018. PubMed PMID: 19800470; PubMed Central PMCID: PMC2764289.

26. Ramanujam N. Fluorescence spectroscopy of neoplastic and non-neoplastic tissues. Neoplasia. 2000;2(1-2):89-117. Epub 2000/08/10. PubMed PMID: 10933071; PubMed Central PMCID: PMC1531869.

27. Evans CL, Potma EO, Puoris'haag M, Cote D, Lin CP, Xie XS. Chemical imaging of tissue in vivo with video-rate coherent anti-Stokes Raman scattering microscopy. Proceedings of the National Academy of Sciences of the United States of America. 2005;102(46):16807-12. Epub 2005/11/03. doi: 10.1073/pnas.0508282102. PubMed PMID: 16263923; PubMed Central PMCID: PMC1283840.

28. Brezinski ME. Optical Coherence Tomography: Principles and Applications: Academic Press; 2006.

29. Huang D, Swanson E, Lin C, Schuman J, Stinson W, Chang W, et al. Optical coherence tomography. Science. 1991;254(5035):1178-81. doi: 10.1126/science.1957169.

30. Ramiro S. Maldonado JAI, Neeru Sarin, David K. Wallace, Sharon Freedman, C. Michael Cotten, and Cynthia A. Toth. Optimizing Hand-held Spectral Domain Optical Coherence Tomography Imaging for Neonates, Infants, and Children. Investigative Ophthalmology & Visual Science. 2010;51(5):2678–85.

31. Tao YK, Ehlers JP, Toth CA, Izatt JA. Intraoperative spectral domain optical coherence tomography for vitreoretinal surgery. Opt Lett. 2010;35(20):3315-7. doi: 10.1364/OL.35.003315.

32. Paul Hahn JM, Rachelle O’Connell, Ramiro S. Maldonado, Joseph A. Izatt, and Cynthia A. Toth. The Use of Optical Coherence Tomography in Intraoperative Ophthalmic Imaging. Ophthalmic Surgery, Lasers and Imaging Retina. 2011;42(4):85-94.

33. Woonggyu Jung JK, Mansik Jeon, Eric J. Chaney, Charles N. Stewart, and Stephen A. Boppart. Handheld Optical Coherence Tomography Scanner for Primary Care Diagnostics. IEEE Trans Biomed Engineering. 2012;58(3):9.

34. Joos KM, Shen J-H. Miniature real-time intraoperative forward-imaging optical coherence tomography probe. Biomed Opt Express. 2013;4(8):1342-50. doi: 10.1364/BOE.4.001342.

35. LaRocca F, Nankivil D, Farsiu S, Izatt JA. Handheld simultaneous scanning laser ophthalmoscopy and optical coherence tomography system. Biomed Opt Express. 2013;4(11):2307-21. doi: 10.1364/BOE.4.002307.

36. Lucia Pelosini HBS, John B Schofield, Adam Meeckings, Anish Dhital, Mona Khandwala. In vivo optical coherence tomography (OCT) in periocular basal cell carcinoma: correlations between in vivo OCT images and postoperative histology. British Journal of Ophthalmology. 2013;97(7):890-4.

37. Lu CD, Kraus MF, Potsaid B, Liu JJ, Choi W, Jayaraman V, et al. Handheld ultrahigh speed swept source optical coherence tomography instrument using a MEMS scanning mirror. Biomed Opt Express. 2014;5(1):293-311. doi: 10.1364/BOE.5.000293.

38. Bouma BE, Tearney GJ. Power-efficient nonreciprocal interferometer and linear-scanning fiber-optic catheter for optical coherence tomography. Opt Lett. 1999;24(8):531-3. doi: 10.1364/OL.24.000531.

39. Jang I-K, Bouma BE, Kang D-H, Park S-J, Park S-W, Seung K-B, et al. Visualization of coronary atherosclerotic plaques in patients using optical coherence tomography: comparison with intravascular ultrasound. Journal of the American College of Cardiology. 2002;39(4):604-9. doi: http://dx.doi.org/10.1016/S0735-1097(01)01799-5.

40. Ferrante G, Presbitero, P., Whitbourn, R., Barlis, P. Current applications of optical coherence tomography for coronary intervention. International Journal of Cardiology. 2013;165(1):7-16. doi: 10.1016/j.ijcard.2012.02.013.

41. Nguyen FT, Zysk, A. M., Chaney, E. J., Kotynek, J. G., Oliphant, U. J., Bellafiore, F. J., Rowland, K. M., Johnson, P. A., Boppart, S. A. Intraoperative Evaluation of Breast Tumor Margins with Optical Coherence Tomography. Cancer Research. 2009;69(22):8790-6.

42. Palanker DV, Blumenkranz MS, Andersen D, Wiltberger M, Marcellino G, Gooding P, et al. Femtosecond Laser–Assisted Cataract Surgery with Integrated Optical Coherence Tomography. Science Translational Medicine. 2010;2(58):58-85. doi: 10.1126/scitranslmed.3001305.

43. Poh CF, Zhang LW, Anderson DW, Durham JS, Williams RM, Priddy RW, et al. Fluorescence visualization detection of field alterations in tumor margins of oral cancer patients. Clinical cancer research : an official journal of the American Association for Cancer Research.

2006;12(22):6716-22. doi: Doi 10.1158/1078-0432.Ccr-06-1317. PubMed PMID: ISI:000242263300017.

44. Kim C, Erpelding TN, Maslov K, Jankovic L, Akers WJ, Song L, et al. Handheld array-based photoacoustic probe for guiding needle biopsy of sentinel lymph nodes. Journal of biomedical optics. 2010;15(4):046010-4. Epub 2010/08/31. doi: 10.1117/1.3469829. PubMed PMID: 20799812; PubMed Central PMCID: PMC2937045.

45. Schaafsma BE, Mieog JS, Hutteman M, van der Vorst JR, Kuppen PJ, Lowik CW, et al. The clinical use of indocyanine green as a near-infrared fluorescent contrast agent for image-guided oncologic surgery. Journal of surgical oncology. 2011;104(3):323-32. Epub 2011/04/16. doi: 10.1002/jso.21943. PubMed PMID: 21495033; PubMed Central PMCID: PMC3144993.

46. Gioux S, Choi HS, Frangioni JV. Image-guided surgery using invisible near-infrared light: fundamentals of clinical translation. Molecular imaging. 2010;9(5):237-55. Epub 2010/09/28. PubMed PMID: 20868625; PubMed Central PMCID: PMC3105445.

47. Takahashi M, Ishikawa T, Higashidani K, Katoh H. SPY: an innovative intra-operative imaging system to evaluate graft patency during off-pump coronary artery bypass grafting. Interactive cardiovascular and thoracic surgery. 2004;3(3):479-83. Epub 2007/08/03. doi: 10.1016/j.icvts.2004.01.018. PubMed PMID: 17670291.

48. Coles C, Taggart D, Choudhary B, Abu-Omar Y, Balacumaraswami L, Pigott D. The use of a novel imaging technique to evaluate patency of coronary grafts. Anaesthesia. 2003;58(3):304. doi: 10.1046/j.1365-2044.2003.03093_1.x.

49. Tagaya N, Yamazaki R, Nakagawa A, Abe A, Hamada K, Kubota K, et al. Intraoperative identification of sentinel lymph nodes by near-infrared fluorescence imaging in patients with

breast cancer. American journal of surgery. 2008;195(6):850-3. Epub 2008/03/21. doi: 10.1016/j.amjsurg.2007.02.032. PubMed PMID: 18353274.

50. Gotoh K, Yamada T, Ishikawa O, Takahashi H, Eguchi H, Yano M, et al. A novel image-guided surgery of hepatocellular carcinoma by indocyanine green fluorescence imaging navigation. Journal of surgical oncology. 2009;100(1):75-9. Epub 2009/03/21. doi: 10.1002/jso.21272. PubMed PMID: 19301311.

51. Troyan SL, Kianzad V, Gibbs-Strauss SL, Gioux S, Matsui A, Oketokoun R, et al. The FLARE intraoperative near-infrared fluorescence imaging system: a first-in-human clinical trial in breast cancer sentinel lymph node mapping. Annals of Surgical Oncology. 2009;16(10):2943-52. Epub 2009/07/08. doi: 10.1245/s10434-009-0594-2. PubMed PMID: 19582506; PubMed Central PMCID: PMC2772055.

52. Mieog JS, Troyan SL, Hutteman M, Donohoe KJ, van der Vorst JR, Stockdale A, et al. Toward optimization of imaging system and lymphatic tracer for near-infrared fluorescent sentinel lymph node mapping in breast cancer. Annals of Surgical Oncology. 2011;18(9):2483-91. Epub 2011/03/02. doi: 10.1245/s10434-011-1566-x. PubMed PMID: 21360250; PubMed Central PMCID: PMC3139732.

53. Hutteman M, van der Vorst JR, Gaarenstroom KN, Peters AA, Mieog JS, Schaafsma BE, et al. Optimization of near-infrared fluorescent sentinel lymph node mapping for vulvar cancer. American journal of obstetrics and gynecology. 2012;206(1):1-5. Epub 2011/10/04. doi: 10.1016/j.ajog.2011.07.039. PubMed PMID: 21963099; PubMed Central PMCID: PMC3246078.

54. Liu Y, Bauer AQ, Akers WJ, Sudlow G, Liang K, Shen D, et al. Hands-free, wireless goggles for near-infrared fluorescence and real-time image-guided surgery. Surgery.

2011;149(5):689-98. Epub 2011/04/19. doi: 10.1016/j.surg.2011.02.007. PubMed PMID: 21496565; PubMed Central PMCID: PMC3079879.

55. Liu Y, Akers WJ, Bauer AQ, Mondal S, Gullicksrud K, Sudlow GP, et al. Intraoperative detection of liver tumors aided by a fluorescence goggle system and multimodal imaging. The Analyst. 2013;138(8):2254-7. Epub 2013/03/08. doi: 10.1039/c3an00165b. PubMed PMID: 23467534; PubMed Central PMCID: PMC3650133.

56. Liu Y, Njuguna R, Matthews T, Akers WJ, Sudlow GP, Mondal S, et al. Near-infrared fluorescence goggle system with complementary metal-oxide-semiconductor imaging sensor and see-through display. Journal of biomedical optics. 2013;18(10):101303. Epub 2013/06/04. doi: 10.1117/1.JBO.18.10.101303. PubMed PMID: 23728180; PubMed Central PMCID: PMC3667841.

57. Mondal SB, Gao S, Zhu N, Sudlow GP, Liang K, Som A, et al. Binocular Goggle Augmented Imaging and Navigation System provides real-time fluorescence image guidance for tumor resection and sentinel lymph node mapping. Scientific reports. 2015;5:12117. Epub 2015/07/17. doi: 10.1038/srep12117. PubMed PMID: 26179014; PubMed Central PMCID: PMC4503986.

58. Handa T, Katare RG, Nishimori H, Wariishi S, Fukutomi T, Yamamoto M, et al. New device for intraoperative graft assessment: HyperEye charge-coupled device camera system. General thoracic and cardiovascular surgery. 2010;58(2):68-77. Epub 2010/02/16. doi: 10.1007/s11748-009-0536-8. PubMed PMID: 20155342.

59. Darne CD, Lu Y, Tan IC, Zhu B, Rasmussen JC, Smith AM, et al. A compact frequency-domain photon migration system for integration into commercial hybrid small animal imaging scanners for fluorescence tomography. Physics in medicine and biology. 2012;57(24):8135-52.

Epub 2012/11/23. doi: 10.1088/0031-9155/57/24/8135. PubMed PMID: 23171509; PubMed Central PMCID: PMC3533362.

60. Marshall MV, Rasmussen JC, Tan IC, Aldrich MB, Adams KE, Wang X, et al. Near-Infrared Fluorescence Imaging in Humans with Indocyanine Green: A Review and Update. Open surgical oncology journal. 2010;2(2):12-25. Epub 2010/01/01. doi: 10.2174/1876504101002010012. PubMed PMID: 22924087; PubMed Central PMCID: PMC3424734.

61. Themelis G, Yoo JS, Soh KS, Schulz R, Ntziachristos V. Real-time intraoperative fluorescence imaging system using light-absorption correction. Journal of biomedical optics. 2009;14(6):064012-9. Epub 2010/01/12. doi: 10.1117/1.3259362. PubMed PMID: 20059250.

62. Crane LM, Themelis G, Pleijhuis RG, Harlaar NJ, Sarantopoulos A, Arts HJ, et al. Intraoperative multispectral fluorescence imaging for the detection of the sentinel lymph node in cervical cancer: a novel concept. Molecular imaging and biology : MIB : the official publication of the Academy of Molecular Imaging. 2011;13(5):1043-9. Epub 2010/09/14. doi: 10.1007/s11307-010-0425-7. PubMed PMID: 20835767; PubMed Central PMCID: PMC3179588.

63. van Dam GM, Themelis G, Crane LM, Harlaar NJ, Pleijhuis RG, Kelder W, et al. Intraoperative tumor-specific fluorescence imaging in ovarian cancer by folate receptor-alpha targeting: first in-human results. Nature medicine. 2011;17(10):1315-9. Epub 2011/09/20. doi: 10.1038/nm.2472. PubMed PMID: 21926976.

64. Sekijima M, Tojimbara T, Sato S, Nakamura M, Kawase T, Kai K, et al. An intraoperative fluorescent imaging system in organ transplantation. Transplantation proceedings.

2004;36(7):2188-90. Epub 2004/11/03. doi: 10.1016/j.transproceed.2004.09.001. PubMed PMID: 15518796.

65. Keereweer S, Kerrebijn JD, van Driel PB, Xie B, Kaijzel EL, Snoeks TJ, et al. Optical image-guided surgery--where do we stand? Molecular imaging and biology : MIB : the official publication of the Academy of Molecular Imaging. 2011;13(2):199-207. Epub 2010/07/10. doi: 10.1007/s11307-010-0373-2. PubMed PMID: 20617389; PubMed Central PMCID: PMC3051067.

66. Mieog JS, Vahrmeijer AL, Hutteman M, van der Vorst JR, Drijfhout van Hooff M, Dijkstra J, et al. Novel intraoperative near-infrared fluorescence camera system for optical image-guided cancer surgery. Molecular imaging. 2010;9(4):223-31. Epub 2010/07/21. PubMed PMID: 20643025.

67. Mondal SB, Gao S, Zhu N, Liu Y, Sudlow GP, Akers WJ, et al., editors. Intraoperative imaging and fluorescence image guidance in oncologic surgery using a wearable fluorescence goggle system. Proc SPIE 8936, Design and Quality for Biomedical Technologies VII; 2014.

68. Andersson, Baechi, Hoechl, Richter. Autofluorescence of living cells. Journal of Microscopy. 1998;191(1):1-7. doi: 10.1046/j.1365-2818.1998.00347.x.

69. Croce AC, Spano A, Balzarini P, Locatelli D, Barni S, Pippia P, et al., editors. Autofluorescence properties of normal and transformed fibroblasts. Proceedings of SPIE 2926, Optical Biopsies and Microscopic Techniques, 108; 1996 December 6, 1996.

70. Ramanujam N, Mitchell MF, Mahadevan A, Warren S, Thomsen S, Silva E, et al. In vivo diagnosis of cervical intraepithelial neoplasia using 337-nm-excited laser-induced fluorescence. Proceedings of the National Academy of Sciences of the United States of America.

1994;91(21):10193-7. Epub 1994/10/11. PubMed PMID: 7937860; PubMed Central PMCID: PMC44984.

71. Koenig F, McGovern FJ, Althausen AF, Deutsch TF, Schomacker KT. Laser induced autofluorescence diagnosis of bladder cancer. The Journal of urology. 1996;156(5):1597-601. Epub 1996/11/01. PubMed PMID: 8863546.

72. Jayaprakash V, Sullivan M, Merzianu M, Rigual NR, Loree TR, Popat SR, et al. Autofluorescence-Guided Surveillance for Oral Cancer. Cancer Prev Res. 2009;2(11):966-74. doi: Doi 10.1158/1940-6207.Capr-09-0062. PubMed PMID: ISI:000271458400008.

73. Poh CF, MacAulay CE, Zhang L, Rosin MP. Tracing the "at-risk" oral mucosa field with autofluorescence: steps toward clinical impact. Cancer Prev Res. 2009;2(5):401-4. Epub 2009/04/30. doi: 10.1158/1940-6207.CAPR-09-0060. PubMed PMID: 19401533; PubMed Central PMCID: PMC2726429.

74. Alexander S, Koehl G, Hirschberg M, Geissler E, Friedl P. Dynamic imaging of cancer growth and invasion: a modified skin-fold chamber model. Histochemistry and Cell Biology. 2008;130(6):1147-54. doi: 10.1007/s00418-008-0529-1.

75. DaCosta RS, Andersson, H., and Wilson, B. C. Molecular fluorescence excitation-emission matrices relevant to tissue spectroscopy. Photochemistry and Photobiology. 2003;78(4):384-92.

76. Rassmussen-Taxdal DS, Ward GE, Figge FHJ. Fluorescence of human lymphatic and cancer tissues following high doses of intravenous hematoporphyrin. Cancer. 1955;8(1):78-81. doi: 10.1002/1097-0142(1955)8:1<78::aid-cncr2820080109>3.0.co;2-l.

77. Lee BT, Hutteman M, Gioux S, Stockdale A, Lin SJ, Ngo LH, et al. The FLARE intraoperative near-infrared fluorescence imaging system: a first-in-human clinical trial in

perforator flap breast reconstruction. Plastic and reconstructive surgery. 2010;126(5):1472-81. Epub 2010/11/03. doi: 10.1097/PRS.0b013e3181f059c7. PubMed PMID: 21042103; PubMed Central PMCID: PMC2974179.

78. Sevick-Muraca EM, Rasmussen, J. C. Molecular imaging with optics: primer and case for near-infrared fluorescence techniques in personalized medicine. Journal of Biomed Optics. 2008;13(4):041303-16.

79. Adams KE, Ke S, Kwon S, Liang F, Fan Z, Lu Y, et al. Comparison of visible and near-infrared wavelength-excitable fluorescent dyes for molecular imaging of cancer. Journal of biomedical optics. 2007;12(2):024017-9. doi: 10.1117/1.2717137.

80. Lim YT, Kim S, Nakayama A, Stott NE, Bawendi MG, Frangioni JV. Selection of quantum dot wavelengths for biomedical assays and imaging. Molecular imaging. 2003;2(1):50-64. Epub 2003/08/21. PubMed PMID: 12926237.

81. Smith AM, Mancini MC, Nie S. Bioimaging: second window for in vivo imaging. Nature nanotechnology. 2009;4(11):710-1. Epub 2009/11/10. doi: 10.1038/nnano.2009.326. PubMed PMID: 19898521; PubMed Central PMCID: PMC2862008.

82. Sexton K, Davis SC, McClatchy D, Valdes PA, Kanick SC, Paulsen KD, et al. Pulsed-light imaging for fluorescence guided surgery under normal room lighting. Opt Lett. 2013;38(17):3249-52. doi: 10.1364/OL.38.003249.

83. Moore GE. Fluorescein as an Agent in the Differentiation of Normal and Malignant Tissues. Science. 1947;106(2745):130-1. Epub 1947/08/08. doi: 10.1126/science.106.2745.130-a. PubMed PMID: 17750790.

84. Moore GE, Peyton WT, et al. The clinical use of fluorescein in neurosurgery; the localization of brain tumors. Journal of neurosurgery. 1948;5(4):392-8. Epub 1948/07/01. doi: 10.3171/jns.1948.5.4.0392. PubMed PMID: 18872412.

85. Folli S, Wagnieres G, Pelegrin A, Calmes JM, Braichotte D, Buchegger F, et al. Immunophotodiagnosis of colon carcinomas in patients injected with fluoresceinated chimeric antibodies against carcinoembryonic antigen. Proceedings of the National Academy of Sciences of the United States of America. 1992;89(17):7973-7. Epub 1992/09/01. PubMed PMID: 1518823; PubMed Central PMCID: PMC49837.

86. Matsui A, Tanaka E, Choi HS, Winer JH, Kianzad V, Gioux S, et al. Real-time intra-operative near-infrared fluorescence identification of the extrahepatic bile ducts using clinically available contrast agents. Surgery. 2010;148(1):87-95. Epub 2010/02/02. doi: 10.1016/j.surg.2009.12.004. PubMed PMID: 20117813; PubMed Central PMCID: PMC2886157.

87. Tanaka E, Chen FY, Flaumenhaft R, Graham GJ, Laurence RG, Frangioni JV. Real-time assessment of cardiac perfusion, coronary angiography, and acute intravascular thrombi using dual-channel near-infrared fluorescence imaging. The Journal of thoracic and cardiovascular surgery. 2009;138(1):133-40. Epub 2009/07/07. doi: 10.1016/j.jtcvs.2008.09.082. PubMed PMID: 19577070; PubMed Central PMCID: PMC2706783.

88. Winer JH, Choi HS, Gibbs-Strauss SL, Ashitate Y, Colson YL, Frangioni JV. Intraoperative localization of insulinoma and normal pancreas using invisible near-infrared fluorescent light. Annals of Surgical Oncology. 2010;17(4):1094-100. Epub 2009/12/25. doi: 10.1245/s10434-009-0868-8. PubMed PMID: 20033320; PubMed Central PMCID: PMC2841719.

89. Colditz MJ, Leyen K, Jeffree RL. Aminolevulinic acid (ALA)-protoporphyrin IX fluorescence guided tumour resection. Part 2: theoretical, biochemical and practical aspects. Journal of clinical neuroscience : official journal of the Neurosurgical Society of Australasia. 2012;19(12):1611-6. Epub 2012/10/13. doi: 10.1016/j.jocn.2012.03.013. PubMed PMID: 23059058.

90. Stummer W, Pichlmeier U, Meinel T, Wiestler OD, Zanella F, Reulen HJ. Fluorescence-guided surgery with 5-aminolevulinic acid for resection of malignant glioma: a randomised controlled multicentre phase III trial. The lancet oncology. 2006;7(5):392-401. Epub 2006/05/02. doi: 10.1016/S1470-2045(06)70665-9. PubMed PMID: 16648043.

91. Brouwer OR, Klop WM, Buckle T, Vermeeren L, van den Brekel MW, Balm AJ, et al. Feasibility of sentinel node biopsy in head and neck melanoma using a hybrid radioactive and fluorescent tracer. Annals of Surgical Oncology. 2012;19(6):1988-94. Epub 2011/12/31. doi: 10.1245/s10434-011-2180-7. PubMed PMID: 22207047; PubMed Central PMCID: PMC3356513.

92. Valdes PA, Leblond F, Kim A, Harris BT, Wilson BC, Fan X, et al. Quantitative fluorescence in intracranial tumor: implications for ALA-induced PpIX as an intraoperative biomarker. Journal of neurosurgery. 2011;115(1):11-7. Epub 2011/03/29. doi: 10.3171/2011.2.JNS101451. PubMed PMID: 21438658; PubMed Central PMCID: PMC3129387.

93. Jocham D, Stepp H, Waidelich R. Photodynamic diagnosis in urology: state-of-the-art. European urology. 2008;53(6):1138-48. Epub 2007/12/22. doi: 10.1016/j.eururo.2007.11.048. PubMed PMID: 18096307.

94. Moiyadi A, Syed P, Srivastava S. Fluorescence-guided surgery of malignant gliomas based on 5-aminolevulinic acid: paradigm shifts but not a panacea. Nature Reviews Cancer. 2014;14(2):146. doi: 10.1038/nrc3566-c1.

95. Schaafsma BE, Mieog JS, Hutteman M, van der Vorst JR, Kuppen PJ, Lowik CW, et al. The clinical use of indocyanine green as a near-infrared fluorescent contrast agent for image-guided oncologic surgery. J Surg Oncol. 2011;104(3):323-32. Epub 2011/04/16. doi: 10.1002/jso.21943. PubMed PMID: 21495033; PubMed Central PMCID: PMC3144993.

96. Kraft JC, Ho RJ. Interactions of indocyanine green and lipid in enhancing near-infrared fluorescence properties: the basis for near-infrared imaging in vivo. Biochemistry. 2014;53(8):1275-83. Epub 2014/02/12. doi: 10.1021/bi500021j. PubMed PMID: 24512123; PubMed Central PMCID: PMC3985908.

97. De Grand AM, Frangioni JV. An operational near-infrared fluorescence imaging system prototype for large animal surgery. Technology in cancer research & treatment. 2003;2(6):553-62. Epub 2003/12/04. PubMed PMID: 14640766.

98. Matsui A, Lee BT, Winer JH, Vooght CS, Laurence RG, Frangioni JV. Real-time intraoperative near-infrared fluorescence angiography for perforator identification and flap design. Plastic and reconstructive surgery. 2009;123(3):125-7. Epub 2009/03/26. doi: 10.1097/PRS.0b013e31819a3617. PubMed PMID: 19319038.

99. Aoki T, Yasuda D, Shimizu Y, Odaira M, Niiya T, Kusano T, et al. Image-guided liver mapping using fluorescence navigation system with indocyanine green for anatomical hepatic resection. World journal of surgery. 2008;32(8):1763-7. Epub 2008/06/11. doi: 10.1007/s00268-008-9620-y. PubMed PMID: 18543027.

100. Nimura H, Narimiya N, Mitsumori N, Yamazaki Y, Yanaga K, Urashima M. Infrared ray electronic endoscopy combined with indocyanine green injection for detection of sentinel nodes of patients with gastric cancer. The British journal of surgery. 2004;91(5):575-9. Epub 2004/05/04. doi: 10.1002/bjs.4470. PubMed PMID: 15122608.

101. Miyashiro I, Miyoshi N, Hiratsuka M, Kishi K, Yamada T, Ohue M, et al. Detection of sentinel node in gastric cancer surgery by indocyanine green fluorescence imaging: comparison with infrared imaging. Annals of Surgical Oncology. 2008;15(6):1640-3. Epub 2008/04/02. doi: 10.1245/s10434-008-9872-7. PubMed PMID: 18379850.

102. Kusano M, Tajima Y, Yamazaki K, Kato M, Watanabe M, Miwa M. Sentinel node mapping guided by indocyanine green fluorescence imaging: a new method for sentinel node navigation surgery in gastrointestinal cancer. Digestive surgery. 2008;25(2):103-8. Epub 2008/04/02. doi: 10.1159/000121905. PubMed PMID: 18379188.

103. Fujiwara M, Mizukami T, Suzuki A, Fukamizu H. Sentinel lymph node detection in skin cancer patients using real-time fluorescence navigation with indocyanine green: preliminary experience. Journal of plastic, reconstructive & aesthetic surgery : JPRAS. 2009;62(10):373-8. Epub 2008/06/17. doi: 10.1016/j.bjps.2007.12.074. PubMed PMID: 18556255.

104. Tsujino Y, Mizumoto K, Matsuzaka Y, Niihara H, Morita E. Fluorescence navigation with indocyanine green for detecting sentinel nodes in extramammary Paget's disease and squamous cell carcinoma. The Journal of dermatology. 2009;36(2):90-4. Epub 2009/03/17. doi: 10.1111/j.1346-8138.2009.00595.x. PubMed PMID: 19284452.

105. Hutteman M, Choi HS, Mieog JS, van der Vorst JR, Ashitate Y, Kuppen PJ, et al. Clinical translation of ex vivo sentinel lymph node mapping for colorectal cancer using invisible near-infrared fluorescence light. Annals of Surgical Oncology. 2011;18(4):1006-14. Epub

2010/11/17. doi: 10.1245/s10434-010-1426-0. PubMed PMID: 21080086; PubMed Central PMCID: PMC3052497.

106. Verbeek FP, van der Vorst JR, Schaafsma BE, Hutteman M, Bonsing BA, van Leeuwen FW, et al. Image-guided hepatopancreatobiliary surgery using near-infrared fluorescent light. Journal of hepato-biliary-pancreatic sciences. 2012;19(6):626-37. Epub 2012/07/14. doi: 10.1007/s00534-012-0534-6. PubMed PMID: 22790312; PubMed Central PMCID: PMC3501168.

107. Shinoda J, Yano H, Yoshimura S, Okumura A, Kaku Y, Iwama T, et al. Fluorescence-guided resection of glioblastoma multiforme by using high-dose fluorescein sodium. Technical note. Journal of neurosurgery. 2003;99(3):597-603. Epub 2003/09/10. doi: 10.3171/jns.2003.99.3.0597. PubMed PMID: 12959452.

108. Varghese P, Abdel-Rahman AT, Akberali S, Mostafa A, Gattuso JM, Carpenter R. Methylene blue dye--a safe and effective alternative for sentinel lymph node localization. The breast journal. 2008;14(1):61-7. Epub 2008/01/12. doi: 10.1111/j.1524-4741.2007.00519.x. PubMed PMID: 18186867.

109. Winer JH, Choi HS, Gibbs-Strauss SL, Ashitate Y, Colson YL, Frangioni JV. Intraoperative localization of insulinoma and normal pancreas using invisible near-infrared fluorescent light. Annals of surgical oncology. 2010;17(4):1094-100. Epub 2009/12/25. doi: 10.1245/s10434-009-0868-8. PubMed PMID: 20033320; PubMed Central PMCID: PMC2841719.

110. Nguyen QT, Tsien RY. Fluorescence-guided surgery with live molecular navigation -- a new cutting edge. Nature Reviews Cancer. 2013;13(9):653-62. doi: 10.1038/nrc3566.

111. Tanis PJ, Nieweg OE, Valdes Olmos RA, Th Rutgers EJ, Kroon BB. History of sentinel node and validation of the technique. Breast Cancer Res. 2001;3(2):109-12. Epub 2001/03/16. PubMed PMID: 11250756; PubMed Central PMCID: PMC139441.

112. Chen SL, Iddings DM, Scheri RP, Bilchik AJ. Lymphatic mapping and sentinel node analysis: current concepts and applications. CA: a cancer journal for clinicians. 2006;56(5):292-309; quiz 16-7. Epub 2006/09/29. PubMed PMID: 17005598.

113. Morton DL, Bostick PJ. Will the true sentinel node please stand? Annals of Surgical Oncology. 1999;6(1):12-4. Epub 1999/02/25. PubMed PMID: 10030408.

114. Giuliano AE, Kirgan DM, Guenther JM, Morton DL. Lymphatic mapping and sentinel lymphadenectomy for breast cancer. Annals of surgery. 1994;220(3):391-401. Epub 1994/09/01. PubMed PMID: 8092905; PubMed Central PMCID: PMC1234400.

115. van den Berg NS, Brouwer OR, Klop WM, Karakullukcu B, Zuur CL, Tan IB, et al. Concomitant radio- and fluorescence-guided sentinel lymph node biopsy in squamous cell carcinoma of the oral cavity using ICG-(99m)Tc-nanocolloid. European journal of nuclear medicine and molecular imaging. 2012;39(7):1128-36. Epub 2012/04/25. doi: 10.1007/s00259-012-2129-5. PubMed PMID: 22526966.

116. Vera DR, Wallace AM, Hoh CK, Mattrey RF. A synthetic macromolecule for sentinel node detection: (99m)Tc-DTPA-mannosyl-dextran. Journal of nuclear medicine : official publication, Society of Nuclear Medicine. 2001;42(6):951-9. Epub 2001/06/08. PubMed PMID: 11390562.

117. Ting R, Aguilera TA, Crisp JL, Hall DJ, Eckelman WC, Vera DR, et al. Fast 18F labeling of a near-infrared fluorophore enables positron emission tomography and optical imaging of

sentinel lymph nodes. Bioconjugate chemistry. 2010;21(10):1811-9. Epub 2010/09/30. doi: 10.1021/bc1001328. PubMed PMID: 20873712; PubMed Central PMCID: PMC2957852.

118. Leong SP, Kim J, Ross M, Faries M, Scoggins CR, Metz WL, et al. A phase 2 study of (99m)Tc-tilmanocept in the detection of sentinel lymph nodes in melanoma and breast cancer. Annals of Surgical Oncology. 2011;18(4):961-9. Epub 2011/02/19. doi: 10.1245/s10434-010-1524-z. PubMed PMID: 21331809; PubMed Central PMCID: PMC3071527.

119. Brouwer OR, Buckle T, Vermeeren L, Klop WM, Balm AJ, van der Poel HG, et al. Comparing the hybrid fluorescent-radioactive tracer indocyanine green-99mTc-nanocolloid with 99mTc-nanocolloid for sentinel node identification: a validation study using lymphoscintigraphy and SPECT/CT. Journal of nuclear medicine : official publication, Society of Nuclear Medicine. 2012;53(7):1034-40. Epub 2012/05/31. doi: 10.2967/jnumed.112.103127. PubMed PMID: 22645297.

120. van der Poel HG, Buckle T, Brouwer OR, Valdes Olmos RA, van Leeuwen FW. Intraoperative laparoscopic fluorescence guidance to the sentinel lymph node in prostate cancer patients: clinical proof of concept of an integrated functional imaging approach using a multimodal tracer. European urology. 2011;60(4):826-33. Epub 2011/04/05. doi: 10.1016/j.eururo.2011.03.024. PubMed PMID: 21458154.

121. van der Vorst JR, Schaafsma BE, Verbeek FP, Hutteman M, Mieog JS, Lowik CW, et al. Randomized comparison of near-infrared fluorescence imaging using indocyanine green and 99(m) technetium with or without patent blue for the sentinel lymph node procedure in breast cancer patients. Annals of Surgical Oncology. 2012;19(13):4104-11. Epub 2012/07/04. doi: 10.1245/s10434-012-2466-4. PubMed PMID: 22752379; PubMed Central PMCID: PMC3465510.

122. Ishizawa T, Fukushima N, Shibahara J, Masuda K, Tamura S, Aoki T, et al. Real-time identification of liver cancers by using indocyanine green fluorescent imaging. Cancer. 2009;115(11):2491-504. Epub 2009/03/28. doi: 10.1002/cncr.24291. PubMed PMID: 19326450.

123. Uchiyama K, Ueno M, Ozawa S, Kiriyama S, Shigekawa Y, Yamaue H. Combined use of contrast-enhanced intraoperative ultrasonography and a fluorescence navigation system for identifying hepatic metastases. World journal of surgery. 2010;34(12):2953-9. Epub 2010/08/25. doi: 10.1007/s00268-010-0764-1. PubMed PMID: 20734045.

124. Peloso A, Franchi E, Canepa MC, Barbieri L, Briani L, Ferrario J, et al. Combined use of intraoperative ultrasound and indocyanine green fluorescence imaging to detect liver metastases from colorectal cancer. HPB : the official journal of the International Hepato Pancreato Biliary Association. 2013;15(12):928-34. Epub 2013/03/06. doi: 10.1111/hpb.12057. PubMed PMID: 23458105; PubMed Central PMCID: PMC3843610.

125. Ishizuka M, Kubota K, Kita J, Shimoda M, Kato M, Sawada T. Intraoperative observation using a fluorescence imaging instrument during hepatic resection for liver metastasis from colorectal cancer. Hepato-gastroenterology. 2012;59(113):90-2. Epub 2012/01/21. doi: 10.5754/hge11223. PubMed PMID: 22260827.

126. Satou S, Ishizawa T, Masuda K, Kaneko J, Aoki T, Sakamoto Y, et al. Indocyanine green fluorescent imaging for detecting extrahepatic metastasis of hepatocellular carcinoma. Journal of gastroenterology. 2013;48(10):1136-43. Epub 2012/11/28. doi: 10.1007/s00535-012-0709-6. PubMed PMID: 23179608.

127. Yokoyama N, Otani T, Hashidate H, Maeda C, Katada T, Sudo N, et al. Real-time detection of hepatic micrometastases from pancreatic cancer by intraoperative fluorescence

imaging: preliminary results of a prospective study. Cancer. 2012;118(11):2813-9. Epub 2011/10/13. doi: 10.1002/cncr.26594. PubMed PMID: 21990070.

128. Hwang SW, Malek AM, Schapiro R, Wu JK. Intraoperative use of indocyanine green fluorescence videography for resection of a spinal cord hemangioblastoma. Neurosurgery. 2010;67(3 Suppl Operative):300-3. Epub 2010/08/04. doi: 10.1227/01.NEU.0000383876.72704.7B. PubMed PMID: 20679920.

129. Ferroli P, Acerbi F, Albanese E, Tringali G, Broggi M, Franzini A, et al. Application of intraoperative indocyanine green angiography for CNS tumors: results on the first 100 cases. Acta neurochirurgica Supplement. 2011;109:251-7. Epub 2010/10/21. doi: 10.1007/978-3-211-99651-5_40. PubMed PMID: 20960352.

130. Hojo M, Arakawa Y, Funaki T, Yoshida K, Kikuchi T, Takagi Y, et al. Usefulness of Tumor Blood Flow Imaging by Intraoperative Indocyanine Green Videoangiography in Hemangioblastoma Surgery. World neurosurgery. 2013:Epub ahead of print. Epub 2013/02/12. doi: 10.1016/j.wneu.2013.02.009. PubMed PMID: 23396070.

131. Keaveny TV, Fitzgerald PA, McMullin JP. Selective parathyroid and pancreatic staining. The British journal of surgery. 1969;56(8):595-7. Epub 1969/08/01. PubMed PMID: 4183792.

132. Keaveny TV, Tawes R, Belzer FO. A new method for intra-operative identification of insulinomas. The British journal of surgery. 1971;58(3):233-4. Epub 1971/03/01. PubMed PMID: 4100889.

133. van der Vorst JR, Vahrmeijer AL, Hutteman M, Bosse T, Smit VT, van de Velde CJ, et al. Near-infrared fluorescence imaging of a solitary fibrous tumor of the pancreas using methylene blue. World journal of gastrointestinal surgery. 2012;4(7):180-4. Epub 2012/08/21.

doi: 10.4240/wjgs.v4.i7.180. PubMed PMID: 22905287; PubMed Central PMCID: PMC3420986.

134. Wallner C, Lange MM, Bonsing BA, Maas CP, Wallace CN, Dabhoiwala NF, et al. Causes of fecal and urinary incontinence after total mesorectal excision for rectal cancer based on cadaveric surgery: a study from the Cooperative Clinical Investigators of the Dutch total mesorectal excision trial. Journal of Clinical Oncology. 2008;26(27):4466-72. Epub 2008/09/20. doi: 10.1200/JCO.2008.17.3062. PubMed PMID: 18802159.

135. Miranda-Sousa AJ, Davila HH, Lockhart JL, Ordorica RC, Carrion RE. Sexual function after surgery for prostate or bladder cancer. Cancer control : journal of the Moffitt Cancer Center. 2006;13(3):179-87. Epub 2006/08/04. PubMed PMID: 16885913.

136. Flum DR, Koepsell T, Heagerty P, Sinanan M, Dellinger EP. Common bile duct injury during laparoscopic cholecystectomy and the use of intraoperative cholangiography: adverse outcome or preventable error? Archives of Surgery. 2001;136(11):1287-92. Epub 2001/12/26. PubMed PMID: 11695975.

137. Selzman AA, Spirnak JP. Iatrogenic ureteral injuries: a 20-year experience in treating 165 injuries. The Journal of urology. 1996;155(3):878-81. Epub 1996/03/01. PubMed PMID: 8583597.

138. Spinoglio G, Priora F, Bianchi PP, Lucido FS, Licciardello A, Maglione V, et al. Real-time near-infrared (NIR) fluorescent cholangiography in single-site robotic cholecystectomy (SSRC): a single-institutional prospective study. Surgical endoscopy. 2013;27(6):2156-62. Epub 2012/12/29. doi: 10.1007/s00464-012-2733-2. PubMed PMID: 23271272.

139. Ishizawa T, Bandai Y, Ijichi M, Kaneko J, Hasegawa K, Kokudo N. Fluorescent cholangiography illuminating the biliary tree during laparoscopic cholecystectomy. The British

journal of surgery. 2010;97(9):1369-77. Epub 2010/07/14. doi: 10.1002/bjs.7125. PubMed PMID: 20623766.

140. Mitsunaga M, Kosaka N, Choyke PL, Young MR, Dextras CR, Saud SM, et al. Fluorescence endoscopic detection of murine colitis-associated colon cancer by topically applied enzymatically rapid-activatable probe. Gut. 2013;62(8):1179-86. Epub 2012/06/16. doi: 10.1136/gutjnl-2011-301795. PubMed PMID: 22698650.

141. Liu Y, York T, Akers W, Sudlow G, Gruev V, Achilefu S. Complementary fluorescence-polarization microscopy using division-of-focal-plane polarization imaging sensor. Journal of biomedical optics. 2012;17(11):116001. Epub 2012/11/03. doi: 10.1117/1.JBO.17.11.116001. PubMed PMID: 23117796; PubMed Central PMCID: PMC3484265.

142. Zhang X, Shoushun C, Culurciello E, editors. A second generation 3D integrated feature-extracting image sensor. Sensors, 2011 IEEE; 2011 28-31 Oct. 2011.

143. Gruev V, Perkins R, York T. CCD polarization imaging sensor with aluminum nanowire optical filters. Opt Express. 2010;18(18):19087-94. doi: 10.1364/oe.18.019087.

144. Johansson R, Storm A, Stephansen C, Eikedal S, Willassen T, Skaug S, et al., editors. A 1/13-inch 30fps VGA SoC CMOS image sensor with shared reset and transfer-gate pixel control. Solid-State Circuits Conference Digest of Technical Papers (ISSCC), 2011 IEEE International; 2011 20-24 Feb. 2011.

Chapter 2: Emerging Clinical Optical Devices

This chapter is based on a pending invited review article: Dolonchampa Maji*, Suman B Mondal*, Nalinikanth Kotagiri and Samuel Achilefu. Emerging Clinical Optical Devices. *To be submitted.* * denotes equal contribution. I wrote the manuscript in collaboration with the co-authors, compiled the information, made comparative tables and edited the manuscript.

2.1 Abstract

Imaging plays a critical role in disease diagnosis and medical interventions. Conventional medical imaging modalities such as MRI, X-Ray, PET and CT provide excellent diagnostic information. However, these modalities are usually costly, bulky and have poor resolution. Optical imaging can fill these needs by enabling real-time high resolution imaging at a low cost and small form factor. As a result optical imaging methods are being rapidly developed since the past few decades. In this review, we list some of the emerging optical imaging systems that are being now used in the clinic or undergoing clinical investigation with high probability of inclusion in clinical practice. We also provide our perspective on the barriers to wide adoption of optical imaging and possible solutions to these issues as we move forward to translate the promise of optical imaging for better human health.

2.2 Introduction

Medical imaging has brought about a revolution in the management of diseases by enabling early diagnosis, better treatment planning and guiding surgical interventions. Clinical imaging modalities consisting of X-rays, CT, MRI, PET and ultrasound scans are routine investigative tools used in clinical centers today to diagnose and treat illness and injury. While these modalities provide excellent diagnostic capabilities for deep seated disease, they lack the resolution necessary to detect microscopic lesions or residual diseased tissue. In addition these modalities are typically complicated, bulky and costly hardware, lack real-time imaging capabilities and may involve use of ionizing radiation that puts patients and caregivers at risk. Alternatively, optical imaging can enable real-time high resolution imaging with simple hardware, amenable to miniaturization. Intuitive visualization make it very user-friendly. Optical methods can obtain images of soft tissue structures across a wide range of sizes and tissue types.

The wide range of colors in the visible spectrum can be exploited to study various light-tissue interactions and visualize different photo-excitable properties simultaneously. It is also widely preferred over other imaging modalities to image superficial and certain subsurface features since patients are not exposed to harmful ionizing radiation, the scans are significantly faster and can be used to monitor disease progression over time. Moreover, it is the only imaging modality that can capture both macroscopic and microscopic details simultaneously in an *in vivo* setting.

Optical imaging has been used in the clinic for many years.[1, 2] It was pioneered by ophthalmologists for imaging ocular diseases. Among optical methods, fluorescence imaging, OCT and spectroscopic methods have been most widely used in clinical investigations. Fluorescence imaging vis-à-vis white light optical imaging also provides higher contrast through the use of fluorescent reporters to tag diseased tissue. Development of novel fluorescent reporters such as fluorescent proteins, peptides, organic dyes, inorganic nanoparticles and other probes is an area of active research. Reporters with high molecular selectivity to surface receptors and enzyme cleavable activatable probes, specific to a disease event, are already available and many currently in clinical trials. Alongside the progress in fluorescent molecular probes, there has been tremendous enthusiasm and a surge in activity in the design and development of fluorescence imaging hardware. While novel fluorescent molecular reporters are essential to enhance pertinent features in tissues of interest through improved contrast, the development of next-generation advanced fluorescence imaging systems also relies on imaging endogenous fluorophores such as NADH and tryptophan with improved sensitivity. OCT methods have been used in the clinic especially for ophthalmic applications. Recently they are being investigated for cancer diagnosis and image guidance. Spectroscopic methods can tell about tissue composition through label free contrast and is widely being investigated for disease diagnosis and more recently for guiding interventions like surgery.

With recent advances in development of ultrasensitive charge-coupled devices (CCD) and complementary metal-oxide-semiconductor (CMOS) imaging sensors, optical imaging is transitioning well to the portable domain, at the same time offering high resolution imaging and scanning rates permitting real-time image acquisition. In this review we will cover some of the clinically used optical systems and also currently in development that have shown high translational potential. We will cover open surgical guidance systems typically used for surgical navigation, minimally invasive endoscope based probes typically used to image lesions in the gastrointestinal tract and diagnostic imaging systems typically based on OCT and spectroscopic methods. We will then provide an overview of the barriers to routine clinical usage of optical methods and possible solutions, followed by our concluding remarks and perspectives.

2.3 Open-field surgical guidance systems

Table 4: Open-field surgical guidance systems. NIR: near-infrared, WL: white light.

System	Description	Clinical Application	Approval
QUEST Spectrum (Artemis)	Handheld dual-channel fluorescence and WL imaging. Laparoscope compatible.	Liver metastasis (NCT02106598)	CE, FDA
GAINS	Wearable NIR fluorescence and WL imaging. Head mounted display.	SLNM breast cancer and melanoma (NCT02316795)	No
FLARE	Standalone dual channel fluorescence and WL imaging.	SLN mapping (NCT01468649, NCT02142244), solid tumor and non-cancer surgeries.	?
Fluobeam	Handheld co-axial NIR fluorescence and WL imaging. Fits on extended arm.	Liver surgery (NCT01738217), Thyroid surgery (NCT02089542, NCT01598727), perforator flaps (NCT01681797)	CE, FDA
FluoSTIC	Handheld NIR fluorescence and WL imaging. Miniaturized for intra cavital access.	*Ex vivo* visualization of colorectal carcinomatosis	CE, FDA 510(k) pending
VELscope	Handheld auto- fluorescence imaging	Oral cancer surgery and diagnosis NCT02251639 NCT00655421NCT01816841	FDA, Health Canada

2.3.1 QUEST Spectrum^{TM}

Principle

The Quest Spectrum is a handheld dual-channel fluorescence imaging system designed to provide image guidance in both open and minimally invasive surgical applications. It was developed by a consortium including the University Medical Centre in Leiden (LUMC) and Quest Medical Imaging (BV, Middenmeer, Netherlands) under the umbrella of the public-private part-ner-ship CTMM (Center for Translational Molecular Medicine).[3]

Hardware

A picture of the second generation Quest Spectrum is shown in Fig. 6.[4] The system features has been adapted for both open surgical and minimally invasive surgical laparoscopic procedures by using a detachable ring light or a laparoscope can be attached interchangeably to the handheld camera head. This procedure is designed to be easy and smooth so that it can be performed if need arises during surgery. According to the product website, many customizable versions of the system has been realized, for example for imaging with indocyanine green (ICG), methylene blue, fluorescein and such other dyes. Light sources determine which fluorophores can be imaged and are housed in the spectrum light engine module that can deliver both visible (four LEDs with peak at blue, cyan, green and red) and light to excite the fluorophore (for example 793 nm for near infrared (NIR) fluorophore). The camera uses a prism technology that enables object viewing on three different sensors (one white light and two fluorescence) simultaneously, and thereafter smooth overlaying of the visible image and one fluorescence image for the surgeon at video mode. The images are overlaid very well (being off by 0.25 pixels at maximum). For example, for a single channel NIR fluorescence imaging, the reflected excitation light is blocked by a notch filter (750–800 nm). The light then enters a prism containing a dichroic coating (<785 mm) which separates the visible and NIR light. The visible light is passed through a low-pass filter (<640 nm) and the NIR light through a high-pass filter (>808 nm). Both white and NIR images are acquired by a Sony ICX618 sensor with Baylor configuration (640x494) pixels. [4] The system uses a proprietary white light feedback mechanism that can measure and adjust the required amount of NIR light irradiance in order to prevent unnecessary overexposures. Spectrum Capture Suite software allows several functions including image acquisition, display, recording data and patient information, and controlling the hardware modules. The whole system is positioned on a portable trolley cart with compact installation. Customized drapes with optimal fitting are available for the camera, arm, laparoscope base, camera, cables while the laparoscope unit itself is autoclavable.

Figure 6: The Quest Spectrum (Artemis) NIR imaging system. The ring light (1) and lens (2) that have to be attached to the handheld camera (3) to obtain NIR fluorescence images. For minimally invasive applications, a scope (4) can be attached to the handheld camera instead. Reproduced with permission.[4]

Applications

The system is a Class 1 CE certified medical device according to the medical device directive. Also, it is a US FDA approved class II medical device based on a 510(k).[3] The Artemis camera system was used for investigating a FDA investigational new drug approved dual modal nanoparticle (optical-PET) for sentinel lymph node mapping, stratifying nodal tumor burden and monitoring treatment response in a spontaneous miniswine model of melanoma.[5] The authors chose the Artemis system primarily because the handheld camera allowed its easy positioning thus enabling viewing otherwise difficult anatomical locations such as the head and the neck. Apart from that, the capability to acquire motion free high resolution images, simultaneous multispectral image acquisition and the ability to control the camera system based on the imaging feedback were added benefits over other similar systems. This combined contrast agent and imaging system are currently under clinical trials for as mentioned in Table 4. [6]

The system was characterized and evaluated in a recently published study using two fluorescence guidance surgical procedures – sentinel lymph node mapping in mice and imaging liver metastasis in human using different fluorescent dyes and injection protocols. [4] (Fig. 7) Through this preliminary results the authors pointed out possible improvements needed which are generally applicable to any intraoperative fluorescence guidance system. The field of view needs to be illuminated homogenously in order to minimize location dependency of the signal and increase imaging reliability. In the current system the illumination dropped sharply at the edges of the field which introduced location dependency in measurements. The need for better filtering of the reflected excitation light arises. In the current configuration, the filters being used to block the excitation light cannot block most specular reflections. The authors propose use of filters with higher optical density or usage of cross polarization or the same. Also, currently the camera has a low depth and no autofocus mechanism, and so the focus needs to be adjusted frequently. The focal lengths between the visible and NIR images requires changing of the focus between them at close imaging distance (<15 cm), which is clearly undesirable for simultaneous acquisition. The dynamic range of the camera can be improved from the current status.

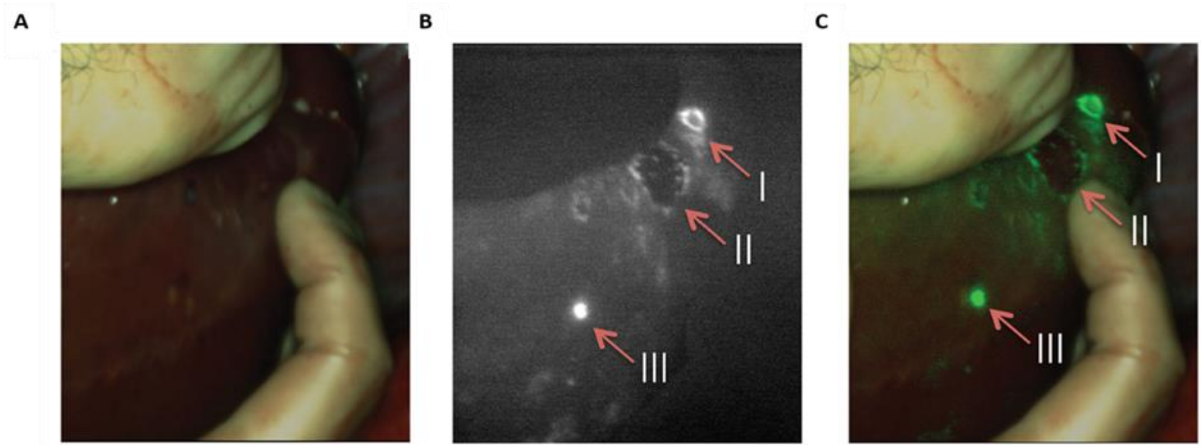

Figure 7: Near infrared fluorescence guided imaging of colorectal liver metastasis. Images were acquired 24 h after injection of indocyanine green. Metastatic lesions are recognizable due to their fluorescent rim (I and II). Benign lesion (III) could be identified by fluorescence without the rim and was confirmed by histology. Images shown depict white light image (A) NIR fluorescence signal (B) and real-time overlay (C). Reproduced with permission.[4]

2.3.2 NIR Goggles

Principle

An NIR goggles system for intraoperative image guidance has been developed by team led by the Achilefu Lab at Washington University in St. Louis (Fig. 8). The unique feature of the system is the use of head mounted display (HMD) for the surgeon instead of monitor projection aimed at making a compact, wearable, battery operated and affordable image guidance system. In addition to the HMD exclusively for the surgeon, the system is capable of simultaneous display of information on a PC for the rest of the surgical team. Thus the goggle system is able to provide hands free operation and image guidance to the surgeon bypassing potentially disruptive information display on a monitor unlike other such devices.

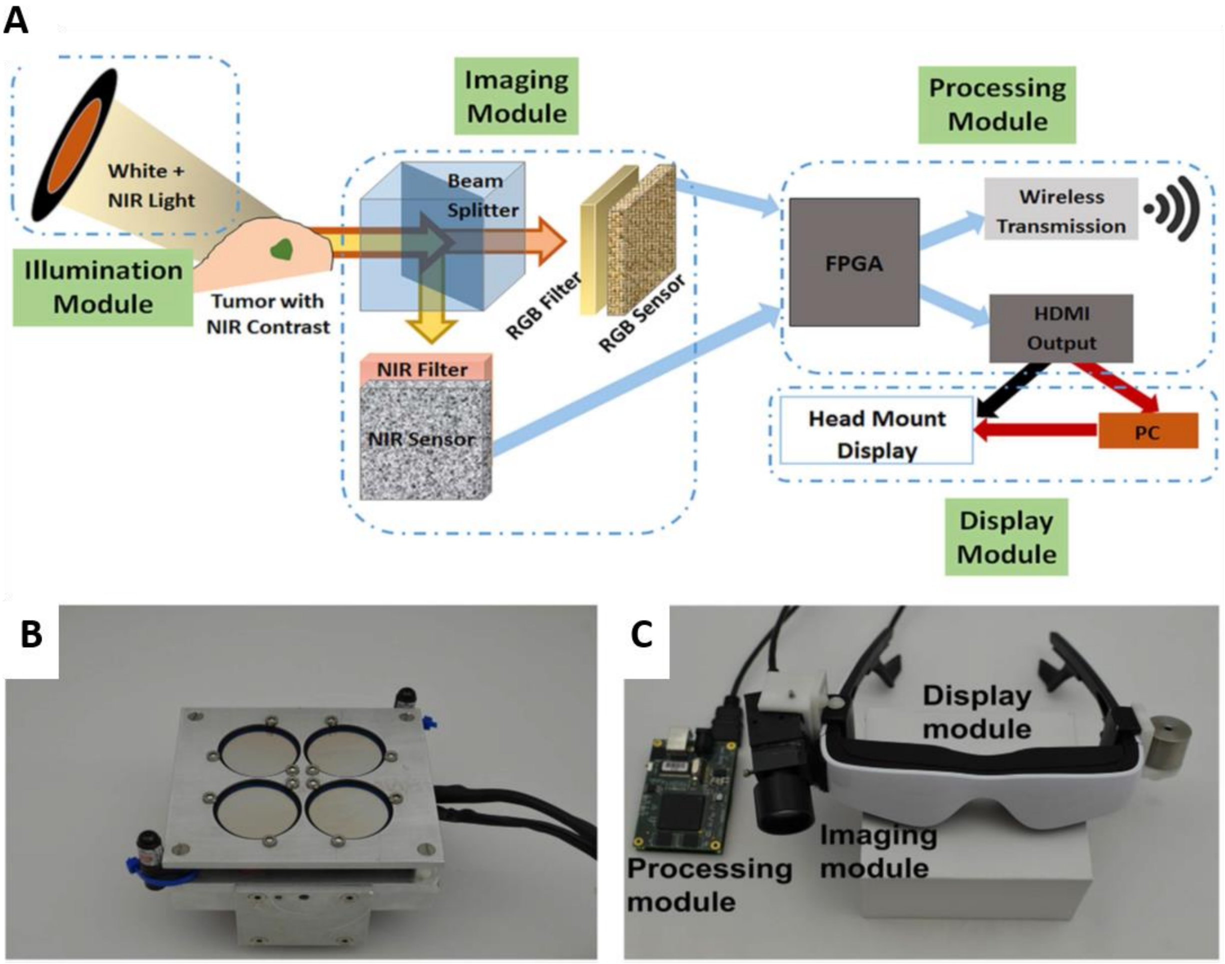

Figure 8: (A) Schematic demonstration of the information flow through different modules of the GAINS system. (B) Photograph of the NIR light source. (C) Photograph of the integrated display and imaging module, along with the processing module, which are worn by the user. Reproduced with permission.[8]

Hardware

The conceptual design of the most recent prototype, also known as the goggle augmented imaging and navigation system (GAINS) is shown in Fig. 8. The authors mention that the major challenges in developing the GAINS system was to avoid bulky optics and yet be able to perform sensitive simultaneous acquisition of the color image which has abundant signal and the relatively photon starved NIR fluorescence image. This challenge was addressed by using a single color-NIR lens instead of separate lenses and a compact lightweight camera. The signal acquisition module separates the acquired color and NIR signals with a custom beam splitter and focuses them onto color and NIR complementary metal-oxide semiconductor (CMOS) sensors equipped with 694 nm shortpass and 805 nm longpass filters respectively. Independent exposure times are used for the color and NIR sensors to be able to acquire adequate signal at spatial resolution of 320 µm. The data processing unit is also custom designed and is able generate video rate superimposed NIR and color images (disparity <0.1 mm at 50 cm distance) displayed via a lightweight 1080 p high resolution HMD system from Carl Zeiss. The software running the system provides a GUI that can be used to perform multiple functions including displaying images, recording data, image processing. It allows displaying images on the HMD for the surgeon and a PC for simultaneous information availability to the surgical team. The software platform has designed to be user friendly and compatible with any windows based PC system.

In the current system, the light source consists of sixteen 760 nm LEDs with 769±41 nm bandpass filter. These hardware components were chosen after careful analysis their spectral properties in order to obtain optimal spectral separation and minimal light leakage for fluorescent dyes such as indocyanine green (ICG). The number and arrangement of LEDs were also optimized with simulations. White light for the color reflectance image can be provided either by surgical lights or high power LED flashlights covered with shortpass filters. The LEDs can be mounted on a tripod along with the flashlights setup or on the surgical light. To help with pointing the NIR light to the region of interest the stand incorporate two laser pointers at the corners of the LED submodule.

Applications

The initial prototypes of the device was validated in a series of small animal studies and also applied in a pilot study involving surgical resection of hepatocellular carcinoma in human patient.[7] The current system was characterized in small imaging and phantom studies and its clinical feasibility was recently demonstrated in a pilot study involve 15 human patients during sentinel lymph node (SLN) mapping (cite paper again). Using ICG as the contrast agent, GAINS was able to visualize 30 sentinel lymph nodes in 10 breast cancer and 5 melanoma patients. The system was compared to conventional methods of tracking SLN using methylene blue dye, ^{99m}Tc-sulfur colloid radioactive tracking and gold standard histology, and demonstrated superior sensitivity to all. In multiple patients GAINS was able to pick up deeply seated SLNs the traditional methods failed. (Fig. 9).[8]

Through this pilot study, it was established that GAINS can provide high sensitivity detection of NIR fluorescence for surgical guidance in the OR. The superior sensitivity can allow the detection of low expression cancer biomarkers in the future applications. The compact system results in substantial reduction in hardware footprint in the OR compared to currently portable yet bulky systems. While it increases usable space in the OR, allows more flexibility, the hands free operation means lesser training needs for the surgeon compared to current handheld systems. Use of miniaturized components makes it considerably low cost than current systems and favors use of GAINs in low resource areas.

The authors point out limitations of the current system, which are critical for any such imaging systems. There is need to incorporate autofocus feature in the current prototype which will prevent image blurring upon large changes of working distance. To further reduce hardware footprint and expand user's radius of movement the wired connections between the computer and the google system needs to be converted to wireless connections. Wireless transmission will also enable telemedicine applications such as remote guidance from exports and remote surgical training.

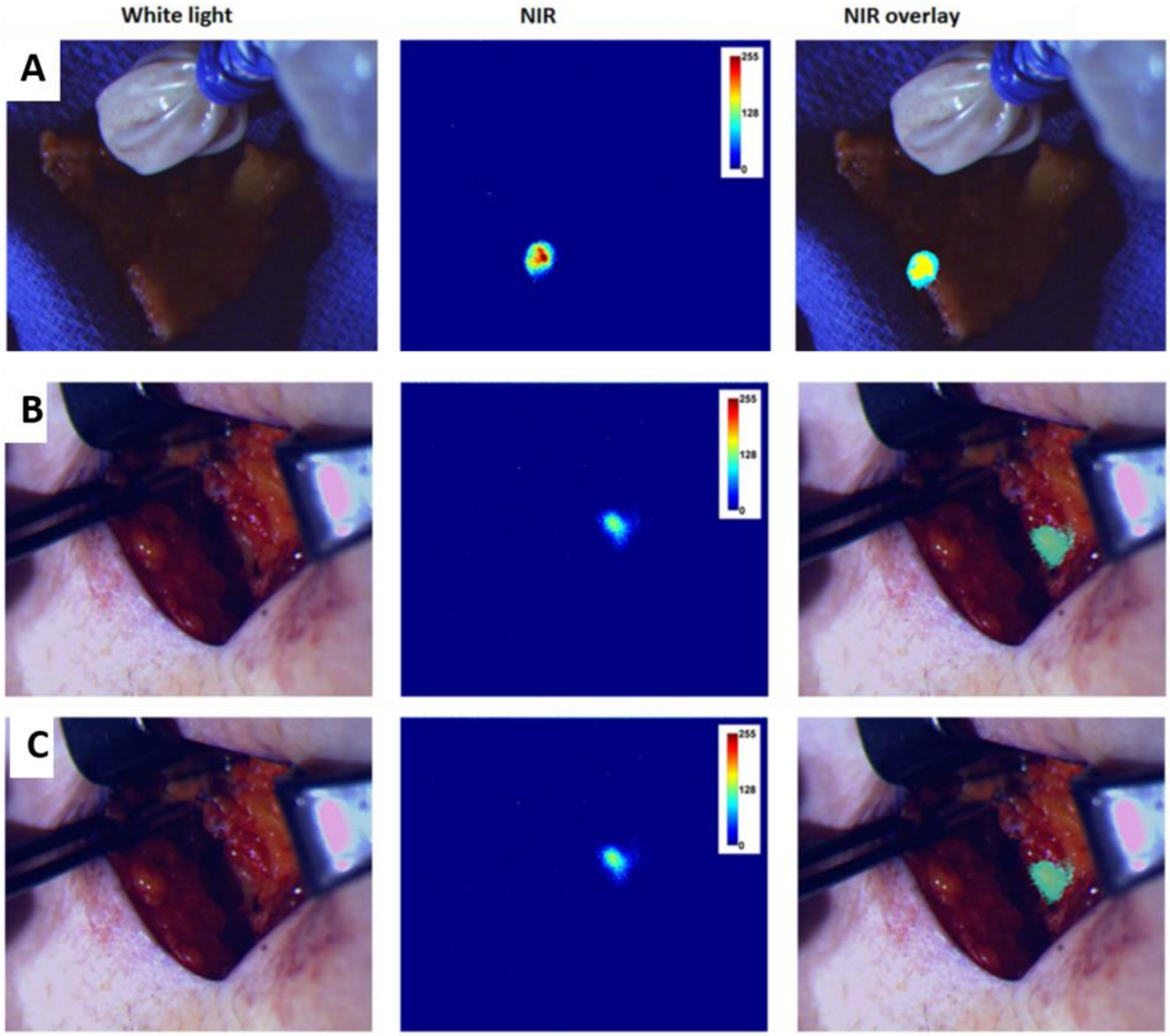

Figure 9: White light, NIR and overlay images acquired by GANS in three different scenarios – (A) NIR image shows excised SLN in a melanoma patient not identified by blue dye. (B) NIR images shows high fluorescence area from non-apparent sentinel lymph node by visual inspection and no blue dye in a breast cancer patient. (C) In the same patient, the lymph node was apparent and blue spot was visible after removal of superficial tissue while NIR image showing a larger clear high fluorescence area. Reproduced with permission.[8]

2.3.3 Fluorescence-Assisted Resection and Exploration (FLARE^{TM})

Principle

The FLARE and later the more compact Mini-FLARE system intraoperative system, developed by the J.V. Frangioni group is the first surgical imaging system with NIR imaging capabilities in real time. (Fig. 10) It is currently in clinical trials and have been used in a large variety of such studies till date.

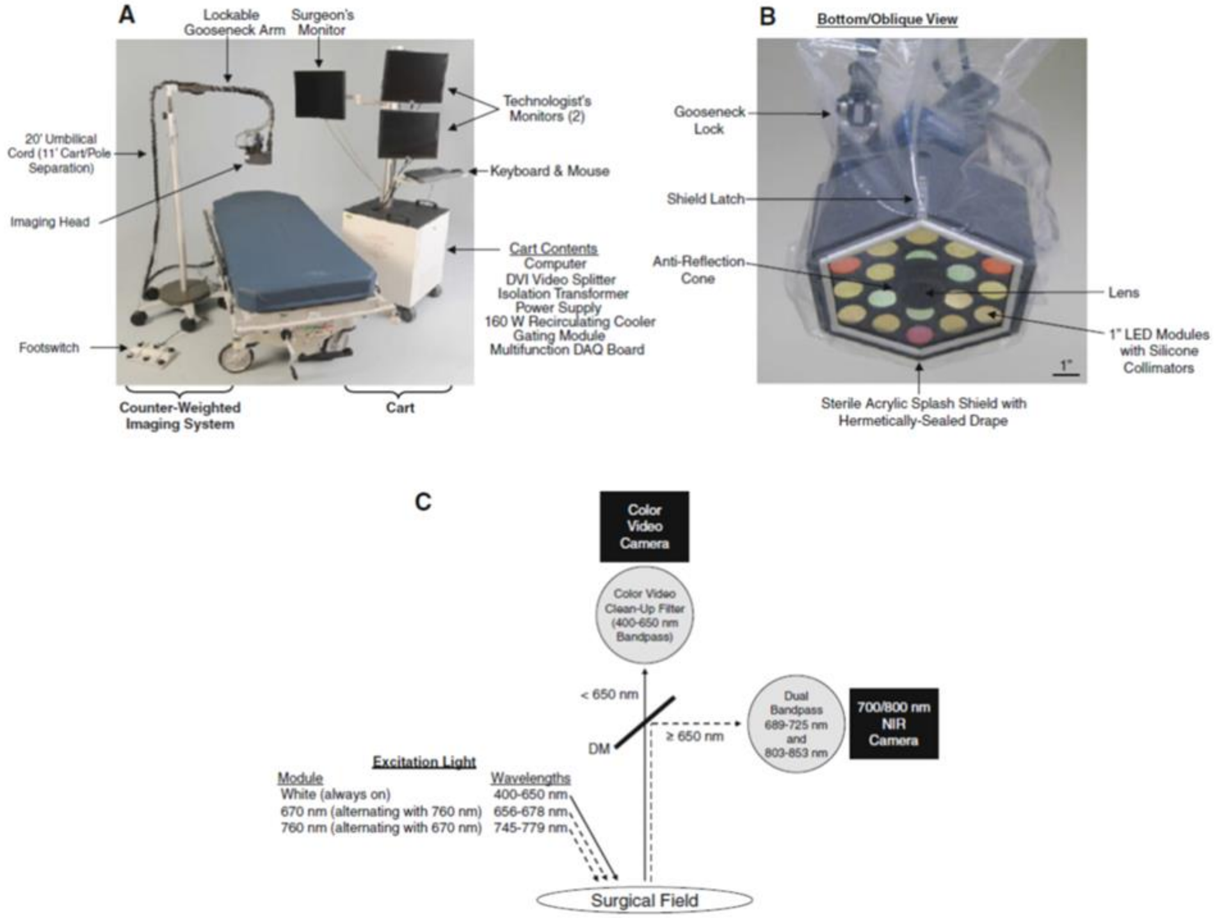

Figure 10: The Mini-FLARE portable near-infrared fluorescence imaging system composed of electronics/monitor cart and counterweighted imaging system pole (A) and the sterile drape/shield attached to the imaging head (B). Excitation and emission light paths, and filtration (C). (DM- 650 nm dichroic mirror). Reproduced with permission.[92]

Hardware

The FLARE™ system and subsequently the more recent mini-FLARE™ system, developed to reduce make the system cost competitive, have been described in details in the previously published papers.[9, 10] (Fig. 10) The light sources consist of LEDs: a white LED light source (filtered at 450 nm – 650 nm), to illuminate the surgical field and to acquiring the color image, and two NIR LED light sources for generating 670 nm and 760 nm fluorescence excitation light. The filtered white is needed to isolate it form the NIR lights, unlike in standard surgical lighting system which generate light above 650 nm. The acquired signal is divided by dichroic mirrors onto the independent and simultaneous 12-bit dynamic range CCD cameras with 400-650 nm bandpass, 689-725 nm bandpass and 800 nm – 848 nm bandpass filters for the color, and NIR channels respectively. Simultaneous and overlaid color-NIR image are displayed on monitors for surgeon and for technologist in separate monitors in real time using custom designed software. Hands free operation is achieved by using a 6-pedal foot switch. The hardware is housed on a portable cart. Sterility required for intraoperative use is achieved using a splash shield /drape combination covering the imaging head, arm and cart and can be applied in the OR. The authors mention that the first clinically used model of the device costs approximately $120,000 USD, which however can be reduced once manufactured and assembled in bulk.[10]

Applications

The FLARE™ or mini-FLARE™ systems have been used in a number of clinical studies. Specifically the dual channel capability has given it flexibility to work with more than one contrast agent in small animals and humans. However, the large hardware footprint and thus space needed for the system in the OR and the expense remain important thing to be considered during its application. Below we provide a summary including the major clinical studies being done with the system.

Sentinel lymph node mapping (SLNM): The FLARE™, and subsequently the mini-FLARE™ systems were used for studies involving *in vivo* and *ex vivo* mapping of sentinel lymph nodes in cancers of the breast[10-13], cervix[14, 15], vulva[15, 16], colon/rectus[12, 13, 16], head and neck[17], and melanoma[13, 18]. In these studies, ICG combined with human serum albumin or ICG alone was used/evaluated as the contrast agent to arrive at optimal formulations and doses. The system was compared to and other fluorescence image guidance systems and conventional methods for sentinel lymph node mapping. For example, in a recent published study, a pre-optimized dose of ICG (1.6 mL of 0.5 mM) was used for the mini-FLARE™ system in SLNM in breast cancer patients[19].

Imaging solid tumor and metastasis: The feasibility of using mini-FLARE™ system for image guidance during breast cancer surgery using methylene blue (MB) was recently demonstrated.[20] (Fig. 11) MB is a visible blue stain and have been evaluated for intraoperative detection of tumors, primarily neuroendocrine tumors. Its fluorescence in the 700 nm channel was used for the mini-FLARE™ system. In one study aimed at neuroendocrine tumors in a patient, unexpectedly an extremely rare solitary fibrous tumor was identified in the pancreas.[21] In another study with breast cancer resection, NIR fluorescence detection of tumor corresponded to histological presence in at least 83% cases.[22] Using ICG as a contrast agent, mini- FLARE was used for intraoperative guidance of liver cancer resection.[23] [24]

Non-cancer surgeries: The FLARE™ system has also been used for surgical guidance in a variety of non-oncologic surgeries as well. Using ICG as contrast agent, the ability to visualize vasculature in real time was used for identification of perforator flap location and size, and flap perfusion in breast reconstructive surgeries.[25, 26] According to the authors, FLARE™ provided advantages over conventional ICG angiography methods as it provides better resolution, easier real time assessment of flap perfusion, simultaneous color + NIR acquisition, and avoids laser excitation. Using MB for contrast in patients undergoing lower abdominal surgeries, the ureters could be visualized in order to avoid the commonly encountered iatrogenic ureteral injury. This method can provide an alternative to current investigational methods using radioactivity, however, application of MB limited to patients with uncompromised renal function.[27] In a similar approach, ICG contrast was used with the mini-FLARE system for NIR cholangiography and it was demonstrated that a long interval between administration of contrast agent and the surgical procedure could minimize background fluorescence from the liver.[28]

In a recent pre-clinical study, the Frangioni group utilized the dual channel of the FLARE™ system image guidance during pancreatic surgery with pancreas specific 700 nm emitting fluorophores and 800 nm emitting fluorophores targeting blood vessel, kidney, lymph node and adrenal tissue. [29] Such studies, if and when they can be translated to humans, will be able to provide comprehensive image guidance in complex surgeries for fairer outcome and minimal risk of collateral tissue injury.

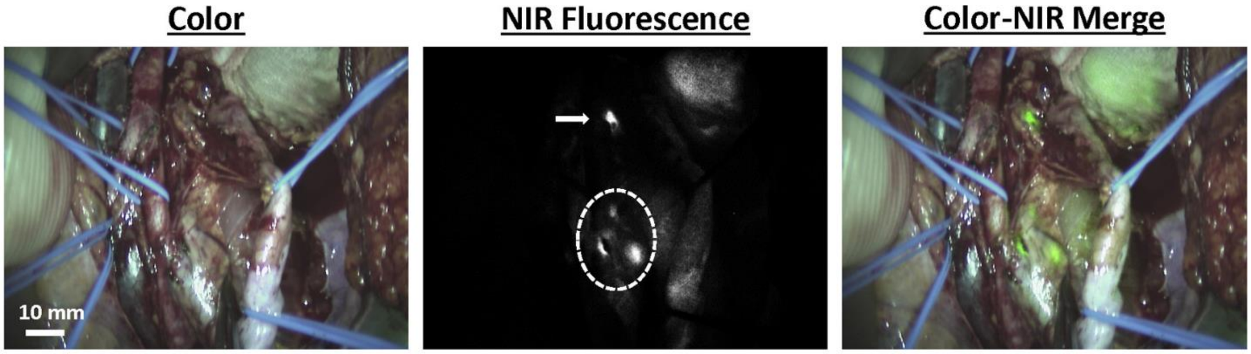

Figure 11: Mini-FLARE guided intraoperative NIR fluorescence imaging of primary and metastatic paragangliomas. Intraoperative NIR fluorescence imaging of the surgical field shows a bright, patchy fluorescent signal was identified at the location of the tumor (dashed circle). A second, small, lesion located approximately 5 cm cranial to the main lesion, was also identified using NIR fluorescence imaging (arrow). Reproduced with permission.[20]

2.3.4 Fluobeam

Principle

The Fluobeam is a handheld intraoperative camera system marketed by Fluoptics, Grenoble, France[30] (Fig. 12).

Figure 12: The Fluobeam preclinical system.

Hardware

The Fluobeam consists of a handheld camera head that can also be fixed on an extended arm for fixed imaging in both pre-clinical and clinical settings[30]. Excitation is provided by 100 mW, 690 nm continuous wave laser, passing through a diffuser to provide 2.6 mW/cm^2 of homogenous (> 30% field homogeneity) to an area of 6-8 cm in diameter. White light is provided co-axially passing through a bandpass filter (350 – 650 nm) to provide 7 X 10^3 of irradiance. The emitted fluorescence passes through a 700 nm longpass filter and imaged using a 12-bit CCD camera using a fixed focus lens, with exposure times in the 1 to 1,000 ms range. IT was found that exposures of 10- 20 ms provided tumor to background contrast. The spatial resolution was 0.17 mm/pixel. The system is operated by a desktop computer where the fluorescence is displayed in real-time.

Applications

The initial report evaluated the system in rat models of breast cancer and colorectal cancer for intraoperative image guidance[30]. The authors showed that Fluobeam allowed fluorescence-guided resection of primary mammary tumors with a tumor-to-background ratio of 2.34 at 10 ms camera exposure time. They also demonstrated utility in visualizing metastatic colorectal tumors in rats. However, use of cathepsin based probes led to high background signal in abdominal organs. The system was also evaluated for detection and visualization of peritoneal carcinomatosis in mice[31]. The system was able to detect all tumor nodules compared to only 50.6 % detect visually. It was also able to decrease surgery time from 19 minutes to 14 minutes. The smallest tumors nodules detected had as little as 227 tumor cells. Fluobeam was subsequently used to interrogate surgical margins in an orthotopic syngeneic rat model of primary breast cancer[32]. Real-time image guidance allowed complete resection of 17 tumors with minimal excision of healthy tissue. The tumor free margin ranged from 0.2 to 1.3 mm. Fluobeam also enabled identification of residual tumors in the surgical cavity. Fluobeam has also been used for intraoperative detection of colorectal metastasis in a syngeneic rat model[33]. The authors detected a two-fold higher NIR signal in colorectal metastasis compared to healthy liver tissue. The tumor-to-background ratio was independent of imaging time point when comparing 24 hr vs 48 hr post injection of ICG and thus allowed flexible surgical planning. Additionally the size of metastatic nodules correlated with the fluorescence intensity. Other studies have evaluated the Fluobeam for preclinical fluorescence imaging of peritoneal dissemination of ovarian carcinomas[34], and for imaging cancer in mice using quantum dot bioconjugates[35]. Fluobeam was shown to guide complete tumor resection and preserve more healthy tissue using fluorescence contrast from AngioStamp (marketed by Fluoptics) that targets αvβ3 integrins, in an orthotopic rat model of metastatic osteosarcoma[36]. Using methylene blue contrast Fluobeam was shown to be able to differentiate thyroid and parathyroid glands in rabbits[37]. Orthotopic glioblastoma in mice was successfully visualized and resected under guidance of Fluobeam, using novel alkylphosphocholine analogs CLR1501 and CLR11502 contrast[38].

Recently the Fluobeam system has been used for imaging the lymphatic system and sentinel lymph nodes in pigs[39] (Fig. 13). Using ICG fluorescence, Fluobeam was able to identify a mean of 2 lymphatic vessels and 1-2 sentinel lymph nodes in 20/20 lymph node stations in 5 pigs. This study demonstrated its potential for clinical translation in lymphatic reconstruction surgery and sentinel lymph node biopsy. It is being evaluated in several clinical trials listed in Table 4.

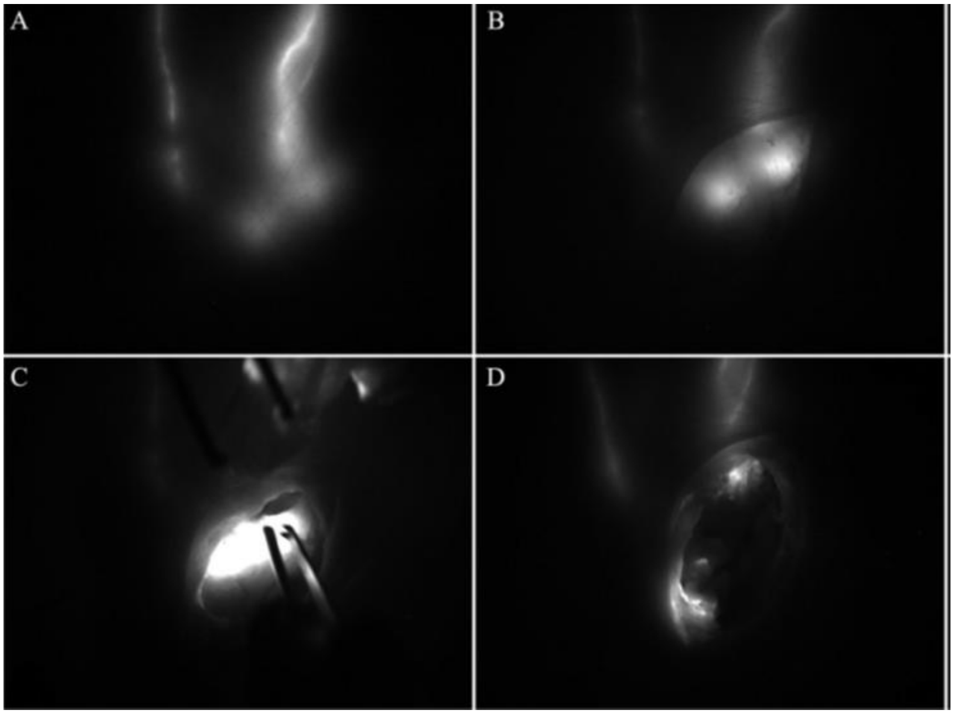

Figure 13: Fluobeam acquires planar fluorescence image after injection of ICG providing lymphatic imaging with guidance to the SLN: Local enrichment after ICG retention (A), after incision of the skin with clearer visualization of afferent vessels and the SLN (B), after dissection into a depth between 1.5- 2 cm and identification of 2 LNs with clear, high definition (C), and after excision, the afferent lymphatic vessels are still clearly visualized (D).

2.3.5 FluoSTIC

Principle

FluoSTIC is a handheld miniaturized near infrared image guidance system. (Fig. 14) It is optimized for use during oral cancer and intra cavital surgery and imaging where the features of interest are not easily acessible. It utilizes a novel miniature lipstick camera for image capture and cylindrical fiber array for white light and NIR illumination. It has comparable performance to large image guidance systems, while being extremely small (22 mm diameter, 200 mm height) and lightweight (< 200 g).

Figure 14: The Fluostick™, optical head and control box. Reproduced with permission.[41] Copyright 2015 Springer International Publishing.

Hardware

The initial prototype was developed in consultation with surgeons to impose a size limitation of 25 mm in diameter and < 250 mm in length[40]. Additionally the authors specified a goal of working distance > 100 mm and a field of view of 20 - 50 mm. The prototype used an off-the shelf 17 mm diameter “lipstick” camera with cylindrical geometry, with 1/3 rd inch monochrome CCD sensors, 656 X 494 pixel resolution with maximum 120 fps and 10 bits of dynamic range. A 15-mm focal objective lens adjusted for F/2.0 was used for achieving high depth of field. NIR illumination was provided by a SMA-coupled 500 mW 740- nm laser diode and white light was provided by a SMA-coupled 7 mW cold white LED. Both NIR and whitle light was combined using a custom coupler consisting of NIR and white light filters, three collimating lenses, a dichroic mirror and a diffuser to ensure a homogenous illumination. The combined NIR-white light was delivered to a custom multifiber bundle. The multifiber bundle composed of 19 fiber bundles composed of individual 300 µm, 0.37 NA fibers spaced equally on a three 1.5 mm thick

17 mm inner diameter brass rings. The bottom ring controls the exit angle of the fibers and an exit angle of 3 degrees was found to provide maximum illumination field flatness. The lipstick camera is secured inside of the hollow brass rings of the multifiber system. Emitted fluorescence was collected from 772 to 857 nm. This scheme while using sub-optimal excitation for ICG, allowed a wider collection band that could accommodate larger number of fluorophores and was shown to have comparable performance to typical illumination and filtration schemes.

The assembled FLuoSTIC system measured 22 mm in diameter, 200 mm in length and weighed 180 g. It has a field of view of 30 – 40 mm at a working distance of 126 mm and delivers 8 mW/cm^2 of NIR excitation and 1000 lux of white light. The system resolution is 70 µm and a depth of field of 20 mm. The camera exposure time is adjustable from 32.5 µs to 2 s and custom Labview software was used for image capture and storage functions.

Applications

FluoSTIC was validated in vivo in preclinical image guided resection of positive tumor nodules in the peritoneal cavity in mice[40]. Positive nodules could be easily visualized by FluoSTIC and excised during surgery. It was eventually commercialized by Fluoptics, France under the trade name of FluoStick Clinical System. This system directly houses the laser and LED and camera in the handheld unit that has an oblong cross section providing better performance and ergonomics[41] (Fig. 15). The FluoStick Clinical System was used in an orthotopic mouse model of head and neck squamous cell carcinoma to guide resection during survival surgery[42]. It was shown that FluoStick enabled fluorescence guided surgery increased the disease free survival by 50% by detecting fluorescent cancer residues as small as 185 µm, which were not otherwise detected visually. The FluoStick Clinical System is currently being evaluated for ex vivo visualization of colorectal peritoneal carcinomatosis in human patients[41]. Tissue excised by conventional surgery was examined by the system to visualize NIR fluorescence to delineate the periphery of the peritoneal metastasis. Fluostick was also recently used for ex vivo visualization of metastatic hepatic tumors using ICG fluorescence[43]. Fluostick enabled identification of tumors with positive margins that would have been missed by standard of care ultrasound.

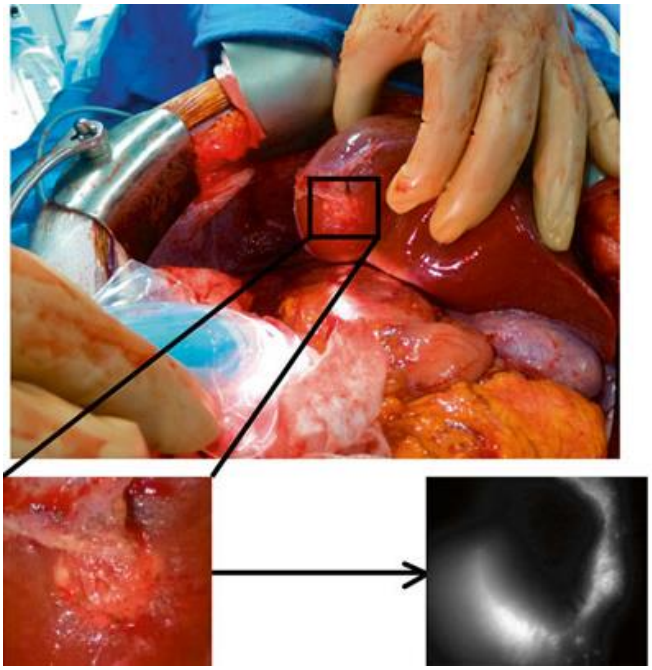

Figure 15: Fluostick™ assisted surgery of hepatic metastasis of adenocarcinoma of the left colon. The circumference of the metastasis is made fluorescent through the injection of ICG. Reproduced with permission.[41] Copyright 2015 Springer International Publishing.

2.3.6 VELscope

Principle

VELscope is a handheld device for visualization of autofluorescence in oral cancer patients. (Fig. 16) It was developed in close collaboration of imaging scientists and dental surgeons. VELscope allows coaxial illumination and visualization of autofluorescence directly by the user in a handheld format. It was designed for easy usability and intuitive operation for facilitating intraoperative surgical guidance and regular screening of patients for early detection of oral cancer.

Figure 16: VelScope VX enhanced oral system.

Hardware

The initial device design consisted of a bench-top light source coupled to a handheld unit for direct user visualization[44]. The light source consisted of a 120-W metal halide arc lamp with an integral elliptical reflector optimized for near-UV/blue light output. The excitation light was coupled with user defined power input to a 0.59 numerical aperture, 3 mm diameter liquid light guide that delivers it to the handheld unit. The excitation light passes through a 2 lens system (f = 25 mm) which nearly collimates it and projects on to the tissue through a 425/60 nm bandpass excitation filter. A dichroic mirror allows co-axial excitation and emission pathway. The emitted fluorescence is sent through a 475 nm longpass filter and a notch filter that divides the emitted fluorescence into red and green components. This instrument has since then been commercialized. The most recent version called VELscope Vx has battery powered blue light source integrated into the handheld unit.

Applications

VELscope has been used for guiding surgical resection in oral cancer patients and routine patient screening. In the pilot study with 44 oral cancer patients, the device achieved a sensitivity of 98% and specificity of 100% in discriminating normal mucosa from severe dysplasia/carcinoma in situ or invasive carcinoma[44]. It was also shown that the device was able to detect clinically occult lesions in patients during longitudinal follow-up, that were not otherwise detected using conventional white-light examination[45] (Fig. 17). This highlighted the ability of the device to sensitively indicate the occurrence of high-risk changes in patients. Based on these initial studies the device was used to guide surgical resection in the operating in 20 consecutive patients with early stage oral cancer[46]. The authors first visually marked the margin for clinically apparent tumor followed by marking of the loss of autofluorescence areas. Autofluorescence based surgical margins went beyond the clinical margins in 19/20 cases and extended from 4 to 25 mm beyond the clinically defined margin. Biopsies from these areas defined by fluorescence by outside of the clinical margin showed that they were either cancerous, low grade dysplasia or precancerous tissue at high-risk of becoming cancerous due to high-risk molecular clones and loss of heterozygosity.

These studies indicated the applicability of using autofluorescence visualization as a tool for patient diagnosis, surgical guidance and treatment follow-up. VELscope was approved for usage by FDA and Health Candae in 2008 and since then has been widely used by dentists for screening patients for oral cancer and high risk precancerous tissue or low-grade dysplasia. VELscope mediated autofluorescence guidance for surgical resection is currently being evaluated in the ongoing Candian Optically-guided approach for Oral Lesions Surgical (COOLS) trial[47]. It is a randomized 9-cenetr trial that aims to recruit 400 patients with severe dysplasia or carcinoma in situ (n = 160) and invasive squamous cell carcinoma (n = 240) and randomly divide them into fluorescence-guided and visual surgery. The primary endpoints are to evaluate recurrence at or within 1 cm of the surgery site and evaluation of further treatment due to presence of severe dysplasia or higher degree of change at the follow-up. The latest study update shows that it has reached close to its patient accrual targets and is beginning to get patients at the primary endpoints[48]. While final analysis remains pending, this trial has already led to the building of the first pan Canadian surgical network for oral cancer control. Velscope is widely used in the clinic today and many studies have evaluated its efficacy. In a prospective randomized trial, Velscope was found to have higher detection sensitivity for detection of oral cancer[49]. In a single blinded clinical evaluation, Velscope was shown to have higher detection sensitivity for oral premalignant lesions[50]. It was also found to be suitable as tool to visualize necrotic areas of the bone in patients with bisphosphate related osteonecrosis of the jaw[51].

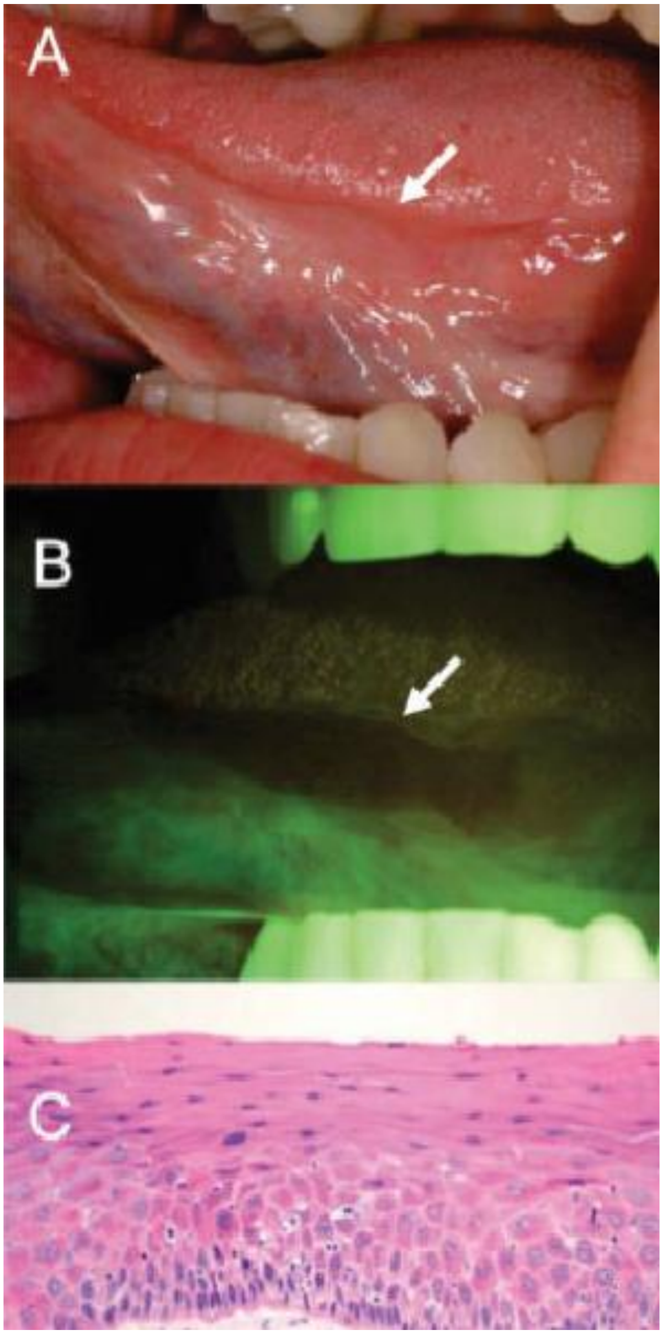

Figure 17: Velscope device guided detection of occult disease enhanced oral system. (A) White light image showing occult lesion (B) identification by fluorescence image (C) corresponding histology showing moderate dysplasia. Reproduced with permission.[45] Copyright 2007 John Wiley & Sons Inc.

2.4 Minimally invasive surgical guidance systems

Table 5: Minimally invasive surgical guidance systems.

System	Description	Clinical Application	Approval
Novadaq PINPOINT	Handheld/standalone NIR/blue fluorescence and WL laparoscopic imaging	Low anterior resection (NCT02205307), Left anterior resection (NCT01560377), Colorectal surgery (NCT02459405), Biliary and hepatic (NCT02070068), SLNM in oral cancer (NCT02478138) SLNM in cervical cancer (NCT02209532), Bowel perfusion.	Yes?
HRME	Handheld visible fluorescence imaging. High resolution optical biopsy.	Esophageal cancer (NCT01384708, NCT02018367, NCT02029937), Digestive track (NCT01321892), Head & neck cancer (NCT01456143), Oral cancer (NCT01269190), Gastric cancer (NCT02207959), Barret's esophagus (NCT01694511), Bladder cancer (NCT02340650), Cervical cancer (NCT02714439, NCT02494310, NCT02206048, NCT02420665), Liver cancer, pancreatic cancer, colorectal polyps	?

2.4.1 Novadac PINPOINT endoscopic fluorescence imaging system

Principle

The Novadaq PINPOINT is a commercially available high definition video laproscopy system that combines conventional white light laparoscopy with near-infrared fluorescence imaging using indocyaninegreen (ICG). (Fig. 18)

Figure 18: The Novadaq PINPOINT system. Reproduced with permission.[52] Copyright 2015 ACPGBI.

Hardware

The technical description of the system has been published earlier.[52] Here we have provided a summary of the same. The system's basic hardware is that of a laparoscope**.** The camera sensor used is sensitive to both NIR and visible light. Additionally, the optics are coated with an anti-reflective material in order to be able to transmit both visible and NIR light. Reflected NIR signal is rejected by using a filter before forming the image. The camera produces high resolution and smooth video by projecting the true high-definition signal at a 1080p frame rate (60 Hz). Both white light and NIR images can be overlaid for viewing or toggled as needed. The camera is made user-friendly by equipping with a series of switches which can be activated by the user's thumb to control several functions such as the power focus of the camera. The camera can be very easily attached to the laparoscope by inserting the eyepiece into the springloaded coupler at the camera's front and detached by applying a short rotation to the thumb lever of the coupling ring on the camera. The system parts are sealed in the portable PINPOINT camera housing and thus are protected from contamination and damage during use.

Applications

The laparoscopic capability of PINPOINT enable its applications for image guidance in many minimally invasive procedures where open surgical systems may not be used. It has been used extensively in human studies to evaluate tissue perfusion with the help of ICG fluorescence. It was initially used in an ethics review board approved study to evaluate colorectal anastomotic perfusion in 20 patients undergoing low anterior resection. The authors hypothesized an NIR image guidance system which has been useful in evaluation tissue perfusion in other surgical situations could also be applied here. [53] The PINPOINT system which is designed for laparoscopy was modified for transanal use by using a custom built introducer. It produced high resolution overlaid angiographic image in real time that helped the surgeon to distinguish between normal and abnormal angiograms, and the course of treatment thereafter. However, at this time the data was not quantitative but subjective, and hence it limited any conclusions on the predictive value for an abnormal angiogram. In a similar study, this system was for visualizing tissue perfusion in a laparoscopic colorectal surgery of 30 patients.[54] In another study, the application was extended for evaluating bowel perfusion patients with the emergency situations of mesenteric ischemia.[55] (Fig. 19)The system proved to be easy to handle, fast, and produced angiographic images showing perfusion in tissue which helped surgeons to recover them. The subjective evaluation of NIR fluorescence signal, however, again was a limitation of this study. In a recent case report, the system was used for image guidance to prevent liver and bile duct injury during laparoscopic cholecystectomy in one patient.

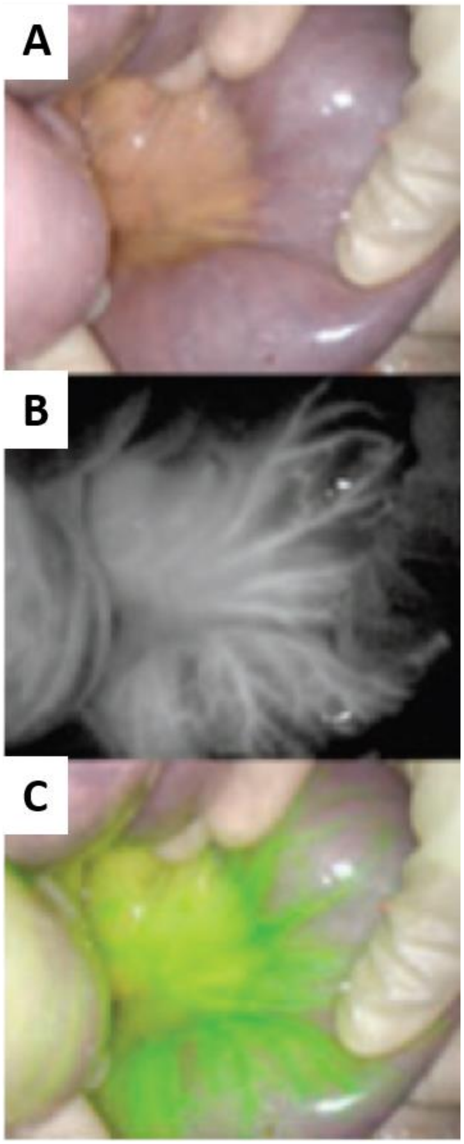

Figure 19: Novadaq PINPOINT provide image guidance to detect perfusion in macroscopically critical segments by which the segments could be preserved in a case of mesenteric ishemia. (A) White light image (B) NIR fluorescence signal (C) Overlay image. Reproduced with permission.[55] Copyright 2015 ACPGBI.

2.4.2 High-resolution microendoscopy (HRME)

Principle

HRME is a low-cost optical biopsy technique with sub-cellular resolution. This compact, robust, and inexpensive system is based around wide-field LED illumination, a flexible 1 mm diameter fiber-optic bundle, and a color CCD camera (Fig 20). It allows for subcellular imaging at 1000x magnification at 4 micrometer resolution. Use of wide-field imaging through a coherent fiber bundle eliminates all scanning requirements. Due to use of LED illumination and CCD imaging, this system is both simple to implement and robust in use. Low-cost (<$2000) and low learning curve makes HRME an effective complementary imaging tool to white-light endoscopy.

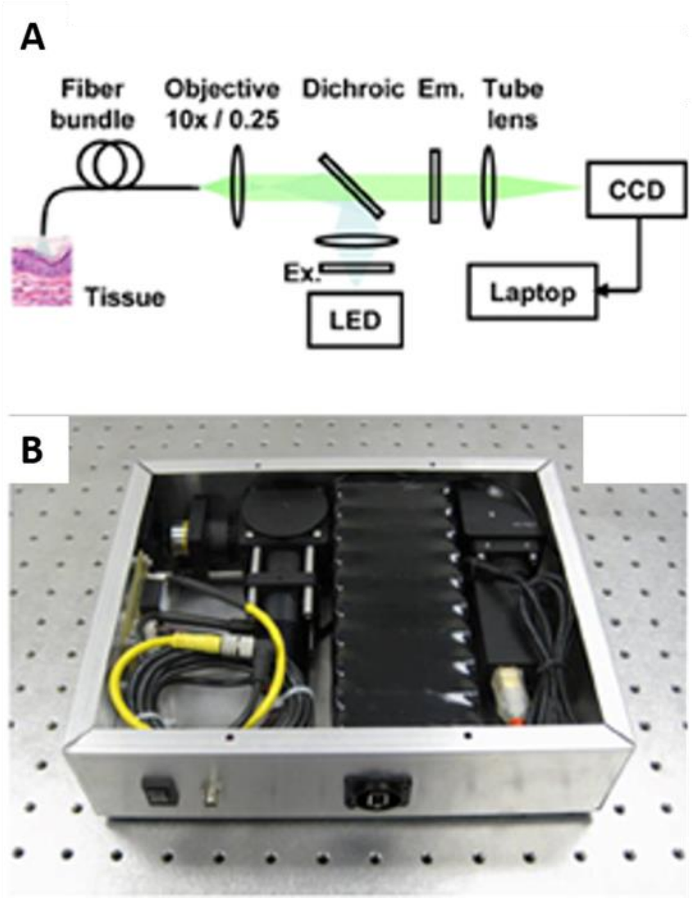

Figure 20: (A) Schematic diagram of the high-resolution microendoscope. (B) Photograph of the system, packaged in a 10" x 8" x 2.5" enclosure. Reproduced with permission.[59]

Hardware

The HRME device was first reported by Muldoon et al[56] and is also described subsequently[57]. It primarily consists of a light source, a fiber-optic bundle, a microscope objective lens, and a CCD camera. The excitation light is provided by a LED light source (455 nm, 20 nm FWHM) and is directed via a collimator, an infinity corrected objective lens (10x/0.25 NA) and a 475 nm cut-off dichroic mirror to the proximal end of a flexible fiber-optic bundle (3 m long, 30,000 individual fibers). The fiber bundle coherently transfers the excitation light to the distal end which is in direct contact with the sample, delivering 1 mW excitation power and can be easily passed through the biopsy port of a standard endoscope. The emitted fluorescence is collected by the same fiber and transmitted through the dichroic mirror and imaged onto a CCD camera by a magnifying tube lens. The tube lens magnification was chosen to optimize between requirements of sampling individual fibers with a sufficient number of pixels at the CCD and confining the magnified image of the bundle to the area of the CCD array. The CCD camera used a Bayer mask for color imaging and was digitized at 8-bit resolution. The field of view of the system was determined by the diameter of the active area of the fiber bundle and was reported as 750 microns. The spatial resolution of the system was determined by the spacing of the individual fibers and the system used a fiber bundle with individual fiber core size of 2.2 µm, and a center-to-center spacing of <4 µm, achieving a spatial resolution of 4.4 µm. The total cost of the fiber microendoscopy system was $2500 using a standard CCD camera, and $11,000 using a scientific-grade unit.

Applications

The HRME prototype was initially used to access subcutaneous tumors in an *in vivo* murine model, allowing direct comparison of microendoscopy images with macroscopic images and histopathology[56]. A surgically resected tissue specimen from the human oral cavity was imaged across the clinical margin, demonstrating qualitative and quantitative distinction between normal and cancerous tissue based on sub-cellular image features. Finally, the fiber-optic microendoscope was used on topically-stained normal human oral mucosa *in vivo*, resolving epithelial cell nuclei and membranes in real-time fluorescence images.

It was then used for high-resolution imaging of Barret's esophagus and compared with pathologic findings[57]. A quantitative image analysis criteria was developed to identify neoplastic lesions in patients with Barret's esophagus[58]. In situ cellular imaging was also demonstrated[59]. Its feasibility for use in the clinic for Barrett's esophagus was demonstrated[60]. It used in liver and pancreatic cancer[61]. A classficication system was developed for colorectal polyps[62]. The accuracy and interrater reliability for Barret's esophagus was evaluated[63]. The accuracy of in vivo diagnosis of colorectal polyps was reported[64] (Fig. 21). It has also been evaluated for a variety of other applications such as imaging of the inner ear cholesteatoma[65], and diagnosis of esophageal squamous cell carcinoma[66], and has had consistently good performance in evaluation of various diseases[67].

Other similar systems are the Karl Stroz fluorescence endoscopes.[68]

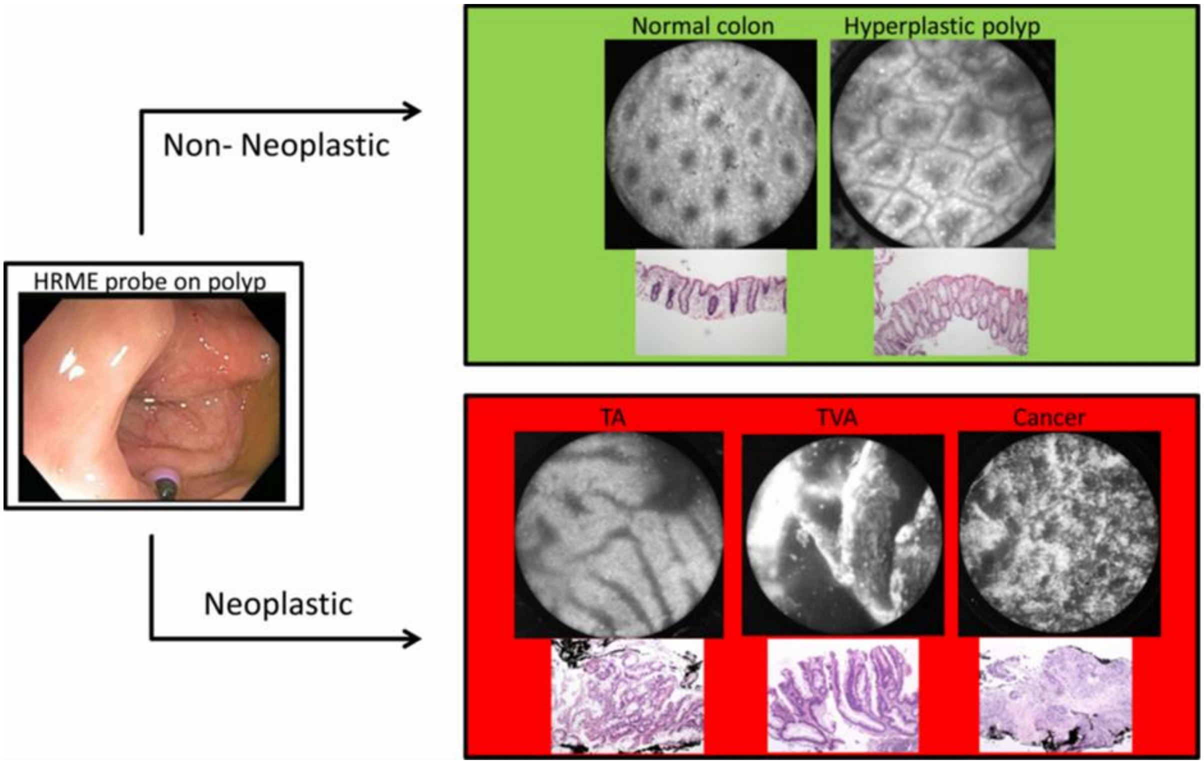

Figure 21: HRME classification of tissue at various stages of pathological development. Reproduced with permission.[64] Copyright 2014 Nature Publishing Group.

2.5 Spectroscopic and diagnostic imaging systems

Table 6: Spectroscopic and Diagnostic Imaging systems.

System	Description	Clinical Application	Approval
Dermainspect	Standalone autofluorescence and WL imaging	Skin cancer, dermatological disorders, ageing, leg ulcers, ocular tissue.	?
SpectroPen	Handheld NIR fluorescence and Raman spectral imaging	Ex vivo evaluation of lung cancer (NCT02280954)	No
SD OCT	Handheld OCT imaging	Macular degeneration (NCT00734487), Intraocular surgery (NCT01588041), retinal development in premature babies	FDA CE?

2.5.1 SpectroPen

Principle

The SpectroPen connects a hand-held sampling head, via a fiber optic cable, to a spectrometer that can record fluorescence and Raman signals[69] (Fig. 22). The ability to resolve NIR fluorescent and Raman signals from background tissue arises from the optical filtering that takes place in the hand-held portion of the SpectroPen. The laser light is transmitted through the excitation fiber into the pen. A first lens collimates the excitation light. Wavelength selectivity is provided by a band pass filter. Excitation light is then focused onto the sample of interest. Back scattered light is collected through the same lens. A dichroic mirror and a long pass filter attenuate Rayleigh scattering by a factor of 10^8 in the collection fiber. Thus, only Stokes-shifted light is transmitted to the spectrometer. Silica Raman bands arising from the optical fibers are attenuated by physical filtering in both the excitation and emission optical paths. The device's overall performance was evaluated by comparing the polystyrene Raman spectra obtained with the SpectroPen and a standard Raman spectrometer. The results show well matched Raman signals between the two spectrometers and also with the literature spectra of polystyrene. The differences in peak positions (wavenumbers) are less than 0.5% across the entire range of 200–2000 cm^{-1}. In general, the SpectroPen system performs as well as the standard Raman spectrometer as judged by signal-to-noise ratio, resolution, and wavelength accuracy.

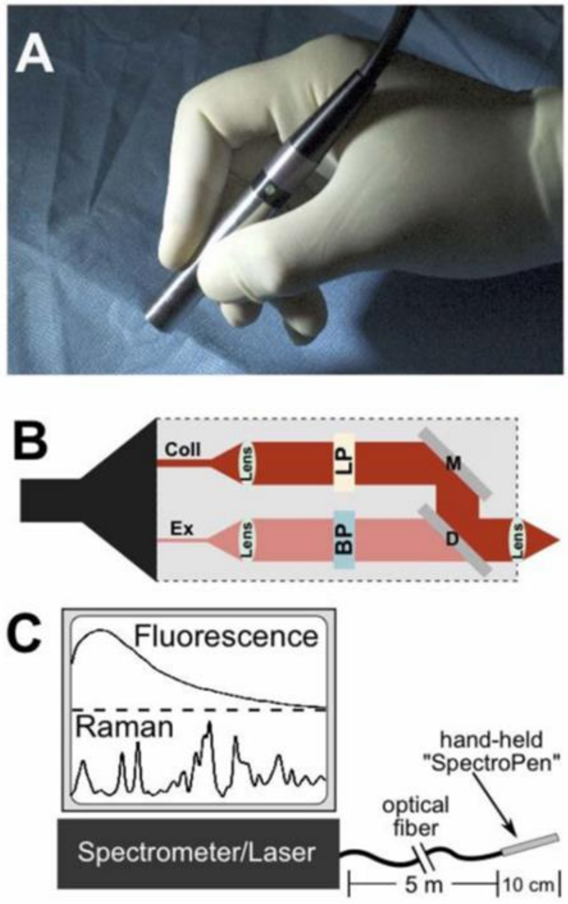

Figure 22: (A) Photograph showing the SpectroPen held in the operator's hand in a surgical setting. (B) Optical beam paths of the SpectroPen. Ex = excitation fiber, Coll = collection fiber, BP = band pass filter, LP = long pass filter, D = dichroic filter, M = reflective mirror. (C) Schematic diagram of the complete system for wavelength-resolved fluorescence and Raman measurements. Reproduced with permission.[69] Copyright 2014 ACS Publications.

Hardware

A RamanProbe™ sampling head and connecting fiber optics were purchased from InPhotonics (Norwood, MA). The cylindrical stainless steel sampling head (diameter = 1.3 mm, length = 10 cm) was integrated with a 5 m two-fiber cable, one for laser excitation and the other for light collection. The sampling head and fiber cable were coupled via an FC connector to a spectrometer designed by Delta Nu (Laramie, WY). The combined sampling head and spectrometer system has a wavelength range of 800–930 nm with 0.6 nm spectral resolution for fluorescence measurement, and a Raman shift range of 200–2000 cm^{-1} with 8 cm^{-1}resolution for Raman measurement. Laser excitation was provided by a continuous-wave 200 mW diode laser emitting at 785 nm.

Applications

The SpectroPen allows sensitive detection of both fluorescent and SERS contrast agents. A linear relationship is found between the recorded signal intensity and contrast agent concentration. The minimum spectrally resolvable concentrations (that is, limits of detection) are $2–5 \times 10^{-11}$ M for ICG and $0.5–1 \times 10^{-13}$ M for the SERS agent. For both fluorescence and Raman measurements, the SpectroPen provides a 50–60 fold dynamic range. This finding has significance because weak tumor-margin signals that are 50–60 fold lower than the central tumor signals can be measured simultaneously without adjusting the data acquisition parameters. The background signal of fat can be accurately subtracted, allowing nearly pure ICG contrast signals. The background Raman spectrum can be subtracted to reveal predominantly the SERS contrast signals. SpectroPen can detect sub-surface signal. Recently the spectroPen was used for ex vivo evaluation of resected tissue from lung cancer patients in order to detect pulmonary nodules[70] (Fig. 23). It was compared with two other imaging instruments and its performance was found to be better than or as good as these instruments in quantifying the fluorescence information and predicting presence of cancer.

Figure 23: Photograph of bisected nodule from human adenocarcinoma patient. Reproduced with permission.[70]

2.5.2 Dermainspect/MPTflex

Principle

The DermaInspect system is a CE-certified class 1 device that can perform non-invasive *in vivo* multiphoton tomography of the human skin with capability of submicron spatial resolution and 250-ps temporal resolution[71] (Fig. 24). The system use multiphoton excitation for obtaining auto fluorescence or second harmonic generation signals of endogenous fluorophores in skin such as melanin, NAD(P)H, flavins, porphyrins, elastins, collagens. Molecular and structural information from these images are used to detect abnormalities of pathological importance. Non-invasive optical biopsies give this device advantages of being painless, allowing examination under in situ conditions, rapid diagnosis, and possibility of longitudinal studies on the same region of interest.

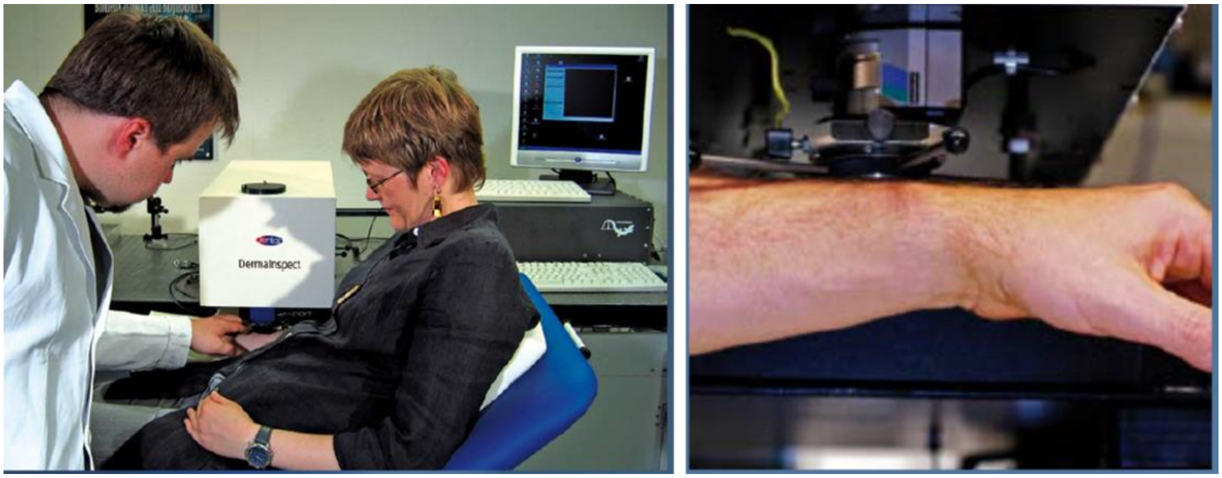

Figure 24: Dermainspect device in action. Reproduced with permission from ref 76. Copyright 2013 John Wiley & Sons Inc.

Hardware

The system hardware has been described in the publications and on the product website.[71-73] (Fig. 24). The excitation source consists of a compact, turn-key tunable (750 nm-850 mm) femtosecond NIR Ti:sapphire laser. The scanning module consists of a computer controlled motorized beam attenuator and a shutter, a fast x-,y- galvoscanner and of piezo driven optical parts and a trigger for the TCSPC module. Signal detection is performed PMT detectors with short rise time. Bandpass filters have been used when needed for separating signals. The system is controlled by a control module containing all power supplied and a single photon counting board, and the signal/image processing hardware and software. The basic DermaInspect system can be upgraded with the additional hardware in order to be able to perform fluorescence lifetime imaging and spectral imaging and provide 4-D and 5-D data.

Applications

The DermaInspect system was majorly developed for the diagnosis of skin cancer, particularly melanoma and other dermatological disorders; for wound healing and skin ageing research as well as quantification of uptake of drug molecules useful for monitoring of treatment response. The combined fluorescence lifetime imaging provides additional information in many such studies. The system was first assessed in 2003 for multiphoton tomography of normal and dermatological disorder containing human skin biopsies at submicron spatial resolution and 250-ps temporal resolution.[72] The system also collected data from the skin on the forearm of two caucasians human volunteers. Single cells, extracellular materials such as keratin, sub cellular components such as NAD(P)H containing mitochondria's, as well as transitions between various tissue layers could be visualized from the auto fluorescence signals. Unlike histological methods to study dermal matrix composition, DermaInspect's capability to image the same in vivo was utilized to assess skin ageing in white European volunteers.[27] The authors mention that specific quantitative features such as ratio of dermal elastin to collagen content of can be evaluated by in the multiphoton tomography; and attribute differences form previously published data to external factors such as optical system properties and movement artifact. This in in turn calls for standardization of optical systems and analysis algorithms so as to enable comparison between data collected by different devices. In another study, compared to conventional biophysical measurements, DermaInspect was able to produce consistent information of skin matrix composition in various skin aging cases.[74] In a different approach, a miniaturized GRIN lens microendoscope was attached to the DermaInspect system for imaging the skin.[75] Although spatial resolution of this microendoscopic system was reduced due to lower numerical aperture, the miniaturization allowed visualization of the largely damaged skin regions with complex topography in chronic leg ulcers patients. Cellular NAD(P)H contents in the facial skin of young and old women were quantified using DermaInspect/MPTflex system, and statistically significant difference values were observed.[76] (Fig. 25)

DermaInspect has been used to study non-skin tissues as well, where its capability to extract valuable functional information from in vivo measurements has been utilized. In such a work, the potential of the system to extract quantitative functional information from ocular tissue was demonstrated by studying freshly excised ocular surface.[77] Collagen fibrils could be visualized with high spatial resolution as well as lifetime measurements allowed detection of various cell types such as nerve clusters, goblet cells and erythrocytes. This shows DermaInspect can be used for imaging cases where there is lack of tissue for biopsy and high chances of functional loss.

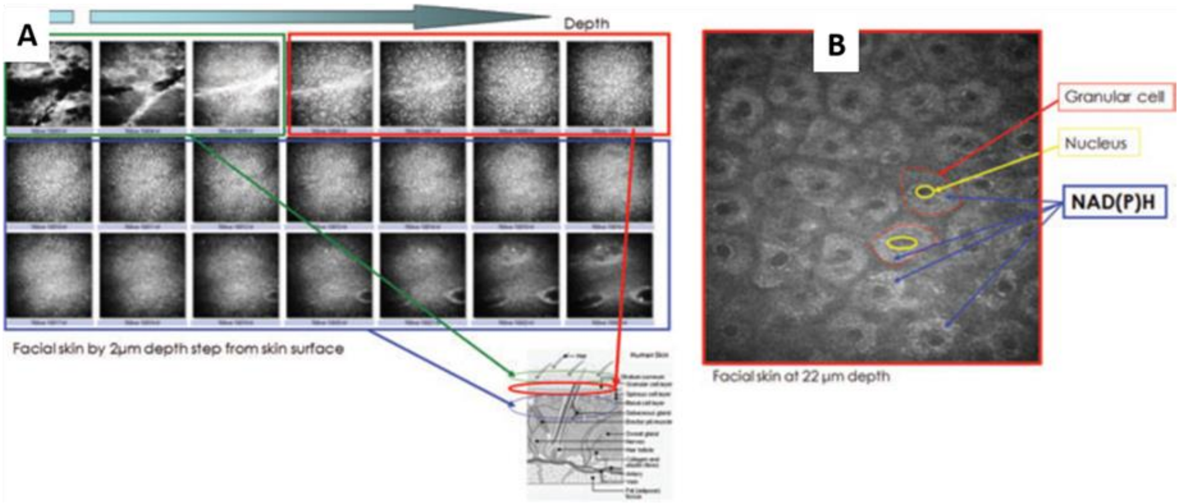

Figure 25: (A) In vivo two-photon autoflourescence images of different skin layers from the skin surface to the lower epidermal layer up to 42 μm in depth on the facial skin. The major fluorophores are keratin in the stratum corneum layer, NAD(P)H in the granular and spinosum layer, melanin in the lower epidermal and basal layer, and elastin in the dermis layer. (B) Two-photon autofluorescence image of the granular layer at a depth of 22 μm. The main fluorophore in this image is NAD(P)H. The shape of the granular cell and its nucleus can be observed by its contrast of fluorescence in the field of view. Reproduced with permission.[76] Copyright 2013 John Wiley & Sons Inc.

2.5.3 Handheld spectral domain OCT (SD OCT)

Principle

SD OCT allows is a fast, non-invasive, and non-contact method for imaging intraocular tissue. The limitation associated with a conventional SD-COT system which needs the patient in upright position has been addressed by developing a handheld OCT scanner. The handheld OCT scanner that enables for patients in supine position, for uncooperative pedriatic patients or patients with limited mobility.

Figure 26: (A) The Envisu C2300 system from Leica Microsystems. (B)The handheld OCT scanner.

Hardware

Here we have provided the description of Envisu C2300, the world's only FDA cleared handheld OCT system from Leica microsystems (who have started producing OCT systems after acquiring Bioptigen Inc. in 2015).[78] The system consists of a handheld OCT probe connected to the SD-OCT system by a flexible fiberoptic cable. (Fig. 26). The system uses 870 nm imaging wavelength for imaging and is capable of producing images with resolution upto 3 um. The handheld scanner can be available with various types of lenses for posterior and anterior imaging suiting various patient needs. For example, the high-resolution anterior lenses can produce images with 8 um lateral resolution whereas the general retina lens gives a 70 degree field of view with a working distance of 13 mm. These retinal and cornea lens can be switched quickly. The system can operated via the InVivoVue OCT management software. The whole system sits on a mobile cart. Foot pedal click through allows for hands free operation. Also this system can be mounted on a surgical microscope for steady, high quality live imaging. Further details can be found at the product website.[78] (Fig. 26)

Applications

Here, we have discussed some applications using the handheld SD OCT system from Bioptigen Inc. The development of this system was pioneered by Dr. Cynthia Toth at Duke University with a vision of employing a handheld scanner to address challenges associated with pediatric patients.[79] In a landmark study, the prototype was used for imaging and gather new insights into retinal development in premature babies with and without sedation.[80] (Fig. 27). Later, the system was improved for imaging children, neonates and children by incorporating calculated optical parameters from such subjects.[81] The system since has the Bioptigen system has been used for many imaging applications in such patients.[82-85] The Toth group also applied the handheld OCT for other application such as for intraoperative imaging during macular surgery, where the handheld probe could allow imaging in patents in supine position.[86]

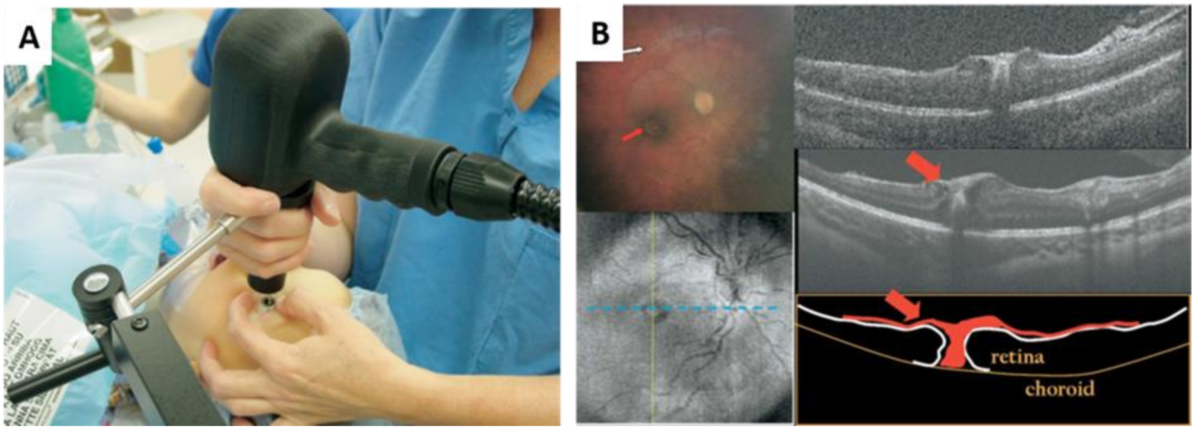

Figure 27: (A) Photograph showing the Bioptigen handheld clinical SD-OCT being used to image an infant eye under supine position and under endotracheal anesthesia. (B) Ret Cam photograph of a female infant with Shaken Baby syndrome (SBS) showing a hyperpigmented perifoveal ring (red arrow) and a white, elevated ring outside the major vascular arcades consistent with a perimacular fold. The (Bottom left) SVP, (Top right) enhanced B-scan, (Middle right) and registered-summed lateral repeated image are shown. The yellow line on the SVP marks the exact location of the enhanced B-scan (sweeping from inferior to superior), whereas the blue line represents the approximate location of the lateral repeated image (sweeping from temporal to nasal). These SD OCT images revealed a highly reflective stalk of tissue (probably chorioretinal fibrotic tissue; yellow arrow) centered within a full-thickness chronic macular hole. (Bottom right) Schematic representation. Reproduced with permission.[80] Copyright 2009 Elsevier Inc.

2.6 Barriers to clinical translation

Table 7: Clinical considerations.

Feature	Detail
Hardware	Real-time operation, non-disruptive, sensitive, user-friendly
Standardization	Camera performance, optical phantoms, detection sensitivity and specificity, signal quantification
Regulatory	PMA and 510(k), combination product
Clinical Trials	Trial outcome definition, disease and patient selection

2.6.1 Design Considerations

The hardware design needs to follow some considerations that we have previously discussed in more details[91]. These considerations include should focus on functionality and ease of integration in the surgical workflow. For surgical guidance systems real-time operation is critical. This translates to image capture, processing and display with >24 frames per second. Operating at less than real-time will lead to image breaks and perceptibly slower response times. Similarly, how the information is displayed has an impact on ease of usage, especially for open surgery guidance applications. If the information is displayed on a remote monitor, surgeons are forced to look away from the surgical bed, which can be distracting. A possible solution may to use head-mounted displays. However, this may not be a big issue in minimally invasive surgery where surgeons are trained to look at a remote monitor and operate while not looking directly at the surgical region of interest. In terms of ergonomics, a hands free design may be better compared to a handheld one, because that then frees the operating surgeon to use both hands for the surgery. Using a handheld system then would involve fixing it on stand or a member of the surgical team to hold it while the surgeon operates, which are non-ideal situations.

Diagnostic systems are not bound by the constraints of real-time operation and non-disruptive information display. However, both diagnostic as well as image guidance systems should have high sensitivity of detection as well as a compact design so that it may be easily integrated in the operating room or physician office. In addition if the system has a great learning curve, it may require a specialized operator, which can add cost. If any or a combination of these considerations are not met then it becomes difficult for a system to be readily integrated into clinical practice.

2.6.2 Standardization of imaging systems and imaging methods

Standard and widely accepted metrics are needed to compare the performance of imaging systems and the imaging method. A commonly used metric is detection sensitivity and specificity for diseased tissue. The gold standard used is often histology. However using histology as the gold standard provides its own unique challenges. It often suffers from sampling errors. Therefore a tissue extracted by say fluorescence signal detected in a large lump of tissue may be called negative by histology because the small cancerous part was not sampled by the histology. This can lead to false positives.

The threshold for a metric beyond which the tissue is considered diseased versus healthy should be ideally defined. For image guidance systems another key metric is tumor-to-background ratio. However the background must defined clearly. A widely accepted threshold is a TBR of 2 to designate cancerous versus healthy tissue. A better method may be to use a patient matched tissue sample as the normalization tissue such as skin or muscle. However these would depend on the system, contrast method and disease condition. However global thresholds like this may lead to ignoring of small tumor nodules that may have a small amount of contrast agent uptake, leading to lower detection sensitivity.

2.6.3 Regulatory approval

Optical imaging systems are usually considered low-risk devices. They must approved through a PMA use in humans. The 510(k) pathway allows approval if substantial equivalence can be demonstrated with a previously approved device through the PMA. Current practice for medical devices is to pair devices to contrast agents. This is known as combination product. People generally tend to specify pre-approved agents such as ICG as the conjugate contrast agent to potentially ease the approval process. Typically, if a device can successfully image a fluorophore, then it can be applied to any targeting agent linked to that fluorophore[87]. Similarly, if a device can successfully image a specific range of wavelengths, it can be used to image any fluorophore with excitation/emission spectrum that fall within that range. However, it is not clear that moving forward, if FDA will still require optical imaging systems to be paired with a specific contrast agent for the review and approval process. Furthermore, it remains unclear how industry will view an open format device approach compared to a combination device strategy. Our view is that it is best to consult FDA early in the application process to get necessary clarification as this is an evolving area.

Another approach used by researchers is to use a FDA cleared device with established installation base for clinical trials in order to expedite the approval process for a investigative application and or an use of an investigative contrast agent. However, this may be counter-productive if the device is not optimized for that particular imaging application and agent and may lead to falsely discouraging results. Additionally adapted devices may not match the ideal hardware and performance features for a particular application, such as detection sensitivity, ergonomics and ease of use etc.

2.6.4 Clinical Trial Design

Endpoints in clinical trials should be designed carefully keeping in mind the application and device being tested. For initial evaluation of an investigational device it may be beneficial to start with a small pilot study, focusing on proof-of-concept demonstration of the feasibility of using the device in the operating room. Typically no medical decision is made based on the device output in these trials and they are used for data collection and system evaluation. Pilot studies can accelerate the firs-in-human experience, data collection and clinical feedback from physicians who may become the end user for an investigational device. Usually, in these cases, a human approved contrast agent such as ICG is used. Our view is that these pilot studies have a better chance of getting IRB approval from an institution compared.

Pilot studies can be followed by a larger traditional clinical trial evaluating the safety and efficacy of the intervention based on the investigational device. For example, endpoints for surgical guidance systems may include evaluation of the efficacy of visualizing the diseased tissue versus the normal tissue enabled by the system under investigation as compared to standard of care surgery. Metrics to compare may be disease detection sensitivity and specificity, rate of tumor margin positivity or predictive values. These trials will typically need descriptive animal usage data with the system showing benefit of the intervention proposed. If medical decision is to be based on the device intervention, then it is our view that a pre-approved contrast agent be used for the trial, as it might have a better chance of being approved by the IRB. However, if investigators wish to use an investigational contrast agent, then an IND application is required. Typically a second pilot study is often done to evaluate the safety and disease-specific uptake of the investigational contrast agent, which is then imaged using the investigational device. However, no medical decisions are based on the imaging information and standard-of-care procedure is followed. Once this trail demonstrates the safety of the method and proof-of-concept of clinical usage, investigators can apply for a larger trial to base medical decision on the investigational imaging intervention.

2.7 Conclusions

Optical imaging is on the cusp of routine clinical usage due to its various advantages. However before its wide adoption in the clinic is possible, the issues relating to standardization of methods need to be resolved and better clinical trials showing clear benefits must be conducted.

2.8 References

1. N. Iftimia, D. X. Hammer and W. R. Brugge, in *Advances in Optical Imaging for Clinical Medicine*, John Wiley & Sons, Inc., 2011, DOI: 10.1002/9780470767061.ch1, pp. 1-10.
2. C. G. Hadjipanayis, H. Jiang, D. W. Roberts and L. Yang, *Seminars in oncology*, 2011, **38**, 109-118.
3. Q. M. Imaging, Quest Spectrum^{TM} Platform, http://www.quest-mi.com/spectrum-overview).
4. P. B. van Driel, M. van de Giessen, M. C. Boonstra, T. J. Snoeks, S. Keereweer, S. Oliveira, C. J. van de Velde, B. P. Lelieveldt, A. L. Vahrmeijer, C. W. Lowik and J. Dijkstra, *Molecular imaging and biology : MIB : the official publication of the Academy of Molecular Imaging*, 2015, **17**, 413-423.
5. M. S. Bradbury, E. Phillips, P. H. Montero, S. M. Cheal, H. Stambuk, J. C. Durack, C. T. Sofocleous, R. J. C. Meester, U. Wiesner and S. Patel, *Integr Biol-Uk*, 2013, **5**, 74-86.
6. M. S. K. C. Center, Artemis Imaging Technology: A New Standard of Care in the Operating Room?, https://www.mskcc.org/videos/artemis-imaging-technology-new-standard-care-operating-room).
7. Y. Liu, R. Njuguna, T. Matthews, W. J. Akers, G. P. Sudlow, S. Mondal, R. Tang, V. Gruev and S. Achilefu, *Journal of biomedical optics*, 2013, **18**, 101303.
8. S. B. Mondal, S. Gao, N. Zhu, G. P. Sudlow, K. Liang, A. Som, W. J. Akers, R. C. Fields, J. Margenthaler, R. Liang, V. Gruev and S. Achilefu, *Scientific reports*, 2015, **5**, 12117.
9. S. Gioux, H. S. Choi and J. V. Frangioni, *Mol Imaging*, 2010, **9**, 237-255.

10. S. L. Troyan, V. Kianzad, S. L. Gibbs-Strauss, S. Gioux, A. Matsui, R. Oketokoun, L. Ngo, A. Khamene, F. Azar and J. V. Frangioni, *Annals of surgical oncology*, 2009, **16**, 2943-2952.

11. F. P. Verbeek, S. L. Troyan, J. S. Mieog, G. J. Liefers, L. A. Moffitt, M. Rosenberg, J. Hirshfield-Bartek, S. Gioux, C. J. van de Velde, A. L. Vahrmeijer and J. V. Frangioni, *Breast cancer research and treatment*, 2014, **143**, 333-342.

12. M. Hutteman, J. S. D. Mieog, J. R. van der Vorst, G. J. Liefers, H. Putter, C. W. G. M. Lowik, J. V. Frangioni, C. J. H. van de Velde and A. L. Vahrmeijer, *Breast cancer research and treatment*, 2011, **127**, 163-170.

13. B. E. Schaafsma, F. P. R. Verbeek, D. D. D. Rietbergen, B. van der Hiel, J. R. van der Vorst, G. J. Liefers, J. V. Frangioni, C. J. H. van de Velde, F. W. B. van Leeuwen and A. L. Vahrmeijer, *Brit J Surg*, 2013, **100**, 1037-1044.

14. J. R. van der Vorst, M. Hutteman, K. N. Gaarenstroom, A. A. Peters, J. S. Mieog, B. E. Schaafsma, P. J. Kuppen, J. V. Frangioni, C. J. van de Velde and A. L. Vahrmeijer, *International journal of gynecological cancer : official journal of the International Gynecological Cancer Society*, 2011, **21**, 1472-1478.

15. M. Hutteman, J. R. van der Vorst, K. N. Gaarenstroom, A. A. Peters, J. S. Mieog, B. E. Schaafsma, C. W. Lowik, J. V. Frangioni, C. J. van de Velde and A. L. Vahrmeijer, *American journal of obstetrics and gynecology*, 2012, **206**, 89 e81-85.

16. B. E. Schaafsma, F. P. R. Verbeek, A. A. W. Peters, J. R. van der Vorst, C. D. de Kroon, M. I. E. van Poelgeest, J. B. M. Z. Trimbos, C. J. H. van de Velde, J. V. Frangioni, A. L. Vahrmeijer and K. N. Gaarenstroom, *Bjog-Int J Obstet Gy*, 2013, **120**, 758-764.

17. J. R. van der Vorst, B. E. Schaafsma, F. P. R. Verbeek, S. Keereweer, J. C. Jansen, L. A. van der Velden, A. P. M. Langeveld, M. Hutteman, C. W. G. M. Lowik, C. J. H. van de Velde, J. V. Frangioni and A. L. Vahrmeijer, *Oral Oncol*, 2013, **49**, 15-19.

18. D. M. Gilmore, O. V. Khullar, S. Gioux, A. Stockdale, J. V. Frangioni, Y. L. Colson and S. E. Russell, *Annals of surgical oncology*, 2013, **20**, 2357-2363.

19. F. P. R. Verbeek, S. L. Troyan, J. S. D. Mieog, G. J. Liefers, L. A. Moffitt, M. Rosenberg, J. Hirshfield-Bartek, S. Gioux, C. J. H. van de Velde, A. L. Vahrmeijer and J. V. Frangioni, *Breast cancer research and treatment*, 2014, **143**, 333-342.

20. Q. R. Tummers, M. C. Boonstra, J. V. Frangioni, C. J. van de Velde, A. L. Vahrmeijer and B. A. Bonsing, *International journal of surgery case reports*, 2015, **6C**, 150-153.

21. J. R. van der Vorst, A. L. Vahrmeijer, M. Hutteman, T. Bosse, V. T. Smit, C. J. van de Velde, J. V. Frangioni and B. A. Bonsing, *World journal of gastrointestinal surgery*, 2012, **4**, 180-184.

22. Q. R. Tummers, F. P. Verbeek, B. E. Schaafsma, M. C. Boonstra, J. R. van der Vorst, G. J. Liefers, C. J. van de Velde, J. V. Frangioni and A. L. Vahrmeijer, *European journal of surgical oncology : the journal of the European Society of Surgical Oncology and the British Association of Surgical Oncology*, 2014, **40**, 850-858.

23. J. R. van der Vorst, B. E. Schaafsma, M. Hutteman, F. P. Verbeek, G. J. Liefers, H. H. Hartgrink, V. T. Smit, C. W. Lowik, C. J. van de Velde, J. V. Frangioni and A. L. Vahrmeijer, *Cancer*, 2013, **119**, 3411-3418.

24. L. S. Boogerd, H. J. Handgraaf, H. D. Lam, A. E. Braat, A. G. Baranski, R. J. Swijnenburg, J. V. Frangioni, A. L. Vahrmeijer and J. Ringers, *Surgery*, 2016, DOI: 10.1016/j.surg.2015.11.024.

25. B. T. Lee, A. Matsui, M. Hutteman, S. J. Lin, J. H. Winer, R. G. Laurence and J. V. Frangioni, *J Reconstr Microsurg*, 2010, **26**, 59-65.

26. B. T. Lee, M. Hutteman, S. Gioux, A. Stockdale, S. J. Lin, L. H. Ngo and J. V. Frangioni, *Plast Reconstr Surg*, 2010, **126**, 1472-1481.

27. F. P. Verbeek, J. R. van der Vorst, B. E. Schaafsma, R. J. Swijnenburg, K. N. Gaarenstroom, H. W. Elzevier, C. J. van de Velde, J. V. Frangioni and A. L. Vahrmeijer, *The Journal of urology*, 2013, **190**, 574-579.

28. F. P. Verbeek, B. E. Schaafsma, Q. R. Tummers, J. R. van der Vorst, W. J. van der Made, C. I. Baeten, B. A. Bonsing, J. V. Frangioni, C. J. van de Velde, A. L. Vahrmeijer and R. J. Swijnenburg, *Surgical endoscopy*, 2014, **28**, 1076-1082.

29. H. Wada, H. Hyun, C. Vargas, J. Gravier, G. Park, S. Gioux, J. V. Frangioni, M. Henary and H. S. Choi, *Theranostics*, 2015, **5**, 1-11.

30. J. S. Mieog, A. L. Vahrmeijer, M. Hutteman, J. R. van der Vorst, M. Drijfhout van Hooff, J. Dijkstra, P. J. Kuppen, R. Keijzer, E. L. Kaijzel, I. Que, C. J. van de Velde and C. W. Lowik, *Mol Imaging*, 2010, **9**, 223-231.

31. M. Keramidas, V. Josserand, C. A. Righini, C. Wenk, C. Faure and J. L. Coll, *The British journal of surgery*, 2010, **97**, 737-743.

32. J. S. Mieog, M. Hutteman, J. R. van der Vorst, P. J. Kuppen, I. Que, J. Dijkstra, E. L. Kaijzel, F. Prins, C. W. Lowik, V. T. Smit, C. J. van de Velde and A. L. Vahrmeijer, *Breast cancer research and treatment*, 2011, **128**, 679-689.

33. M. Hutteman, J. S. Mieog, J. R. van der Vorst, J. Dijkstra, P. J. Kuppen, A. M. van der Laan, H. J. Tanke, E. L. Kaijzel, I. Que, C. J. van de Velde, C. W. Lowik and A. L.

Vahrmeijer, *European journal of surgical oncology : the journal of the European Society of Surgical Oncology and the British Association of Surgical Oncology*, 2011, **37**, 252-257.

34. E. Mery, E. Jouve, S. Guillermet, M. Bourgognon, M. Castells, M. Golzio, P. Rizo, J. P. Delord, D. Querleu and B. Couderc, *Gynecol Oncol*, 2011, **122**, 155-162.

35. Y. Li, Z. Li, X. Wang, F. Liu, Y. Cheng, B. Zhang and D. Shi, *Theranostics*, 2012, **2**, 769-776.

36. A. Dutour, V. Josserand, D. Jury, S. Guillermet, A. V. Decouvelaere, F. Chotel, T. Pointecouteau, P. Rizo, J. L. Coll and J. Y. Blay, *Bone*, 2014, **62**, 71-78.

37. R. Antakia, P. Gayet, S. Guillermet, T. J. Stephenson, N. J. Brown, B. J. Harrison and S. P. Balasubramanian, *Journal of Surgical Research*, 2014, **192**, 480-486.

38. K. I. Swanson, P. A. Clark, R. R. Zhang, I. K. Kandela, M. Farhoud, J. P. Weichert and J. S. Kuo, *Neurosurgery*, 2015, **76**, 115-124.

39. C. Hirche, H. Engel, L. Kolios, J. Cognie, M. Hunerbein, M. Lehnhardt and T. Kremer, *Surgical innovation*, 2013, **20**, 516-523.

40. S. Gioux, J. G. Coutard, M. Berger, H. Grateau, V. Josserand, M. Keramidas, C. Righini, J. L. Coll and J. M. Dinten, *Journal of biomedical optics*, 2012, **17**, 106014.

41. P. Dorval, I. Atallah, G. Barabino, M. Henry, M. Keramidas, F. Stenard, C. Milet, C. Righini, P. Rizo, S. Guillermet, V. Josserand and J.-L. Coll, in *Fluorescence Imaging for Surgeons*, eds. F. D. Dip, T. Ishizawa, N. Kokudo and R. J. Rosenthal, Springer International Publishing, 2015, DOI: 10.1007/978-3-319-15678-1_37, ch. 37, pp. 341-351.

42. I. Atallah, C. Milet, M. Henry, V. Josserand, E. Reyt, J. L. Coll, A. Hurbin and C. A. Righini, *Head & neck*, 2014, DOI: 10.1002/hed.23980.

43. G. Barabino, J. Porcheron, M. Cottier, M. Cuilleron, J.-G. Coutard, M. Berger, S. Molliex, B. Beauchesne, J. M. Phelip, A. Grichine and J.-L. Coll, *Surgical innovation*, 2015, DOI: 10.1177/1553350615618287.

44. P. M. Lane, T. Gilhuly, P. Whitehead, H. Zeng, C. F. Poh, S. Ng, P. M. Williams, L. Zhang, M. P. Rosin and C. E. MacAulay, *Journal of biomedical optics*, 2006, **11**, 024006.

45. C. F. Poh, S. P. Ng, P. M. Williams, L. Zhang, D. M. Laronde, P. Lane, C. MacAulay and M. P. Rosin, *Head & neck*, 2007, **29**, 71-76.

46. C. F. Poh, L. Zhang, D. W. Anderson, J. S. Durham, P. M. Williams, R. W. Priddy, K. W. Berean, S. Ng, O. L. Tseng, C. MacAulay and M. P. Rosin, *Clinical cancer research : an official journal of the American Association for Cancer Research*, 2006, **12**, 6716-6722.

47. C. F. Poh, J. S. Durham, P. M. Brasher, D. W. Anderson, K. W. Berean, C. E. MacAulay, J. J. Lee and M. P. Rosin, *BMC cancer*, 2011, **11**, 462.

48. C. F. Poh, J. S. Durham, D. W. Anderson and P. M. Brasher, *Oral Oncol*, 2013, **49, Supplement 1**, S43-S44.

49. M. Rana, A. Zapf, M. Kuehle, N. C. Gellrich and A. M. Eckardt, *European journal of cancer prevention : the official journal of the European Cancer Prevention Organisation*, 2012, **21**, 460-466.

50. H. Hanken, J. Kraatz, R. Smeets, M. Heiland, M. Blessmann, W. Eichhorn, T. S. Clauditz, A. Gröbe, A. Kolk and M. Rana, *Head & Face Medicine*, 2013, **9**, 23-23.

51. A. T. Assaf, T. A. Zrnc, B. Riecke, J. Wikner, J. Zustin, R. E. Friedrich, M. Heiland, R. Smeets and A. Gröbe, *Journal of Cranio-Maxillofacial Surgery*, 2014, **42**, e157-e164.

52. J. Fengler, *Colorectal disease : the official journal of the Association of Coloproctology of Great Britain and Ireland*, 2015, **17 Suppl 3**, 3-6.

53. D. A. Sherwinter, J. Gallagher and T. Donkar, *Colorectal disease : the official journal of the Association of Coloproctology of Great Britain and Ireland*, 2013, **15**, 91-96.

54. F. Ris, R. Hompes, C. Cunningham, I. Lindsey, R. Guy, O. Jones, B. George, R. A. Cahill and N. J. Mortensen, *Surgical endoscopy*, 2014, **28**, 2221-2226.

55. K. Nowak, F. Sandra-Petrescu, S. Post and K. Horisberger, *Colorectal disease : the official journal of the Association of Coloproctology of Great Britain and Ireland*, 2015, **17 Suppl 3**, 12-15.

56. T. J. Muldoon, M. C. Pierce, D. L. Nida, M. D. Williams, A. Gillenwater and R. Richards-Kortum, *Opt. Express*, 2007, **15**, 16413-16423.

57. T. J. Muldoon, S. Anandasabapathy, D. Maru and R. Richards-Kortum, *Gastrointestinal endoscopy*, 2008, **68**, 737-744.

58. T. J. Muldoon, N. Thekkek, D. Roblyer, D. Maru, N. Harpaz, J. Potack, S. Anandasabapathy and R. Richards-Kortum, *Journal of biomedical optics*, 2010, **15**, 026027.

59. M. Pierce, D. Yu and R. Richards-Kortum, *Journal of visualized experiments : JoVE*, 2011, DOI: 10.3791/2306.

60. M. C. Pierce, P. M. Vila, A. D. Polydorides, R. Richards-Kortum and S. Anandasabapathy, *The American journal of gastroenterology*, 2011, **106**, 1722-1724.

61. R. Regunathan, J. Woo, M. C. Pierce, A. D. Polydorides, M. Raoufi, S. Roayaie, M. Schwartz, D. Labow, D. Shin, R. Suzuki, M. S. Bhutani, L. G. Coghlan, R. Richards-Kortum, S. Anandasabapathy and M. K. Kim, *Gastrointestinal endoscopy*, 2012, **76**, 293-300.

62. S. S. Chang, R. Shukla, A. D. Polydorides, P. M. Vila, M. Lee, H. Han, P. Kedia, J. Lewis, S. Gonzalez, M. K. Kim, N. Harpaz, J. Godbold, R. Richards-Kortum and S. Anandasabapathy, *Endoscopy*, 2013, **45**, 553-559.

63. P. M. Vila, M. J. Kingsley, A. D. Polydorides, M. A. Protano, M. C. Pierce, J. Sauk, M. K. Kim, K. Patel, J. H. Godbold, J. D. Waye, R. Richards-Kortum and S. Anandasabapathy, *Diseases of the esophagus : official journal of the International Society for Diseases of the Esophagus / I.S.D.E*, 2014, **27**, 55-62.

64. N. D. Parikh, D. Perl, M. H. Lee, B. Shah, Y. Young, S. S. Chang, R. Shukla, A. D. Polydorides, E. Moshier, J. Godbold, E. Zhou, J. Mitcham, R. Richards-Kortum and S. Anandasabapathy, *The American journal of gastroenterology*, 2014, **109**, 68-75.

65. J. Bradley, N. Jiang, L. Levy, R. Richards-Kortum, A. Sikora and E. Smouha, *Otolaryngology -- Head and Neck Surgery*, 2014, **150**, 654-658.

66. D. Shin, M.-A. Protano, A. D. Polydorides, S. M. Dawsey, M. C. Pierce, M. K. Kim, R. A. Schwarz, T. Quang, N. Parikh, M. S. Bhutani, F. Zhang, G. Wang, L. Xue, X. Wang, H. Xu, S. Anandasabapathy and R. R. Richards-Kortum, *Clinical gastroenterology and hepatology : the official clinical practice journal of the American Gastroenterological Association*, 2015, **13**, 272-279.e272.

67. J. S. Louie, R. Richards-Kortum and S. Anandasabapathy, *Clinical gastroenterology and hepatology : the official clinical practice journal of the American Gastroenterological Association*, 2014, **12**, 1789-1792.

68. K. Storz, Fluorescence Imaging, https://www.karlstorz.com/au/en/fi.htm).

69. A. M. Mohs, M. C. Mancini, S. Singhal, J. M. Provenzale, B. Leyland-Jones, M. D. Wang and S. Nie, *Analytical Chemistry*, 2010, **82**, 9058-9065.

70. R. P. Judy, J. J. Keating, E. M. DeJesus, J. X. Jiang, O. T. Okusanya, S. Nie, D. E. Holt, S. P. Arlauckas, P. S. Low, E. J. Delikatny and S. Singhal, *Scientific reports*, 2015, **5**, 16208.

71. JenLab, *Journal*.

72. K. Konig and I. Riemann, *Journal of biomedical optics*, 2003, **8**, 432-439.

73. M. J. Koehler, K. Konig, P. Elsner, R. Buckle and M. Kaatz, *Optics letters*, 2006, **31**, 2879-2881.

74. M. J. Koehler, A. Preller, N. Kindler, P. Elsner, K. Konig, R. Buckle and M. Kaatz, *Skin research and technology : official journal of International Society for Bioengineering and the Skin*, 2009, **15**, 357-363.

75. K. Konig, A. Ehlers, I. Riemann, S. Schenkl, R. Buckle and M. Kaatz, *Microscopy research and technique*, 2007, **70**, 398-402.

76. K. Miyamoto and H. Kudoh, *The British journal of dermatology*, 2013, **169 Suppl 2**, 25-31.

77. P. Steven, M. Muller, N. Koop, C. Rose and G. Huttmann, *Journal of biomedical optics*, 2009, **14**.

78. L. Microsystems, OCT for Opthalmology Envisu C-Class, http://www.leica-microsystems.com/products/optical-coherence-tomography-oct/details/product/envisu-c-class/).

79. DukeTODAY.

80. A. W. Scott, S. Farsiu, L. B. Enyedi, D. K. Wallace and C. A. Toth, *American journal of ophthalmology*, 2009, **147**, 364-373 e362.

81. R. S. Maldonado, J. A. Izatt, N. Sarin, D. K. Wallace, S. Freedman, C. M. Cotten and C. A. Toth, *Investigative ophthalmology & visual science*, 2010, **51**, 2678-2685.

82. A. Y. Tong, M. El-Dairi, R. S. Maldonado, A. L. Rothman, E. L. Yuan, S. S. Stinnett, L. Kupper, C. M. Cotten, K. E. Gustafson, R. F. Goldstein, S. F. Freedman and C. A. Toth, *Ophthalmology*, 2014, **121**, 1818-1826.

83. M. T. Cabrera, R. V. O'Connell, C. A. Toth, R. S. Maldonado, T. V. Du, M. J. Allingham, S. J. Chiu, S. Farsiu, G. M. M. Panayotti, G. K. Swamy and S. F. Freedman, *Ophthal Surg Las Im*, 2013, **44**, 448-454.

84. M. T. Cabrera, R. S. Maldonado, C. A. Toth, R. V. O'Connell, B. B. Chen, S. J. Chiu, S. Farsiu, D. K. Wallace, S. S. Stinnett, G. M. M. Panayotti, G. K. Swamy and S. F. Freedman, *American journal of ophthalmology*, 2012, **153**, 167-175.

85. D. B. Rootman, E. Gonzalez, A. Mallipatna, C. Vandenhoven, L. Hampton, H. Dimaras, H. S. Chan, B. L. Gallie and E. Heon, *The British journal of ophthalmology*, 2013, **97**, 59-65.

86. P. N. Dayani, R. Maldonado, S. Farsiu and C. A. Toth, *Retina*, 2009, **29**, 1457-1468.

87. E. L. Rosenthal, J. M. Warram, E. de Boer, J. P. Basilion, M. A. Biel, M. Bogyo, M. Bouvet, B. E. Brigman, Y. L. Colson, S. R. DeMeester, G. C. Gurtner, T. Ishizawa, P. M. Jacobs, S. Keereweer, J. C. Liao, Q. T. Nguyen, J. Olson, K. D. Paulsen, D. Rieves, B. D. Sumer, M. F. Tweedle, A. L. Vahrmeijer, J. P. Weichert, B. C. Wilson, M. R. Zenn, K. R. Zinn and G. M. van Dam, *Journal of nuclear medicine : official publication, Society of Nuclear Medicine*, 2016, **57**, 144-150.

88. T. J. A. Snoeks, P. B. A. A. Driel, S. Keereweer, S. Aime, K. M. Brindle, G. M. Dam, C. W. G. M. Löwik, V. Ntziachristos and A. L. Vahrmeijer, *Molecular Imaging and Biology*, 2013, **16**, 147-151.

89. R. J. Nordstrom, *Current Molecular Imaging*, 2014, **3**, 129-143.

90. J. M. Warram, E. de Boer, L. S. Moore, C. E. Schmalbach, K. P. Withrow, W. R. Carroll, J. S. Richman, A. B. Morlandt, M. Brandwein-Gensler and E. L. Rosenthal, *Journal of Surgical Oncology*, 2015, **112**, 2-8.

91. S. B. Mondal, S. Gao, N. Zhu, R. Liang, V. Gruev and S. Achilefu, *Advances in cancer research*, 2014, **124**, 171-211.

92. J. S. Mieog, S. L. Troyan, M. Hutteman, K. J. Donohoe, J. R. van der Vorst, A. Stockdale, G. J. Liefers, H. S. Choi, S. L. Gibbs-Strauss, H. Putter, S. Gioux, P. J. Kuppen, Y. Ashitate, C. W. Lowik, V. T. Smit, R. Oketokoun, L. H. Ngo, C. J. van de Velde, J. V. Frangioni and A. L. Vahrmeijer, *Annals of surgical oncology*, 2011, **18**, 2483-2491.

Chapter 3: Goggle Augmented Imaging and Navigation System

This chapter is based on a published article: Suman B Mondal*, Shengkui Gao*, Nan Zhu*, Gail P Sudlow, Kexiang Liang, Avik Som, Walter J Akers, Ryan C Fields, Julie Margenthaler, Rongguang Liang, Viktor Gruev, Samuel Achilefu. Binocular Goggle Augmented Imaging and Navigation System provides real-time fluorescence image guidance for tumor resection and sentinel lymph node mapping. Sci. Rep. 5:12117 (2015). * These authors contributed equally. I developed the prototype in collaboration with Dr. Gruev, Dr. Gao, Dr. Liang and Dr. Achilefu, performed the characterization tests, animal studies and led efforts for clinical studies. I assisted the surgeons during the clinical procedures. I analyzed the data for characterization tests, animal studies and human studies and wrote the manuscript with inputs from co-authors.

3.1 Abstract

The inability to identify microscopic tumors and assess surgical margins in real-time during oncologic surgery leads to incomplete tumor removal, increases the chances of tumor recurrence, and necessitates costly repeat surgery. To overcome these challenges, we have developed a wearable goggle augmented imaging and navigation system (GAINS) that can provide accurate intraoperative visualization of tumors and sentinel lymph nodes in real-time without disrupting normal surgical workflow. GAINS projects both near-infrared fluorescence from tumors and the natural color images of tissue onto a head mounted display without latency. Aided by tumor-targeted contrast agents, the system detected tumors in subcutaneous and metastatic mouse models with high accuracy (sensitivity = 100%, specificity = 98% ±5%). Human pilot studies in breast cancer and melanoma patients using a near-infrared dye show that the GAINS detected sentinel lymph nodes with 100% sensitivity. Clinical use of the GAINS to guide tumor resection and sentinel lymph node mapping promises to improve surgical outcomes, reduce rates of repeat surgery, and improve accuracy of cancer staging.

3.2 Introduction

Surgical resection is the standard of care for many solid tumors such as breast cancer and melanoma, and sentinel lymph node (SLN) mapping is used for cancer staging(1). Incomplete tumor removal increases the chances of cancer recurrence and necessitates repeat surgery, whereas inaccurate SLN identification may misdiagnose the cancer stage. Despite recent advances in pre-operative imaging methods, surgeons rely on visual inspection, palpation, and tactile evaluation to distinguish cancerous from uninvolved tissue intraoperatively, leading to subjective decision-making and variable outcomes. For example, 14-50%(2-4) and 20-70%(5-7) of patients undergoing melanoma in situ and breast conserving surgery, respectively, require repeat surgery. Similarly, inaccurate SLN removal often requires additional surgical interventions(8). Surgery is most effective when performed before cancer becomes a metastatic disease. Assessment of the SLN for the presence of cancer cells is a standard of care for staging breast cancer and melanoma(1). Conventionally, patients are injected peritumorally with ^{99m}Tc sulfur-colloid and a visible lymphotrophic dye. A handheld gamma-counter is used to localize the region of highest radioactivity and the blue dye can be used to visualize the SLN. However, radioactive SLN tracking exposes patients and health professionals to ionizing radiation, without SLN visualization capability. Although blue dyes can be visualized, SLN tracking by this method is limited to inspection of only superficial lymph nodes and requires high dose of the dye, which may lead to harmful side-effects(9, 10).

The above challenges have spurred interest in developing methods for accurate intraoperative imaging of tumors and SLNs. Conventional modalities such as magnetic resonance imaging , computed tomography , and positron emission tomography can provide exquisite anatomic and functional information(11, 12). However, they are not amenable for use in the operating room (OR) due to their large hardware footprint, specialized operator requirement, prohibitive cost, and the use of ionizing radiation. Slow image reconstruction, lack of microscopic imaging capability, and disruptive information display on a remote monitor affects their wide adoption in the OR for real-time image guidance(13). Intraoperative ultrasonography can be used for tumor detection based primarily on tissue morphology, leading to significant false positive and negative rates(14-17). As a contact based method with relatively poor resolution, intraoperative ultrasonography is less useful for identifying tumor boundaries or microscopic tumors during open surgeries. Advanced instruments that mimic global positioning systems have been developed, where pre-operative computed tomography or magnetic resonance images can be projected onto the appropriate anatomical structures. These systems suffer from limitations of the pre-operative imaging method, unsatisfactory registration due to tissue deformation and motion during surgery, and the inability to directly interrogate boundaries of tumors.

Alternatively, optical imaging uses nonionizing radiation and simple imaging setup for real-time readout and detection of microscopic lesions(18, 19). In particular, near-infrared (NIR) fluorescence imaging in the 700 – 900 nm range is attractive because the low absorption by intrinsic photoactive biomolecules minimizes tissue autofluorescence and facilitates thick tissue assessment. The use of nonionizing radiation decreases safety hazards in the OR(18-20). Additionally, several tumor-targeted optical contrast agents have been developed(21) including peptide(22) and nanoparticle-based agents with promising features(23). These advantages have generated interest in NIR fluorescence image-guided surgery (NIR-FIGS). To date, several NIR-fluorescence image guided surgery (NIR-FIGS) systems have been developed, and successfully used for intraoperative tumor imaging and SLN mapping (SLNM), including FLARE(24), Fluobeam(25), SPY(26), and Hamamatsu PDE(27). However, each of these systems have some limitations, including the use of bulky hardware, potentially disruptive information display on a remote monitor, mismatch between the system’s and surgeon’s field of view (FOV), and require support from other workers to control the device.

Adaptation of head mounted displays (HMDs) for surgery(28-33) could overcome the issue of disruptive information display. We have previously demonstrated the feasibility of using wearable cameras and HMDs for FIGS(34-36). Our initial prototypes used a monocular projection eyepiece, which posed perception problems during surgery, or a binocular system, which only captured white light reflectance and fluorescence images sequentially using the same sensor, thereby preventing display of real-time composite color-fluorescence images.

Additionally, the issues of camera and user FOV mismatch, bulky design, non-optimized optics, and fast processing to generate real-time color-fluorescence composite images with minimum latency remain unaddressed. The primary goal of this study is to test the hypothesis that simultaneous, sensitive detection of color and NIR fluorescence information, fast image processing and image output via a HMD would allow non- disruptive access to accurately co-registered color-NIR images for real-time image guidance in oncologic surgery. Toward this goal, we have developed a new wearable goggle aided imaging and navigation system (GAINS) and evaluated the accuracy of using the well-characterized system for real-time intraoperative tumor visualization and image-guided tumor resection in small animals, as well as SLNM in human breast cancer and melanoma patients.

3.3 Materials and Methods

Animal and human study protocols were approved respectively by the Animal Studies Committee and the Institutional Review Board of Washington University. The human procedure was carried out in accordance with the approved guidelines. All patients gave informed consent for this HIPAA compliant study.

3.3.1 Contrast Agents

ICG (Cardio green, Sigma-Aldrich, MO) and LS301(35) were used as NIR contrast agents. Clinical grade ICG for human SLNM was provided by the Siteman Cancer Center (Washington University in St. Louis, MO). ICG and LS301 have similar spectral profiles, allowing the translation of findings with the tumor-targeted LS301 in small animals to humans using FDA-approved ICG, under similar conditions, without major changes in the detection scheme.

3.3.2 GAINS Development

GAINS conceptual design is summarized in Fig. 28a. To maximize spectral separation and minimize light leakage, we recorded an excitation scan of ICG using a fluorimeter (Horiba Jobin) to identify the best excitation wavelengths (Fig. 29). We then measured the spectral profiles of LEDs using a spectrometer (Ocean Optics) to identify suitable LEDs and the appropriate excitation and emission filters.

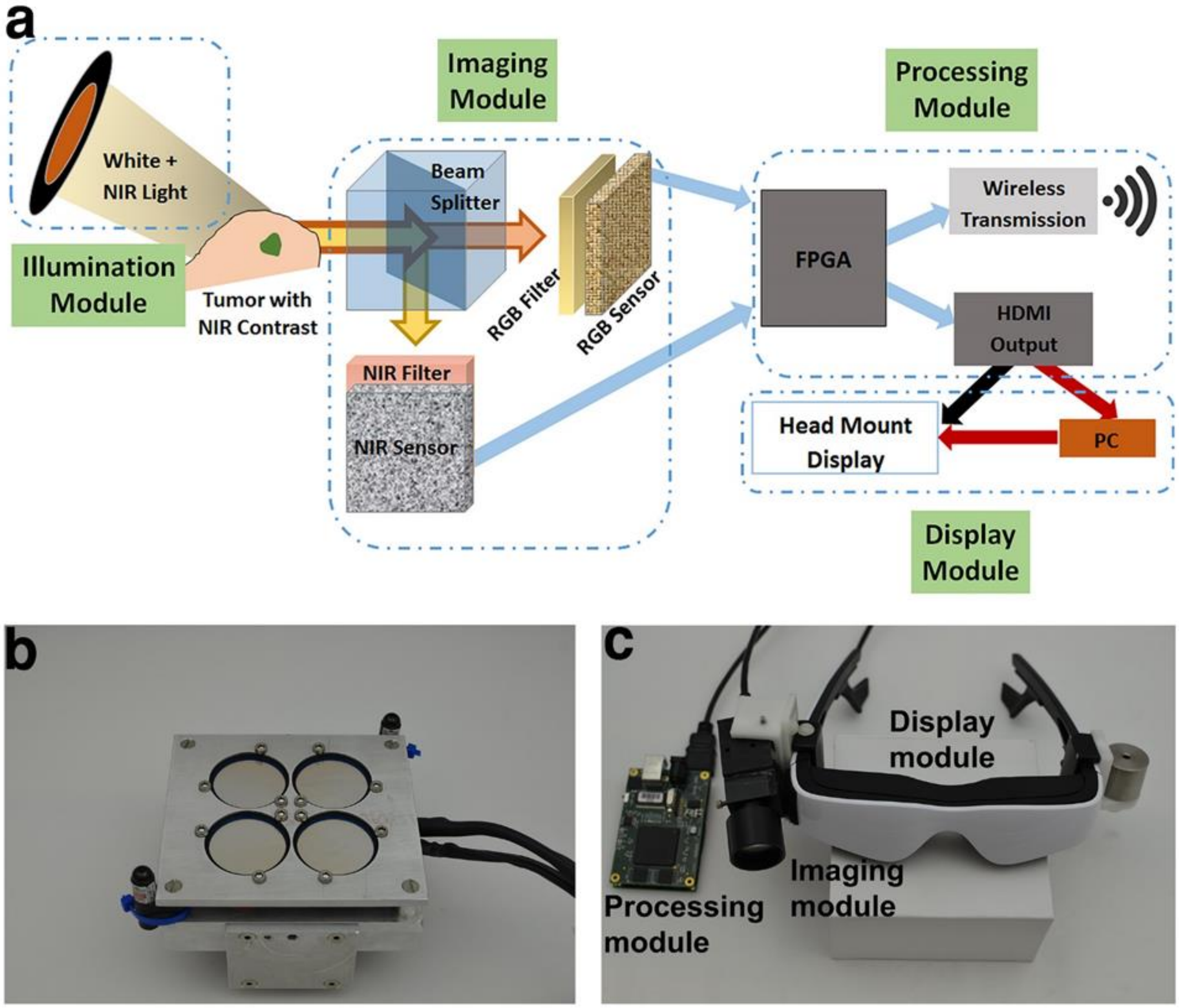

Figure 28: GAINS. (a) Schematic demonstrates the information flow through different modules of the system. (b) Photograph of the NIR source. (c) Photograph of the integrated display and imaging module, along with the processing module, which are worn by the user.

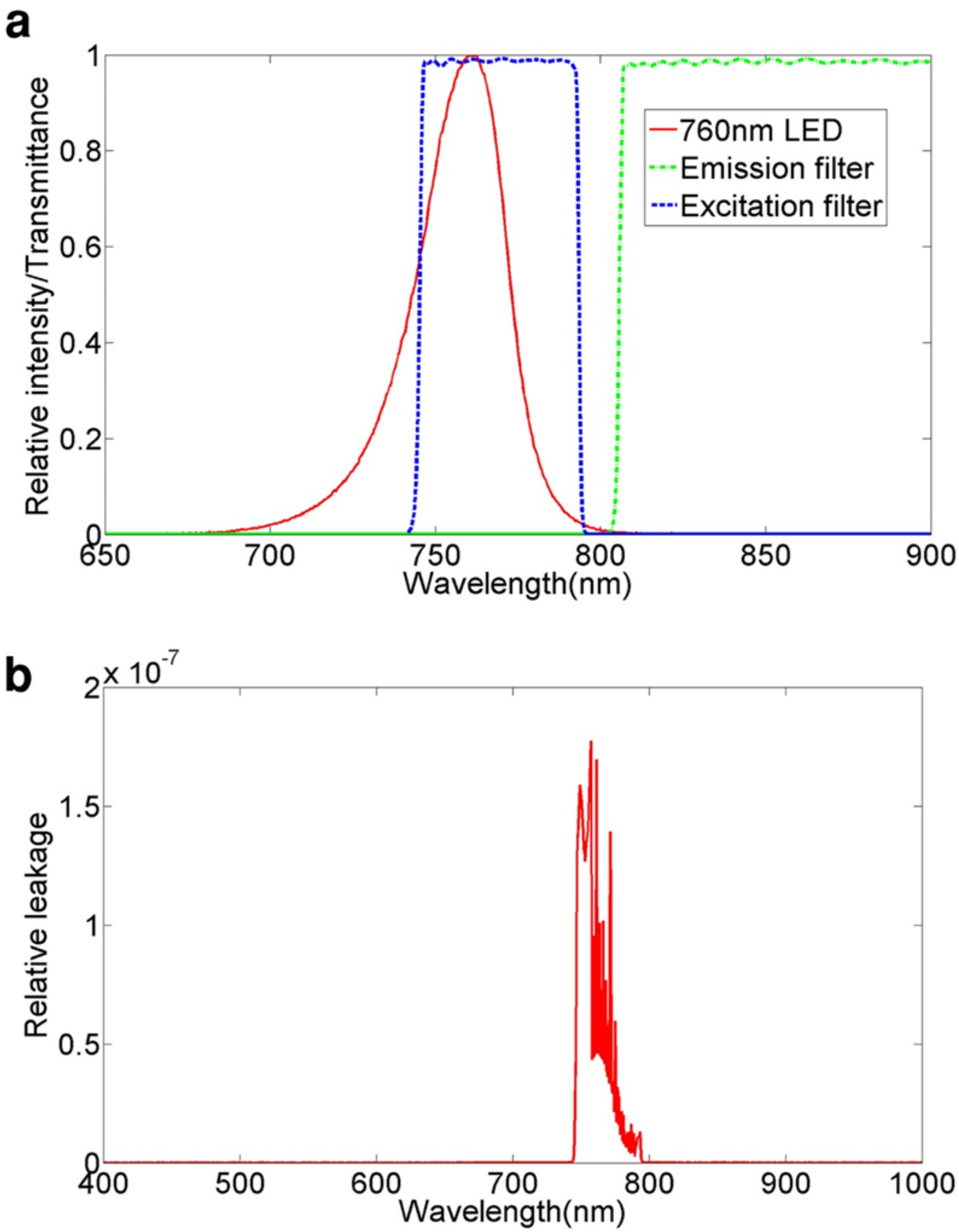

Figure 29: Spectral characterization. (a) Spectral profile of the GAINS system illumination, excitation filter used for illumination and emission filter used for NIR detection showing minimal overlap of the excitation and detected emission spectra. (b) Light leakage relative to NIR LED excitation with our filter choice.

The NIR source (Fig. 28b) consists of 760 nm LEDs (Roithner, Vienna, Austria) with 769±41 nm bandpass filter (Semrock, Rochester, NY). The LED numbers and positions (Fig. 30) were optimized using simulations (LightTools). A prototype light output of 5 mW/cm^2 at a distance of 50 cm was used. White flashlights or surgical light (Steris, Mentor, OH) covered with shortpass filters (Cool mirror 330, 3M, St Paul, MN) served as the white light source (Fig. 30).

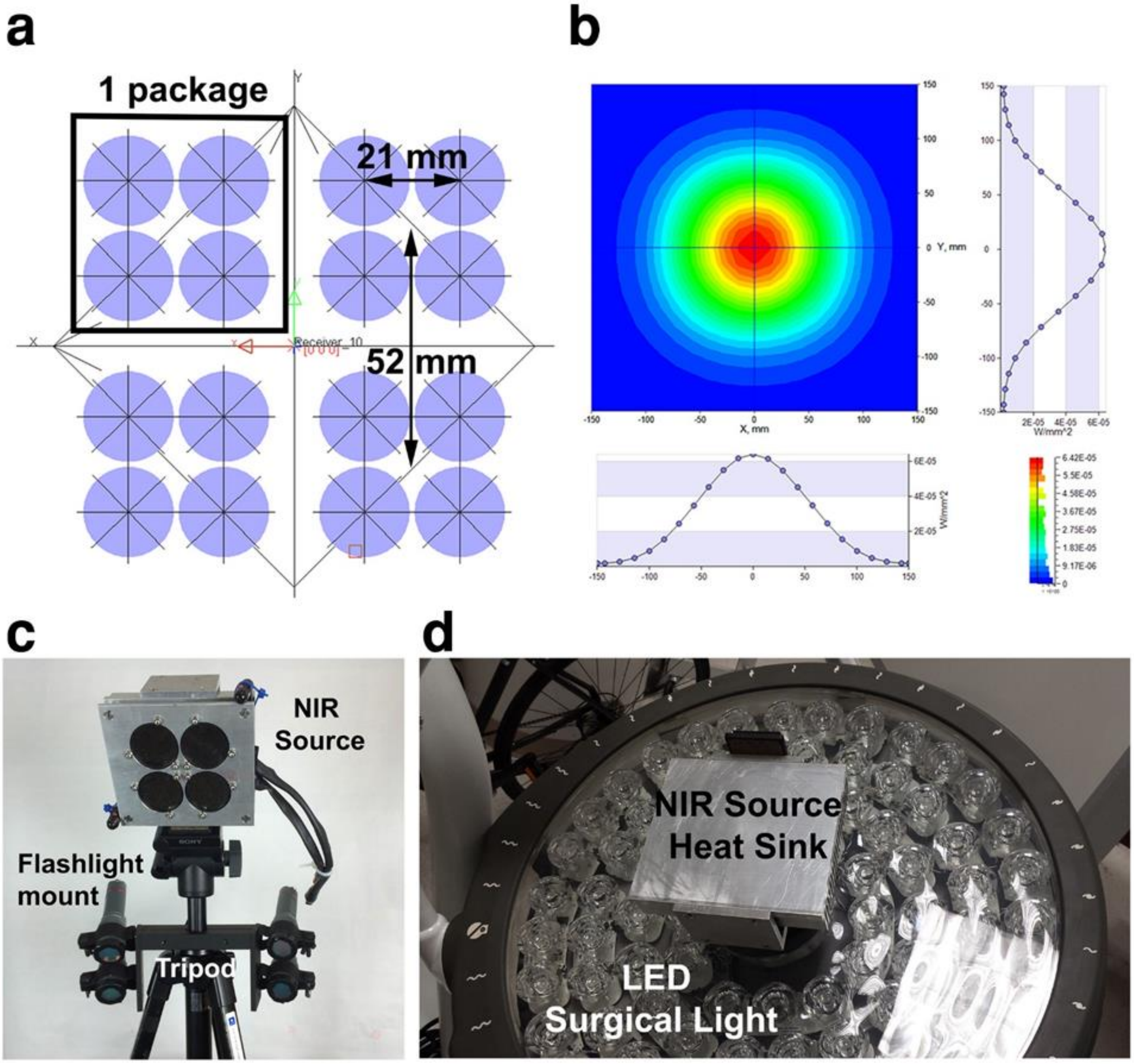

Figure 30: Illumination module design and prototype. (a) The schematic of the standalone NIR illumination sub-module showing arrangement of 16 LEDs divided in four packages, each consisting of 4 LEDs. Each package has a dimension that allows it to be covered by a 50 mm diameter excitation filter. (b) Simulation result of light output of the four package configuration while running at the typical forward current and at a distance of 50 cm. (c) Tripod configuration with for illumination. Two laser pointers are attached on two corners of the NIR sub-module to easily point the NIR source at the region of interest. A fabricated flashlight mount is used to hold four high power LED flashlights fixed on the central column of the tripod. These flashlights provide the white light illumination for color reflectance imaging. The mount is designed to provide necessary angle for convergence of the flashlight beams with the NIR illumination area at typical working distances. (d) The surgical light configuration uses the threaded back of the NIR light source to attach it to the center of a LED surgical light. The surgical light provides the while

illumination for color reflectance imaging. The white LEDs of the surgical light is covered by a filter to cut off the NIR components of the surgical light.

The imaging module collects combined color-NIR signal via a custom F/1.75 glass lens (Fig. 31). The incoming signal was divided into visible and NIR components by a custom dichroic beamsplitter cube and directed to a color and NIR complementary metal-oxide semiconductor (CMOS) sensor (Aptina, San Jose, CA). The NIR and color sensors were co-registered (disparity <0.1 mm at 50 cm distance). An 805 nm longpass and a 694 nm shortpass filter (Semrock, Rochester, NY) were placed in front of the NIR and color sensors, respectively, which work in stereoscopic mode (25 MHz clock frequency, 24 frames per second (fps)). A single pair low-voltage differential signaling communicated 16-bits data (8-bits from each sensor) to the processing module at 480 MHz (25 MHz x 18) data transmission rate (Table 8).

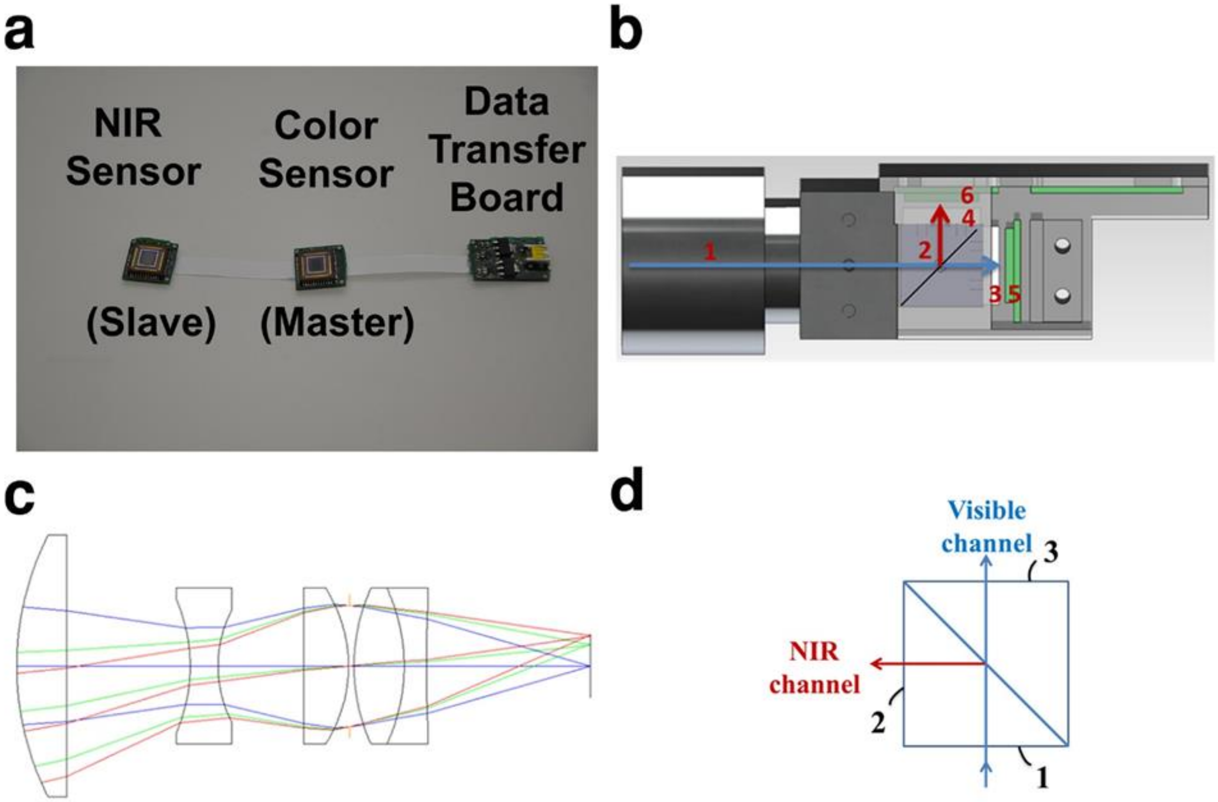

Figure 31: Imaging module. (a) Imaging module sensors showing the NIR sensor, color sensor and the conversion board. (b) Schematic of Imaging Module internal structure: 1, Lens; 2, dichroic beamsplitter; 3, short-pass filter for visible channel; 4, long-pass filter for NIR channel; 5, visible CMOS sensor; 6, NIR CMOS sensor. (c) Optical structure of the lens. (d) Design specifications of the dichroic beamsplitter: surface 1, broad band AR coating for 450-850 nm; surface 2, near-infrared band (800 nm - 900 nm) AR coating; surface 3, visible band (450 nm - 650 nm) AR coating.

Table 8: GAINS specifications.

Characteristics	GAINS Specification
Sensor pixel size	6 µm X 6 µm
NIR sensor quantum efficiency	36% at 810 nm
Lens	F/1.75, focal length= 19.6 mm, full diagonal FOV = 15.5° and working distance = 850 mm
Disparity	<0.1 mm
Weight	30 gm (camera) 330 gm (camera + HMD)
Display	VST HMD
Camera	Dual modal complementary metal-oxide semiconductor (CMOS, monochrome & RGB)
Processing	FPGA and PC
Detection limit	1 nM ICG, 50 cm, 5 mW/cm^2 illumination, 24p fps
Illumination	16 LED light, 760 nm, 5 mW/cm^2 at 50 cm
Spatial resolution	320 µm
Depth resolution	5 mm, 1 µM ICG solution

The processing module consists of a customized printed circuit board connection board and a field-programmable gate array integration module (Opal Kelly, Portland, OR). The printed circuit board powers the imaging module and deserializes the imaging data, which were pre-processed on the field-programmable gate array via optimized Verilog code, and buffered in the on-board 64MB DDR SDRAM. The pre-processed data were transmitted through a high speed USB 2.0 port to a PC (or laptop). The PC runs C++ program using OpenCV and QT C++ libraries that can execute on any regular Windows x64 PC, without extra software and configuration. The program generates superimposed color-NIR images, creates a GUI that gives access to functions such as display/store/process image data and duplicates images for display on the PC and a HMD module simultaneously. The GUI also allows use of different exposure times for the photon-saturated visible channel and photon-starved NIR channel, as well as color correction for best image quality.

The display module consists of a 1080p high resolution HMD (Carl Zeiss, Oberkochen, Germany). Adjustable mechanical mounting and a counter balance for the imaging module were added to match the camera and user FOV for improved user experience (Fig. 28c).

3.3.3 In Vitro Phantom Studies

All characterization studies were performed at 50 cm imaging distance, 5mW/cm2 illumination, and 24p fps.

For detection sensitivity, spatial average intensity (30×30 pixels) was extracted from GAINS images of freshly prepared triplicate samples with different concentrations of ICG (300 pM – 50 µM) and LS301 (1 nM – 10 µM) dissolved in DMSO and imaged in clear glass vials. The spatially averaged intensity values were plotted against concentration to create the intensity detection profile for GAINS. The SBR was calculated for each concentration by using images acquired in pure DMSO as the background and plotted against dye concentration.

For depth sensitivity, plastic straws of 3 mm diameter were filled with 1 µM ICG and imaged at different depths in a tissue mimicking phantom (µa = 0.1, µ́s = 5 cm-1), prepared using intralipid and 2% India ink(37). Pixel intensities corresponding to multiple points on the straw and background were used to calculate SBRs and plotted against depth. For depth resolution, two 3 mm straws filled with 1 µM of ICG were kept 7 mm apart and imaged at various depths in the tissue mimicking phantom. The signal intensity from a cross section of the image were used to create intensity maps and plotted against the depth. Error in color-NIR superimposition was measured by focusing the camera at 50 cm and imaging a target at 50 cm ±5 cm.

3.3.4 In Vivo Mouse Studies

Six to eight-week old nude mice (n=10) were injected subcutaneously in both flanks with 5 ×105 4T1*luc* murine breast cancer cells. At 5-7 mm tumor size (7-10days post implantation), these mice received lateral tail vein LS301 (100 µL, 60 µM in 20% aqueous DMSO) injection. At 1, 4 and 24 h post injection, the mice were imaged noninvasively using the Pearl small animal imager (LI-COR, Lincoln, NE) and the GAINS. After 24 h, the GAINS was used for intraoperative imaging and image-guided resection of tumors. The resected tissues were preserved for histologic analysis.

Additional 6-8 week old nude mice (n=3) were injected intraperitoneally with 1 × 107 SKOV3 human ovarian cancer cells, stably transfected with iRFP (38). When tumors were palpable (5-10 mm, 3 weeks post implantation), mice received lateral tail vein LS301 (100 µL, 60 µM in 20% aqueous DMSO) injection and were imaged noninvasively using the Pearl system and GAINS at 1, 4, and 24 h post injection. At 24 h post injection, GAINS guided the intraoperative tumor visualization and resection. Resected tissue were imaged for iRFP signal using the Pearl system and then frozen for histologic analysis for determination of GAINS tumor detection sensitivity and specificity. The imaging threshold was varied retrospectively from 6.3 % to 7.8% of maximum pixel intensity, and the sensitivity and specificity were calculated for each threshold. ROC analysis was used to calculate the optimal imaging threshold for this model.

3.3.5 Histology

Fresh-frozen, 10 µm tissue sections were imaged for NIR fluorescence, stained with hematoxylin and eosin (H&E) and same areas were imaged under brightfield for co-registration with NIR fluorescence using a epifluorescence microscope (BX51 Olympus, Center Valley, PA).

3.3.6 Pilot Human Studies

Participants were breast cancer patients (n=10) undergoing lumpectomy, partial mastectomy, or radical mastectomy, as well as melanoma patients (n=5) undergoing wide excision of skin lesions, along with SLNM. Breast cancer patients, were given post-anesthesia, peritumoral injection of a mixture of 99mTc-sulfur colloid (834 µCi) and methylene blue (5 mL of 1% solution) immediately followed by ICG (5 mg/mL; 5 mL) and site massage for approximately 5 min. At 10-15 min post injection, the surgeon removed the tumor mass. A handheld gamma probe guided site of axillary incision and invasive SLN identification, which were then examined for presence of blue color and visualized using the GAINS via ICG fluorescence. The cavity was inspected with the GAINS to identify other fluorescence SLNs, which were then checked for blue color and radioactivity, before excision and preservation for histology. A similar procedure was followed in melanoma patients, except that only 1 mL of ICG solution (5 mg/mL) was injected. In all cases, the GAINS was operated at 24p fps with a 40-millisecond acquisition time. NIR-white light illumination during system usage was provided by our illumination module.

3.3.7 Statistical Analysis

Statistical analysis was performed using OriginPro8 (OriginLab Corp., Northampton, MA). SBRs, sensitivity and specificity were expressed as mean and standard deviation. Paired t-tests were used to compare fluorescence signal in tumors and background tissue in mouse models and sensitivity of SLN detection by GAINS, radioactivity and blue dye methods. $P < 0.05$ were considered statistically significant.

3.4 Results

3.4.1 Development of GAINS

The accuracy of image guidance depends on the sensitivity and resolution of the system, as well as the accuracy of fluorescence to color image overlay. The system detection sensitivity is determined by the fluorescence detection sensitivity because the visible light channel has abundant signal compared to the photon-starved fluorescence channel. The system resolution is determined by the sensor and optics of the system, with smaller sensor pixel pitch and smaller lens aperture leading to higher resolution. So there is a trade-off between using a high resolution lens and large aperture lens that allows high fluorescence signal capture for more sensitive detection. Furthermore, the requirement of wearability imposed additional restrictions of compact, lightweight, and ergonomic design. This precluded the use of different cameras with dedicated lenses for both color and fluorescence channels, and large aperture heavy glass lenses that could capture very large amount of fluorescence signal. The amount of fluorescence signal collected may be increased by using large exposure times. However, the requirement of real-time image guidance constrained the imaging exposure to acquire both fluorescence and color information. Therefore, the challenges in developing the GAINS were achieving sensitive simultaneous imaging in the photon-saturated color channel and photon-starved fluorescence channel, real-time image processing, and non- disruptive display, while maintaining a wearable form factor. We overcame these challenges by developing a single lens, color-NIR (Fig. 31), and compact lightweight camera (Table 8), with independent exposure times for both sensors and spatial resolution of 320 µm (Table 8). GAINS conceptual design is summarized in Fig. 28a. The processing unit generates co-registered composite color-fluorescence images, which are displayed in real-time via a lightweight high resolution HMD unit. The NIR source (Fig. 28b) consists of 760 nm light-emitting diodes (LEDs) with 769±41 nm bandpass filter. The display module consists of a 1080p high resolution HMD. Adjustable mechanical mounting and a counter balance for the imaging module were added to match the camera's weight and user FOV for improved user experience (Fig. 28c). Additional information on the system development can be found in the Materials and Methods section.

3.4.2 In-vitro Studies

We used GAINS to determine the fluorescence intensity profile with increasing concentrations of NIR contrast agents indocyanine green (ICG) and LS301(35) (Fig. 32a). In the 1 nM to 10 nM range, significant fluorescence was detected, but the signal is close to the sensor noise floor, indicating noise contribution to the net intensity signal. The intensity did not follow a linear trend. A similar profile was observed when signal-to-background ratios (SBRs) were plotted against concentration (Fig. 32b). Therefore, there was no appreciable increase in fluorescence intensity (Fig. 32a) or the SBR (Fig. 32b) from 1 nM to 10 nM. At concentrations higher than 10 nM we observed a rapid increase in the fluorescence intensity and SBR with increasing molecular probe concentrations. The result suggests that the GAINS was able to detect 1 nM solutions of both ICG and LS301, while maintaining an SBR of ≥ 1.2 (Fig. 32b). This threshold represents the system's detection limit in homogenous dimethyl sulfoxide (DMSO) solution.

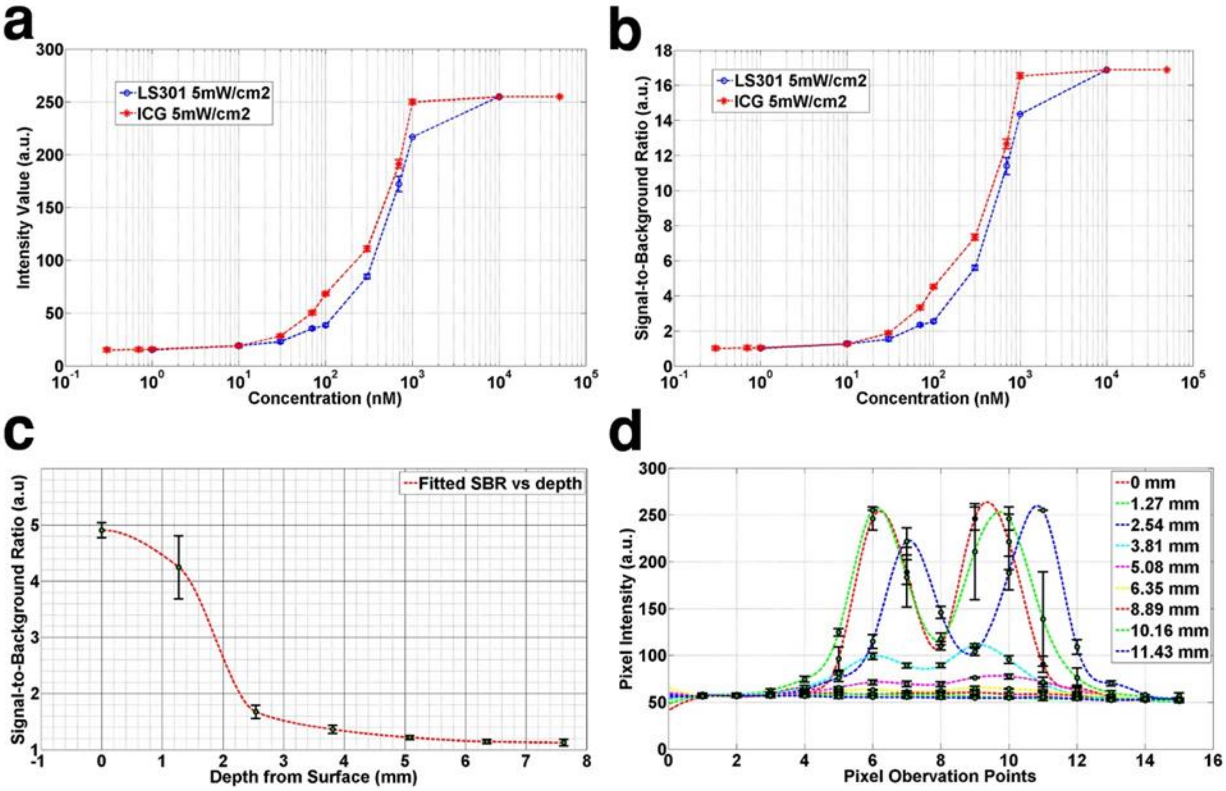

Figure 32: Graphs from phantom experiments for system characterization showing SNR and depth resolution information. (a) Fluorescence intensity response with varying concentrations of ICG and LS301. (b) The SBR for different concentrations of ICG and LS301. (c) SBR for different depths for 1□M ICG. (d) SBR for depth resolution with 1µM straws positioned 7 mm apart.

Analysis of depth and spatial resolution shows that the system is capable of detecting 1 µM ICG inside a tissue mimicking phantom up to a depth of 5 mm and can resolve two 3 mm diameter objects kept 7 mm apart up to a depth of 5 mm with an SBR of ≥1.2 (Fig. 32c and 32d). At the surface, the SBR for 1 µM ICG was 4.9 (Fig. 32c). This is much lower than the SBR observed for 1 µM solution of ICG in DMSO, which was used to calculate the GAINS' detection limit (Fig. 32b). Whereas DMSO solvent has minimal scattering and absorption of light at NIR wavelengths, the tissue mimicking liquid phantom (intralipid and India ink(37)) used for depth sensitivity measurement has significantly higher scattering and absorption than DMSO. As a result, the background signals were higher for depth than sensitivity detection experiments, leading to a decrease in the SBR for studies with tissue phantoms at equivalent ICG concentration.

Time needed for complete surgical resection of tumors can vary from minutes to several hours. Surgeons are trained to have very steady head movements during tumor removal, but they may experience involuntary head movement. This could cause inaccurate fluorescence overlay if the image becomes out of focus. Our tests indicate that if an object is within ± 2.54 cm of the focal plane of the camera at the typical working distance of 50 cm, the accuracy of the fluorescence overlay on the color image will be within 670 µm. Because involuntary head movement and breathing are within the tested range, the error in fluorescence overlay will be minimal. This suggests that there is no need to keep GAINS perfectly stationary during surgery.

3.4.3 In vivo Mouse Studies

We used a subcutaneous breast cancer mouse model to test in vivo GAINS function. Using LS301 fluorescence, the GAINS clearly identified all tumors (n=10 mice), with a mean SBR of 1.21±0.1 and guided resection in real-time (Fig. 33). The fluorescence signal in the tumors was significantly higher than surrounding tissue ($P < 0.05$). Histologic analysis confirmed resected tissue as cancerous. In the metastatic mouse model of ovarian cancer, the GAINS identified 27 tumor nodules in 3 mice, with a mean SBR of 1.19±0.03 (Fig. 34), compared to only 10 tumor nodules identified visually alone. Several tumors that were under the visceral organs (3-5 mm deep) were not visible without GAINS guidance. However, real-time visualization of sub-surface fluorescence guided exploratory surgery revealed tumors that would have been otherwise left behind. The fluorescence signal from suspected tumors were significantly higher than surrounding tissue ($P < 0.05$), facilitating detection of the smallest tumor (3 mm in diameter). All resected tissues were confirmed to be tumors through infrared fluorescent protein (iRFP)(38) imaging and histologic analysis, which showed close overlap of iRFP signal with the LS301 fluorescence (Fig. 35). Imaging threshold provides guidance in delineating the tumor region for resection (Fig. 36) and affects the accuracy of tumor detection. We used receiver operator characteristic (ROC) analysis to determine the best imaging threshold for the metastatic mouse model. The sensitivity and specificity of tumor detection for all images were calculated at several thresholds within the range of 7.8 % to 6.3 % of maximum pixel intensity. Using the best case threshold for each image, the sensitivity and specificity of tumor detection was calculated to be 100% and 98.33% ±5%, respectively. Using the average detection sensitivity and specificity for each threshold tested, ROC analysis shows that a threshold of 7.5 % of maximum pixel intensity is a reasonable imaging threshold to obtain optimal sensitivity and specificity with GAINS, due to high LS301 uptake in tumor and low tissue autofluorescence (Fig. 35). This threshold was used to identify the tumor region prior to resection. The threshold was manually adjusted during tumor resection to accommodate changes in the residual fluorescence intensities. Our graphical user interface (GUI) has the option of adjusting the threshold of the superimposed images so that only fluorescence intensity above the threshold will be displayed in pseudocolor representation in the color-NIR channel. This approach optimizes the tumor detection sensitivity and specificity for each case.

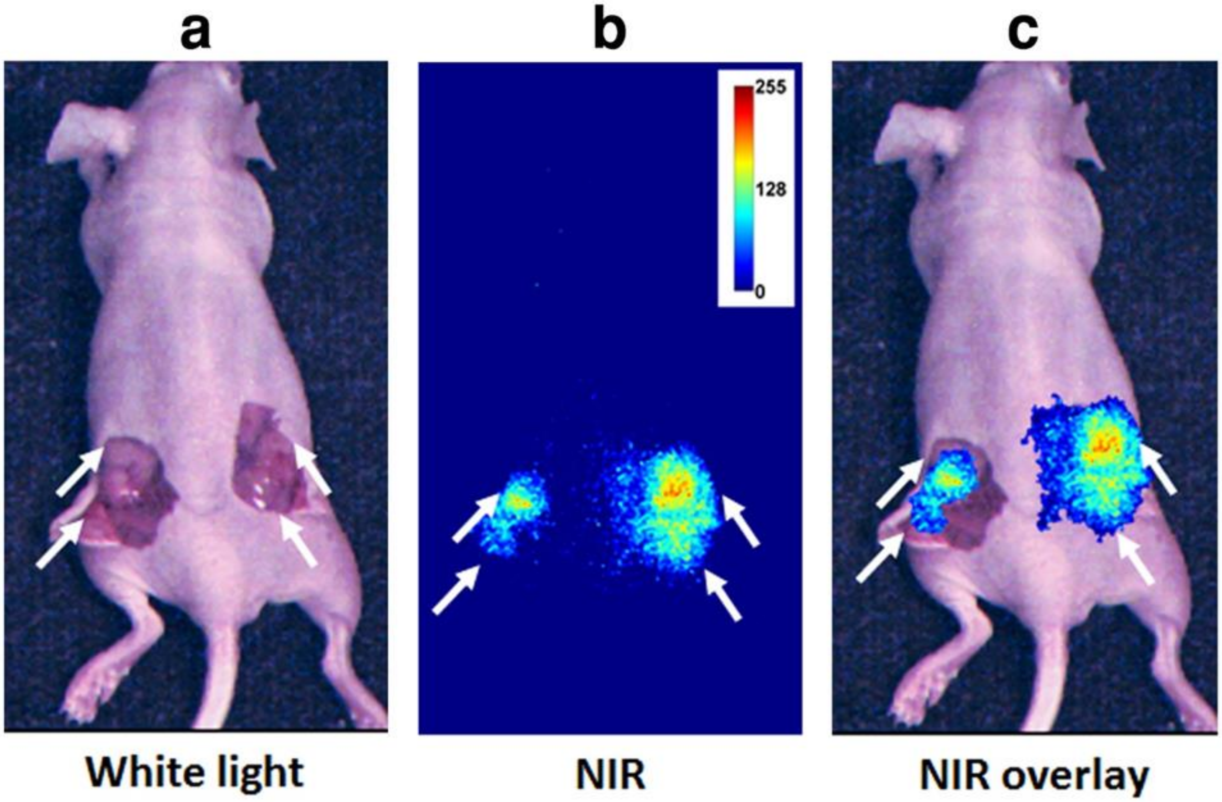

Figure 33: Image-guided tumor visualization in subcutaneous mouse model. (a) Color image of mouse with skin deflected showing tumor nodes. (b) NIR image showing high fluorescence area. (c) Superimposed color-NIR image showing high fluorescence area accurately corresponds to the tumor nodes.

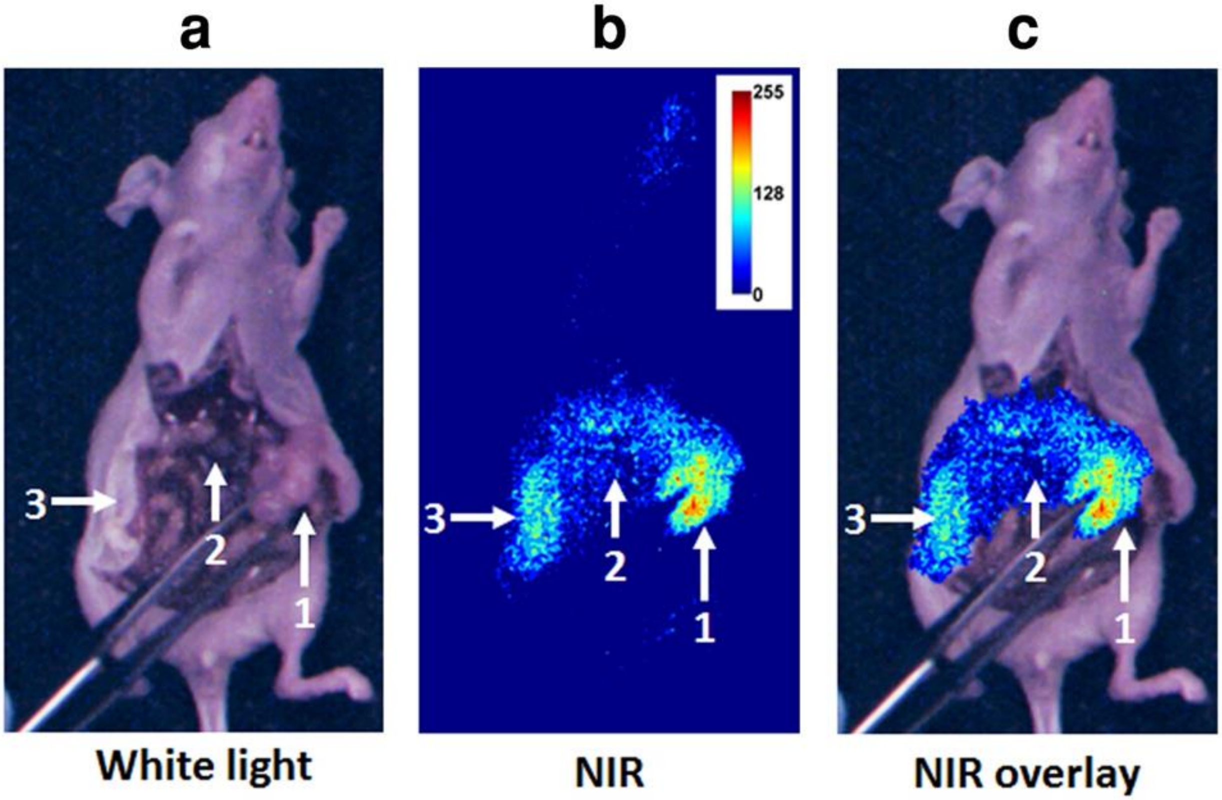

Figure 34: Image-guided exploratory tumor resection in metastatic mouse model. (a) Color image showing a large abdominal tumor. (b) NIR image showing high fluorescence area corresponding to the tumor (marked 1) and two other areas (marked 2 and 3). (c) Superimposed image showing color-NIR overlay image.

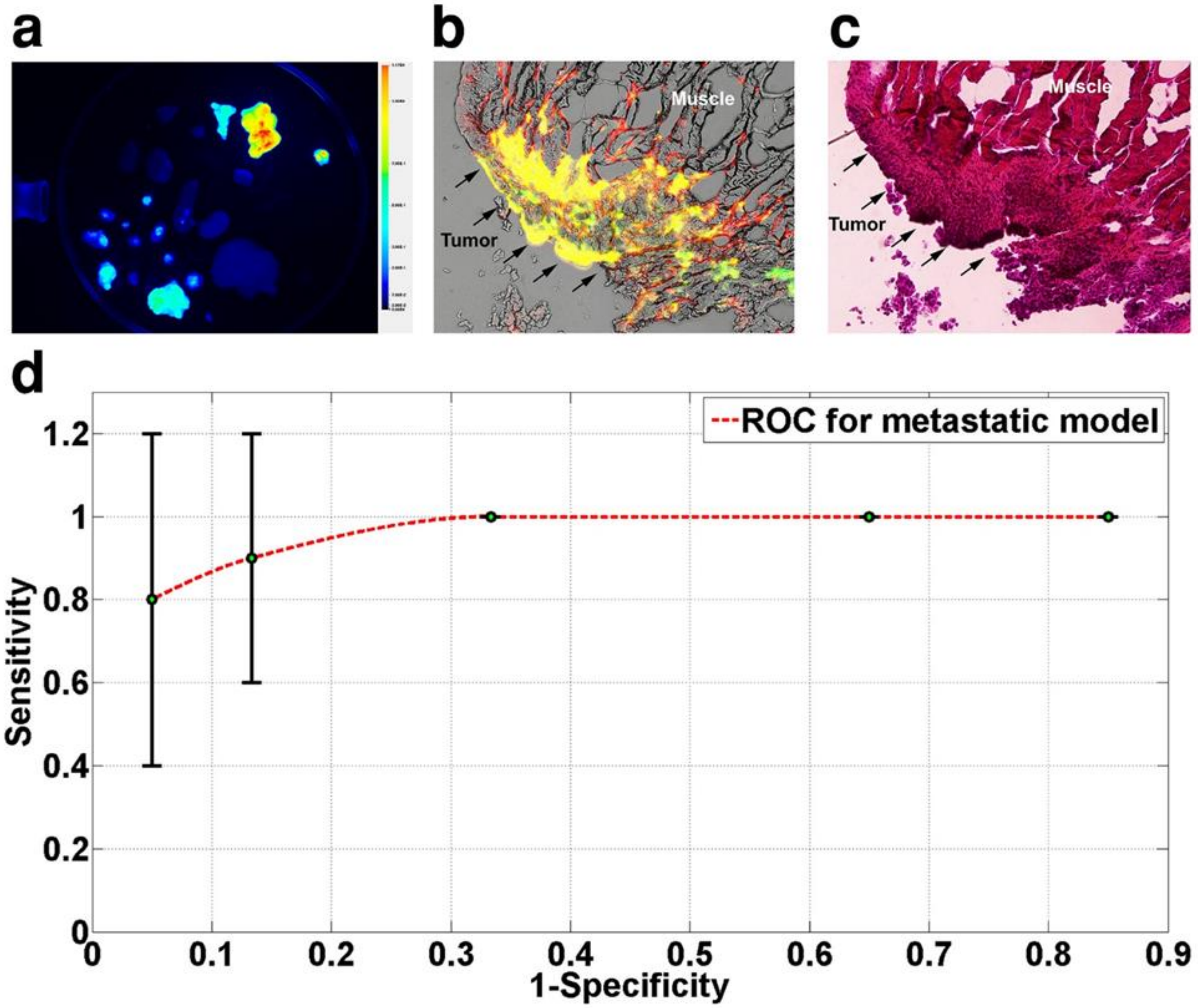

Figure 35: Accuracy of tumor detection in metastatic model. (a) iRFP image of harvested organs and tumors from one of the mice showing confirmatory high signal from tumors. (b) Fluorescence microscopy revealed good co-localization (yellow) of iRFP signal (green) and LS301 fluorescence (red). (c) Histological confirmation of the same slide showing cancerous growth corresponding to the areas marked by iRFP and LS301 fluorescence. (d) ROC curve for GAINS tumor detection sensitivity and specificity at different imaging thresholds.

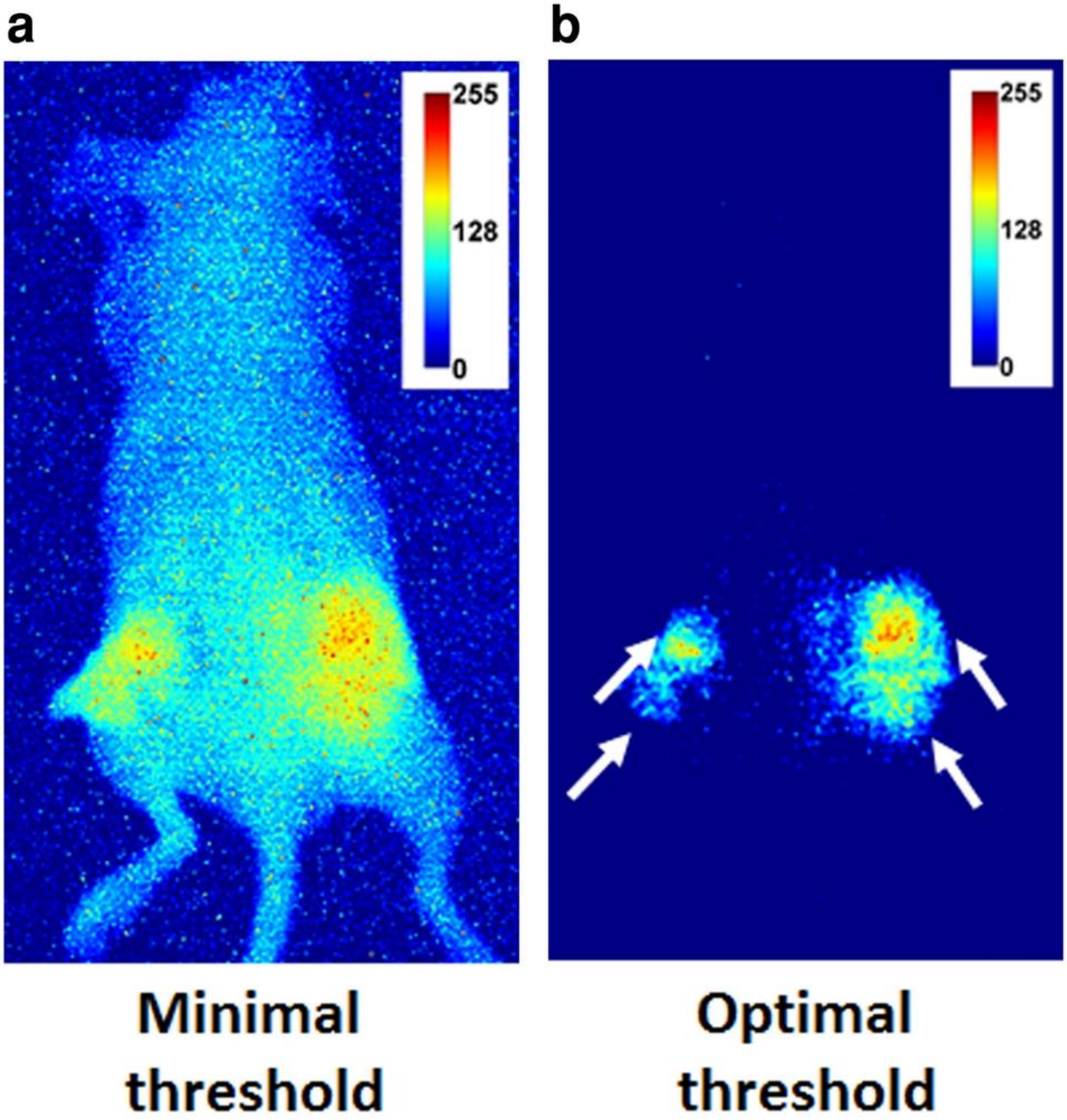

Figure 36: Thresholding during image-guided tumor visualization in subcutaneous mouse model. (a) NIR image with minimal thresholding, showing high fluorescence area corresponding to tumor. (b) NIR image with optimal thresholding, showing well-defined high fluorescence in the tumor region.

3.4.4 Human Pilot Studies

Clinical feasibility was demonstrated in 15 patients during SLNM after lumpectomy/mastectomy or wide excision surgeries. Surgeons used the system comfortably, with minimal disruption to the surgical workflow. The GAINS allowed clear visualization of 30 SLNs from 10 breast cancer (Supplementary Vid. S1) and 5 melanoma (Supplementary Vid. S2) patients. Using histologic analysis as the gold standard, the GAINS had a detection sensitivity of 100% in comparison to 92.86% ±17.5% for the blue dye and 96.43% ±12.9% for radioactive tracking. There was no statistically significant difference in sensitivity of SLN detection sensitivity by GAINS compared to radioactive tracking ($P = 0.34$) or blue dye tracking ($P = 0.36$) methods. In one melanoma patient (Fig. 37), blue dye did not identify two deep-seated SLNs. Similarly, in one breast cancer patient, initial visual inspection did not reveal the SLN (Fig. 38) and in another patient, radioactive tracking was unable to identify two SLNs by. In these cases, the LNs were clearly identified by GAINS. Although the imaging depth with reasonable resolution is about 5 mm, high fluorescence signal from deep-seated SLNs is readily projected to the surface, allowing visualization of SLNs at >5 mm deep after deflection of the overlying tissue layer (Fig. 39). This demonstrates the potential clinical utility of the system for rapid identification of SLNs during surgery.

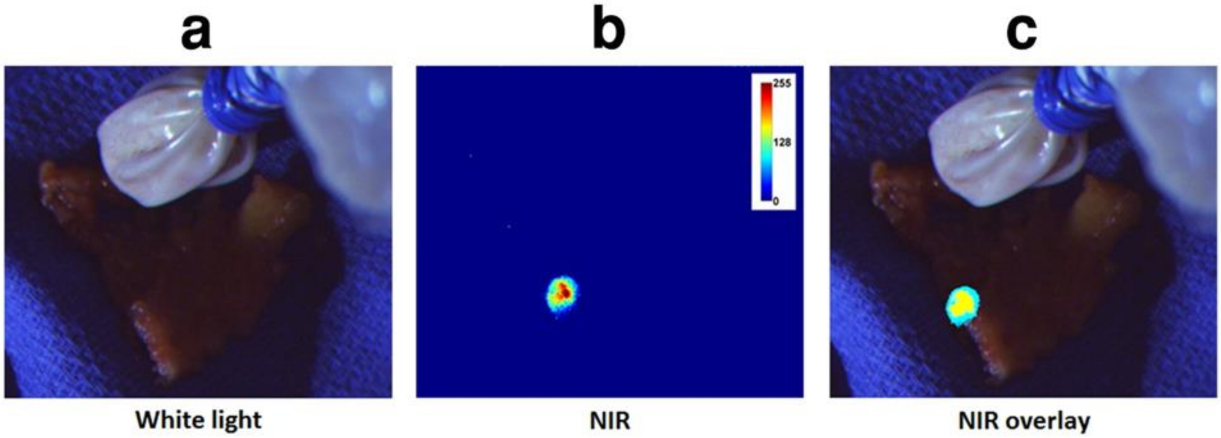

Figure 37: Melanoma patient SLNM showing excised SLN not identified by blue dye. (a) Color image showing no blue dye signal although radioactively hot region was detected. (b) NIR image showing high fluorescence area. (c) Superimposed image showing high fluorescence corresponding to the hot area.

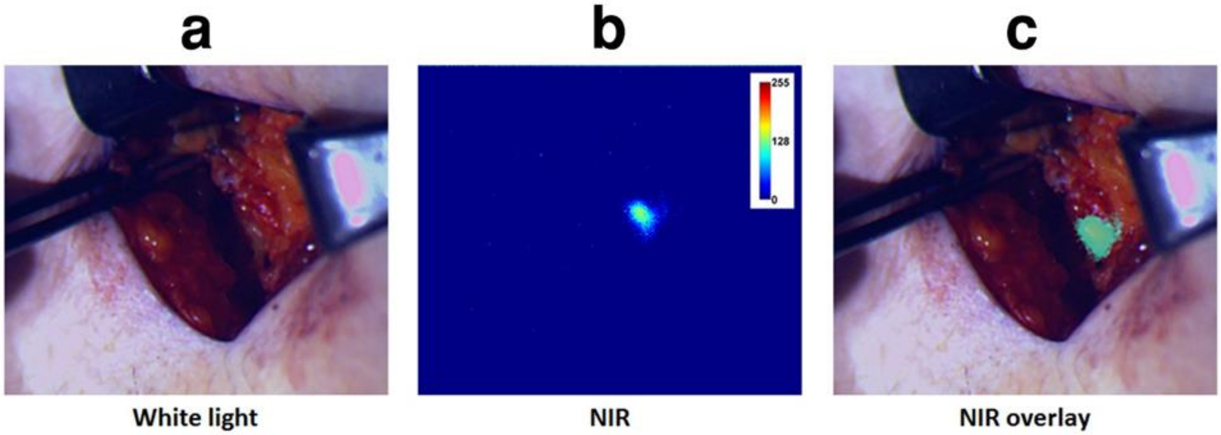

Figure 38: Breast cancer patient SLNM showing non-apparent SLN by visual inspection. (a) Color image showing absence of blue dye. (b) NIR image showing high fluorescence area and (c) NIR-color superimposed image.

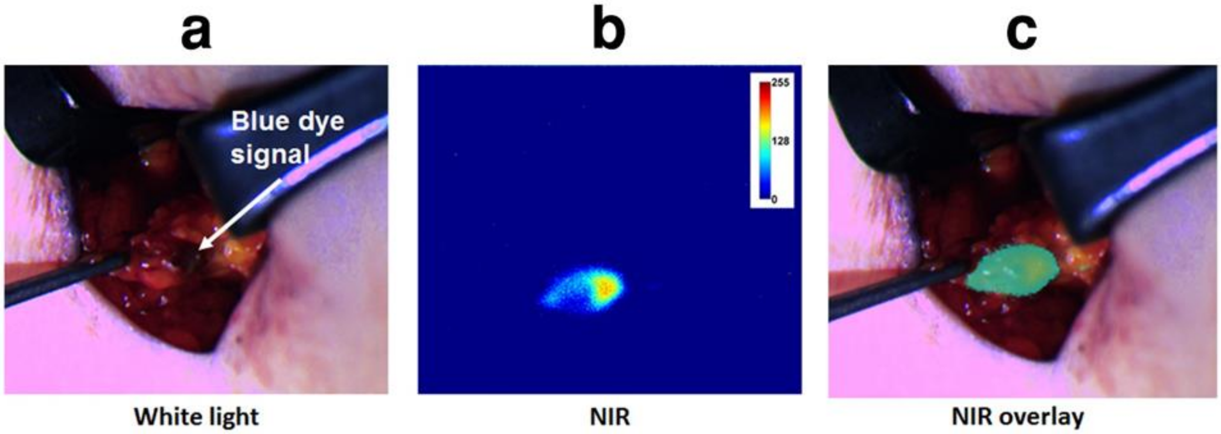

Figure 39: The SLN was apparent after superficial tissue layer was retracted. (a) Color image showing retracted tissue layer and visible blue spot from blue dye. (b) NIR image showing a larger clear high fluorescence area. (c) Color-NIR image showing fluorescence corresponding to the blue dye spot.

3.5 Discussion

We have developed a wearable FIGS system that can provide accurate intraoperative visualization of tumors and SLNs in real-time. The ability to detect low NIR fluorescence favors the use of GAINS for molecular imaging of low- and high-expression cancer biomarkers. We used lightweight components that are robust, durable, low-weight and ergonomic. Our compact design allowed dramatic reduction of hardware footprint in the space-starved OR, compared to large standalone systems such as early version FLARE(24) and SPY(26) systems. Compact camera design and ergonomic HMD allow wearability and hands-free functionality with minimal training requirements, compared to handheld guidance systems such as Fluobeam(25) and PDE(27) that disrupt the normal surgical workflow. The position adjustable camera mounted on the HMD ensures matching of camera and surgeon’s FOV. Our robust image processing algorithm generates composite color-fluorescence images in real-time that are simultaneously displayed on surgeon's HMD and adjacent personal computer (PC) allowing non-disruptive information display to the operating surgeon and simultaneous information availability to the surgical team in the OR. These features are not available in other FIGS systems (24-27). The software and GUI are easy to use and compatible with any Windows-based PC. Importantly, superimposed fluorescence information on the normal visual landscape, allows rapid intraoperative visualization of tumors.

In conjunction with LS301, our method clearly identified local and metastatic tumors in murine cancer models, demonstrating the potential for using GAINS to improve the accuracy of tumor resection and decrease the rates of repeat surgeries. Our method allows SLNM with relatively low concentrations of the NIR contrast agent, eliminating exposure to ionizing radiation and minimizing the risk of adverse reactions in patients(9). The GAINS SLN detection sensitivity was slightly higher than radioactivity and blue dye tracking, although we did not find any statistically significant differences between the methods. Our findings agree with previous studies that have showed ICG fluorescence has comparable or better SLN detection sensitivity compared to radioactivity and blue dye methods(10, 39-42). Although other emerging clinical systems have reported capability of fluorescence detection in the OR, this is the first demonstration of "direct" visualization of NIR fluorescence-color images by surgeons.

A current limitation is the lack of automated focusing, which may lead to image blurring due to large changes in viewing distance. We also currently require a wired connection to a PC for final image processing that restricts the user's radius of movement. We envision future versions that will automate detection of working distance and adjust the focus according to the working distance of users. We currently use a single camera to capture the user's FOV, which is displayed in 2D. Future versions will transition to two-camera stereoscopic system to allow 3D information capture and display for enhanced surgical guidance. We are also developing robust wireless transmission of image data to enable constraint-free movement. This feature will enable telemedicine applications, remote guidance from experts, and remote training of surgical fellows. Low cost prototype development and minimal learning curve for the user favors the use of GAINS in low resource areas.

In summary, we have developed an ergonomic wearable real-time fluorescence image guidance system that has high detection sensitivity and resolution. The GAINS was able to successfully address the existing limitations of current image guidance systems, including large hardware footprint, field of view mismatch, disruptive information display and real-time image guidance. In conjunction with a tumor-selective NIR probe, the GAINS successfully detected tumors and occult metastatic nodes with high accuracy for guided tumor resection in rodents. Importantly, the GAINS was successfully implemented in the OR for identifying SLNs in human breast cancer and melanoma patients with equivalent or better accuracy than standard methods, although larger sample size is needed to validate this finding. Features such as the non-disruptive real-time image guidance and need for minimal training will potentially facilitate wide adoption of this technology by clinicians. Further improvements will enable the detection of microscopic lesions in the surgical field, which might otherwise be missed, and possibly prevent damage to nearby uninvolved vital structures such as nerves.

3.6 Acknowledgements

Funding for this project was through a grant from the US National Institutes of Health (NCI R01 CA171651 and P50 CA094056).

3.7 Author Contribution Statement

SM, SG, and NZ performed goggle experiments. SM, SG, GPS, AS and WJA conducted small animal studies. KL prepared and analyzed LS301. SM, SG, NZ, RL, VG, and SA designed system and preclinical study. RCF, JM, and SA designed clinical study. RCF and JM performed human breast cancer and melanoma surgery, respectively. SM, SG, VG, and SA provided technical assistance in the OR. VG, RL, and SA directed research. SM, SG, NZ, RL, VG, and SA wrote the manuscript; all authors reviewed and edited the manuscript.

3.8 Additional Information

3.8.1 Competing Financial Interests

The authors declare no competing financial interests.

3.9 References

1. Chen SL, Iddings DM, Scheri RP, Bilchik AJ. Lymphatic mapping and sentinel node analysis: current concepts and applications. CA: a cancer journal for clinicians. 2006;56(5):292-309. Epub 2006/09/29. PubMed PMID: 17005598.

2. Agarwal-Antal N, Bowen GM, Gerwels JW. Histologic evaluation of lentigo maligna with permanent sections: implications regarding current guidelines. Journal of the American Academy of Dermatology. 2002;47(5):743-8. Epub 2002/10/26. PubMed PMID: 12399768.

3. Kunishige JH, Brodland DG, Zitelli JA. Surgical margins for melanoma in situ. Journal of the American Academy of Dermatology. 2012;66(3):438-44. Epub 2011/12/27. doi: 10.1016/j.jaad.2011.06.019. PubMed PMID: 22196979.

4. Moller MG, Pappas-Politis E, Zager JS, Santiago LA, Yu D, Prakash A, et al. Surgical management of melanoma-in-situ using a staged marginal and central excision technique. Annals

of surgical oncology. 2009;16(6):1526-36. Epub 2008/12/04. doi: 10.1245/s10434-008-0239-x. PubMed PMID: 19050971.

5. Jacobs L. Positive margins: The challenge continues for breast surgeons. Annals of surgical oncology. 2008;15(5):1271-2. PubMed PMID: ISI:000254623100002.

6. Collins L, Schnitt S, Achacoso N, Haque R, Nekhlyudov L, Fletcher S, et al. Outcome of Women with Ductal Carcinoma In Situ (DCIS) Treated with Breast-Conserving Surgery Alone: A Case-Control Study of 225 Patients from the Cancer Research Network. Mod Pathol. 2009;22:34-5. PubMed PMID: ISI:000262371500144.

7. Vicini FA, Kestin LL, Goldstein NS, Chen PY, Pettinga J, Frazier RC, et al. Impact of young age on outcome in patients with ductal carcinoma-in-situ treated with breast-conserving therapy. J Clin Oncol. 2000;18(2):296-306. PubMed PMID: ISI:000084836100009.

8. Nieweg OE, Veenstra HJ. False-negative sentinel node biopsy in melanoma. Journal of surgical oncology. 2011;104(7):709-10. Epub 2011/07/28. doi: 10.1002/jso.22043. PubMed PMID: 21792944.

9. Bezu C, Coutant C, Salengro A, Darai E, Rouzier R, Uzan S. Anaphylactic response to blue dye during sentinel lymph node biopsy. Surgical oncology. 2011;20(1):55-9. Epub 2010/11/16. doi: 10.1016/j.suronc.2010.10.002. PubMed PMID: 21074413.

10. van den Berg NS, Brouwer OR, Schaafsma BE, Matheron HM, Klop WM, Balm AJ, et al. Multimodal Surgical Guidance during Sentinel Node Biopsy for Melanoma: Combined Gamma Tracing and Fluorescence Imaging of the Sentinel Node through Use of the Hybrid Tracer Indocyanine Green-Tc-Nanocolloid. Radiology. 2014:140322. Epub 2014/12/19. doi: 10.1148/radiol.14140322. PubMed PMID: 25521776.

11. Weissleder R, Pittet MJ. Imaging in the era of molecular oncology. Nature. 2008;452(7187):580-9. Epub 2008/04/04. doi: 10.1038/nature06917. PubMed PMID: 18385732; PubMed Central PMCID: PMC2708079.

12. Frangioni JV. New technologies for human cancer imaging. Journal of clinical oncology : official journal of the American Society of Clinical Oncology. 2008;26(24):4012-21. Epub 2008/08/20. doi: 10.1200/JCO.2007.14.3065. PubMed PMID: 18711192; PubMed Central PMCID: PMC2654310.

13. van der Vorst JR, Schaafsma BE, Hutteman M, Verbeek FP, Liefers GJ, Hartgrink HH, et al. Near-infrared fluorescence-guided resection of colorectal liver metastases. Cancer. 2013;119(18):3411-8. Epub 2013/06/25. doi: 10.1002/cncr.28203. PubMed PMID: 23794086; PubMed Central PMCID: PMC3775857.

14. Arii S, Tanaka S, Mitsunori Y, Nakamura N, Kudo A, Noguchi N, et al. Surgical strategies for hepatocellular carcinoma with special reference to anatomical hepatic resection and intraoperative contrast-enhanced ultrasonography. Oncology. 2010;78 Suppl 1:125-30. Epub 2010/07/17. doi: 10.1159/000315240. PubMed PMID: 20616594.

15. van Vledder MG, Torbenson MS, Pawlik TM, Boctor EM, Hamper UM, Olino K, et al. The effect of steatosis on echogenicity of colorectal liver metastases on intraoperative ultrasonography. Arch Surg. 2010;145(7):661-7. Epub 2010/07/21. doi: 10.1001/archsurg.2010.124. PubMed PMID: 20644129.

16. Ukimura O, Okihara K, Kamoi K, Naya Y, Ochiai A, Miki T. Intraoperative ultrasonography in an era of minimally invasive urology. International journal of urology : official journal of the Japanese Urological Association. 2008;15(8):673-80. Epub 2008/06/20. doi: 10.1111/j.1442-2042.2008.02090.x. PubMed PMID: 18564203.

17. Kane RA. Intraoperative ultrasonography: history, current state of the art, and future directions. Journal of ultrasound in medicine : official journal of the American Institute of Ultrasound in Medicine. 2004;23(11):1407-20. Epub 2004/10/23. PubMed PMID: 15498905.

18. Vahrmeijer AL, Hutteman M, van der Vorst JR, van de Velde CJ, Frangioni JV. Image-guided cancer surgery using near-infrared fluorescence. Nature reviews Clinical oncology. 2013;10(9):507-18. Epub 2013/07/25. doi: 10.1038/nrclinonc.2013.123. PubMed PMID: 23881033; PubMed Central PMCID: PMC3755013.

19. Nguyen QT, Tsien RY. Fluorescence-guided surgery with live molecular navigation--a new cutting edge. Nature reviews Cancer. 2013;13(9):653-62. Epub 2013/08/09. doi: 10.1038/nrc3566. PubMed PMID: 23924645.

20. Weissleder R, Mahmood U. Molecular Imaging. Radiology. 2001;219(2):316-33. doi: doi:10.1148/radiology.219.2.r01ma19316. PubMed PMID: 11323453.

21. Achilefu S. Lighting up tumors with receptor-specific optical molecular probes. Technology in cancer research & treatment. 2004;3(4):393-409. Epub 2004/07/24. PubMed PMID: 15270591.

22. Achilefu S, Bloch S, Markiewicz MA, Zhong T, Ye Y, Dorshow RB, et al. Synergistic effects of light-emitting probes and peptides for targeting and monitoring integrin expression. Proceedings of the National Academy of Sciences of the United States of America. 2005;102(22):7976-81. Epub 2005/05/25. doi: 10.1073/pnas.0503500102. PubMed PMID: 15911748; PubMed Central PMCID: PMC1142399.

23. Nie L, Chen M, Sun X, Rong P, Zheng N, Chen X. Palladium nanosheets as highly stable and effective contrast agents for in vivo photoacoustic molecular imaging. Nanoscale. 2014;6(3):1271-6. Epub 2013/12/10. doi: 10.1039/c3nr05468c. PubMed PMID: 24317132.

24. Troyan SL, Kianzad V, Gibbs-Strauss SL, Gioux S, Matsui A, Oketokoun R, et al. The FLARE Intraoperative Near-Infrared Fluorescence Imaging System: A First-in-Human Clinical Trial in Breast Cancer Sentinel Lymph Node Mapping. Ann Surg Oncol. 2009;16(10):2943-52. PubMed PMID: ISI:000270155200037.

25. Hirche C, Engel H, Kolios L, Cognie J, Hunerbein M, Lehnhardt M, et al. An experimental study to evaluate the Fluobeam 800 imaging system for fluorescence-guided lymphatic imaging and sentinel node biopsy. Surgical innovation. 2013;20(5):516-23. Epub 2013/01/01. doi: 10.1177/1553350612468962. PubMed PMID: 23275469.

26. Tobis S, Knopf JK, Silvers CR, Marshall J, Cardin A, Wood RW, et al. Near infrared fluorescence imaging after intravenous indocyanine green: initial clinical experience with open partial nephrectomy for renal cortical tumors. Urology. 2012;79(4):958-64. Epub 2012/02/18. doi: 10.1016/j.urology.2011.10.016. PubMed PMID: 22336035.

27. Gotoh K, Yamada T, Ishikawa O, Takahashi H, Eguchi H, Yano M, et al. A novel image-guided surgery of hepatocellular carcinoma by indocyanine green fluorescence imaging navigation. J Surg Oncol. 2009;100(1):75-9. Epub 2009/03/21. doi: 10.1002/jso.21272. PubMed PMID: 19301311.

28. Sielhorst T, Feuerstein M, Navab N. Advanced Medical Displays: A Literature Review of Augmented Reality. J Display Technol. 2008;4(4):451-67. doi: 10.1109/jdt.2008.2001575.

29. Levy ML, Chen JC, Moffitt K, Corber Z, McComb JG. Stereoscopic head-mounted display incorporated into microsurgical procedures: technical note. Neurosurgery. 1998;43(2):392-5. Epub 1998/08/08. PubMed PMID: 9696099.

30. Wanschitz F, Birkfellner W, Figl M, Patruta S, Wagner A, Watzinger F, et al. Computer-enhanced stereoscopic vision in a head-mounted display for oral implant surgery. Clinical oral implants research. 2002;13(6):610-6. Epub 2003/01/10. PubMed PMID: 12519335.

31. Kihara K, Fujii Y, Masuda H, Saito K, Koga F, Matsuoka Y, et al. New three-dimensional head-mounted display system, TMDU-S-3D system, for minimally invasive surgery application: procedures for gasless single-port radical nephrectomy. International journal of urology : official journal of the Japanese Urological Association. 2012;19(9):886-9. Epub 2012/05/17. doi: 10.1111/j.1442-2042.2012.03044.x. PubMed PMID: 22587397.

32. Salb T, Brief J, Hassfeld S, Dillmann R. See-through head-mounted display augmented reality for maxillofacial surgery. Biomedizinische Technik Biomedical engineering. 2002;47 Suppl 1 Pt 1:65-8. Epub 2002/11/28. PubMed PMID: 12451774.

33. Aidlen JT, Glick S, Silverman K, Silverman HF, Luks FI. Head-motion-controlled video goggles: preliminary concept for an interactive laparoscopic image display (i-LID). Journal of laparoendoscopic & advanced surgical techniques Part A. 2009;19(4):595-8. Epub 2009/08/13. doi: 10.1089/lap.2009.0123. PubMed PMID: 19670983.

34. Liu Y, Akers WJ, Bauer AQ, Mondal S, Gullicksrud K, Sudlow GP, et al. Intraoperative detection of liver tumors aided by a fluorescence goggle system and multimodal imaging. The Analyst. 2013;138(8):2254-7. Epub 2013/03/08. doi: 10.1039/c3an00165b. PubMed PMID: 23467534; PubMed Central PMCID: PMC3650133.

35. Liu Y, Bauer AQ, Akers WJ, Sudlow G, Liang K, Shen D, et al. Hands-free, wireless goggles for near-infrared fluorescence and real-time image-guided surgery. Surgery. 2011;149(5):689-98. Epub 2011/04/19. doi: 10.1016/j.surg.2011.02.007. PubMed PMID: 21496565; PubMed Central PMCID: PMC3079879.

36. Liu Y, Njuguna R, Matthews T, Akers WJ, Sudlow GP, Mondal S, et al. Near-infrared fluorescence goggle system with complementary metal-oxide-semiconductor imaging sensor and see-through display. Journal of biomedical optics. 2013;18(10):101303. Epub 2013/06/04. doi: 10.1117/1.JBO.18.10.101303. PubMed PMID: 23728180; PubMed Central PMCID: PMC3667841.

37. Flock ST, Jacques SL, Wilson BC, Star WM, van Gemert MJ. Optical properties of Intralipid: a phantom medium for light propagation studies. Lasers in surgery and medicine. 1992;12(5):510-9. Epub 1992/01/01. PubMed PMID: 1406004.

38. Filonov GS, Piatkevich KD, Ting LM, Zhang J, Kim K, Verkhusha VV. Bright and stable near-infrared fluorescent protein for in vivo imaging. Nature biotechnology. 2011;29(8):757-61. Epub 2011/07/19. doi: 10.1038/nbt.1918. PubMed PMID: 21765402; PubMed Central PMCID: PMC3152693.

39. Guo W, Zhang L, Ji J, Gao W, Liu J, Tong M. Evaluation of the benefit of using blue dye in addition to indocyanine green fluorescence for sentinel lymph node biopsy in patients with breast cancer. World journal of surgical oncology. 2014;12:290. Epub 2014/09/23. doi: 10.1186/1477-7819-12-290. PubMed PMID: 25239029; PubMed Central PMCID: PMC4182872.

40. Wishart GC, Loh SW, Jones L, Benson JR. A feasibility study (ICG-10) of indocyanine green (ICG) fluorescence mapping for sentinel lymph node detection in early breast cancer. European journal of surgical oncology : the journal of the European Society of Surgical Oncology and the British Association of Surgical Oncology. 2012;38(8):651-6. Epub 2012/06/19. doi: 10.1016/j.ejso.2012.05.007. PubMed PMID: 22704050.

41. Sugie T, Sawada T, Tagaya N, Kinoshita T, Yamagami K, Suwa H, et al. Comparison of the indocyanine green fluorescence and blue dye methods in detection of sentinel lymph nodes in early-stage breast cancer. Ann Surg Oncol. 2013;20(7):2213-8. Epub 2013/02/23. doi: 10.1245/s10434-013-2890-0. PubMed PMID: 23429938.

42. van der Vorst JR, Schaafsma BE, Verbeek FP, Hutteman M, Mieog JS, Lowik CW, et al. Randomized comparison of near-infrared fluorescence imaging using indocyanine green and 99(m) technetium with or without patent blue for the sentinel lymph node procedure in breast cancer patients. Ann Surg Oncol. 2012;19(13):4104-11. Epub 2012/07/04. doi: 10.1245/s10434-012-2466-4. PubMed PMID: 22752379; PubMed Central PMCID: PMC3465510.

Chapter 4: Optical-see through GAINS

This chapter is based on a pending article: Suman B. Mondal, Julie Margenthaler, Shengkui Gao, Nan Zhu, Walter J. Akers, Rongguang Liang, Viktor Gruev, and Samuel Achilefu. In vivo evaluation of an optical see-through binocular goggle augmented imaging and navigation system for real-time fluorescence-guided surgery for tumor resection, lymphatic tracking and sentinel lymph node mapping. *To be submitted.* I designed the experiments, conducted the preclinical studies, led efforts for the clinical studies, helped surgeons during clinical procedures, analyzed the data and wrote the manuscript.

4.1 Abstract

4.1.1 Background

Intraoperative near-infrared (NIR) fluorescence imaging using indocyanine green (ICG) can potentially improve sentinel lymph node (SLN) mapping in breast cancer patients. However, it is not widely used due to limitations of NIR FGS systems.

4.1.2 Methods

We evaluated in vivo an optical see-through (OST) goggle augmented imaging and navigation system (GAINS) which had a minimal hardware footprint and allowed direct visual access to the surgical field while projecting fluorescence information. For pre-clinical validation, three mice with subcutaneous tumors were injected with a tumor targeted NIR contrast agent LS301 (60μM, 100μl) and subjected to fluorescence-guided surgery. Three 35-kg female Yorkshire pigs received 300 ul of 5 mg/ml ICG, intradermally at their hind leg and lymphatics were tracked to the popliteal lymph node from the injection site. Four consecutive breast cancer patients scheduled to undergo partial mastectomy and SLN biopsy received ^{99m}Tc-sulfur and 5ml, 5mg/ml ICG retroareolarly. SLN biopsy was done using handheld gamma probe and OST GAINS enabled ICG imaging.

4.1.3 Results

The OST GAINS allowed direct visual access to the surgical bed while projecting fluorescence information directly to surgeon’s eyes. It guided complete tumor resection in the subcutaneous mouse model of cancer with a SBR of 1.45 ± 0.19. It non-invasively tracked lymphatics in pigs with a SBR of 2.74 ± 1.74 and accurately identified 4 popliteal LNs in three pigs with a SBR of 3.19 ± 1.81. A total of 11 SLNs were identified from 4 patients. Radioactive tracking SLN identified 9 (81.82%) SLNs with a detection sensitivity of 86.67± 0.27% and the OST GAINS

identified 11 (100%) SLNs with a detection sensitivity of 100% and SBR of 2.14±0.83. There was no statistically significant difference in the detection sensitivities of the two methods (P=0.374).

4.1.4 Conclusions

The see-through GAINS prototype is feasible for use in the operating room for NIR FGS for lymphatic tracking transcutaneously and SLN mapping in breast cancer patients.

4.2 Introduction

Sentinel lymph node (SLN) mapping(1) is the standard-of-care in breast cancer for disease staging(2). Conventional radioactive and blue dye tracking can achieve 95-97% SLN detection(3-6). However, radioactive tracers expose patients and caregivers to ionizing radiation, require involvement of nuclear medicine trained personnel, increasing costs and difficulty in scheduling surgery. Additionally, radioactive tracers may not be available everywhere readily. Blue dyes stain the tissue and so are not appropriate for visualizing deep seated lymph nodes. They also pose the risk of anaphylactic reactions in 1-2% of patients.

Near-infrared (NIR) fluorescence using indocyanine green (ICG) injection has been shown to enable intraoperative SLN mapping(7-15). Several intraoperative ICG imaging systems have been developed and tested clinically(13, 16-18). However, they often suffer from a large hardware footprint that may be difficult to accommodate in the crowded operating room (OR). The field of view (FOV) of the system cameras are usually different than the surgeon’s FOV which necessitates a learning curve for system usage. These systems display images on a computer monitor that requires the surgeon to look away from the surgical bed. Additionally, handheld devices require the surgeon to stop working or need someone from the surgical team to operate the instrument. The combination of these factors disrupt the normal surgical workflow and may increase surgery time.

In our previous work we reported the goggle augmented imaging and navigation system (GAINS) for real-time fluorescence-guided surgery (FGS) that can detect both anatomic color reflectance information and NIR fluorescence from contrast agents, displaying accurately aligned superimposed color-NIR images to a video see-through (VST) head-mounted display (HMD) worn by the surgeon(19). The VST GAINS guided complete tumor resection in a subcutaneous and metastatic mouse model of cancer using a tumor-taregeted NIR contrast agent and identified SLNs using ICG fluorescence in 10 breast cancer and 5 melanoma patients with 100% sensitivity, compared to 93% and 96% detection sensitivity for blue dye and radioactive tracking. However, the opaque VST HMD did not allow direct visual access to the surgical field, which limited its usage for only SLN visualization and not for tissue resection.

Based on surgeon feedback, we have developed an optical see-through (OST) HMD based GAINS prototype that allows direct visualization of the surgical bed with provision to project fluorescence information directly to the user’s eyes(20). In this study we performed in vivo evaluation of the OST GAINS prototype in a subcutaneous mouse model of cancer for guiding tumor resection, lymphatic tracking in a porcine model and SLN mapping in human breast cancer patients.

4.3 Methods

4.3.1 Fluorescence-Guided Surgery

Real-time intraoperative fluorescence-guided surgery was performed using the OST GAINS prototype (**Fig. 41**) as described earlier(20). Briefly, it uses a focus-adjustable single camera to capture color reflectance and NIR fluorescence images, which are processed to generate an accurately aligned color-NIR superimposed image. The color, NIR or superimposed images are directly projected to the user's eyes via a custom OST HMD. This OST HMD allows direct visual access to the surgical field, with contrast- and transparency-adjusted projection of augmented fluorescence information. NIR illumination was provided by a 780 nm, 0.8 W laser (BW Tek), while white light illumination is provided by a surgical light covered with a short-pass film filter(21) (**Fig. 40**). The optical head for the NIR laser was mounted on a flexible neck, allowing easy movement to point it on the surgical bed as necessary. Adjusting the laser direction took 1-3 minutes. However this was usually done when the surgeon was using the gamma probe to locate the SLN, since the NIR channel even if it is not being visibly projected to the surgeon's HMD, can be seen on the laptop as it is continuously being recorded. So light adjustment was done simultaneously with regular surgical processes and did not add significant time to the overall surgery. The pointing red laser on top of the NIR laser optics allowed us to visible know where the invisible NIR laser was pointing. The camera mounted HMD (worn on head) and pre-processing module (carried in a wais pouch under the sterile gown) constitute the wearable part of the system. The laptop used for final processing (carried on a cart) and illumination modules form separate standalone parts of the system.

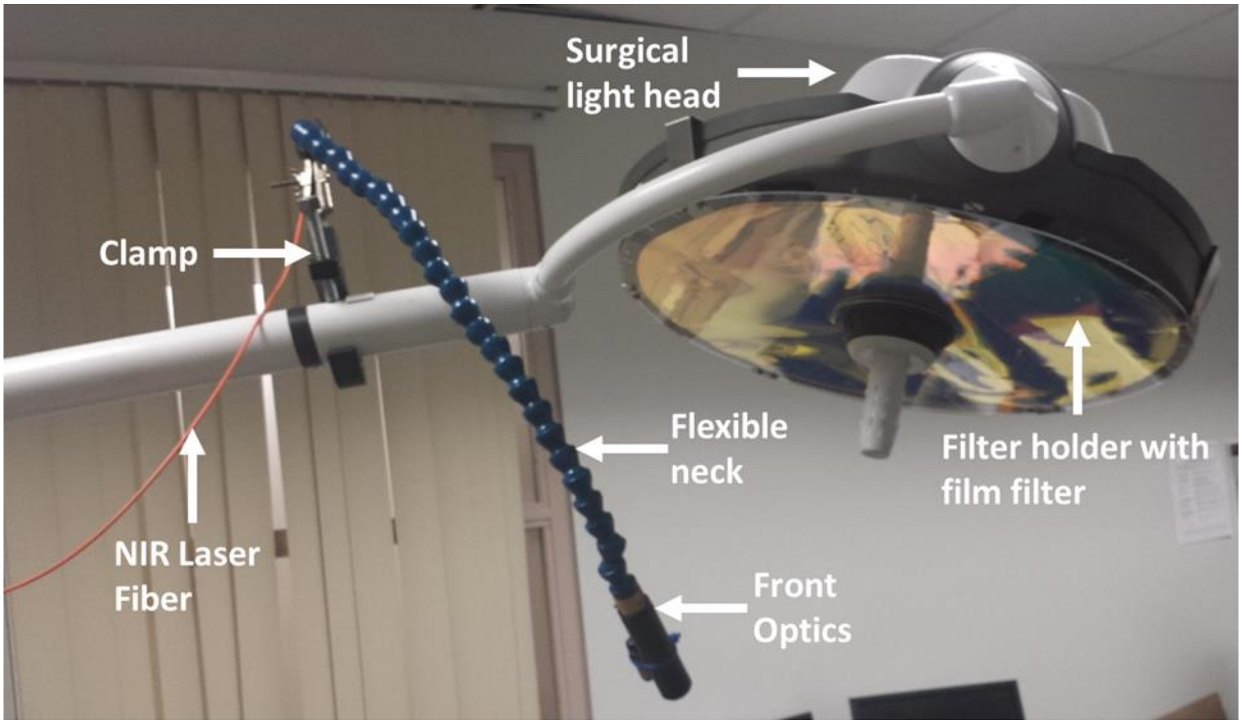

Figure 40: The illumimation module.

4.3.2 Animal Studies

All animal studies were approved by the Washington University Animal Studies Committee. TO evaluate tumor resection, a subcutaneous mouse tumor xenograft model was developed by injecting 10^6 PNEC cells in left hind flanks of three 6 week-old Balb/c nu/mu mice. They were injected with a tumor-targeted NIR contrast agent LS301 (60 µl, 100µl) via tail vein injection, 10-12 days after tumor implantation. At 24 h post-injection, the mice were anaesthetized using 2% isolfluorane and OST GAINS prototype was used to visualize NIR fluorescence from the tumors and guide surgical resection. After debulking the tumor bed was surveyed for presence of residual fluorescence and all suspected tumor tissue were resected. The animals were sacked by cervical dislocation, its organs were harvested and resected tissue were preserved for frozen section histopathologic analysis.

To evaluate SLN biopsy, three 35-kg female Yorkshire pigs were premedicated with atropine (0.04 mg/kg given intramuscularly) and a cocktail consisting of Telazol (tiletamine and zolazepam), ketamine, and xylazine (1 mL/50 lb [22.7 kg] of body weight given intramuscularly) prior to induction and maintenance of anesthesia with isoflurane (1-5% v/v in O_2) by intubation. Vital signs were monitored during anesthesia. ICG (5 mg/ml) was dissolved in sterile water (Sigma Aldrich, St. Louis, MO) and injected intradermally (0.3 ml) into the leg using a 29-gauge needle insulin syringe. The lymphatic movement of the ICG were tracked using the OST GAINS prototype in real-time, transcutaneously to locate the popliteal LN and guide its resection. The resected LN was preserved in formalin. All pigs were euthanized after FGS by intravenous potassium chloride.

4.3.3 Pilot Human Study

This pilot human study to evaluate clinical feasibility of using the GAINS prototype for intraoperative visualization of SLNs and comparison with conventional radioactive tracking was approved by the Institutional Review Board at Washington University and was performed in accordance with the approved ethical guidelines. The study was registered on clinicaltrials.gov website (NCT02316795). Women, 18 years or older with newly diagnosed clinically node-negative breast cancer, negative nodal basin clinical exam and scheduled to undergo partial mastectomy with SLN biopsy were eligible for the study. Exclusion criteria were contraindication to surgery, receiving any investigational agents, history of allergic reaction to iodine, seafood and ICG, presence of uncontrolled inter-current illness, pregnant or breastfeeding. All patients gave informed consent for this HIPAA-compliant study and data was deidentified.

Patients received ^{99m}Tc-sulfur colloid (834 µCi) 2- 3 hours before surgery for needle localization and then brought to the operating room. Patients were injected with ICG (5mg/mL; 5 mL) in the retroareolar breast, followed by site massage for 5 min. About 10-15 min after injection, the surgeon performed standard-of-care partial mastectomy and the tumor mass was removed with a rim of grossly normal tissue. The tissue was marked with sutures to indicate orientation before submission for standard-of-care histologic evaluation. A handheld gamma probe was used by the surgeon to identify the site of axillary incision. The exposed SLNs were examined for radioactivity and then visualized using the OST GAINS via ICG fluorescence. The cavity was inspected with the GAINS to identify other fluorescent SLNs, which were then checked for radioactivity, before excision and preservation for histology. The surgeon wore the waist pouch carrying the image pre-processing module for the OST GAINS under the sterile gown. The camera mounted HMD was fitted onto the surgeon’s head and connections to the camera, laptop, HMD and power sources were established without compromising the sterile field. In all cases, the GAINS was operated at 24p fps with a 40-millisecond acquisition time. NIR-white light illumination during system usage was provided by our illumination module. A remote laptop used for final image processing, mirrored the surgeon’s view. The camera focus, projected fluorescence contrast and transparency of pseudocolored fluorescence overlay was adjusted using the laptop based on surgeon’s verbal feedback to ensure optimal viewing experience.

4.3.4 Statistical Analysis

Statistical analysis was performed using OriginPro8 (OriginLab Corp., Northampton, MA). Signal-to-background ratios (SBRs), and sensitivity were expressed as mean and standard deviation. Paired t-tests were used to compare fluorescence signal for non-invasive and invasive imaging in the mouse model of tumor, fluorescence signal during transcutaneous lymphatic tracking and exposed lymph nodes in pigs and sensitivity of SLN detection by GAINS and radioactive tracking. $P < 0.05$ were considered statistically significant.

4.4 Results

4.4.1 Tumor resection in mice

The OST GAINS allowed direct visual access to the surgical bed while projecting real-time high-contrast fluorescence information to guide complete tumor resection in three mice (**Fig. 41**). Transcutaneous tumor fluorescence was observed with a SBR of 1.41±0.24 and guided the incision to deflect the skin and expose the tumor. Exposed tumor fluorescence was observed with a SBR of 1.49±0.1 and guided tumor resection (**Fig. 42**). Exposed tumor fluorescence was significantly higher than transcutaneous tumor fluorescence ($P<0.05$) as expected due to optical scattering by tissue. However the background signal after skin deflection was also significantly higher than that for intact skin ($P<0.1$) (**Table 9**), probably because the peritoneum is more reflective than the skin. There was no statistically significant difference between the SBR for transcutaneous and exposed tumor fluorescence ($P=0.37$) (**Fig. 44**). Survey of the tumor bed for residual fluorescence ensured no suspected tumor tissue was left behind. All tissue were confirmed to be cancerous through histology.

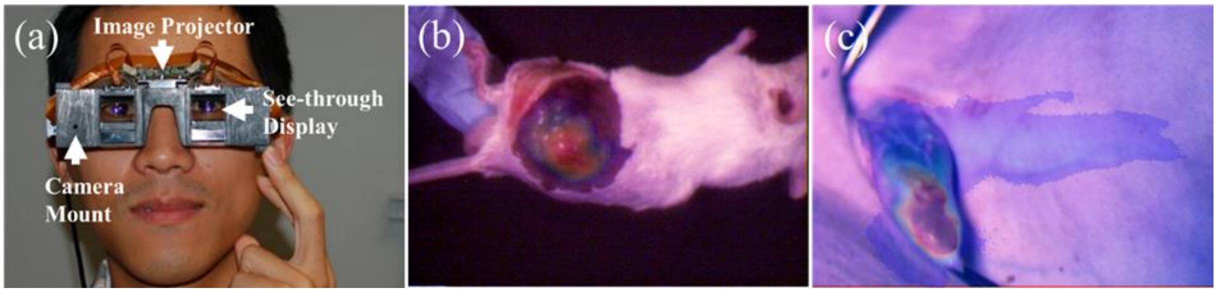

Figure 41: Imaging system and preclinical validation **a** OST GAINS prototype head mounted display **b** Image-guided tumor resection in a mouse model of cancer **c** Lymphatic tracking and LN detection in Yorkshire pigs.

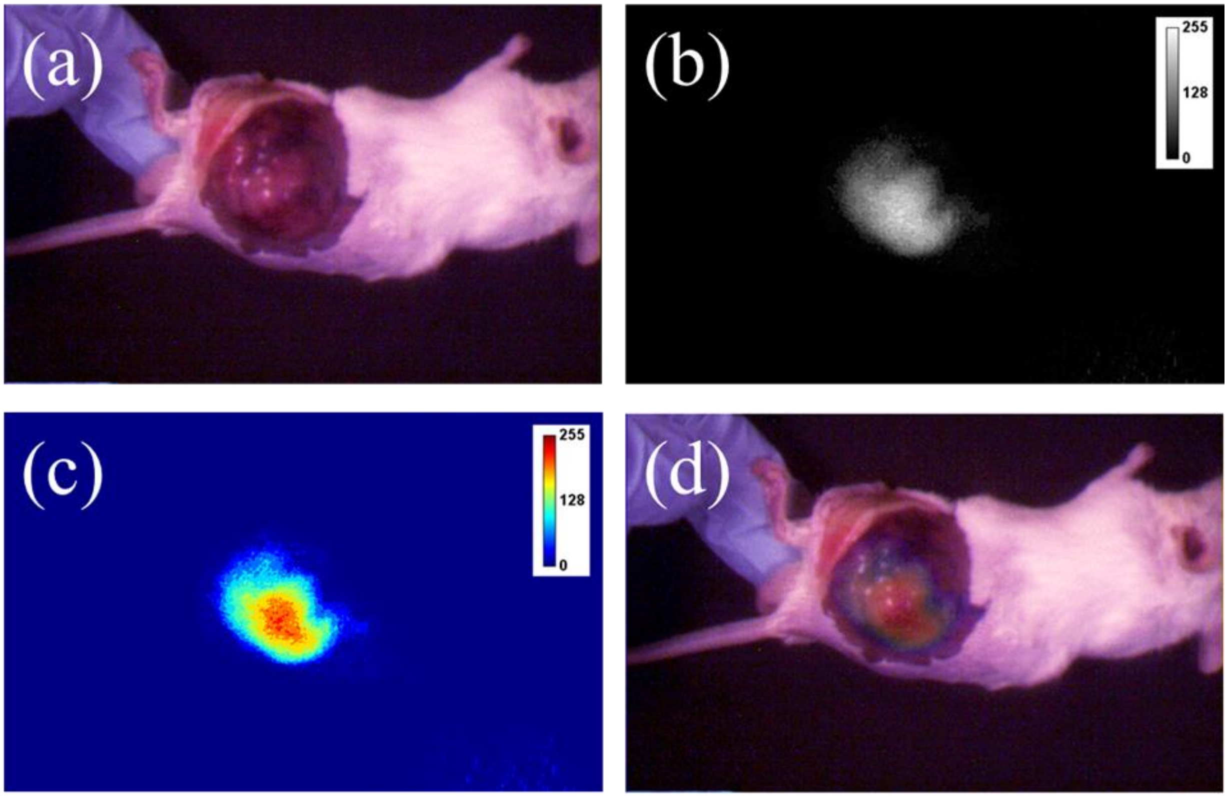

Figure 42: Fluorescence-guided surgery in a mouse model of cancer. **a** Color image of mouse with exposed tumor. **b** Grayscale NIR image showing high fluorescence from the tumor. **c** Pseudocolored fluorescence image. **d** Superimposed color-fluorescence image at 40% opacity of projected fluorescence.

Table 9: Statistical analyses.

Characteristic	Mean ± SD	P value
Mouse study		
Transcutaneous tumor signal	24.18 ± 5.49	0.03961
Exposed tumor signal	26.62 ± 2.1	
Transcutaneous background signal	16.58 ± 1.12	4.71768E-5
Exposed background signal	17.83 ± 0.54	
Transcutaneous tumor SBR	1.45 ± 0.24	0.3681
Exposed tumor SBR	1.49 ± 0.13	
Overall SBR	1.45 ± 0.19	
Pig study		
Transcutaneous lymphatics signal	99.04 ± 70.12	1.88848E-4
Exposed LN signal	123.89 ± 77.23	
Transcutaneous lymphatics background signal	34.25 ± 7.68	1.12583E-13
Exposed LN background signal	37.44 ± 6.97	
Transcutaneous lymphatics SBR	2.74 ± 1.74	0.01082
Exposed LN SBR	3.19 ± 1.81	
Human study		
SLN signal	69.05 ± 39.9	
SLN background signal	30.95 ± 13.15	
SLN SBR	2.14 ± 0.82	
SLN detection sensitivity by radioactive tracking	86.67 ± 0.3 %	0.3739
SLN detection sensitivity by OST GAINS and ICG	100%	

4.4.2 Lymphatic Tracking in Pigs

Using ICG fluorescence, the GAINS prototype allowed real-time transcutaneous lymphatic tracking in three pigs, from the injection site in the leg to the popliteal LN (**Fig 41**) with a SBR of 2.1±0.84. Along with surgeon's a priori knowledge of porcine anatomy and palpation, the NIR lymphatic tracking identified the location of the popliteal LN (**Fig. 43**) and guided the incision for its resection (**Vid. 1**) without the use of radioactive tracking. A total of 4 popliteal LNs were detected with a SBR of 3.87±1.94 and allowed their accurate resection. The exposed LN fluorescence signal as well as background tissue signals were significantly higher than the transcutaneous fluorescence from lymphatics and background from skin ($P<0.1$) (**Table 9**) as seen in the mouse model of tumor. The LN SBR was significantly higher than the SBR for transcutaneous lymphatic tracking ($P<0.05$) (**Fig. 44**).

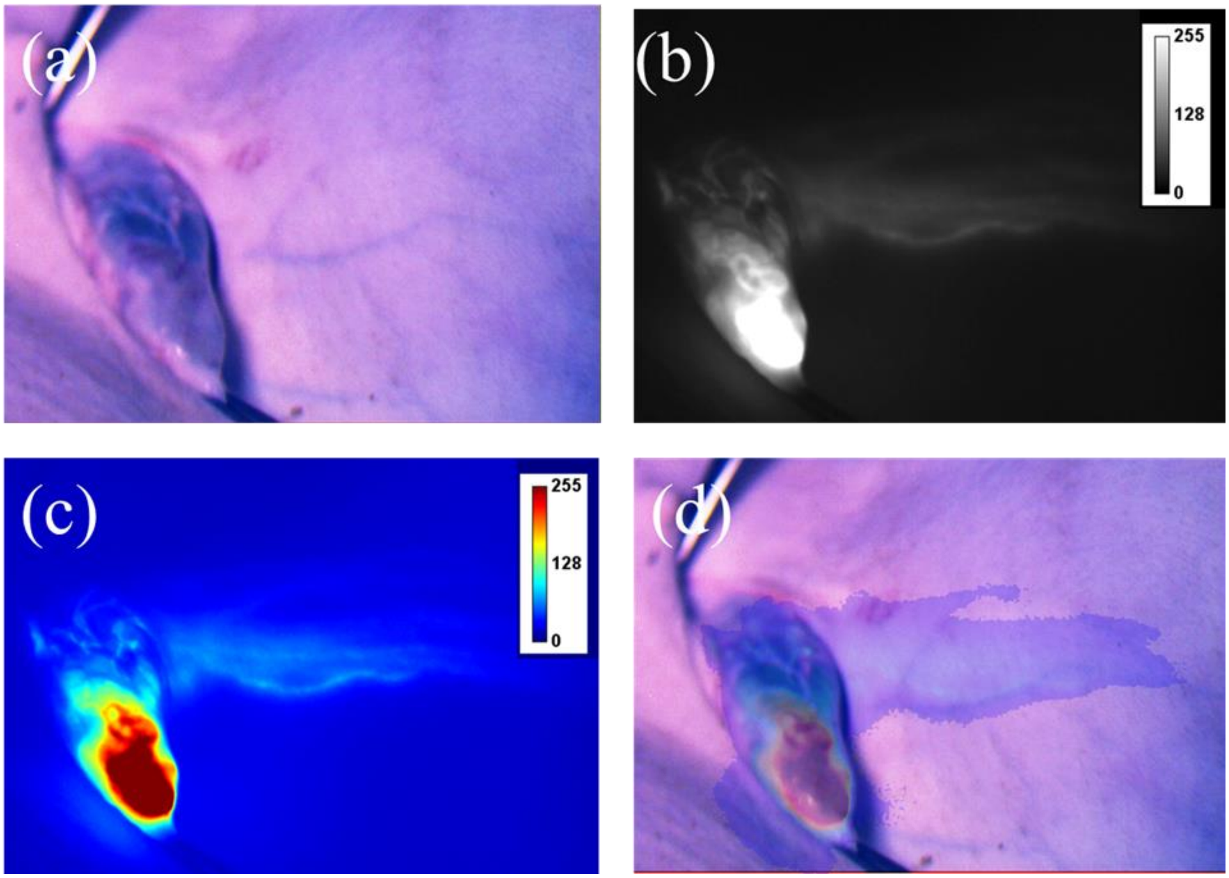

Figure 43: Lymphatic tracking and LN detection in pigs. **a** Color image showing exposed popliteal LN. **b** Grayscale fluorescence image showing lymphatic drainage transcutaenously and high fluorescence in the LN. **c** Pseudocolored fluorescence image. **d** Superimposed color-fluorescence image as seen by surgeon with projected fluorescence at 40% opacity.

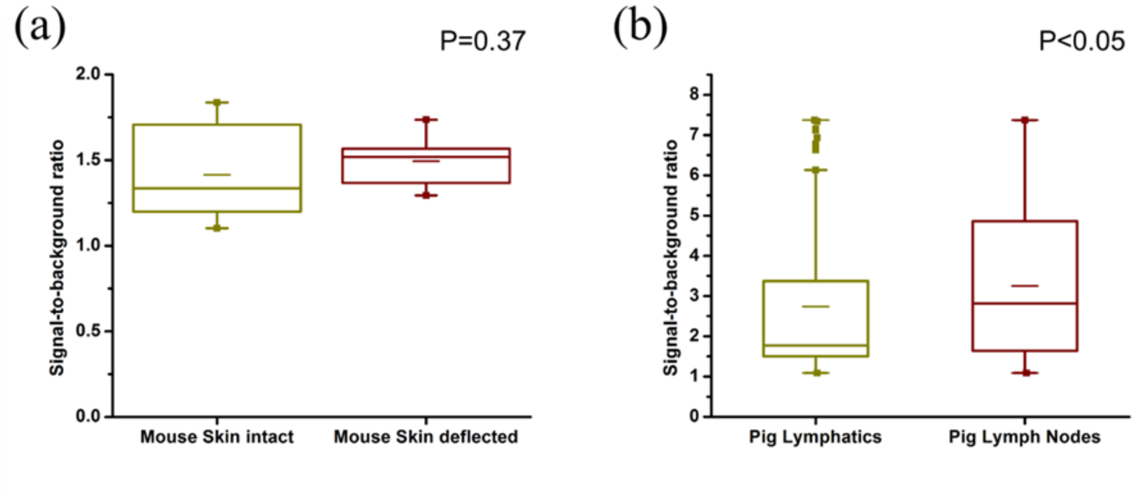

Figure 44: Signal-to-background ratios. **a** SBR for tumors detected in mouse model of cancer with skin intact and skin deflected. **b** SBR for transcutaneous lymphatic tracking and exposed lymph nodes imaged in Yorkshire pigs.

4.4.3 SLN Biopsy in Human Breast Cancer Patients

The study aimed to study to evaluate clinical feasibility of the see-through GAINS prototype in guiding SLN biopsy using ICG fluorescence in breast cancer patients, in comparison to conventional radioactive tracking method. Four consecutive patients underwent standard-of-care partial mastectomy with wire localization and SLN biopsy using ^{99m}Tc-sulfur with the addition of OST GAINS guided SLN visualization using ICG fluorescence. The patient and tumor characteristics are listed in **Table 10**. In one patient the partial mastectomy was also carried out by the surgeon while wearing the OST GAINS prototype, using the unhindered visual access for standard-of-care partial mastectomy surgical procedure. The fluorescence information was projected as and when the surgeon requested, for visualizing the SLN. No adverse reactions associated with the use of ICG or the OST GAINS prototype occurred. No postoperative complications of the SLN procedure were observed.

Table 10: Patient and tumor characteristics.

Characteristic	N
No. of patients	4
Age (median, range)	63.5, (39-76)
Diagnosis	
Left Breast Cancer	2 (50%)
Right Breast Cancer	1 (25%)
Bilateral Breast Cancer	1 (25%)
Type of operation	
Partial mastectomy with needle localization	4 (80%)
Partial mastectomy with ultrasound guidance	1 (20%)
Partial mastectomy with GAINS guidance	1 (20%)
No. of tumors excised	5
Tumor type	
Invasive ductal carcinoma	5 (100%)
Tumor size (mm) (median, range)	14 (9-28)
Tumor localization	
8’o clock	1 (20%)
9’o clock	1 (20%)
10’o clock	1 (20%)
Unspecified	2 (40%)
Histological grade	
I	3 (60%)
III	2 (40%)
Margin status	

Positive	2 (40%)
Negative	3 (60%)
Ductal carcinoma in situ status	
Present	4 (80%)
<5% of total tumor tissue	3 (75%)
10-15% of total tumor tissue	1 (25%)
DCIS nuclear grade	
Low	1 (25%)
Intermediate	2 (50%)
High	1 (25%)
Final tumor staging	
Stage I A	4 (80%)
Stage II B	1 (20%)

A total of 11 SLNs were identified from 4 patients with a mean of 2.2 ± 0.98 SLNs identified per patient (**Table 11**). Radioactive tracking identified 9 (81.82%) of SLNs with a detection sensitivity of 86.67± 0.27%. The OST GAINS, using ICG fluorescence, identified 11 (100%) of the SLNs with a detection sensitivity of 100% (**Fig 45**). The detection sensitivity of the fluorescence method was not significantly different than that of the radioactive tracking (P=0.374). The fluorescence from the SLNs were observed with a SBR of 2.14±0.83 (**Table 9**).

Table 11: SLN biopsy results.

Characteristic	N
Total no of sentinel lymph node biopsies	5
Type of procedure	
SLN biopsy with radioactive tracking	5 (100%)
SLN biopsy with ICG and GAINS guidance	5 (100%)
Injection site ICG	
Retroareolar	5 (100%)
SLNs identified	
Total	11
Mean ± SD	2.2 ± 0.98
Method of detection	
Radioactive tracking	9 (81.82%)
ICG-OST GAINS	11 (100%)
Detection sensitivity	
Radioactive tracking, mean ± SD	86.67 % ± 0.27
ICG-OST GAINS, mean ± SD	100% ± 0.0
SBR for fluorescence detection, mean ± SD	2.14 ± 0.83
Histology of SLN	
Negative	10 (90.91%)
Macrometastases	1 (9.09%)

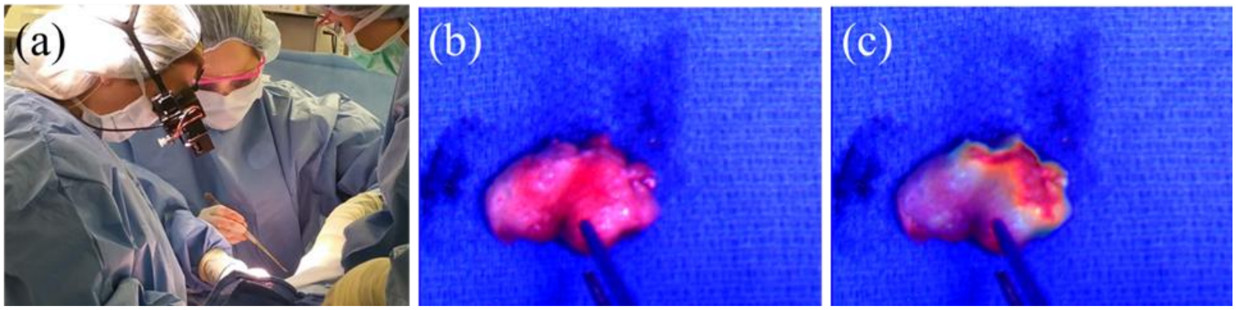

Figure 45: Fluorescence image-guided SLN mapping. **a** The surgeon wearing the GAINS during SLN visualization in a breast cancer patient. **b** The color image of the excised SLN. **c** The superimposed color-fluorescence image of the excised SLN as seen by the surgeon.

The user experience was very favorable due to the unhindered visual access to the surgical field (**Fig 45**). The contrast of projected fluorescence on to the surgeon's eyes were controlled remotely based on surgeon feedback and ambient to light to ensure fluorescence information availability as well as tissue visibility (**Fig 46**). This allowed the surgeon to perform tissue incision and resection while wearing the GAINS HMD with minimal fluorescence projection contrast with the option of turning on high-contrast user requested contrast of projected fluorescence as required. Additionally this enabled all FGS to be performed with the surgical light on. These factors in combination with the compact, wearable and portable system design, allowed easy and non-disruptive integration in to the normal surgical workflow. Some fogging was observed after 15 minutes of usage due to breath condensation on the inner surface of the HMD. This was easily addressed by using anti-fogging face masks with adhesive upper lining to seal in the warm breath, which prevented fogging for up to 45 minutes of continued usage.

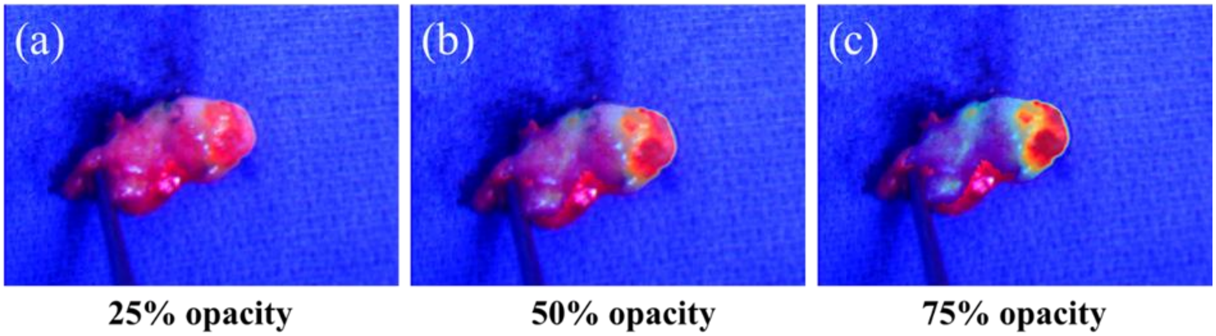

Figure 46: Variable contrast of projected fluorescence on an excised SLN as viewed by the surgeon with projected fluorescence at **a** 25% opacity. **b** 50% opacity. **c** 75% opacity.

4.5 Discussion

NIR FGS for SLN mapping has emerged as an important tool recently. It is currently limited by the standalone or handheld FGS systems that are not able to match the camera and user field of view, are bulky and show the information in a remote display. The combination of these factors disrupt the normal surgical workflow and has led to minimal adaptation of FGS in clinics beyond research initiatives and small clinical trials. Disruptive information display may be addressed by using a HMD(22, 23). There has been a lot of interest in doing surgical planning and navigation using HMDs especially in the neurosurgical community(24). It has been shown that a VST HMD can improve surgical performance in endoscopic surgeons(25-27). In our previous work we applied a VST HMD to cancer surgery and demonstrated that the video see-through GAINS has very sensitive SLN detection comparable to conventional radioactive and blue dye tracking(19). However it was limited due to no direct visual access to the surgical field. The advantages of OST HMDs are well accepted(22) and its ability to provide direct visual access to the surgical field is critical for open surgery. However very limited work has been done on using OST HMDs for surgical navigation(28) due to technical challenges involved(22, 23). We reported the first

OST HMD developed specifically for fluorescence-guided surgery(20) and this is the first report to the best of our knowledge of clinical evaluation of an OST HMD based system for fluorescence-guided SLN mapping and cancer surgery. Our current study demonstrates that the OST GAINS, by providing direct visual access to the surgical field with option of projected fluorescence information significantly improves the usability of the system. The see-through feature allows direct visualization with the provision of fluorescence information whenever needed. In one patient the OST GAINS was used by the surgeon throughout the partial mastectomy using the direct visual access, while during the SLN biopsy the fluorescence projection was turned on as and when requested by the surgeon. The surgeon had the option of having the grayscale fluorescence, pseducolored fluorescence (blue through red color indicating low through highest NIR fluorescence intensity) or superimposed pseudcolored fluorescence-color images to be projected (**Fig. 47**). All surgeries were done with OR surgical lights on, which did not put major hindrance to the NIR imaging, unlike other FGS systems that require to turn off the surgical light. This allowed seamless integration of FGS in to the regular surgical workflow.

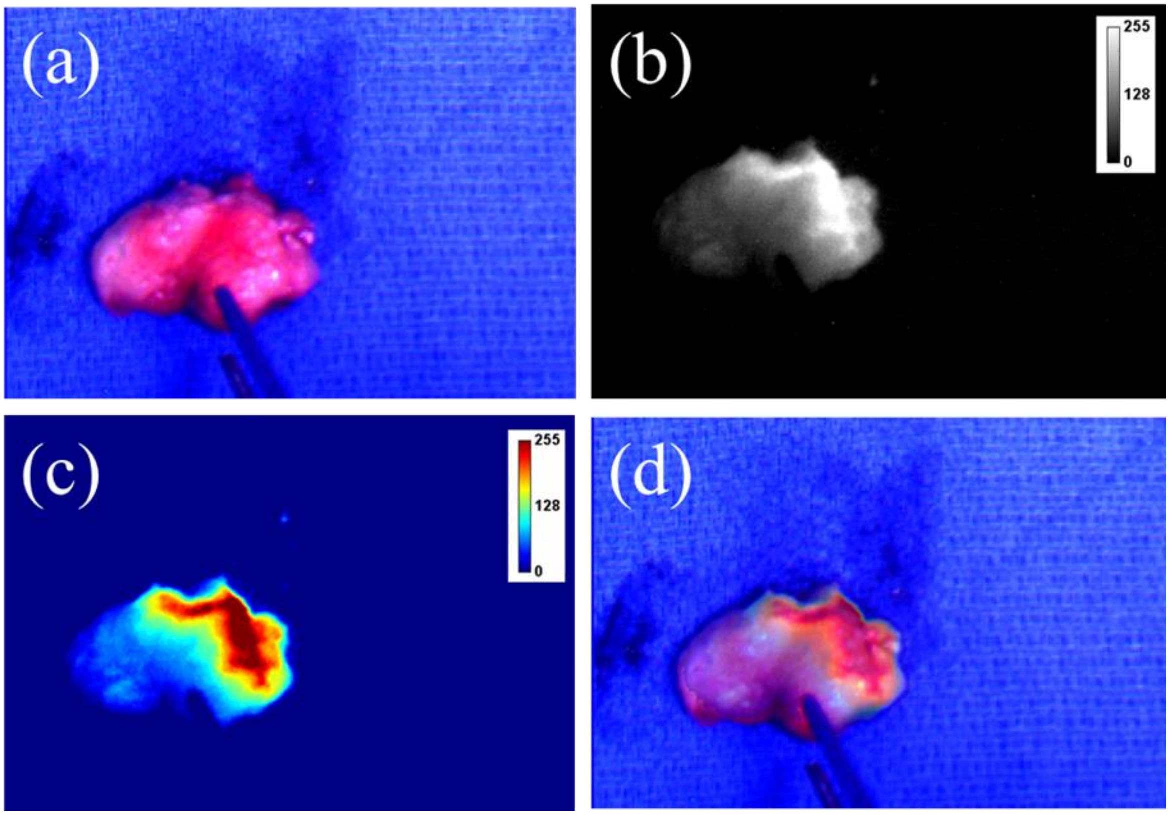

Figure 47: Fluorescence-guided SLN visualization during. **a** Color image of excised SLN. **b** Grayscale NIR image showing areas of high fluorescence in the SLN. **c** Pseudocolored fluorescence image of the SLN. **d** Superimposed color-fluorescence image at 40% opacity of projected fluorescence.

A major issue in FGS is complex image adjustment based on surgeon feedback, without disrupting the surgical workflow or compromising sterility. Solutions like foot pedals cannot implement complex image adjustments, while voice commands may have difficulty operating in the high noise atmosphere in the operating room. In our system the surgeon’s view is mirrored on the remote laptop and a custom graphical user interface (GUI) allowed real-time modifications of imaging parameters by a member of the surgical team to incorporate surgeon feedback immediately, without stopping the surgery, while ensuring highest quality user experience. Camera focus was adjusted to compensate for large head movements and to ensure the image was always in focus. Contrast of the projected fluorescence was adjusted as requested by the surgeon to ensure optimal visibility of fluorescence information on the HMD. Additionally the built-in fail-safe of the see-through feature can allow surgeons to carry-on regular surgery in case of system failure.

The OST GAINS was able to guide complete tumor resection in a mouse model of tumor. It also allowed non-invasive transcutaneous lymphatic tracking in pigs and allowed identification of the sentinel lymph node with fluorescence guidance only. Recent studies have reported the feasibility of using ICG for SLN mapping and our results agree well with these studies. Our results indicate that it is feasible to detect SLNs with the same sensitivity as radioactive tracking. Though, our patient data set is very small and we would need a larger patient study to support our statement, our initial findings are very encouraging.

The system currently performs final image processing on the laptop, tethering the surgeon to the cart carrying the laptop using a wired connection. Additionally, a mismatch in the perceived distance of the projected fluorescence and actual object distance as seen by the surgeon may cause parallax. Efforts are currently under way to ensure complete onboard image processing, with wirelsess data and GUI transmission to the laptop as well as to ensure minimal parallax by remote adjustment of perceived distance of projected fluorescence images.

4.6 Acknowledgements

Funding for this project was through a grant from the US National Institutes of Health (NCI R01 CA171651 and P50 CA094056).

4.7 References

1. Giuliano AE, Kirgan DM, Guenther JM, Morton DL. Lymphatic mapping and sentinel lymphadenectomy for breast cancer. Annals of surgery. 1994;220(3):391-8; discussion 8-401. Epub 1994/09/01. PubMed PMID: 8092905; PubMed Central PMCID: PMC1234400.

2. Cox CE, Pendas S, Cox JM, Joseph E, Shons AR, Yeatman T, et al. Guidelines for sentinel node biopsy and lymphatic mapping of patients with breast cancer. Annals of surgery. 1998;227(5):645-51; discussion 51-3. Epub 1998/05/30. PubMed PMID: 9605656; PubMed Central PMCID: PMC1191339.

3. Goyal A, Newcombe RG, Chhabra A, Mansel RE, Group AT. Factors affecting failed localisation and false-negative rates of sentinel node biopsy in breast cancer--results of the ALMANAC validation phase. Breast cancer research and treatment. 2006;99(2):203-8. Epub 2006/03/17. doi: 10.1007/s10549-006-9192-1. PubMed PMID: 16541308.

4. Krag DN, Anderson SJ, Julian TB, Brown AM, Harlow SP, Ashikaga T, et al. Technical outcomes of sentinel-lymph-node resection and conventional axillary-lymph-node dissection in patients with clinically node-negative breast cancer: results from the NSABP B-32 randomised phase III trial. The Lancet Oncology. 2007;8(10):881-8. Epub 2007/09/14. doi: 10.1016/S1470-2045(07)70278-4. PubMed PMID: 17851130.

5. Straver ME, Meijnen P, van Tienhoven G, van de Velde CJ, Mansel RE, Bogaerts J, et al. Sentinel node identification rate and nodal involvement in the EORTC 10981-22023 AMAROS trial. Annals of surgical oncology. 2010;17(7):1854-61. Epub 2010/03/20. doi: 10.1245/s10434-010-0945-z. PubMed PMID: 20300966; PubMed Central PMCID: PMC2889289.

6. Zavagno G, De Salvo GL, Scalco G, Bozza F, Barutta L, Del Bianco P, et al. A Randomized clinical trial on sentinel lymph node biopsy versus axillary lymph node dissection

in breast cancer: results of the Sentinella/GIVOM trial. Annals of surgery. 2008;247(2):207-13. Epub 2008/01/25. doi: 10.1097/SLA.0b013e31812e6a73. PubMed PMID: 18216523.

7. Hirche C, Murawa D, Mohr Z, Kneif S, Hunerbein M. ICG fluorescence-guided sentinel node biopsy for axillary nodal staging in breast cancer. Breast cancer research and treatment. 2010;121(2):373-8. Epub 2010/02/09. doi: 10.1007/s10549-010-0760-z. PubMed PMID: 20140704.

8. Hojo T, Nagao T, Kikuyama M, Akashi S, Kinoshita T. Evaluation of sentinel node biopsy by combined fluorescent and dye method and lymph flow for breast cancer. Breast. 2010;19(3):210-3. Epub 2010/02/16. doi: 10.1016/j.breast.2010.01.014. PubMed PMID: 20153649.

9. Kitai T, Inomoto T, Miwa M, Shikayama T. Fluorescence navigation with indocyanine green for detecting sentinel lymph nodes in breast cancer. Breast cancer. 2005;12(3):211-5. Epub 2005/08/20. PubMed PMID: 16110291.

10. Murawa D, Hirche C, Dresel S, Hunerbein M. Sentinel lymph node biopsy in breast cancer guided by indocyanine green fluorescence. The British journal of surgery. 2009;96(11):1289-94. Epub 2009/10/23. doi: 10.1002/bjs.6721. PubMed PMID: 19847873.

11. Sevick-Muraca EM, Sharma R, Rasmussen JC, Marshall MV, Wendt JA, Pham HQ, et al. Imaging of lymph flow in breast cancer patients after microdose administration of a near-infrared fluorophore: feasibility study. Radiology. 2008;246(3):734-41. Epub 2008/01/29. doi: 10.1148/radiol.2463070962. PubMed PMID: 18223125; PubMed Central PMCID: PMC3166516.

12. Tagaya N, Yamazaki R, Nakagawa A, Abe A, Hamada K, Kubota K, et al. Intraoperative identification of sentinel lymph nodes by near-infrared fluorescence imaging in patients with

breast cancer. American journal of surgery. 2008;195(6):850-3. Epub 2008/03/21. doi: 10.1016/j.amjsurg.2007.02.032. PubMed PMID: 18353274.

13. Troyan SL, Kianzad V, Gibbs-Strauss SL, Gioux S, Matsui A, Oketokoun R, et al. The FLARE intraoperative near-infrared fluorescence imaging system: a first-in-human clinical trial in breast cancer sentinel lymph node mapping. Annals of surgical oncology. 2009;16(10):2943-52. Epub 2009/07/08. doi: 10.1245/s10434-009-0594-2. PubMed PMID: 19582506; PubMed Central PMCID: PMC2772055.

14. Mieog JS, Troyan SL, Hutteman M, Donohoe KJ, van der Vorst JR, Stockdale A, et al. Toward optimization of imaging system and lymphatic tracer for near-infrared fluorescent sentinel lymph node mapping in breast cancer. Annals of surgical oncology. 2011;18(9):2483-91. Epub 2011/03/02. doi: 10.1245/s10434-011-1566-x. PubMed PMID: 21360250; PubMed Central PMCID: PMC3139732.

15. van der Vorst JR, Schaafsma BE, Verbeek FP, Hutteman M, Mieog JS, Lowik CW, et al. Randomized comparison of near-infrared fluorescence imaging using indocyanine green and 99(m) technetium with or without patent blue for the sentinel lymph node procedure in breast cancer patients. Annals of surgical oncology. 2012;19(13):4104-11. Epub 2012/07/04. doi: 10.1245/s10434-012-2466-4. PubMed PMID: 22752379; PubMed Central PMCID: PMC3465510.

16. Hirche C, Engel H, Kolios L, Cognie J, Hunerbein M, Lehnhardt M, et al. An experimental study to evaluate the Fluobeam 800 imaging system for fluorescence-guided lymphatic imaging and sentinel node biopsy. Surgical innovation. 2013;20(5):516-23. Epub 2013/01/01. doi: 10.1177/1553350612468962. PubMed PMID: 23275469.

17. Tobis S, Knopf JK, Silvers CR, Marshall J, Cardin A, Wood RW, et al. Near infrared fluorescence imaging after intravenous indocyanine green: initial clinical experience with open partial nephrectomy for renal cortical tumors. Urology. 2012;79(4):958-64. Epub 2012/02/18. doi: 10.1016/j.urology.2011.10.016. PubMed PMID: 22336035.

18. Gotoh K, Yamada T, Ishikawa O, Takahashi H, Eguchi H, Yano M, et al. A novel image-guided surgery of hepatocellular carcinoma by indocyanine green fluorescence imaging navigation. Journal of surgical oncology. 2009;100(1):75-9. Epub 2009/03/21. doi: 10.1002/jso.21272. PubMed PMID: 19301311.

19. Mondal SB, Gao S, Zhu N, Sudlow GP, Liang K, Som A, et al. Binocular Goggle Augmented Imaging and Navigation System provides real-time fluorescence image guidance for tumor resection and sentinel lymph node mapping. Scientific reports. 2015;5:12117. Epub 2015/07/17. doi: 10.1038/srep12117. PubMed PMID: 26179014; PubMed Central PMCID: PMC4503986.

20. Zhu N, Huang CY, Mondal S, Gao S, Huang C, Gruev V, et al. Compact wearable dual-mode imaging system for real-time fluorescence image-guided surgery. Journal of biomedical optics. 2015;20(9):96010. Epub 2015/09/12. doi: 10.1117/1.JBO.20.9.096010. PubMed PMID: 26358823.

21. Zhu N, Mondal S, Gao S, Achilefu S, Gruev V, Liang R. Engineering light-emitting diode surgical light for near-infrared fluorescence image-guided surgical systems. Journal of biomedical optics. 2014;19(7):076018. Epub 2014/07/25. doi: 10.1117/1.JBO.19.7.076018. PubMed PMID: 25057962; PubMed Central PMCID: PMC4109625.

22. Rolland JP, Fuchs H. Optical Versus Video See-Through Head-Mounted Displays in Medical Visualization. Presence: Teleoperators & Virtual Environments. 2000;9(3):287-309. doi: 10.1162/105474600566808. PubMed PMID: 3301327.

23. Sielhorst T, Feuerstein M, Navab N. Advanced Medical Displays: A Literature Review of Augmented Reality. Display Technology, Journal of. 2008;4(4):451-67. doi: 10.1109/jdt.2008.2001575.

24. Levy ML, Chen JCT, Moffitt K, Corber Z, McComb GJ. Stereoscopic Head-mounted Display Incorporated into Microsurgical Procedures: Technical Note. Neurosurgery. 1998;43(2):392-5. PubMed PMID: 00006123-199808000-00141.

25. Cheah WK, Lenzi JE, So J, Dong F, Kum CK, Goh P. Evaluation of a head-mounted display (HMD) in the performance of a simulated laparoscopic task. Surg Endosc. 2001;15(9):990-1. doi: 10.1007/s004640090026.

26. Maithel SK, Villegas L, Stylopoulos N, Dawson S, Jones DB. Simulated laparoscopy using a head-mounted display vs traditional video monitor: an assessment of performance and muscle fatigue. Surgical Endoscopy And Other Interventional Techniques. 2005;19(3):406-11. doi: 10.1007/s00464-004-8177-6.

27. Prendergast CJ, Ryder BA, Abodeely A, Muratore CS, Crawford GP, Luks FI. Surgical performance with head-mounted displays in laparoscopic surgery. Journal of laparoendoscopic & advanced surgical techniques Part A. 2009;19 Suppl 1:S237-40. Epub 2008/11/13. doi: 10.1089/lap.2008.0142. PubMed PMID: 18999982.

28. Sudra G, Marmulla R, Salb T, Ghanai S, Eggers G, Giesler B, et al. First clinical tests with the augmented reality system INPRES. Studies in health technology and informatics. 2005;111:532-7. Epub 2005/02/19. PubMed PMID: 15718792.

Chapter 5: Tumor margin assessment

This chapter is based on a pending article: S. B. Mondal, J. Margenthaler, S. Gao, N. Zhu, G. P. Sudlow, K. Liang, W. J. Akers, V. Gruev, R. Liang, S. Achilefu. Real-time fluorescence image guidance for tumor margin assessment in a spontaneous mouse model of breast cancer and clinical feasibility in breast cancer patients. *To be submitted*. I designed the animal experiments, conducted them and analyzed the animal data. I assisted the surgeon during clinical procedure, collected the clinical data and analyzed them. I wrote the manuscript.

5.1 Abstract

5.1.1 Background

Intraoperative near-infrared (NIR) fluorescence imaging can potentially provide accurate assessment of tumor margin status in breast conserving surgery and improve outcomes. However, it is not widely used due to limitations of NIR FGS systems.

5.1.2 Methods

We evaluated in vivo an optical see-through (OST) goggle augmented imaging and navigation system (GAINS) which had a minimal hardware footprint and allowed direct visual access to the surgical field while projecting fluorescence information. For pre-clinical validation, five PyMT-MMTV mice were used that developed spontaneous breast cancer all along their mammary fat pad. These mice were injected with a tumor targeted NIR contrast agent LS301 (60µM, 100µl) and subjected to fluorescence-guided surgery, 24 hour post-injection. Three consecutive breast cancer patients scheduled to undergo partial mastectomy received 5ml, 5mg/ml ICG retroareolarly. Standard-of-care partial mastectomy was done followed by GAINS-guided fluorescence imaging of the tumor tissue and the tumor cavity to predict tumor margin status.

5.1.3 Results

The OST GAINS allowed direct visual access to the surgical bed while projecting fluorescence information directly to surgeon’s eyes. A total of a total of 97 tumors were resected with a mean of 19.4 ± 7.53 tumors per mouse. GAINS identified 89.61 ± 9.27% of the tumors with a sensitivity of 86.91 ± 11.11% and specificity of 80.0 ± 26.67%. Visual detection identified 78.08 ± 8.16% of the tumors with a sensitivity of 68.84.48 ± 9.57% and specificity of 100 ± 0%. The percentage of tumors detected and tumor detection sensitivity by GAINS were significantly higher than visual only method (P=0.00166, P=0.0022). A combined GAINS-visual approach

identified 93.52 ± 7.33 % of the tumors with a sensitivity of 92.36 ± 7.4% and specificity of 80.0 ± 26.67%. GAINS accurately predicted margin status in all three patients, including clear margins in patients 1 and 2 and positive margins in patient 3. GAINS predicted margin status were confirmed by the final pathology report.

5.1.4 Conclusions

Combined GAINS and visual identification provide best guidance for tumor and margin detection in spontaneous mouse model of breast cancer and it is feasible to use the GAINS for intraoperative margin assessment using ICG in human breast cancer patients.

5.2 Introduction

Breast cancer is the most common cancer in women and the leading cause of cancer death in women in the US(1). For early stage breast cancer, breast conserving surgery (BCS) is the standard-of-care because it has the same survival advantage as compared to the radical mastectomy. However in BCS a major challenge is the identification of tumor margins and ensure a negative margin resection(2). Margin status is an important factor for preventing local recurrence. Achieving negative margin resection can lead to a two-fold decrease in ipsilateral tumor recurrence(3). However, surgeons rely on visual inspection and palpation to distinguish cancer from healthy tissue during BCS. This often leads to subjective choice of surgical margins. Approximately 25% of women undergoing BCS require repeat surgery due to incomplete surgical resection of tumors in the initial BCS surgery, leading to additional costs, anxiety, complications and cosmetic concerns(3). However, significant variability exist based on the facility where the surgery is performed, surgeon experience, and patient’s age and tumor characteristics(4-6).

Intraoperative margin assessment in BCS may reduce the recall rate and improve surgical outcomes. There are several methods currently available for intraoperative margin assessment in breast cancer. Frozen section analysis and imprint cytology are time consuming, have variable accuracy depending on the institution and may not be available everywhere(7-10). Introperative ulatrsound has faster imaging but has poor identification of ductal carcinoma in situ(10). Specimen radiography has good sensitivity but is expensive and adds time to the surgery and may not be as sensitive as frozen section analysis(11). The margin probe device is based on radiofrequency spectroscopy that can analyses the lumpectomy sample to ascertain presence or absence of cancer(12, 13). Several technologies including spectroscopy, X-ray, and high-frequency ultrasound are being investigated(9, 14).

Due to cost effective and compact hardware design, there has been great interest in optical methods of intraoperative margin assessment. For example spectroscopic methods have been used in the clinic with good outcomes. OCT has been shown to be able to provide high rates of margin prediction. Of particular interest is fluorescence based methods due to availability of sensitive imaging systems and various tumor specific contrast agents, at least for preclinical studies. However these systems are often not real-time, provide image information in a remote monitor or disrupt the normal surgical workflow. Some of these instruments also have a large hardware footprint. As a result it is often difficult to integrate them into routine surgical procedures.

We have developed a compact wearable goggle augmented imaging and navigation system that can allows real-time intraoperative fluorescence-guided surgery(15). It sensitively captures color and NIR images from the surgical field and transmits a superimposed color-NIR image directly to the surgeon’s eyes via a see-through head-mounted display. This allows direct visual access to the surgical field, while providing fluorescence information for image guidance to surgeons. We have previously demonstrated that this system is capable of sensitive tumor detection in a metastatic mouse model of cancer and has slightly better sensitivity to radioactive and blue dye tracking for SLN detection in human melanoma and breast cancer patients. In this study we evaluated the ability of the GAINS prototype to assess surgical margins in a preclinical spontaneous mouse model of breast cancer using a tumor targeted NIR contrast agent. We also evaluated the GAINS for tumor margin assessment in breast cancer patients using ICG contrast.

5.3 Methods

5.3.1 Fluorescence-Guided Surgery

Real-time intraoperative fluorescence-guided surgery was performed using the OST GAINS prototype as described earlier(16). Briefly, it uses a focus-adjustable single camera to capture color reflectance and NIR fluorescence images, which are processed to generate an accurately aligned color-NIR superimposed image. The color, NIR or superimposed images are directly projected to the user’s eyes via a custom OST HMD. This OST HMD allows direct visual access to the surgical field, with contrast- and transparency-adjusted projection of augmented fluorescence information. NIR illumination was provided by a 780 nm, 0.8 W laser (BW Tek), while white light illumination is provided by a surgical light covered with a short-pass film filter(17). The optical head for the NIR laser was mounted on a flexible neck, allowing easy movement to point it on the surgical bed as necessary. Adjusting the laser direction took 1-3 minutes. However this was usually done when the surgeon was using the gamma probe to locate the SLN, since the NIR channel even if it is not being visibly projected to the surgeon’s HMD, can be seen on the laptop as it is continuously being recorded. So light adjustment was done simultaneously with regular surgical processes and did not add significant time to the overall surgery. The pointing red laser on top of the NIR laser optics allowed us to visible know where the invisible NIR laser was pointing. The camera mounted HMD (worn on head) and pre-processing module (carried in a wais pouch under the sterile gown) constitute the wearable part of the system. The laptop used for final processing (carried on a cart) and illumination modules form separate standalone parts of the system.

5.3.2 Animal Studies

All animal studies were approved by the Washington University Animal Studies Committee. For preclinical tumor margin assessment and tumor detection, five PyMT-MMTV mice were used(18, 19). Once the largest tumors were 1-2 cm large they were injected with were injected with a tumor-targeted NIR contrast agent LS301(15) (60 µl, 100µl) via tail vein injection. At 24 h post-injection, the mice were anaesthetized using 2% isolfluorane and OST GAINS prototype was used to visualize NIR fluorescence from the tumors and guide surgical resection along with visual inspection. After debulking the tumor bed was surveyed for presence of residual fluorescence and all suspected tumor tissue were resected. The animals were sacked by cervical dislocation, its organs were harvested and resected tissue were preserved for frozen section histopathologic analysis. The tissue resected was saved in four categories to signify tissue that was identified as cancerous by both GAINS and visual inspection (g+ v+), by GAINS and not visually (g+ v-), not by GAINS, but identified visually as cancerous (g- v+) and tissue identified as non-cancerous both by GAINS and visual inspection (g- v-). They were preserved for histologic evaluation.

5.3.3 Pilot Human Study

This pilot human study to evaluate clinical feasibility of using the GAINS prototype for intraoperative inspection of lumpectomy samples and survey of the BCS cavity was approved by the Institutional Review Board at Washington University and was performed in accordance with the approved ethical guidelines. The study was registered on clinicaltrials.gov website (NCT02316795). Women, 18 years or older with newly diagnosed clinically node-negative breast cancer, negative nodal basin clinical exam and scheduled to undergo partial mastectomy with SLN biopsy were eligible for the study. Exclusion criteria were contraindication to surgery, receiving any investigational agents, history of allergic reaction to iodine, seafood and ICG, presence of uncontrolled inter-current illness, pregnant or breastfeeding. All patients gave informed consent for this HIPAA-compliant study and data was deidentified.

Patients received ^{99m}Tc-sulfur colloid (834 µCi) 2- 3 hours before surgery for needle localization and then brought to the operating room. Patients were injected with ICG (5mg/mL; 5 mL) in the retroareolar breast, followed by site massage for 5 min. About 10-15 min after injection, the surgeon performed standard-of-care partial mastectomy and the tumor mass was removed with a rim of grossly normal tissue. The excised tumor tissue was marked with sutures to indicate orientation and examined for fluorescence using the GAINS before submission for standard-of-care histologic evaluation. The GAINS was then used to survey the tumor cavity for fluorescence imaging. The surgeon wore the waist pouch carrying the image pre-processing module for the OST GAINS under the sterile gown. The camera mounted HMD was fitted onto the surgeon's head and connections to the camera, laptop, HMD and power sources were established without compromising the sterile field. In all cases, the GAINS was operated at 24p fps with a 40-millisecond acquisition time. NIR-white light illumination during system usage was provided by our illumination module. A remote laptop used for final image processing, mirrored the surgeon's view. The camera focus, projected fluorescence contrast and transparency of pseudocolored fluorescence overlay was adjusted using the laptop based on surgeon's verbal feedback to ensure optimal viewing experience.

5.3.4 Statistical Analysis

Statistical analysis was performed using OriginPro8 (OriginLab Corp., Northampton, MA). Signal-to-background ratios (SBRs), sensitivities, specificities and percentages were expressed as mean and standard deviation. Paired t-tests were used to compare GAINS, visual and combined GAINS and visual methods for guiding surgery in the mouse model. $P < 0.05$ were considered statistically significant.

5.4 Results

5.4.1 Tumor Resection in Mice

GAINS guided complete tumor resection in all five PyMT-MMTV mice. Based on histologic confirmation (**Fig. 52**), a total of 97 tumors were resected with a mean of 19.4 ± 7.53 tumors per mouse. Using LS301 fluorescence, GAINS identified 89.61 ± 9.27% of the tumors (**Fig 48, 49**) with a sensitivity of 86.91 ± 11.11% and specificity of 80.0 ± 26.67%. Visual detection identified 78.08 ± 8.16% of the tumors with a sensitivity of 68.84.48 ± 9.57% and specificity of 100 ± 0%. The percentage of tumors detected by GAINS was significantly higher than visual only method (P=0.00166). The GAINS tumor detection sensitivity was significantly higher than visual only tumor detection sensitivity (P=0.0022). However no statistically significant difference was found between the tumor detection specificities of the two methods (P=0.11). A combined GAINS and visual identification method was defined as tissue being classified as tumor when either GAINS or visual identification predicted tumor and tissue to be classified as normal only when both GAINS and visual identification predicted no cancer. Based on this definition, combined GAINS-visual approach identified 93.52 ± 7.33 % of the tumors with a sensitivity of 92.36 ±

7.4% and specificity of 80.0 ± 26.67%. The percentage of tumor detection using the combined method was significantly higher compared to visual only identification (P=0.00349), with no significant difference found compared to GAINS tumor detection percentage (P=0.227). The detection sensitivity for the combined method was significantly higher than the visual only method (P=0.00611), but significant difference was found in the detection specificities between the two methods (P=0.108). There were no statistically significant differences between the combined method and GAINS method for tumor detection sensitivity (P=0.20311) and specificity (P=1).

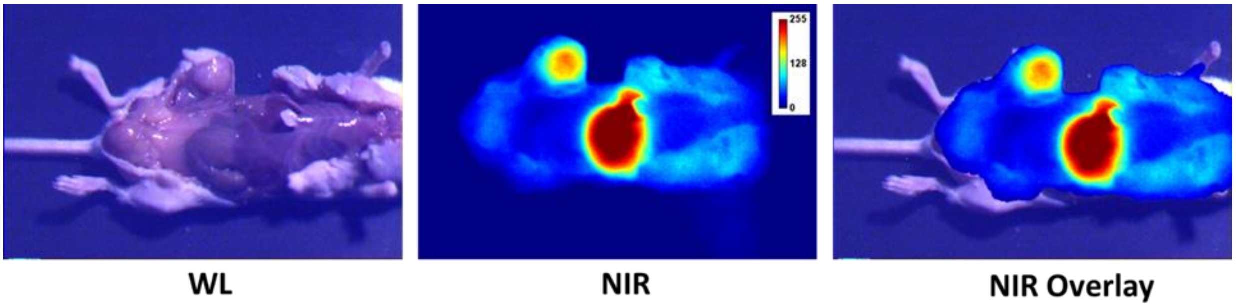

Figure 48: Tumor detection in PyMT spontaneous mouse model of breast cancer by NIR-fluorescence via the GAINS prototype.

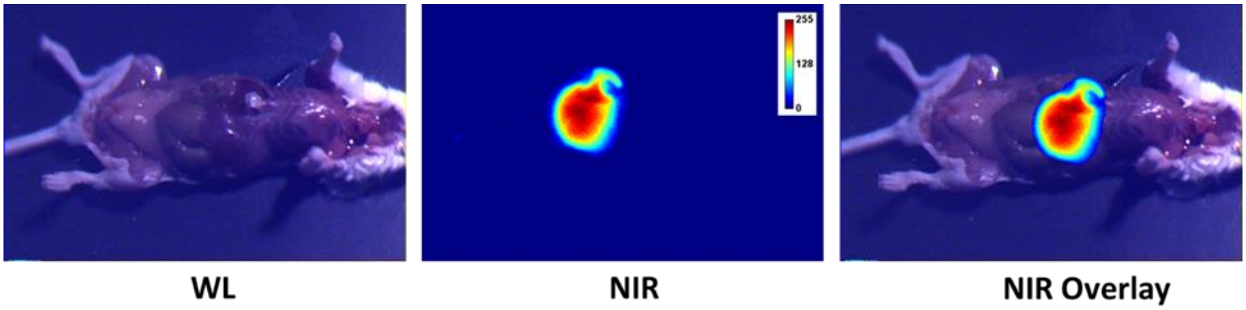

Figure 49: After image-guided tumor resection

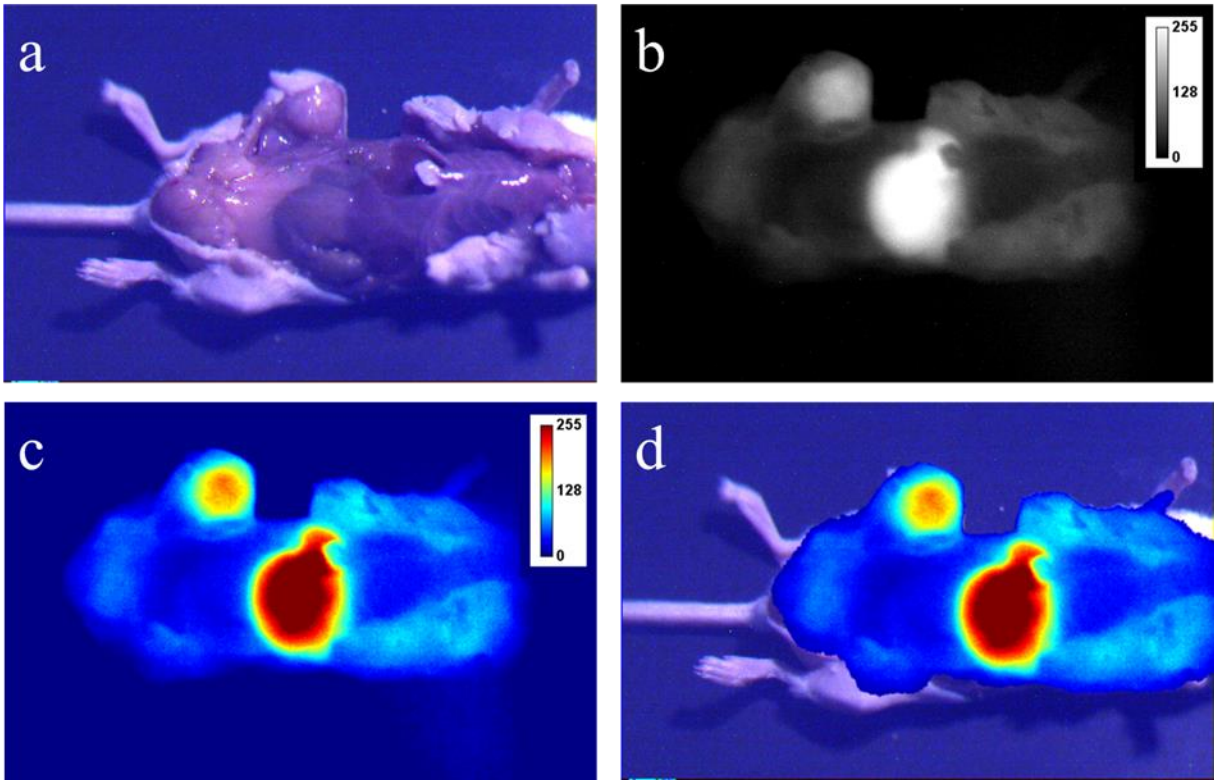

Figure 50: Tumors detection in PyMT mouse showing a) color image, b) grayscale fluorescence image, c) pseudocolored fluorescence image and d) color-NIR overlay image.

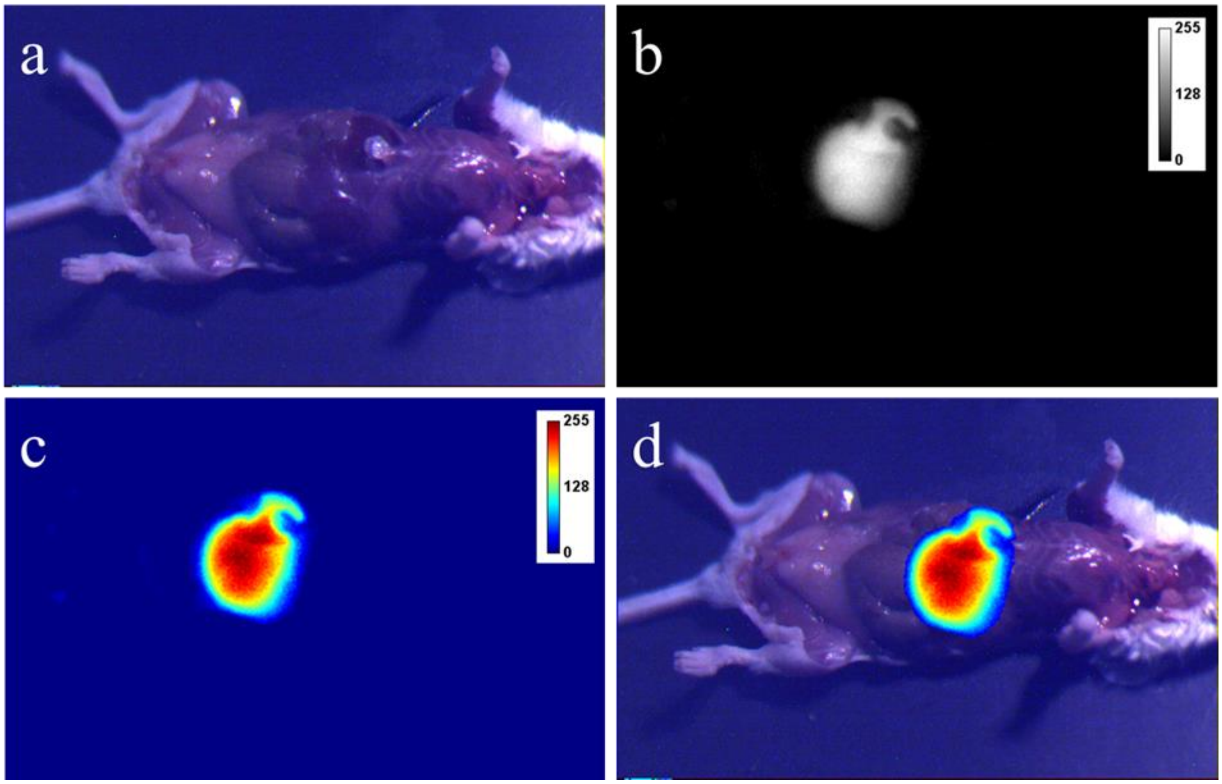

Figure 51: Tumors removed from PyMT mouse showing a) color image, b) grayscale fluorescence image, c) pseudocolored fluorescence image and d) color-NIR overlay image.

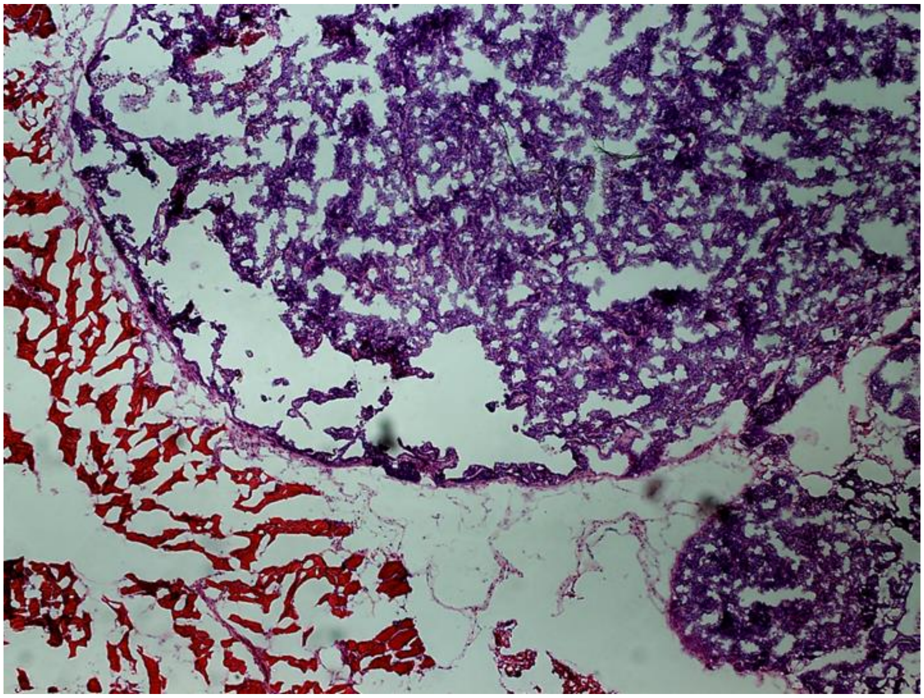

Figure 52: Histology image from a tumor removed from the PyMT mouse showing tumor boundary with bordering muscle tissue.

5.4.2 Tumor Margin Assessment in Human Breast Cancer Patients

The study aimed to study to evaluate clinical feasibility of the GAINS prototype in imaging lumpectomy samples and inspecting tumor cavities to assess tumor margin status. Three consecutive patients underwent standard-of-care partial mastectomy with wire localization with the addition of OST GAINS guided tumor tissue (**Fig. 53**) and tumor cavity visualization using ICG fluorescence. The patient and tumor characteristics are listed in **Table 1**. The fluorescence information was projected as and when the surgeon requested, for visualizing the SLN. No adverse reactions associated with the use of ICG or the OST GAINS prototype occurred. No postoperative complications of the SLN procedure were observed.

GAINS accurately predicted margin status in all three patients (**Table 2**). Based on tumor tissue assessment and cavity imaging it successfully predicted that margins were clear in patients 1 and 2. More importantly based on high fluorescence from the lumpectomy sample surface (**Fig. 53**) and the edges of the lumpectomy cavity (**Fig. 54**) in the third patient, GAINS predicted presence of residual tumor. This prediction of positive margin status was verified through final pathology report.

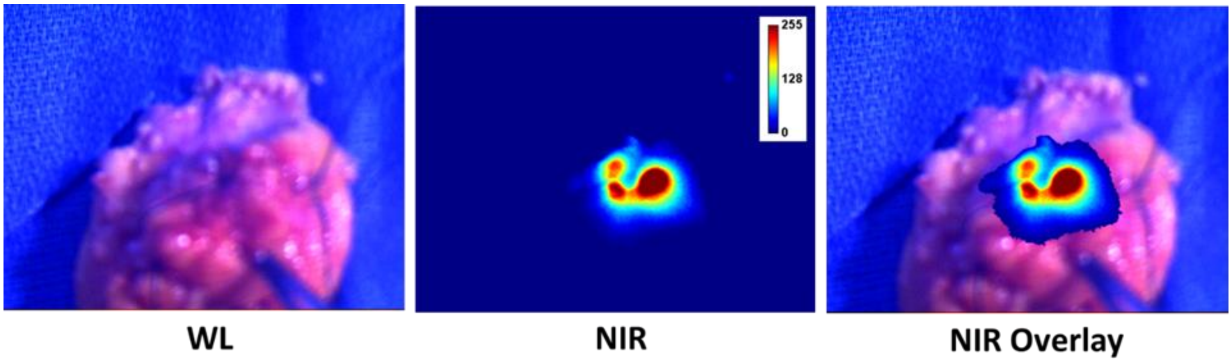

Figure 53: Lumpectomy tissue from patient 3 showing high fluorescence using the GAINS prototype

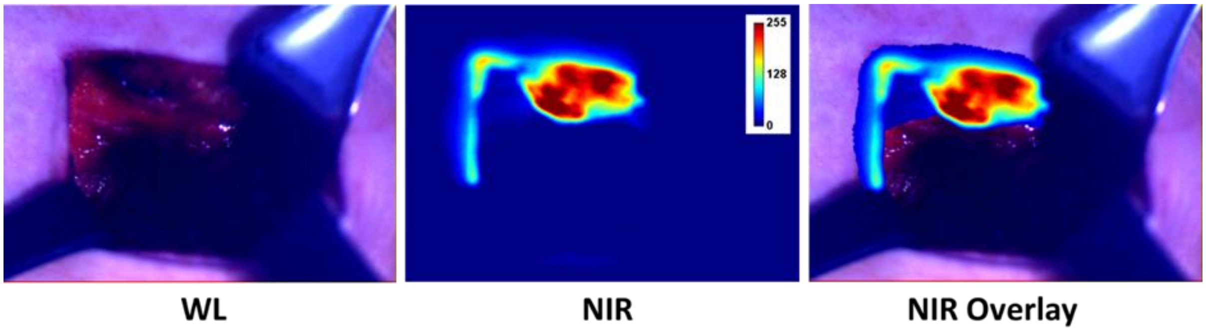

Figure 54: Tumor cavity of patient 3 showing high fluorescence.

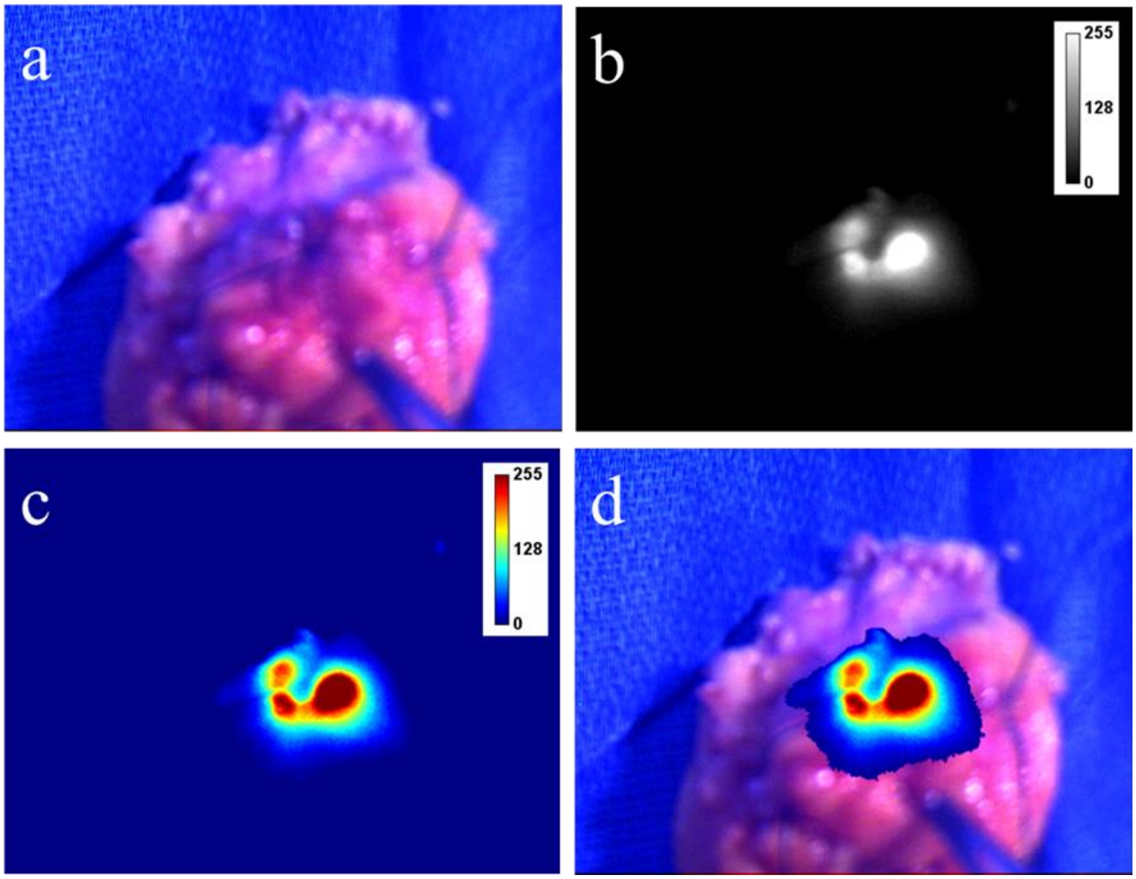

Figure 55: Removed lumpectomy tissue from patient 3 showing a) color image, b) grayscale fluorescence image, c) pseudocolored fluorescence image and d) color-NIR overlay image.

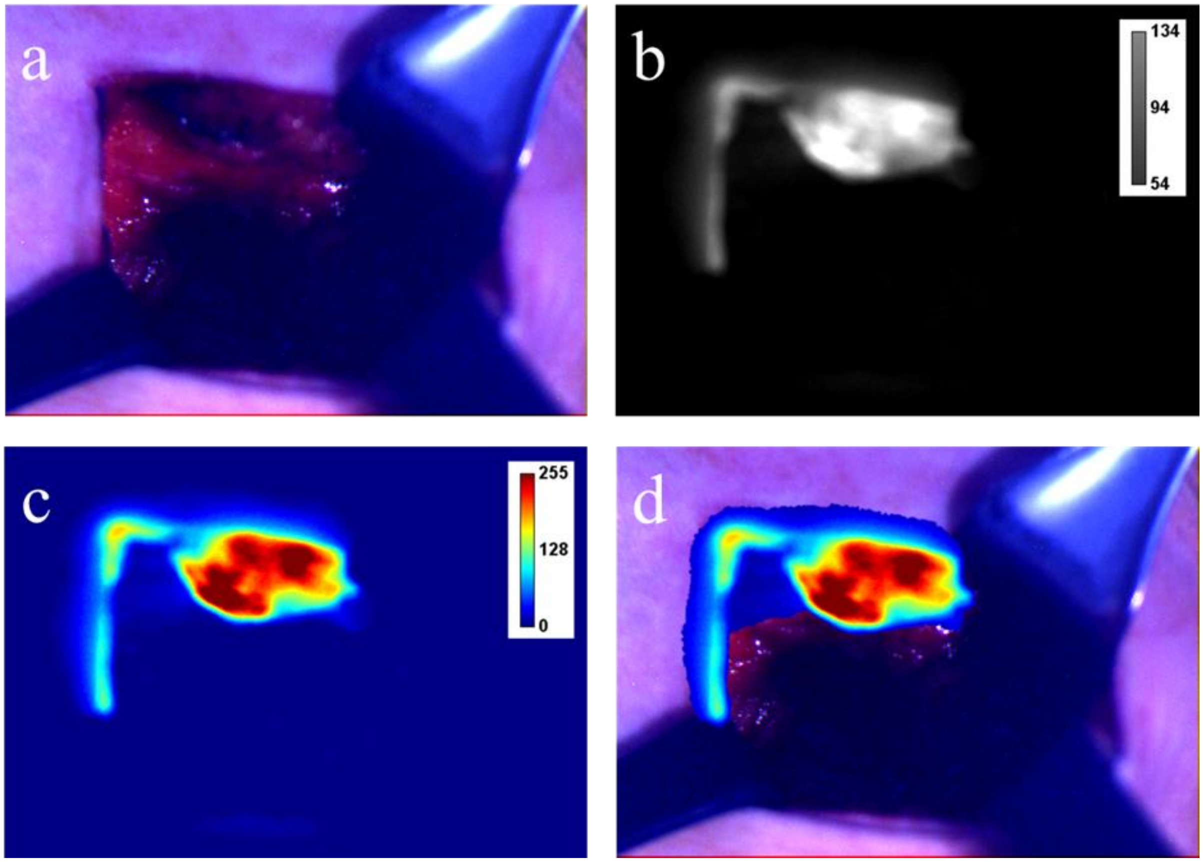

Figure 56: Tumor cavity of patient 3 with high residual fluorescence, showing a) color image, b) grayscale fluorescence image, c) pseudocolored fluorescence image and d) color-NIR overlay image.

5.5 Discussion

NIR FGS for intraoperative cancer imaging has emerged as an important tool recently. It is currently limited by the standalone or handheld FGS systems that are not able to match the camera and user field of view, are bulky and show the information in a remote display. The combination of these factors disrupt the normal surgical workflow and has led to minimal adaptation of FGS in clinics beyond research initiatives and small clinical trials. Disruptive information display may be addressed by using a HMD(20, 21). There has been a lot of interest in doing surgical planning and navigation using HMDs especially in the neurosurgical community(22). It has been shown that a VST HMD can improve surgical performance in endoscopic surgeons(23-25). In our previous work we applied a VST HMD to cancer surgery and demonstrated that the video see-through GAINS has very sensitive SLN detection comparable to conventional radioactive and blue dye tracking(15). However it was limited due to no direct visual access to the surgical field. The advantages of OST HMDs are well accepted(20) and its ability to provide direct visual access to the surgical field is critical for open surgery. However very limited work has been done on using OST HMDs for surgical navigation(26) due to technical challenges involved(20, 21). We reported the first OST HMD developed specifically for fluorescence-guided surgery(16) and this is the first report to the best of our knowledge of clinical evaluation of an OST HMD based system for fluorescence-guided tumor imaging and margin assessment during breast conserving surgery. Our current study demonstrates that the OST GAINS, by providing direct visual access to the surgical field with option of projected fluorescence information significantly improves the usability of the system. The see-through feature allows direct visualization with the provision of fluorescence information whenever needed. In one patient the OST GAINS was able to successfully predict presence of positive surgical margins which was verified by the final pathology report. The surgeon had the option of having the grayscale fluorescence, pseducolored fluorescence (blue through red color indicating low through highest NIR fluorescence intensity) or superimposed pseudcolored fluorescence-color images to be projected. All surgeries were done with OR surgical lights on, which did not put major hindrance to the NIR imaging, unlike other FGS systems that require to turn off the surgical light. This allowed seamless integration of FGS in to the regular surgical workflow.

A major issue in FGS is complex image adjustment based on surgeon feedback, without disrupting the surgical workflow or compromising sterility. Solutions like foot pedals cannot implement complex image adjustments, while voice commands may have difficulty operating in the high noise atmosphere in the operating room. In our system the surgeon's view is mirrored on the remote laptop and a custom graphical user interface (GUI) allowed real-time modifications of imaging parameters by a member of the surgical team to incorporate surgeon feedback immediately, without stopping the surgery, while ensuring highest quality user experience. Camera focus was adjusted to compensate for large head movements and to ensure the image was always in focus. Contrast of the projected fluorescence was adjusted as requested by the surgeon to ensure optimal visibility of fluorescence information on the HMD. Additionally the built-in fail-safe of the see-through feature can allow surgeons to carry-on regular surgery in case of system failure.

The OST GAINS was able to guide complete tumor resection in a spontaneous mouse model of breast cancer. Though, our patient data set is very small and we would need a larger patient study to support our statement, our initial findings are very encouraging.

The system currently performs final image processing on the laptop, tethering the surgeon to the cart carrying the laptop using a wired connection. Additionally, a mismatch in the perceived distance of the projected fluorescence and actual object distance as seen by the surgeon may cause parallax. Efforts are currently under way to ensure complete onboard image processing, with wirelsess data and GUI transmission to the laptop as well as to ensure minimal parallax by remote adjustment of perceived distance of projected fluorescence images.

5.6 References

1. Siegel RL, Miller KD, Jemal A. Cancer statistics, 2015. CA: a cancer journal for clinicians. 2015;65(1):5-29. Epub 2015/01/07. doi: 10.3322/caac.21254. PubMed PMID: 25559415.

2. Singletary SE. Surgical margins in patients with early-stage breast cancer treated with breast conservation therapy. American journal of surgery. 2002;184(5):383-93. Epub 2002/11/16. PubMed PMID: 12433599.

3. Moran MS, Schnitt SJ, Giuliano AE, Harris JR, Khan SA, Horton J, et al. Society of Surgical Oncology-American Society for Radiation Oncology consensus guideline on margins for breast-conserving surgery with whole-breast irradiation in stages I and II invasive breast cancer. Annals of surgical oncology. 2014;21(3):704-16. Epub 2014/02/12. doi: 10.1245/s10434-014-3481-4. PubMed PMID: 24515565.

4. McCahill LE, Single RM, Aiello Bowles EJ, Feigelson HS, James TA, Barney T, et al. Variability in reexcision following breast conservation surgery. Jama. 2012;307(5):467-75. Epub 2012/02/03. doi: 10.1001/jama.2012.43. PubMed PMID: 22298678.

5. Morrow M, Jagsi R, Alderman AK, Griggs JJ, Hawley ST, Hamilton AS, et al. Surgeon recommendations and receipt of mastectomy for treatment of breast cancer. Jama. 2009;302(14):1551-6. Epub 2009/10/15. doi: 10.1001/jama.2009.1450. PubMed PMID: 19826024; PubMed Central PMCID: PMC4137962.

6. Mullen R, Macaskill EJ, Khalil A, Elseedawy E, Brown DC, Lee AC, et al. Involved anterior margins after breast conserving surgery: Is re-excision required? European Journal of Surgical Oncology.38(4):302-6. doi: 10.1016/j.ejso.2012.01.004.

7. Fukamachi K, Ishida T, Usami S, Takeda M, Watanabe M, Sasano H, et al. Total-circumference intraoperative frozen section analysis reduces margin-positive rate in breast-conservation surgery. Japanese journal of clinical oncology. 2010;40(6):513-20. Epub 2010/03/02. doi: 10.1093/jjco/hyq006. PubMed PMID: 20189973.

8. Osborn J, Keeney G, Jakub J, Degnim A, Boughey J. Cost-Effectiveness Analysis of Routine Frozen-Section Analysis of Breast Margins Compared with Reoperation for Positive Margins. Annals of surgical oncology. 2011;18(11):3204-9. doi: 10.1245/s10434-011-1956-0.

9. Butler-Henderson K, Lee AH, Price RI, Waring K. Intraoperative assessment of margins in breast conserving therapy: a systematic review. Breast. 2014;23(2):112-9. Epub 2014/01/29. doi: 10.1016/j.breast.2014.01.002. PubMed PMID: 24468464.

10. Tengher-Barna I, Antoine M, Bricou A, Ziol M. Cavity margins examination in breast-conserving therapy. Diagnostic Histopathology.17(5):232-7. doi: 10.1016/j.mpdhp.2011.02.005.

11. Weber W, Engelberger S, Viehl C, Zanetti-Dallenbach R, Kuster S, Dirnhofer S, et al. Accuracy of Frozen Section Analysis Versus Specimen Radiography During Breast-Conserving Surgery for Nonpalpable Lesions. World J Surg. 2008;32(12):2599-606. doi: 10.1007/s00268-008-9757-8.

12. Karni T, Pappo I, Sandbank J, Lavon O, Kent V, Spector R, et al. A device for real-time, intraoperative margin assessment in breast-conservation surgery. The American Journal of Surgery.194(4):467-73. doi: 10.1016/j.amjsurg.2007.06.013.

13. Schnabel F, Boolbol S, Gittleman M, Karni T, Tafra L, Feldman S, et al. A Randomized Prospective Study of Lumpectomy Margin Assessment with Use of MarginProbe in Patients with Nonpalpable Breast Malignancies. Annals of surgical oncology. 2014;21(5):1589-95. doi: 10.1245/s10434-014-3602-0.

14. Thill M, Baumann K, Barinoff J. Intraoperative assessment of margins in breast conservative surgery—still in use? Journal of Surgical Oncology. 2014;110(1):15-20. doi: 10.1002/jso.23634.

15. Mondal SB, Gao S, Zhu N, Sudlow GP, Liang K, Som A, et al. Binocular Goggle Augmented Imaging and Navigation System provides real-time fluorescence image guidance for tumor resection and sentinel lymph node mapping. Scientific reports. 2015;5:12117. Epub 2015/07/17. doi: 10.1038/srep12117. PubMed PMID: 26179014; PubMed Central PMCID: PMC4503986.

16. Zhu N, Huang CY, Mondal S, Gao S, Huang C, Gruev V, et al. Compact wearable dual-mode imaging system for real-time fluorescence image-guided surgery. Journal of biomedical optics. 2015;20(9):96010. Epub 2015/09/12. doi: 10.1117/1.JBO.20.9.096010. PubMed PMID: 26358823.

17. Zhu N, Mondal S, Gao S, Achilefu S, Gruev V, Liang R. Engineering light-emitting diode surgical light for near-infrared fluorescence image-guided surgical systems. Journal of biomedical optics. 2014;19(7):076018. Epub 2014/07/25. doi: 10.1117/1.JBO.19.7.076018. PubMed PMID: 25057962; PubMed Central PMCID: PMC4109625.

18. Lin EY, Nguyen AV, Russell RG, Pollard JW. Colony-Stimulating Factor 1 Promotes Progression of Mammary Tumors to Malignancy. The Journal of Experimental Medicine. 2001;193(6):727-40. doi: 10.1084/jem.193.6.727.

19. Lin EY, Jones JG, Li P, Zhu L, Whitney KD, Muller WJ, et al. Progression to Malignancy in the Polyoma Middle T Oncoprotein Mouse Breast Cancer Model Provides a Reliable Model for Human Diseases. The American Journal of Pathology.163(5):2113-26. doi: 10.1016/s0002-9440(10)63568-7.

20. Rolland JP, Fuchs H. Optical Versus Video See-Through Head-Mounted Displays in Medical Visualization. Presence: Teleoperators & Virtual Environments. 2000;9(3):287-309. doi: 10.1162/105474600566808. PubMed PMID: 3301327.

21. Sielhorst T, Feuerstein M, Navab N. Advanced Medical Displays: A Literature Review of Augmented Reality. Display Technology, Journal of. 2008;4(4):451-67. doi: 10.1109/jdt.2008.2001575.

22. Levy ML, Chen JCT, Moffitt K, Corber Z, McComb GJ. Stereoscopic Head-mounted Display Incorporated into Microsurgical Procedures: Technical Note. Neurosurgery. 1998;43(2):392-5. PubMed PMID: 00006123-199808000-00141.

23. Cheah WK, Lenzi JE, So J, Dong F, Kum CK, Goh P. Evaluation of a head-mounted display (HMD) in the performance of a simulated laparoscopic task. Surg Endosc. 2001;15(9):990-1. doi: 10.1007/s004640090026.

24. Maithel SK, Villegas L, Stylopoulos N, Dawson S, Jones DB. Simulated laparoscopy using a head-mounted display vs traditional video monitor: an assessment of performance and muscle fatigue. Surgical Endoscopy And Other Interventional Techniques. 2005;19(3):406-11. doi: 10.1007/s00464-004-8177-6.

25. Prendergast CJ, Ryder BA, Abodeely A, Muratore CS, Crawford GP, Luks FI. Surgical performance with head-mounted displays in laparoscopic surgery. Journal of laparoendoscopic & advanced surgical techniques Part A. 2009;19 Suppl 1:S237-40. Epub 2008/11/13. doi: 10.1089/lap.2008.0142. PubMed PMID: 18999982.

26. Sudra G, Marmulla R, Salb T, Ghanai S, Eggers G, Giesler B, et al. First clinical tests with the augmented reality system INPRES. Studies in health technology and informatics. 2005;111:532-7. Epub 2005/02/19. PubMed PMID: 15718792.

Chapter 6: Future Directions

This chapter is based on the preliminary results from ongoing work and envisioned future directions of this research. I designed the studies, performed the experiments, analyzed the results and documented the studies.

6.1 Introduction

We plan to further improve our work by addressing various scopes for improvement that we have identified through the course of this research. We have also identified several research questions that we want to investigate next. The following sections elaborate on potential improvements that we envision and the new applications for this research. We have already worked on some of these areas and our preliminary findings are presented here, while other sections presented here are only at a concept stage.

6.2 Improved prototype design

The current video-see through and optical see-through GAINS prototypes are very functional and robust systems. However, we believe we can further improve performance and ergonomics of the system. One major area of improvement is the head-mounted display. We want to make less bulky than it currently is. This will allow it to be used for long durations without causing discomfort to the surgeon. We have identified a large field of view, HMD with high transparency, that is only 30 gm in weight and we will be using it to develop the next generation of the GAINS prototype (**Fig. 57**).

The current OST-HMD has a fixed perceived distance of the projected fluorescence. Also since the surgeon's eyes can move independent of the head, the projected image does not always maximally cover the field of view of the user. To address these issues we want to add remotely controllable movability to the mirror used to project the fluorescence information to the user's eyes, to change the perceived distance of the projected fluorescence information and thus reduce parallax errors. We also want to integrate LEDs on the HMD to direct the user's gaze to the area where we can ensure maximal coverage of the user field of view by the projected fluorescence.

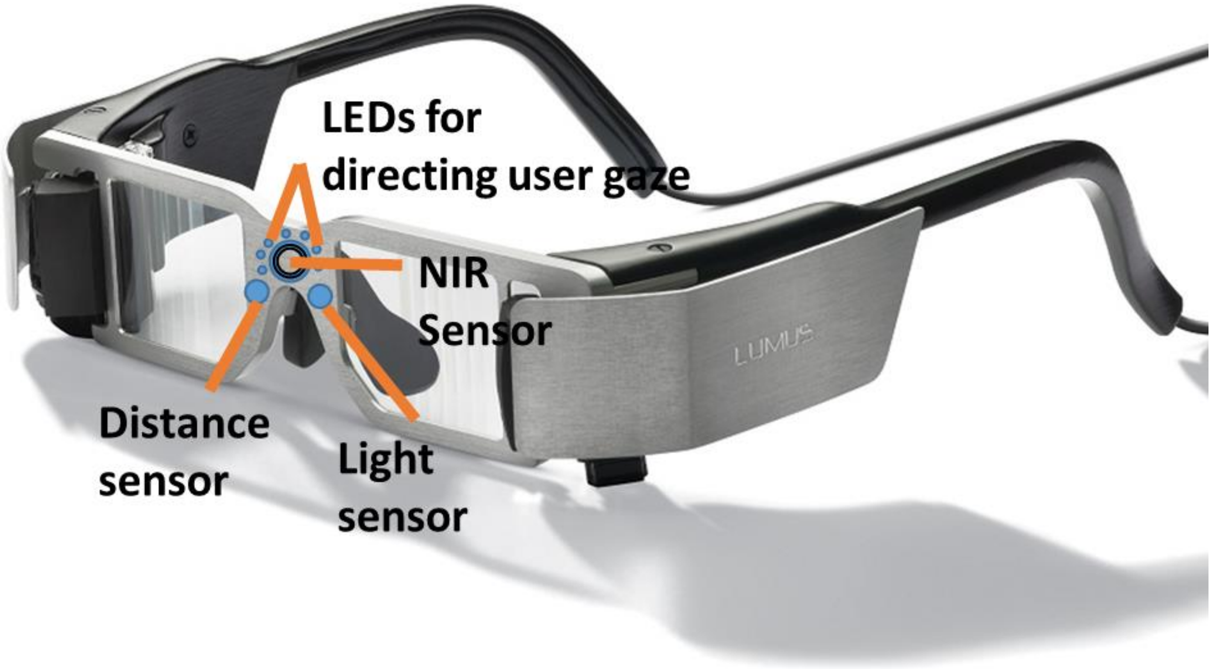

Figure 57: Future design of the GAINS integrated display and imaging module.

Another major issue in the current prototype is that it relies on a laptop for final image processing. As a result the surgeon is tethered to the cart that carries the laptop. Additionally, the FPGA used for pre-processing and HMD video-adapter that are carried in a waist pouch by the surgeon, require power supply from a wall-charger. This prevents true freedom of movement for the surgeon, which can be critical in cases of perioperative complications, when the surgeon needs to move quickly and may need to reach the other side of the patient bed. To address this issue we have identified a mini-PC that can perform all image processing, and we plan to migrate to a completely battery powered operation. This will allow complete freedom of movement for the surgeon. The mini-PC will wirelessly communicate with a laptop in the operating room, which will allow access to the user interface for controlling imaging parameters, identical to when having a wired connection. So we will be able to control all critical functions remotely without restricting the surgeon's movement (**Fig. 58**). This should allow easier integration to the surgical workflow.

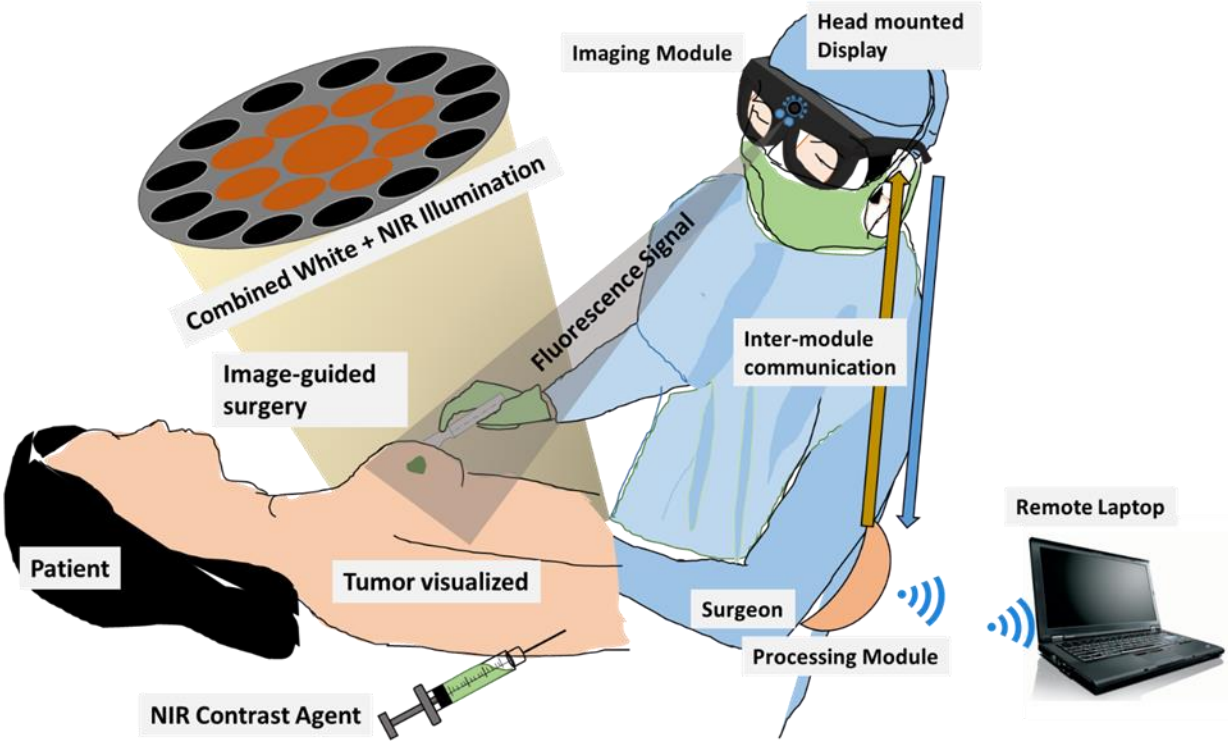

Figure 58: Overview of proposed improved GAINS prototype

6.3 Combined microscopic and macroscopic image guidance

While the current GAINS modules have sub-mm resolution, we currently lack the ability to see cancer cell clusters of a few cells or single cells. This is particularly important in brain cancers, where it is critical to visualize the infiltrating edges of the cancer and it often involves very few cells. In order to achieve this goal we integrated a handheld fluorescence microscope (Dino-lite) with single cell resolution to the GAINS, with the microscope output display on the head-mounted display (**Fig. 59**). The microscope has a USB output and was run using the same PC.

Figure 59: The Diono-lite hand-held microscope.

The microscope used had an LED excitation at 630 nm and emission detection of 650 nm and beyond. Six balb/c mice were implanted with 4T1 luc tumors on their flanks, subcutaneously. The 4T1 Luc cells express the luciferase enzyme that can be used for bioluminescence imaging. These mice were injected with LS301 and LS789 (60 µM, 100 µl). LS789 has far red fluorescence, with absorbance peak at 675 nm and emission peak at 705 nm. The co-injection resulted in good contrast of both compounds in the mouse tumor (**Fig. 60**). At 24 hours post injection, these mice were injected with luciferin and fluorescence guided surgery was performed. Bioluminescence imaging was done to observe decrease in number of cancer cells. While fluorescence was able to guide tumor detection macroscopically, as debulking was done, the fluorescence signal decreased and the images became progressively noisy (**Fig. 61**).

However, the bioluminescence provided information about residual cancer and the handheld microscope was able to guide their resection (**Fig. 62**). Based on data from six mice, GAINS dinolite detected all of the tumors, whereas GAINS could not detect a few of them, which were below its detection capability due to the signal being very close to its noise floor (**Table 12**). Histologic assessment and further statistical analysis is currently underway.

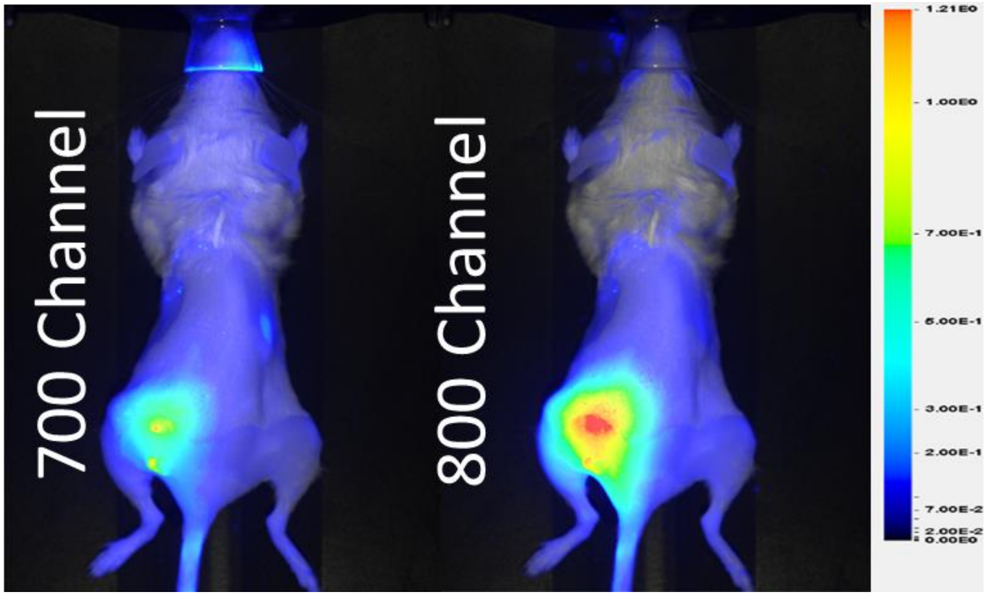

Figure 60: Compound localization in tumor with LS301 shown in the 800 channel and LS789 shown in the 700 channel image for the same mouse. Image was captured using Pearl Imaging system (Licor Biosciences).

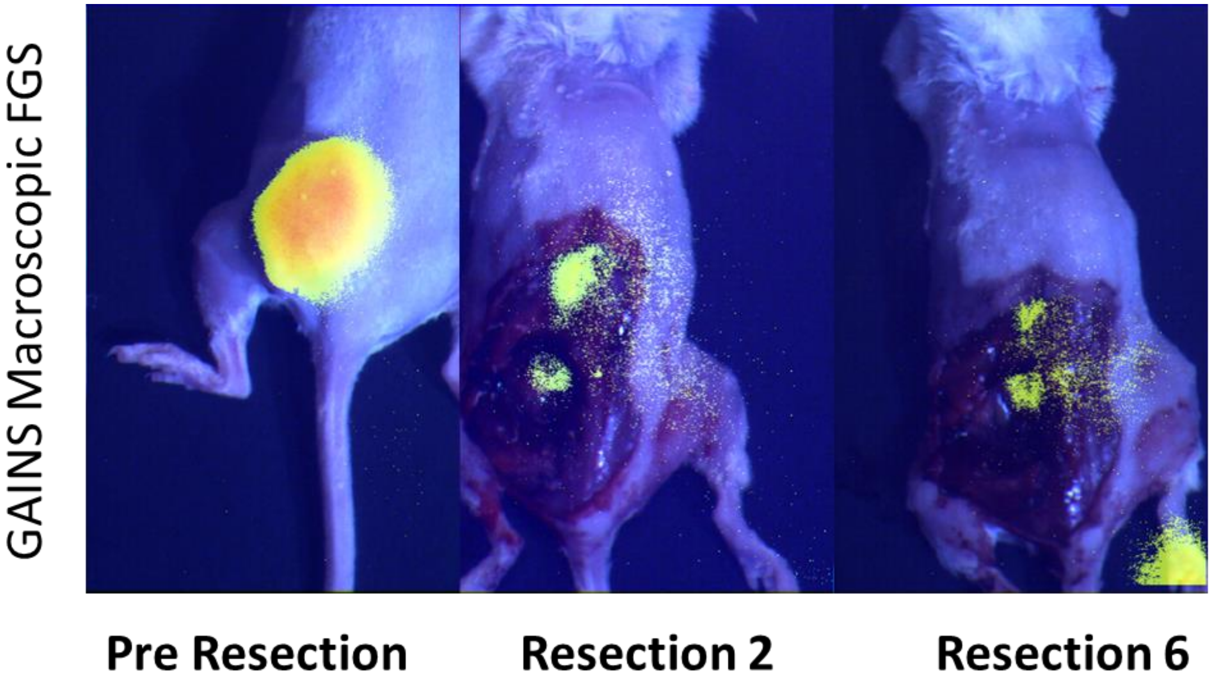

Figure 61: GAINS-guided surgery showing progressively noise images as more tissue is removed. In this case GAINS could not provide sufficient guidance beyond the 6th set of resection.

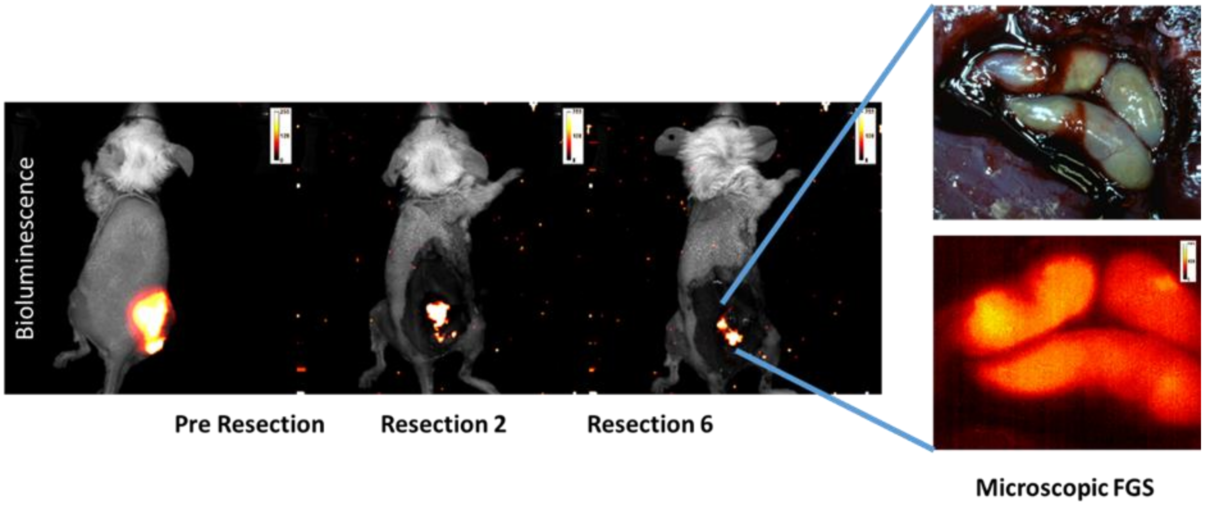

Figure 62: Bioluminescence imaging showing residual tumor signal with progressive resections. The dinolite microscope was able to detect signal when GAINS images had become noisy.

Table 12: The number of tumors detected by GAINS, Dino-lite and bioluminescence methods from six mice.

N = 6 mice	GAINS	Dinolite	Bioluminescence
Tumors sets	16	20	19

6.4 Clinical translation of a targeted near-infrared contrast agent

A major limitation of NIR FGS is the lack of a tumor targeted contrast agent that is approved for human usage. The only NIR contrast agent currently in the clinic is ICG. Though it has been used widely for clinical applications, its specificity for all types of tumors is widely variable and far from desirable. The contrast agent LS301 that we have developed in our lab is a promising contrast agent, because it is highly cancer selective and has been validated in a wide variety of cancer models in animals, including breast cancer, prostate cancer, colorectal cancer, ovarian cancer, brain cancer, multiple myeloma and skin cancer. Therefore we are very interested in clinical translation of LS301 to enable wide usability of this tumor-targeted dye in the clinic and other laboratories. Toward this effort we were able to determine the clinical formulation with albumin and dosage of the contrast agent to be 59 µg/kg in mice (**Fig. 63**). Based on this formulation the clinical dosage in canines was calculated to be 0.09 mg/kg for LS301-canine serum albumin formulation. A toxicity test with 100X clinical dosage in mice and 10X clinical dosage in dogs showed no harmful side-effects (**Table 13**).

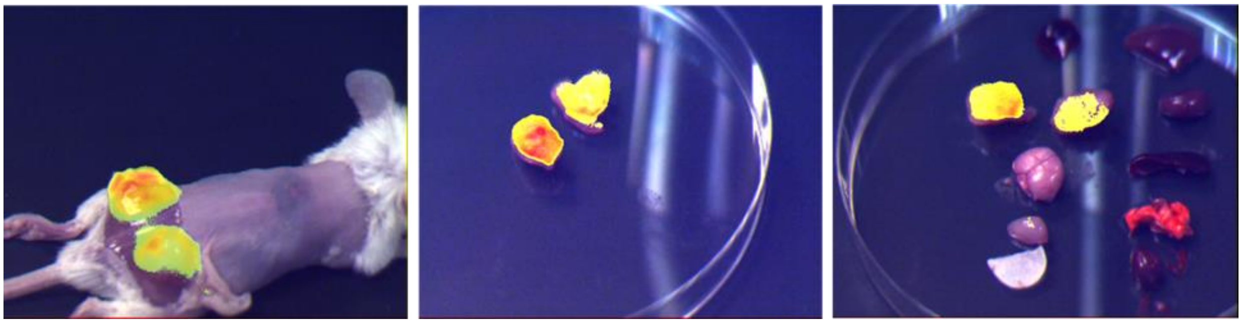

Figure 63: High contrast with clinical formulation of LS301.

Table 13: Toxicity assay results for LS301.

Species	Subjects	Dosage	Outcome
Mice	CD-1 IGS mice N= 40 male and female (drug) N= 20 male and female (control)	5.9 mg/kg (100X)	• No mortality was noted. • All animals survived until the planned sacrifice time points. • No clinical abnormalities were noted in any of the animals. • There were no hematology, clinical chemistry and mean organ weight differences between the treated and control groups
Dogs	4-month-old female N= 3	0.9 mg/kg (10X)	• All subjects remained bright, alert and responsive with no abnormal behavior throughout the study.

Based on these results we are currently doing a randomized clinical trial with canine cancer patients to test the efficacy of LS301 and GAINS for guiding cancer surgery. The study design is shown in **Fig. 64.** This will generate data for FDA application and approval of LS301 for human usage paving the way for targeted NIR FGS in human patients.

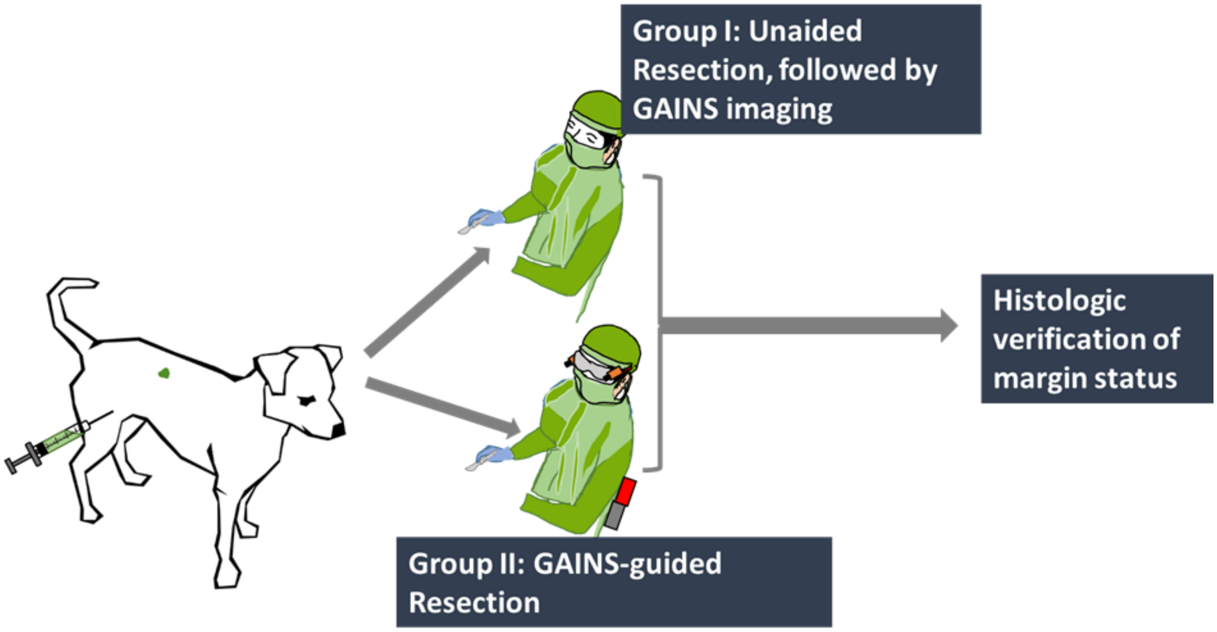

Figure 64: Overview of ongoing companion dog clinical trial to test LS301-GAINS guidance for cancer surgery.

Chapter 7: Conclusions

Surgery remains a critical option for cancer treatment. With widespread usage of cancer screening, more patients are diagnosed with early cancer. This has increased the importance of cancer surgery, as surgery is a curative option for early stage cancer, while minimizing the need for radiation or chemotherapy. However, pre-operative imaging modalities cannot provide real-time feedback to surgeons, and as a result surgeons have to still rely on their vision and touch to distinguish cancer from healthy tissue intraoperatively. This often leads to positive surgical margins that necessitate repeat surgery to avoid the risk of cancer recurrence. This highlights the need for intraoperative image guidance. Adapting preoperative imaging modalities like CT, PET and MRI is impractical due to their large bulk, cost and specialized operation. This has increased interest in optical methods due to high-resolution imaging while using simpler hardware that can be miniaturized (**Chapter 1, 2**). There is particular interest in fluorescence-guided surgery (FGS), especially by using near-infrared (NIR) fluorescence which has low tissue absorbance and allows deeper imaging (**Chapter 1**). **We have developed a set of requirements for an ideal image guidance system and detailed the design considerations for such a system.** While research in NIR-FGS has progressed rapidly, use of various optical imaging methods for image guidance during surgery or diagnosis of diseases has dramatically increased (**Chapter 2**). The time when more and more optical imaging systems will be integrated into routine clinical practice is not far. **We have discussed in detail some of the emerging optical imaging systems currently in the clinic or undergoing clinical investigation and also highlighted some of the barriers to routine clinical usage of optical imaging systems.**

Existing NIR-FGS systems are still bulky, have disruptive information display and cannot match the field of view (FOV) of the user with the camera. Additionally they require the surgical lights to be switched-off while performing FGS. This research aimed to address the limitations of existing NIR FGS systems. To that effect we were able to developed a wearable goggle augmented imaging and navigation system (GAINS) that can provide accurate intraoperative visualization of tumors and sentinel lymph nodes in real-time without disrupting normal surgical workflow (**Chapter 3**). GAINS projects both near-infrared fluorescence from tumors and the natural color images of tissue onto a head mounted display without latency. Aided by tumor-targeted contrast agent LS301, the system detected tumors in subcutaneous and metastatic mouse models with high accuracy (sensitivity = 100%, specificity = 98% ±5%). Human pilot studies in breast cancer and melanoma patients using near-infrared dye ICG show that the GAINS detected sentinel lymph nodes with 100% sensitivity. **We were able to demonstrate that clinical use of the GAINS to guide tumor resection and sentinel lymph node mapping promises to improve surgical outcomes, reduce rates of repeat surgery, and improve accuracy of cancer staging.**

Through our clinical study using the GAINS prototype to guide SLN visualization in human breast cancer and melanoma patients we gathered valuable feedback from surgeons that used the GAINS prototype. While surgeons liked the user experience from the prototype due to is ergonomic design and ease of integration into the surgical workflow, they helped us identify some limitations of the prototype. A major limiting factor was that the head-mounted display was video-see through and did not allow direct visual access to the surgical field. This limited the usage of the prototype for only visualization of the SLNs. Surgeons preferred to be able to directly see the tissue, while cutting and removing something. Another contributing factor to this issue was that we were using our own white light illumination with the NIR tail filtered off, while keeping the surgical light switched-off. Given that surgeons are trained to see and evaluate tissue under the surgical lights, they preferred to have it on, while resecting tissue and making medical decisions. Additionally, the imaging module focal distance had to be changed manually. As a result, large head movements, such as when the surgeon wanted to get a closer look made the images go out of focus.

To address the limitations of the initial VST GAINS prototype we developed an optical see-through (OST) GAINS prototype that had autofocusing and autocontrast capability. Additionally, we developed an illumination module that used a NIR laser for fluorescence excitation and a film-filter to cut-off the surgical light NIR tail. We performed preclinical validation and clinical evaluation of the OST GAINS prototype and the combined NIR-white illumination module (**Chapter 4**). For pre-clinical validation, three mice with subcutaneous tumors were injected with a tumor targeted NIR contrast agent LS301 (60µM, 100µl) and subjected to fluorescence-guided surgery. Three 35-kg female Yorkshire pigs received 300 ul of 5 mg/ml ICG, intradermally at their hind leg and lymphatics were tracked to the popliteal lymph node from the injection site. Four consecutive breast cancer patients scheduled to undergo partial mastectomy and SLN biopsy received ^{99m}Tc-sulfur and 5ml, 5mg/ml ICG retroareolarly. SLN biopsy was done using handheld gamma probe and OST GAINS enabled ICG imaging. The OST GAINS allowed direct visual access to the surgical bed while projecting fluorescence information directly to surgeon's eyes. Using tumor targeted NIR contrast LS301, it guided complete tumor resection in the subcutaneous mouse model of cancer with a SBR of 1.45 ± 0.19. It non-invasively tracked lymphatics in pigs using ICG, with a SBR of 2.74 ± 1.74 and accurately identified 4 popliteal LNs in three pigs with a SBR of 3.19 ± 1.81. A total of 11 SLNs were identified from 4 patients. Radioactive tracking SLN identified 9 (81.82%) SLNs with a detection sensitivity of 86.67± 0.27% and the OST GAINS identified 11 (100%) SLNs with a detection sensitivity of 100% and SBR of 2.14±0.83. There was no statistically significant difference in the detection sensitivities of the two methods (P=0.374). Using the combined NIR-white illumination module, all surgeries were formed with the surgical lights on. **We demonstrated that the see-through GAINS prototype is feasible for use in the operating room for NIR FGS for lymphatic tracking transcutaneously and SLN mapping in breast cancer patients, while keeping the surgical lights on.**

A major motivating factor for the research was identification of small tumor nodules and assessment of tumor margins and we evaluated GAINS for detecting spontaneous mouse tumors and assessment of tumor margins in human breast cancers (**Chapter 5**). For pre-clinical validation, five PyMT-MMTV mice were used that developed spontaneous breast cancer all along their mammary fat pad. These mice were injected with a tumor targeted NIR contrast agent LS301 (60µM, 100µl) and subjected to fluorescence-guided surgery, 24 hour post-injection. Three consecutive breast cancer patients scheduled to undergo partial mastectomy received 5ml, 5mg/ml ICG retroareolarly. Standard-of-care partial mastectomy was done followed by GAINS-guided fluorescence imaging of the tumor tissue and the tumor cavity to predict tumor margin status. The OST GAINS allowed direct visual access to the surgical bed while projecting fluorescence information directly to surgeon’s eyes. A total of a total of 97 tumors were resected with a mean of 19.4 ± 7.53 tumors per mouse. GAINS identified 89.61 ± 9.27% of the tumors with a sensitivity of 86.91 ± 11.11% and specificity of 80.0 ± 26.67%. Visual detection identified 78.08 ± 8.16% of the tumors with a sensitivity of 68.84.48 ± 9.57% and specificity of 100 ± 0%. The percentage of tumors detected and tumor detection sensitivity by GAINS were significantly higher than visual only method (P=0.00166, P=0.0022). A combined GAINS-visual approach identified 93.52 ± 7.33 % of the tumors with a sensitivity of 92.36 ± 7.4% and specificity of 80.0 ± 26.67%. GAINS accurately predicted margin status in all three patients, including clear margins in patients 1 and 2 and positive margins in patient 3. GAINS predicted margin status were confirmed by the final pathology report. **We demonstrated that combined GAINS and visual identification provide best guidance for tumor detection in spontaneous mouse model of breast cancer and it is feasible to use the GAINS for intraoperative margin assessment using ICG in human breast cancer patients.**

We are pursuing several future directions through ongoing work (**Chapter 6**). Based on our experience from animal studies and feedback from surgeons during our clinical studies, we have envisioned several design improvements. **The improved GAINS prototype will be ergonomic and have complete on-board real-time image processing along with real-time wireless data transmission capabilities.** Our current optical design allows only macroscopic image guidance. Microscopic resolution may broaden the scope for using GAINS for microsurgery such as brain cancer resections. **Future GAINS prototypes will be able to switch between macroscopic and microscopic image guidance.** The only NIR contrast agent currently approved for human usage is ICG which is not cancer targeted. We have developed a very cancer-specific NIR dye, LS301, which allowed GAINS to enable complete tumor resections in several animal models of cancer. We have demonstrated no toxicity for LS301 in detailed toxicity screenings and are applying for FDA approval for human usage of LS301 along with GAINS for surgical guidance. **Expected regulatory approval of LS301 and GAINS will pave the way for their wide clinical adoption and routine clinical use of NIR-FGS.**